NASA/TM-20240015880

NASA/FAA High Ice Water Content and Aerosols Flight Campaign (HIWC–2022) Final Report

Thomas P. Ratvasky
Glenn Research Center, Cleveland, Ohio

J. Walter Strapp
Met Analytics Inc., Aurora, Ontario, Canada

Masataka Murakami
Nagoya University, Nagoya, Aichi, Japan

Narihiro Orikasa
Meteorological Research Institute, Tsukuba, Ibaraki, Japan

Fred H. Proctor
Analytical Mechanics Associates, Hampton, Virginia

Aaron Bansemer
National Science Foundation, National Center for Atmospheric Research, Boulder, Colorado

Steven D. Harrah
Langley Research Center, Hampton, Virginia

April 2025

NASA STI Program Report Series

Since its founding, NASA has been dedicated to the advancement of aeronautics and space science. The NASA scientific and technical information (STI) program plays a key part in helping NASA maintain this important role.

The NASA STI program operates under the auspices of the Agency Chief Information Officer. It collects, organizes, provides for archiving, and disseminates NASA's STI. The NASA STI program provides access to the NTRS Registered and its public interface, the NASA Technical Reports Server, thus providing one of the largest collections of aeronautical and space science STI in the world. Results are published in both non-NASA channels and by NASA in the NASA STI Report Series, which includes the following report types:

- TECHNICAL PUBLICATION.
  Reports of completed research or a major significant phase of research that present the results of NASA programs and include extensive data or theoretical analysis. Includes compilations of significant scientific and technical data and information deemed to be of continuing reference value. NASA counterpart of peer-reviewed formal professional papers but has less stringent limitations on manuscript length and extent of graphic presentations.

- TECHNICAL MEMORANDUM.
  Scientific and technical findings that are preliminary or of specialized interest, e.g., quick release reports, working papers, and bibliographies that contain minimal annotation. Does not contain extensive analysis.

- CONTRACTOR REPORT.
  Scientific and technical findings by NASA-sponsored contractors and grantees.

- CONFERENCE PUBLICATION.
  Collected papers from scientific and technical conferences, symposia, seminars, or other meetings sponsored or cosponsored by NASA.

- SPECIAL PUBLICATION.
  Scientific, technical, or historical information from NASA programs, projects, and missions, often concerned with subjects having substantial public interest.

- TECHNICAL TRANSLATION.
  English-language translations of foreign scientific and technical material pertinent to NASA's mission.

Specialized services also include organizing and publishing research results, distributing specialized research announcements and feeds, providing information desk and personal search support, and enabling data exchange services.

For more information about the NASA STI program, see the following:

- Access the NASA STI program home page at http://www.sti.nasa.gov

NASA/TM-20240015880

NASA/FAA High Ice Water Content and Aerosols Flight Campaign (HIWC–2022) Final Report

Thomas P. Ratvasky
Glenn Research Center, Cleveland, Ohio

J. Walter Strapp
Met Analytics Inc., Aurora, Ontario, Canada

Masataka Murakami
Nagoya University, Nagoya, Aichi, Japan

Narihiro Orikasa
Meteorological Research Institute, Tsukuba, Ibaraki, Japan

Fred H. Proctor
Analytical Mechanics Associates, Hampton, Virginia

Aaron Bansemer
National Science Foundation, National Center for Atmospheric Research, Boulder, Colorado

Steven D. Harrah
Langley Research Center, Hampton, Virginia

National Aeronautics and
Space Administration

Glenn Research Center
Cleveland, Ohio 44135

April 2025

Acknowledgments

Many people contributed to the development and completion of this flight campaign, as well as the data acquisition, analyses, reporting, and archiving. The authors are grateful to all who supported and encouraged us through the various obstacles along the way. Special recognition is made to Tom Bond of the Federal Aviation Administration (FAA) for providing the original impetus for this flight campaign and to John Fisher, Chris Dumont, and Stephanie DiVito (all from FAA) for continued advocacy throughout the flight campaign development and execution. We are very grateful to Lyle Lilie and Dan Bouley from Science Engineering Associates for their dedicated support to equip, operate, and repair the in situ icing and aerosol instruments during the fast-paced and demanding schedule, and to Ru-Ching Chen from NASA Glenn for his willingness and enthusiastic support throughout the campaign. We are grateful to Josh DiGangi and Glenn Diskin from NASA Langley for operating the Diode Laser Hygrometer and providing this key dataset. We also thank Kris Bedka from NASA Langley for providing significant support with the precampaign climatology studies and for his guidance and support during and after the flight campaign. We are grateful to Ben Bernstein from Leading Edge Atmospherics and Matt Clarkson from Boeing for their forecast support and real-time tactical guidance, and to the entire NASA DC–8 team for the safe flight operation. We are grateful to Mr. M. Toda and Prof. A. Matsuki from Kanazawa University in Japan and to Dr. A. Iwata from Meteorological Research Institute in Japan for identifying ice-nucleating particle composition and characteristics for this report. We also thank Patricia Hunt from NASA Langley for the processing and quality control of the NASA research radar data, and Joseph Ardizzone from NASA Goddard for his support to retrieve and create Global Modeling and Assimilation Office (GMAO) maps for this report. We recognize Julie Haggerty from the National Center for Atmospheric Research (NCAR) for enabling the NCAR participation in the flight campaign and for the archival of these data for future analyses. Supporting numerical simulations were conducted with the Terminal Areas Simulation System (TASS) using the Pleiades high-performance supercomputer cluster of the NASA Advanced Supercomputing Division. This flight campaign and research was sponsored by the FAA's Aviation Weather Research Program, NASA's Advanced Air Vehicles Program through the Advanced Air Transport Technology project, and by Japan's Ministry of Land, Infrastructure, Transport and Tourism.

This work was sponsored by the Advanced Air Vehicles Program
at the NASA Glenn Research Center.

Level of Review: This material has been technically reviewed by technical management.

This report is available in electronic form at https://www.sti.nasa.gov/ and https://ntrs.nasa.gov/

NASA STI Program/Mail Stop 050
NASA Langley Research Center
Hampton, VA 23681-2199

Contents

NASA/FAA High Ice Water Content and Aerosols Flight Campaign (HIWC–2022) Final Report

Thomas P. Ratvasky
National Aeronautics and Space Administration
Glenn Research Center
Cleveland, Ohio 44135

J. Walter Strapp
Met Analytics Inc.
Aurora, Ontario L4G 4Y1, Canada

Masataka Murakami
Nagoya University
Nagoya, Aichi 464-8601, Japan

Narihiro Orikasa
Meteorological Research Institute
Tsukuba, Ibaraki 305-0052, Japan

Fred H. Proctor
Analytical Mechanics Associates
Hampton, Virginia 23666

Aaron Bansemer
National Science Foundation
National Center for Atmospheric Research
Boulder, Colorado 80307-3000

Steven D. Harrah
National Aeronautics and Space Administration
Langley Research Center
Hampton, Virginia 23681-2199

Executive Summary

This report documents the purpose, formulation, and results of the NASA/Federal Aviation Administration (FAA) High Ice Water Content and Aerosols Flight Campaign (HIWC–2022).

The primary purpose of this flight campaign was to collect new atmospheric data in deep convective storms in regions of high concentrations of anthropogenic aerosols to address a potential gap in the in situ cloud dataset that was collected through three flight campaigns in 2014 and 2015. The first flight campaign was conducted out of Darwin, Australia, using the Service des Avions Français Instrumentés pour la Recherche en Environnement (SAFIRE) Falcon–20 research aircraft. The second flight campaign was conducted from Cayenne, French Guiana, with the SAFIRE Falcon–20 and the National Research Council of Canada (NRC) Convair–580. The third flight campaign, called HIWC RADAR I, was

conducted from Fort Lauderdale, Florida, with the NASA DC–8 research aircraft. The dataset from these three campaigns (hereinafter "original dataset") was analyzed and documented in FAA report DOT/FAA/TC–18/1 to enable an assessment of the United States Title 14 Code of Federal Regulations (CFR) Part 33, Appendix D, and the corresponding identical European Union Aviation Safety Agency Certification Specification 25 (CS–25) Appendix P envelope. Both appendixes became effective in 2015.

In 2019, the Aviation Rulemaking Advisory Committee (ARAC) established an Ice Crystal Icing Working Group (ICIWG) to review the recent Ice Crystal Icing (ICI) flight campaign data and determine if the current regulations reflect the existing ICI environment. The FAA/TC–18/1 report was a primary document for the ICIWG review, and it noted that the original dataset was from regions with relatively low concentrations of anthropogenic aerosols, especially Darwin and Cayenne. The FAA/TC–18/1 report also provided a speculative, first-order hypothesis that high concentrations of aerosols acting as cloud condensation nuclei (CCN) may suppress a warm rain process in convective storm development, which may lead to more condensed water forming into ice above the freezing level—meaning that the total water content (TWC) data collected from regions of the world with high concentrations of CCN aerosol may have higher maximum and 99th-percentile values than data collected from regions with low concentrations of CCN aerosol. A plan to conduct another High Ice Water Content (HIWC) flight campaign in a high-CCN-aerosol region was presented to the ICIWG in November 2019, and the ICIWG subsequently recommended that the FAA and NASA conduct the flight campaign to address possible aerosol impact on their recommendations on Appendix D envelopes.

The flight campaign was originally intended to be conducted in the east Asia oceanic regions in 2021 based from Okinawa, Japan. A climatology study indicated this region had a high frequency of deep convective storms in the month of July along with high concentrations of anthropogenic CCN aerosols originating from continental east Asia. Due to the COVID–19 pandemic, it was necessary to delay the campaign timeframe to 2022. Additional complications with access to desired airspace and a base of operations forced an investigation of alternative locations for the campaign. Ultimately, the campaign was conducted out of Jacksonville, Florida, in July 2022, using the NASA DC–8 instrumented to collect in situ cloud and aerosol data.

Nine flights were made into deep convective oceanic storms off the U.S. mid-Atlantic coastal states, the Gulf of Mexico, and the Caribbean Sea to collect (1) high-TWC data in mesoscale convective systems (MCSs) at altitudes of 30 to 34 kft, (2) supporting in situ data in neighboring towering cumulus (TCu) clouds, and (3) boundary-layer aerosol data at altitudes of about 1 kft. Of these nine flights, only one flight was classified as being in a high-CCN-aerosol environment. One additional flight was dedicated to TCu cloud data at various altitudes and boundary-layer aerosol data to investigate microphysical development in early stages of convection and to look for evidence of the HIWC–2022 first-order hypothesis. Due to the lack of cases with MCSs co-located with high CCN aerosol, it was impossible to reach a conclusion regarding aerosol influence on TWC by simple comparison to the low-CCN-aerosol flights. To supplement the understanding of the influence that aerosols may have on TWC within MCSs, additional efforts were expended to conduct an extended literature review, a detailed investigation of the TCu data acquired in this flight campaign, and expanded cloud modeling.

The HIWC–2022 TCu results, all oceanic, showed that warm rain was always present at early stages of cloud development, even during the single high-CCN-aerosol flight. The literature review indicated that in continental high-CCN cases, warm rain in TCu could be completely suppressed. The differing HIWC–2022 results were attributed to the counteracting influence of large sea-salt aerosols (SSAs) creating large drops necessary for rapid warm rain development. Thus, it was concluded that the requirements for the first-order hypothesis were not met, and possibly would also not be met in highly polluted oceanic clouds in other regions such as east Asia. Ice particles were usually found to form

efficiently at about –9 °C, where an abundance of graupel and/or frozen drops and large droplets conducive to secondary ice production (SIP) were found. This was in contrast to continental observations in the literature that detected a delay in the formation of ice in high-CCN-aerosol clouds due to the apparent suppression of SIP via the absence of large droplets. Thus, the conditions for this possible second mechanism that could result in higher levels of TWC aloft were not found in HIWC–2022, even during the single high-CCN-aerosol flight.

In the absence of direct comparisons of TWC data from high-altitude, mature MCSs for low- and high-CCN cases, results from two cloud models provided the only such comparisons through sensitivity tests to different input aerosol levels. Both the NASA Terminal Area Simulation System (TASS) and the Nagoya University Cloud Resolving Storm Simulator four-ice (CReSS–4ICE) models showed that an increase in CCN resulted in a decrease in the domain-average ice water content (IWC_{Da}) at the mature stage, opposite to the HIWC–2022 first-order hypothesis. The countering results were hypothesized to be due to the complex kinematics and 3D interactions of growing and mature cells. Both models also showed that ice-nucleating particle (INP) concentrations acted in the opposite direction of CCN (i.e., an increase in INPs led to an increase in IWC_{Da}). If both CCN and INPs increased in a polluted environment, a net neutral result in IWC_{Da} could be obtained. It should be noted that although cloud models provide important direction on the behavior of the mature system, they are highly complex and do not strictly simulate all microphysical processes, and TWC levels aloft have not been carefully validated with observational data. Further, other MCS modeling studies in the literature have demonstrated sensitivity to parameters other than aerosol concentrations that should be considered when generalizing conclusions.

The apparent interaction between CCN and INPs in these models indicates that multiple aerosol influences may affect TWC levels aloft, and all should be taken into account when considering regional influences on TWC. For example, the tropical and subtropical regions of the northern hemisphere Atlantic Ocean contain high concentrations of Saharan desert dust, which are efficient INPs. These concentrations are typically at least an order of magnitude higher than those experienced in the oceanic regions of east Asia.

The HIWC–2022 data and the HIWC RADAR II flight campaign data were combined with the original datasets to determine to what degree the original data analysis provided to the ARAC ICIWG might have changed if all campaigns had been initially available. It was concluded that adding these two later campaigns resulted in only minor differences in maximum TWC, 99th percentile TWC, distance factor, and particle median mass diameter (MMD). HIWC–2022 MCSs were found to contain more frequent, short episodes of graupel, which were also present to a lesser degree in the original campaigns. Such graupel episodes with high TWC would likely result in only moderate changes in MMD with a second mass mode at roughly millimeter sizes. Due to reprocessing complexity, graupel effects remain unaccounted for in the particle mass-size dataset. This has been brought to the attention of the ARAC ICIWG, and no follow-up action has been requested.

While more insight into the effect of anthropogenic pollution on TWC levels aloft has been achieved through the HIWC–2022 campaign, in the end, it remains somewhat of an open question. HIWC–2022 demonstrated the difficulties faced by a Government agency in conducting such a campaign: access to the optimum geographical regions, risk of uncooperative weather, competing schedules for aircraft and instrumentation, requirements for expertise from collaborating scientific agencies, and requirements for sufficient funding. There are no current plans for the FAA and NASA to conduct a second high-aerosol flight campaign for ARAC objectives. In view of this, it is recommended that a periodic review be conducted of new in situ datasets and modeling results from the atmospheric and aviation communities to identify any new relevant information filling gaps in the original dataset. For in situ cloud datasets, it is important to note that the high-TWC environment is challenging, and special expertise and

instrumentation was developed specifically for the series of HIWC flight campaigns. Furthermore, for statistical comparison of new and original datasets, a compatible cloud sampling strategy is essential.

1.0 Introduction

1.1 Background on High Ice Water Content (HIWC) Campaigns

Over the past 30 years, high concentrations of ice crystals within deep convective storms have caused over 170 in-flight engine power-loss events and numerous air data probe anomalies on transport category airplanes (Refs. 1 to 9). In 2003, the joint Engine Harmonization Working Group (EHWG) and Power Plant Installation Harmonization Working Group (PPIHWG) was assembled by the Ice Protection Harmonization Working Group (IPHWG) to review requirements for engine and engine installation certification under supercooled large drops (SLD) and mixed-phase/glaciated icing conditions. The IPHWG was a working group tasked by the Aviation Rulemaking Advisory Committee (ARAC). The combined EHWG and PPIHWG was simply referred to as the EHWG (Ref. 10). In 2007, the EHWG proposed an interim mixed-phase/glaciated icing envelope based on engine power-loss event temperature and altitude data, estimates of total water content (TWC) derived from adiabatic calculations scaled to measurements from 1950s-era Royal Aircraft Establishment (RAE) reports, particle size data from the 1990s, and previously recommended liquid water content (LWC) levels in mixed-phase clouds (Ref. 11). The EHWG also recommended a new flight campaign be conducted to collect deep convective cloud measurements with modern instrumentation for assessment of the new interim "Appendix D."

Planning for a High Ice Water Content (HIWC) flight campaign was initiated in 2006 within an international collaboration of NASA, the Federal Aviation Administration (FAA), Environment Canada, the National Research Council of Canada (NRC), the Australian Bureau of Meteorology, the National Center for Atmospheric Research (NCAR), and the Boeing Company. The HIWC Science Plan (Ref. 12) was written to define the aviation and atmospheric science objectives for a flight test campaign to collect cloud in situ data.

In 2012, the European-led High Altitude Ice Crystal (HAIC) and HIWC projects established a collaboration that resulted in two HAIC–HIWC flight campaigns using the Service des Avions Français Instrumentés pour la Recherche en Environnement (SAFIRE) Falcon–20 aircraft. The first HAIC–HIWC campaign was conducted from Darwin, Australia, from January to March 2014 (Darwin 2014). The second HAIC–HIWC campaign was conducted from Cayenne, French Guiana, in May 2015 (Cayenne 2015) with the NRC Convair–580 joining the SAFIRE Falcon–20. Thirty-four Falcon–20 and ten Convair–580 research flights were accomplished during these two flight campaigns, which resulted in a substantial and unique compilation of cloud in situ microphysics data and remote sensing data in high-IWC conditions (Refs. 13 to 16). A third flight campaign (HIWC RADAR I) was conducted in August 2015 out of Fort Lauderdale, Florida (Ref. 17), using NASA's DC–8 research aircraft. The aircraft from these three campaigns were similarly instrumented for primary cloud in situ measurements, and the dataset from these campaigns (hereinafter "original dataset") was used to assess the cloud TWC and particle size in high-IWC conditions. The results of this assessment were documented in the FAA TC–18/1 report (Ref. 18).

Concurrent with the flight campaigns, the proposed rulemaking process was underway, and in 2015, the FAA established Title 14 Code of Federal Regulation (CFR) Part 33, Appendix D (Ref. 19) based on the interim icing envelope (Ref. 11), and the European Union Aviation Safety Agency (EASA) established the corresponding identical Certification Specification 25 (CS–25), Appendix P. This new appendix provided envelopes and tables that defined mixed-phase and ice crystal icing (ICI) atmospheric conditions for compliance with various Part 33 (engines) and Part 25 (transport category airplanes)

regulations that were updated through Amendment 33–34 and Amendment 25–140 in 2015. Appendix D, along with amended aviation regulations, was established to address and mitigate the aviation safety hazards associated with ICI.

1.2 ARAC Assessment of Appendix D and HIWC–2022 First-Order Hypothesis

In 2018, the FAA assigned the ARAC to provide recommendations on the ICI requirements defined by Appendix D and in regulations updated through Amendments 33–34 and 25–140. In 2019, the ARAC established the Ice Crystal Icing Working Group (ICIWG) and assigned the following eight tasks:

1. Evaluate recent ICI environment data obtained from both government and industry to determine whether flight testing data supports the existing Appendix D envelope.
2. Evaluate the results carried out in Task 1 and recommend changes to the existing Appendix D envelope, as required.
    a) Examine how compliance with §33.68(e) and §25.1093(b)(1) can be shown to demonstrate that at the airplane level, engine effects that could prevent the continued safe flight and landing of the airplane during encounters in ice crystal icing conditions would be extremely improbable (10^{-9}). If that cannot be shown, recommend changes to the text of §33.68 or §25.1093 (or a combination of both) that would provide the level of safety described by §25.1309(b)(1).
3. Compare available service data on air data probes from government and industry probes in Appendix D, including any changes proposed in Task 2. Determine whether engine or aircraft data probe responses warrant using a different environmental envelope from those proposed in Task 2 or to the existing Appendix D envelope.
4. Evaluate the results from Task 3 and recommend ICI boundaries relevant to aircraft and engine air data probes. If the working group proposes a different envelope for aircraft engine and air data probes, recommend if these should be included in the existing Appendix D, or create a new appendix to Part 33.
5. Identify nonharmonized FAA or EASA ICI regulations or guidance. If the working group finds significant differences that impact safety, propose changes to increase harmonization that may include icing environments other than Appendix D as a secondary objective.
6. Recommend changes to the Advisory Circular AC20–147A, Turbojet, Turboprop, Turboshaft, and Turbofan Engine Induction System Icing and Ice Ingestion, based on Task 1 through 5 results.
7. Assist the FAA in determining the initial qualitative and quantitative costs and benefits that may result from the working group's recommendations.
8. Develop a recommendations report containing the results of tasks 1 through 6. The report should document both majority and dissenting positions on the findings, the rationale for each position, and reasons for disagreement.

The FAA/TC–18/1 report was a primary source of recent ICI data used to assess Appendix D (Task 1), although Strapp et al. (Ref. 20) and Tritz et al. (Ref. 21) were other significant sources of analysis derived from the same original dataset. As shown in Figure 1, one key finding from these reports was that the flight campaign 99th-percentile TWC[1] (TWC_{99}) values at the reference 17.4-Nm distance

[1]The FAA/TC–18/1 report (Ref. 18) found that mixed phase in the high-altitude MCS traverses was rare, with low liquid water content (LWC) when encountered. The same was found for HIWC RADAR II and HIWC–2022. Therefore, for MCS traverses, total water content (TWC) and ice water content (IWC) are essentially equivalent in this report.

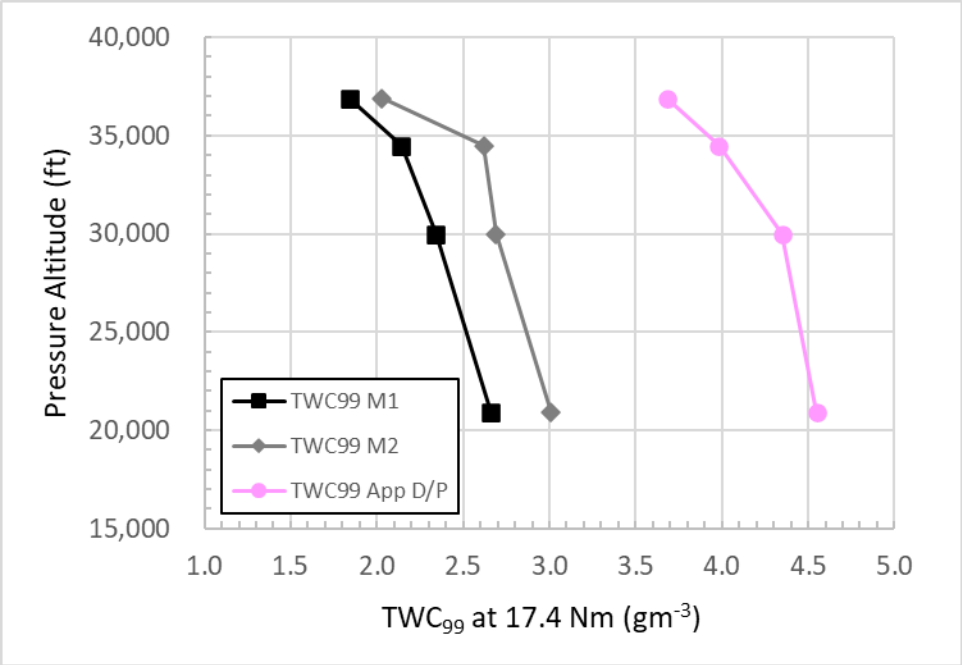

Figure 1.—Flight campaign composite *TWC*$_{99}$ values at 17.4 Nm versus pressure altitude, compared to Appendix D. Data adapted from Strapp et al. (Ref. 20) and Tritz et al. (Ref. 21). M1 refers to Method 1 of Reference 20 using Type 1 data points, and M2 refers to Method 2 of Reference 21 using Type 2 data points.

scale were significantly lower than those derived for Appendix D. In the FAA/TC–18/1 report (Ref. 18) and Reference 20, data were analyzed using what is referred to as "Method 1." This method used multiple back-to-back "Type 1" TWC data points for a given distance scale across a cloud traverse. The same data were reanalyzed in Reference 21 using Method 2. Method 2 retained only a single "Type 2" data point with the highest TWC per traverse, deriving it from a moving window rather than back-to-back points. Although the method of percentile calculation differed, the differences in *TWC*$_{99}$ produced by the two methods resulted almost entirely from the different data point definitions. Method 2 provided fewer data points comprised of only the highest TWC value per traverse, and thus provided a more extreme *TWC*$_{99}$ statistic. The composite flight campaign *TWC*$_{99}$ values ranged from 42 to 50 percent lower than Appendix D using Method 1, and 33 to 45 percent lower than Appendix D using Method 2. The ARAC ICIWG preferred the Method 2 *TWC*$_{99}$ results, as they provided a more conservative metric.

The FAA/TC–18/1 report (Ref. 18) identified four possible issues or gaps related to the global representativeness of the original dataset. First, the dataset was collected entirely during daylight hours, and there was some evidence in the atmospheric science literature that large convective cloud activity might be enhanced over nighttime hours. Second, most of the data were collected in large oceanic mesoscale convective systems (MCSs), with no data collected in large continental MCSs. In the most recent report on ICI engine events (Ref. 6), continental MCSs accounted for about 40 percent of engine-event clouds. Continental MCSs are typically more vigorous than oceanic MCSs, with higher updraft velocities, more lightning, and higher radar reflectivity factor (RRF) at flight altitudes. Accordingly, if continental MCSs were to contain higher TWC at flight altitude than oceanic MCSs, *TWC*$_{99}$ could be increased. But would those high-TWC areas be more likely avoided by pilots due to the lightning and high radar reflectivity? Third, the original dataset was collected from three regions of the world, and other regions could contain MCSs with different properties due to natural influences. Finally, the original flight campaigns were all collected in environments that were thought to have relatively low levels of cloud

condensation nuclei (CCN) aerosol (low pollution levels). The HAIC–HIWC science team recognized the body of atmospheric science work that pointed to potential changes in cloud microphysics in a polluted atmosphere that might yield higher TWC aloft. Such a scenario formed the basis for the HIWC–2022 campaign first-order hypothesis detailed below.

The effect of increasing aerosol levels in the atmosphere due to human activity has been a topic of significant interest in the atmospheric science community, largely due to its potential role in global climate change. Associated increases in CCN have been shown to produce a larger number of smaller droplets early in the cloud development. These smaller, lightweight droplets can ascend to higher altitudes and result in a higher cloud albedo. A second possible consequence of higher CCN concentrations is less likelihood of early "warm rain" during the condensation-coalescence phase of hydrometeor growth. In the presence of lower CCN concentrations, water vapor has fewer CCN particles to condense on, resulting in drops that are fewer in number but larger in size and higher in mass. As these drops interact, collide, and coalesce, their size and mass increase to a point where they are too heavy to be suspended, and they precipitate out of the cloud as drizzle and rain before reaching the freezing level. Rosenfeld (Ref. 22) discussed the suppression of warm rain by high CCN concentrations. Rosenfeld (Ref. 23) contended that in cases of heavy forest-fire smoke, the warm rain process could be practically shut down, and that increasing CCN concentration delayed the formation of warm rain "so that more water can ascend to altitudes where the temperature is colder than 0 °C." Based on these studies, the FAA/TC–18/1 report (Ref. 18) provided speculative statements on the potential effect of high concentrations of CCN aerosol on TWC levels. The statements are rephrased into the first-order hypothesis of HIWC–2022:

> ***High concentrations of aerosols may suppress a warm rain process in convective storm development, which may lead to more condensed water forming into ice above the freezing level.***

This hypothesis implied that the TWC in deep convective clouds from geographical regions with high concentrations of anthropogenic aerosols might have higher maximum and 99th-percentile values than those from regions with low concentrations of aerosols.

The ICIWG considered the original dataset gaps identified by the HAIC–HIWC science team and a potential low bias in the original TWC results. Concurrent to the ICIWG deliberations, a plan to conduct another HIWC flight campaign in a region with high CCN aerosol concentrations was being developed by the FAA, NASA, and Nagoya University. That plan was presented to the ICIWG in November 2019, and the ICIWG subsequently recommended that the FAA and NASA conduct the flight campaign to address the possible aerosol impact on TWC levels. At the time of this report, the ARAC assessment and the recommendations for Appendix D are ongoing.

1.3 Partnerships, Funding, and Schedules

Developing and executing the high-IWC and high-CCN-aerosol flight campaign required the technical expertise and instrumentation developed at NASA and the FAA through the previous HIWC flight campaigns and the technical expertise and instrumentation for cloud and aerosol studies developed at Nagoya University and Japan's Meteorological Research Institute (MRI). New agreements were formed between NASA and the FAA and between the FAA and Nagoya University. These agreements outlined the technical milestones and budget requirements. Additionally, Nagoya University received funding through a grant from Japan's Ministry of Land, Infrastructure, Transportation and Tourism

(MLIT). Each of these agreements and grants had timelines and funding requirements that needed close coordination across these organizations.

The initial plan presented to the ICIWG was to conduct a 3-week flight campaign in 2021 based out of Okinawa, Japan, using the NASA DC–8. The initial estimated budget was $2 million. After detailed planning and coordination with the NASA DC–8 project team and contracting specialists, the estimated budget rose to $3 million. The flight campaign timeframe slipped to July 2022 because of the COVID–19 pandemic and the availability of the NASA DC–8. Also, more time was needed to develop the agreements and contracts and to secure the required funding.

In addition to developing the agreement with Nagoya University, the FAA contracted subject matter expertise with Met Analytics, Inc.; Science Engineering Associates, Inc. (SEA); NCAR; and Leading Edge Atmospherics, LLC. The NASA Glenn Research Center managed the budget and coordinated with the NASA Langley Research Center to secure NASA science team member support and coordinated with the NASA Armstrong Flight Research Center for use of the NASA DC–8.

1.4 Flight Operations Area—Definition and Changes

Planning for the flight campaign required information on location and timing of deep convective storms and aerosols in the oceanic regions of east/southeast Asia. A 5-year (2015 to 2019) climatology study was performed to review aerosol optical depth (AOD) data from the Naval Research Laboratory (NRL) Aerosol Analysis and Prediction System (NAAPS) (Ref. 24) and Himawari Infrared (IR) satellite images for the months of July, September, and October. Although the study was subjective and considered to be nonrigorous, it provided insights into patterns of anthropogenic aerosol regional distribution and several categories of deep convective storms that occurred in that region during the summer months. The study identified July as the best month, with potentially 8.8 flights/month in deep convection with high boundary-layer aerosol concentrations, and enabled an operating area to be defined.

Detailed planning was ongoing during the remainder of 2020 and 2021. Kadena Air Base on the island of Okinawa was identified as a primary basing location for the flight campaign. The NASA DC–8 project managers and HIWC science team held briefings with Kadena officials and the U.S. State Department with assistance from the NASA Office of International and Interagency Relations (OIIR). The development of firm plans was hampered by the COVID–19 pandemic and the travel restrictions that were in place. Additionally, through discussions with NASA OIIR and the State Department, it became clear that political tensions would restrict flight operations in the most promising areas for high concentrations of IWC and CCN aerosol, and the operating area was reduced substantially to exclude the East China Sea Air Defense Identification Zone (ADIZ) and much of the Yellow Sea and South China Sea. Figure 2 shows the reduced operating area (yellow border), red range rings of 450 and 900 Nm from Okinawa, the ADIZs, and regions with high and low levels of CCN aerosol. Additionally, Figure 2 shows numerical values of surface monthly median AOD sulfate[2] levels during the month of July. The climatology study also found a fairly strong overnight strengthening of convection based on visual inspection of the IR satellite images. Results suggested that best takeoff time for high-CCN-aerosol flights would be 03:00 Japan time.

[2]Sulfate is a dominant anthropogenic aerosol and efficient CCN.

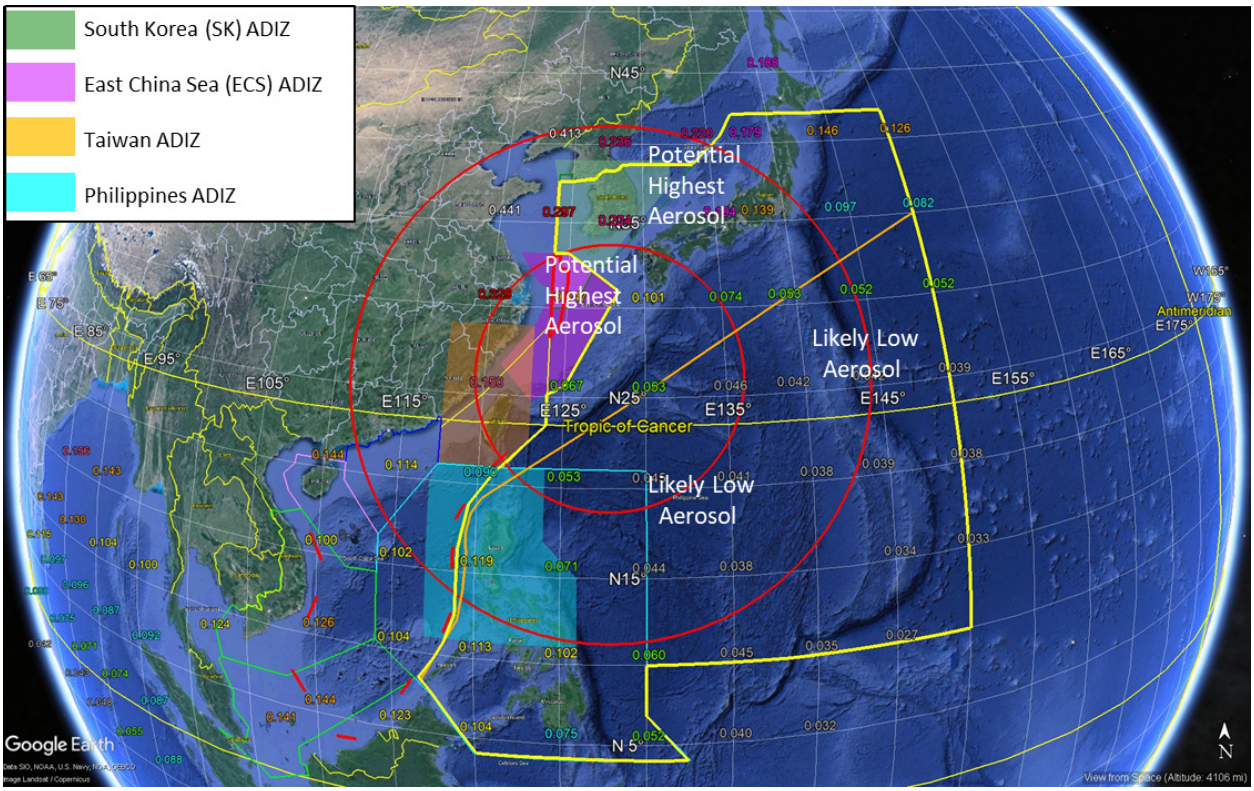

Figure 2.—Plan A: Proposed operating area (yellow border). Orange line approximates separation of high- to low-CCN-aerosol regions, with highest aerosol near coast of China. Range rings of 450 and 900 Nm from Okinawa shown in red. Air Defense Identification Zones (ADIZs) shown as shaded zones defined in legend.

To mitigate the risks that were mounting for the Japan flight campaign, a Plan B alternative was developed. A similar subjective climatology study was performed for the Bay of Bengal region, and it was found that similar opportunities for high-IWC and high-CCN-aerosol flights existed during the months of October and November. Figure 3 shows the region considered in this climatology. Numerical values represent median AOD of sulfate plus smoke during the month of October, showing a larger area in the Bay of Bengal of high CCN aerosol relative to the final flyable Plan A Japan region. For this climatology, high CCN aerosol (AOD values shown in Figure 3 as fuchsia or red) was arbitrarily defined as 3 times higher than the remote background AOD: an AOD ≈ 0.06. The investigation of MCSs identified on Himawari IR images yielded an expected 5.9 flights in a 23-day period, in MCSs lasting at least 11 h in high-CCN-aerosol conditions.

In February 2022, Kadena Air Base informed NASA that it was unable to support the HIWC flight campaign in July 2022 due to other mission priorities. This news, along with complications in obtaining visas to travel into Japan during the COVID–19 pandemic, forced the team to shift to Plan B. However, with only 8 months until the desired campaign start, there was insufficient time to plan and prepare for a Bay of Bengal campaign. Additionally, another NASA airborne science mission expressed interest in using the NASA DC–8 during the August–September 2022 timeframe, so another international deployment in October 2022 was not feasible. Consequently, Plan B was abandoned in late February 2022. A new Plan C was developed, and this plan was ultimately executed as the HIWC–2022 campaign in July 2022 out of Jacksonville, Florida.

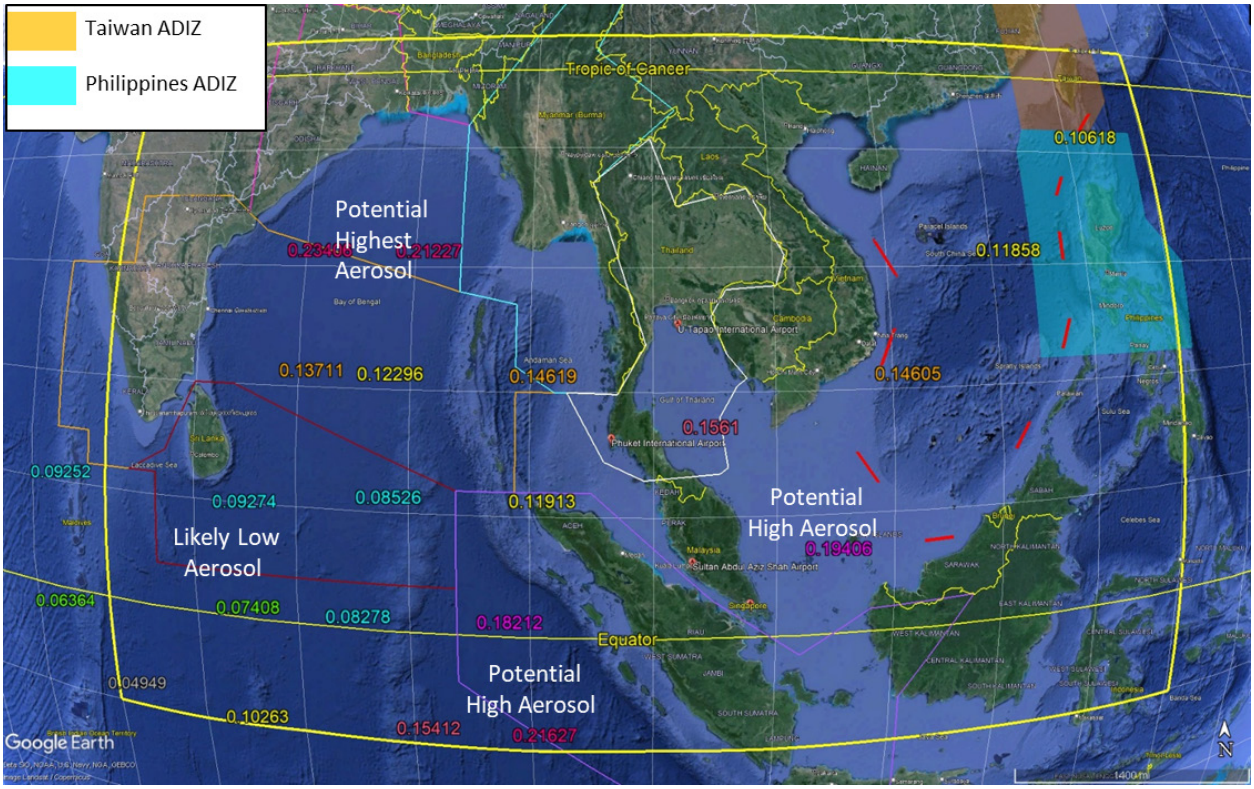

Figure 3.—Plan B: Climatology area (yellow border) with ADIZ. Text values are October median values of AOD of sulfate plus smoke.

A quick, subjective Plan C climatology study was conducted for the eastern Atlantic off the coast of the United States, the Gulf of Mexico, and the Caribbean. A 5-year (2013 to 2017) climatology study was performed again using NAAPS and Geostationary Operational Environmental Satellite 13 (GOES–13) IR satellite images for the month of July. For this study, moderate-to-high concentrations of CCN aerosols were defined as having NAAPS surface sulfate concentrations ≥1 μgm^{-3}. This climatology revealed that suitable MCSs embedded in high-CCN-aerosol regions were possible during July, but with greater risks than Plans A and B. The results indicated that 6.5 flights into MCSs with moderate to high boundary-layer aerosol concentrations were possible during a July campaign. The typical 6-h duration of the MCSs was shorter than for the Plan A and Plan B regions—a challenge for aircraft response time. The climatology suggested that MCSs would be more intense and frequent during nighttime hours, although this did not prove to be the case in July 2022. There was also a higher risk of a climatologically poor year for MCSs; for example, there were only 1.48 suitable targets per 23 days in 2016.

An operational area for Plan C, driven by the climatology, was developed to facilitate discussions with air traffic control (ATC) and to obtain country overflight clearances. Figure 4 shows the proposed operating area along with range rings of 450 and 900 Nm from Jacksonville, Florida. The pink regions indicate the general areas where higher aerosol conditions and MCSs were expected based on the climatology study.

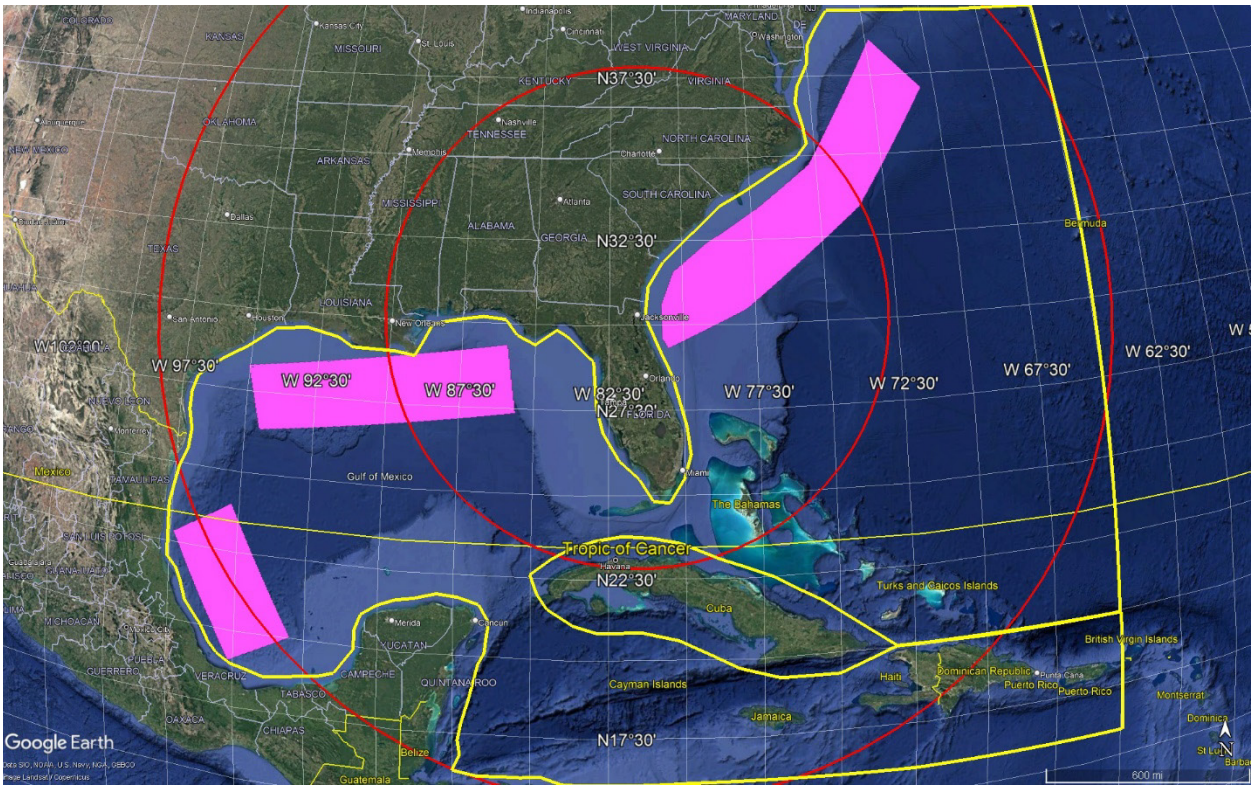

Figure 4.—Plan C: Proposed operating area (yellow border). Red range rings of 450 and 900 Nm from Jacksonville, Florida. Pink regions indicate areas identified by climatology study for MCSs with moderate to high CCN aerosol.

With the issues of funding availability, the NASA DC–8 schedule, partner commitments, and the ARAC ICIWG need for this new data, a delay to 2023 or beyond was not possible. The FAA, NASA, and Nagoya University agreed to accept the risks and proceed with a Florida-based HIWC–2022 campaign. The cost savings of a U.S.-based campaign enabled a 4-week operation instead of 3-week to mitigate the higher climatological risk, and an additional 10 flight-hours for research. It also enabled the HIWC team to piggyback in September 2022 on the NASA Science Mission Directorate's Convective Processes Experiment–Cabo Verde (CPEX–CV) (Refs. 25 and 26), where Nagoya University collected novel aerosol measurements in Saharan dust plumes and a limited TWC dataset was collected in deep convective clouds (Ref. 27), both over the Atlantic Ocean off the west coast of Africa.

2.0 HIWC–2022 Flight Campaign Objectives and Sampling Strategies

2.1 Campaign Objectives

To address the ARAC ICIWG request to the FAA and NASA, the primary objective of the flight campaign was to

- Evaluate the impact of aerosol concentrations on ICI within oceanic MCSs to determine if TWC_{99} values in a high-CCN-aerosol environment would be significantly different from the original dataset. This essentially entailed collecting a new dataset to evaluate the HIWC–2022 first-order hypothesis that was identified in Section 1.2.

Secondary objectives were to

- Measure aerosols in the regions surrounding MCSs and characterize microphysical properties of isolated developing towering cumulus (TCu) clouds in the vicinity of MCSs. The intent was to improve understanding of cloud microphysical processes affected by aerosols and improve cloud model prediction accuracy of MCSs and typhoons.
- Continue validation of satellite nowcasting and onboard weather radar algorithms to identify regions of high-IWC. These were enabling technologies for the current and future aircraft fleet to avoid hazardous ICI conditions.

2.2 Flight Sampling Strategies

The HIWC–2022 flight sampling strategies were similar to those of previous HAIC–HIWC and HIWC RADAR flight campaigns (Refs. 12 and 17) but also included flight legs at low altitude to acquire the aerosol data potentially influencing the MCS development and flight legs through developing TCu clouds (Figure 5). Generally, the flights had two parts. One part was at higher altitudes to collect cloud TWC and ice particle size distributions in a survey pattern of straight and level tracks through large convective storms. Ideally, these were MCSs that developed over the ocean with characteristic sizes larger than about 60 Nm, and cloud tops that reached at least –50 °C or, ideally, the tropopause. The second part of the flight was conducted at lower altitudes to collect aerosol data below cloud base and cloud microphysical data in developing TCu cells with typical diameters less than 10 Nm. In the best-case scenario, this portion of the flight would be in an airmass that fed into the same MCS explored in the high-altitude portion.

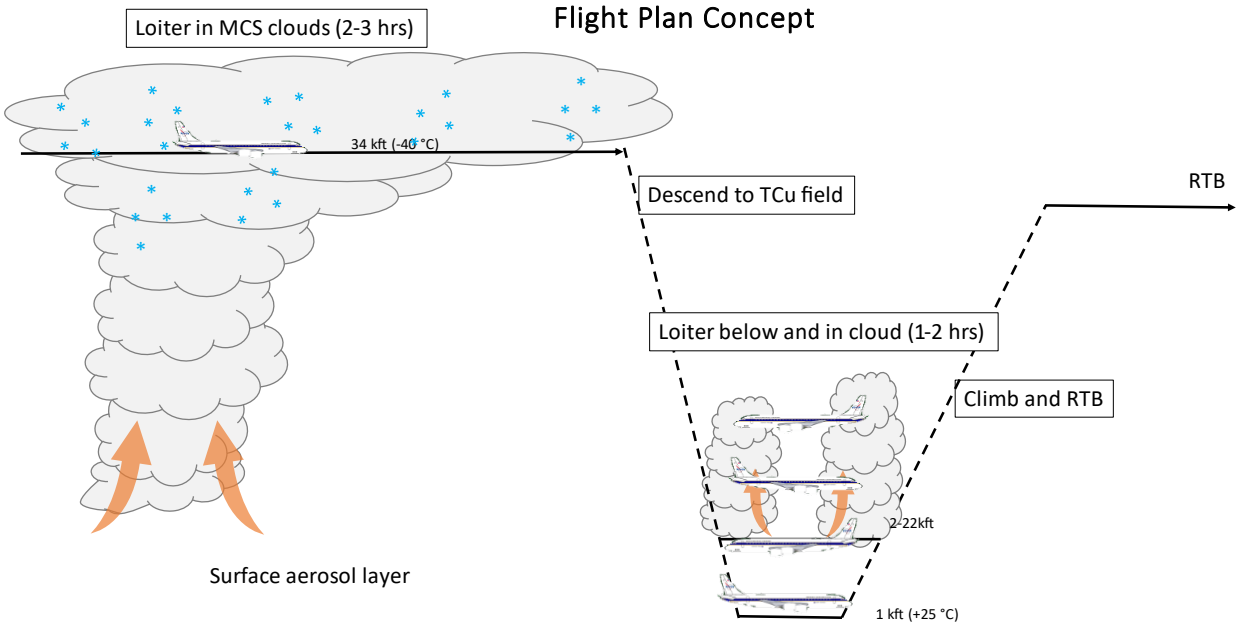

Figure 5.—Flight sampling strategy to acquire high-IWC cloud microphysics data in MCSs, aerosol data near ocean surface, and cloud microphysical data in developing TCu clouds. Return to base, RTB.

The HIWC science team estimated that a typical flight would last 6 to 8 h: 3 h for transit to and from the region of interest, 2 to 3 h for collecting high-IWC data at high altitude, and 1 to 2 h for collecting aerosol and TCu data at low altitude. Within a 4-week campaign, the maximum number of potential flight days was estimated to be about 21. Given the frequency of occurrence of the storms desired, and downtime to service instruments and review data, the science team estimated that seven to nine flights were feasible within a 4-week campaign. To distinguish the effect of boundary-layer aerosol concentrations on high-IWC levels in deep convection, the science team set a goal of five flights in MCSs with high concentrations of CCN aerosol and three flights in MCSs with low concentrations of CCN aerosol.

The original dataset provided TWC_{99} values at distance scales between 0.5 and 100 Nm and at altitudes associated with the following four atmospheric temperature intervals: –50±5, –40±5, –30±5, and –10±5 °C. The flight time planned for high-IWC sampling in this new campaign was insufficient to gather statistically significant high-IWC data at all four altitudes. Consequently, with the agreement of the ICIWG, the HIWC science team prioritized collection of data at the altitude associated with the –40±5 °C interval to collect a larger number of data points that would enable a more balanced comparison with the similar subset of the original dataset.

The TCu clouds were initially nonprecipitating and were present on the outer areas of the MCS. Cloud bases were typically above 2,000 ft, and tops varied between about 4,000 and 26,000 ft. The clouds were identified and selected visually by the flight crew, given that they were not likely to be visible on the pilot weather radar. The plan was to define and work an approximately 50-Nm circular region encompassing suitable TCu clouds in the vicinity of the MCS. The primary aerosol data were collected during an approximately 30-min run, typically about 1,000 ft above the ocean and at an altitude below cloud bases. Subsequent runs were made in TCu clouds just above cloud base, and at increments of several thousands of feet up to altitude corresponding to the approximately –20 °C level. While at each level, only clouds of a particular depth were chosen by the pilots such that the cloud penetration level was roughly 1,000 ft below the cloud top. In a growing cloud, the comparison of properties at each such level would then document the evolution of the microphysical properties with time (height), with minimal influence from the cloud above. Given that the TCu clouds of appropriate depth for the chosen level were not necessarily lined up ahead of the aircraft, pilots made turns to intercept the clouds as shown in the plan view of Figure 6. General observations from the aerosol and TCu measurements will be presented in Sections 5.1 and 6.3.1.

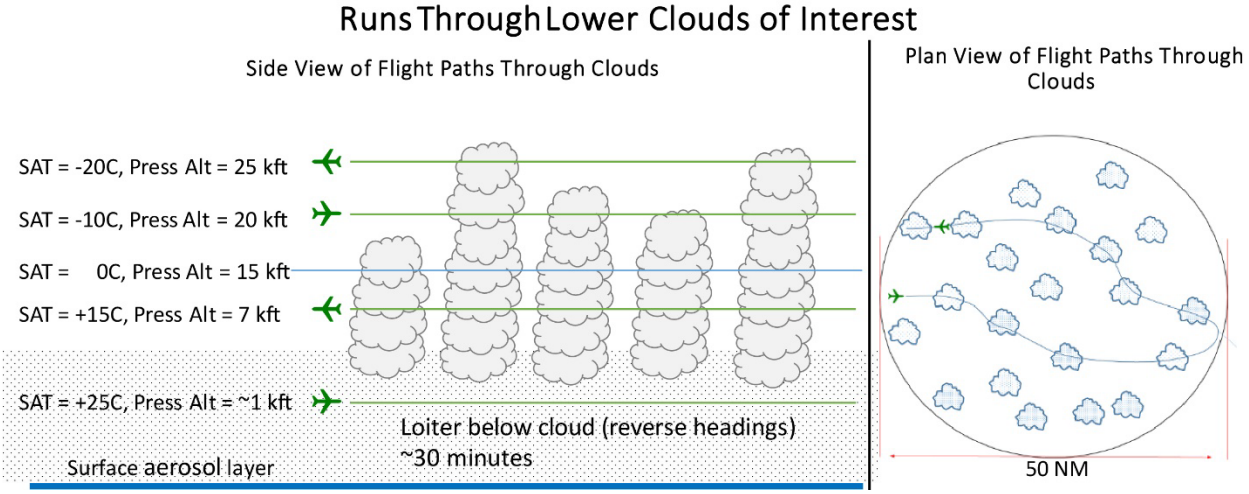

Figure 6.—Initial flight track plans for below-base aerosol sampling and in-cloud sampling of TCu clouds in vicinity of MCSs.

3.0 Instrumentation for High IWC and Aerosol on NASA DC–8

The NASA DC–8 (NASA 817) was an airborne research laboratory used for Earth, atmospheric, and space science missions. The DC–8 was a four-engine, turbojet aircraft with a range of 5,400 Nm, a ceiling of 41,000 ft, and a maximum flight duration of 12 h. The aircraft was highly modified to accommodate a wide variety of flight research experiments. These modifications included electrical power systems, viewports, wing pylons, window blanks, and fuselage panels to supply power and mount instruments and probe heads to measure in situ and remote conditions. These capabilities met or exceeded the HIWC–2022 flight campaign requirements. The NASA DC–8 was retired in May 2024.

The research instrumentation for the HIWC–2022 flight campaign is listed in Table 1 and shown in Figure 7.

Bulk IWC was measured with SEA's second-generation Isokinetic Probe (IKP2), a TWC[3] evaporator probe (Refs. 28 to 29). The IKP2 was mounted on the left-wing pylon at the inboard position. SEA Ice Crystal Detectors (ICDs) (Ref. 30) were mounted on the left-wing pylon near the IKP2 and on the fuselage nose near the pitot and total air temperature (TAT) probes to investigate localized ice concentration enhancement that may contribute to air data probe anomalies (Ref. 31).

TABLE 1.—INSTRUMENTATION FOR HIWC AND AEROSOL MEASUREMENTS FOR HIWC–2022

Water content	**Aerosol**
• SEA–NRC Isokinetic Probe 2 (IKP2) • SEA Ice Crystal Detectors (ICDs), wing and nose	• Particle Measuring Systems® (PMS) Passive Cavity Aerosol Spectrometer Probe (PCASP–100X), 0.1 to 3 μm; operated with deicing heaters on • University of Hawaii (Clarke) Shrouded Solid Diffuser Inlet • DMT Cloud Condensation Nuclei Counter (CCN–200) • TSI® Scanning Mobility Particle Sizer (SMPS 3080, 3081), 0.01 to 0.4 μm • TSI Condensation Particle Counter (CPC 3772) • RION Particle Counter (KC–01E), [Ranges: >0.3, >0.5, >1.0, >2.0, >5.0 μm] • ARIOS AS–24W (AS–TEM) and AS–16M (AS–SW): Impactors for aerosol sampling on electron microscopy (EM) mesh and silicon wafer, respectively; aerosol sampling holder fitted with hydrophobic PTFE membrane filter (MF)
Cloud particle sizing	
• DMT Cloud Droplet Probe (CDP–2), 2 to 50 μm • SPEC Two-Dimensional Stereo probe (2D–S), 11 to 1,408 μm • DMT Precipitation Imaging Probe (PIP), 100 to 6,200 μm	
Background water vapor (BWV)/Relative humidity (RH)	**Radar and lightning detection**
• Diode Laser Hygrometer (DLH) • Licor 850 (inlet on IKP2 canister) • Licor 840/SpectraSensors Water Vapor Sensing System (WVSS–II) (BWV inlet on side window) • Licor 840/Fluke 1620 relative humidity probe (flight deck RH)	• NASA Research RADAR (consists of a modified Honeywell RDR–4000 with LaRC real-time signal/data processing) • L3 Communications WX–1000E Stormscope®
	Airspeed/TAT/Ice accretion detector
	• DC–8 Pitot probes: Rosemount 0851CU–1 • Pitot-TAT: Rosemount 102DG2U–2 • TAT: Goodrich 102LJ2AG • Ice Accretion: Goodrich Ice Detector (0871LM5)

[3]TWC is the total condensed water content, equal to the sum of the cloud liquid water and IWC.

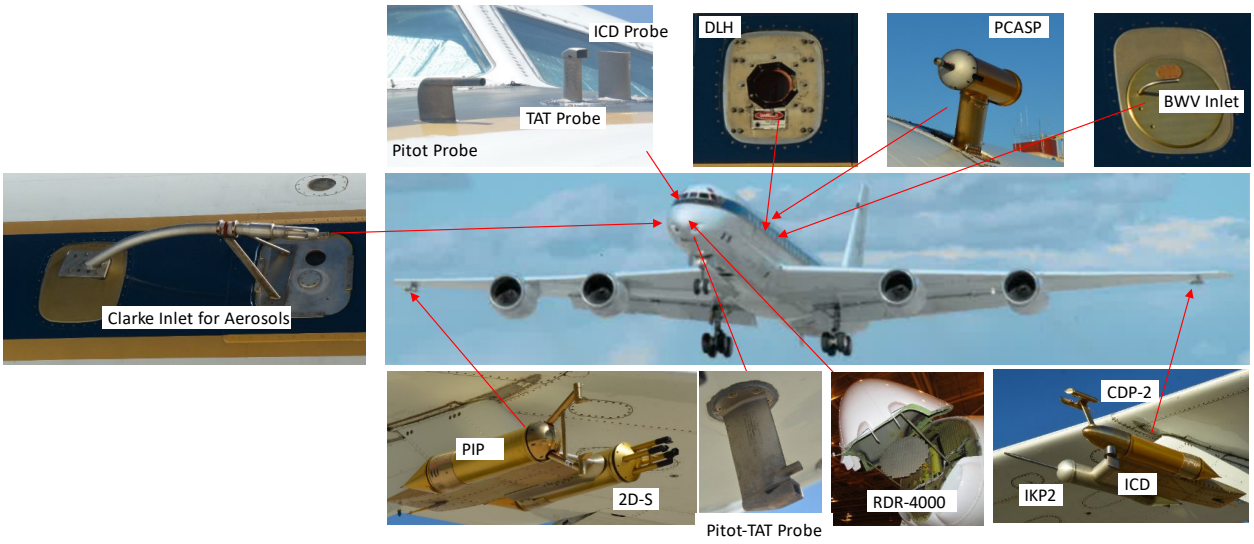

Figure 7.—HIWC and aerosol instrumentation on NASA DC–8.

To support the IKP2 TWC calculations, multiple background water vapor (BWV) measurements were made. The primary BWV measurement used the NASA Langley Diode Laser Hygrometer (DLH) (Refs. 32 to 33). The DLH utilized an open-path, double-pass configuration, where the path was defined on one end by a laser transceiver mounted on the interior of a modified window panel, and on the other end by a panel of retroreflecting material mounted on the DC–8's left outboard engine nacelle. Additional BWV measurements used a Licor LI–850 sampling from an inlet on the IKP2 canister, and a Licor LI–840A and SpectraSensors™ (SpectraSensors, Inc.) Water Vapor Sensing System (WVSS–II) mounted in the cabin and sampling ambient air through a reverse flow BWV inlet on a left side window blank near fuselage station 530.

The particle size distribution (PSD) was measured using the Droplet Measurement Technologies® (DMT) Cloud Droplet Probe 2 (CDP–2), a forward-scattering spectrometry probe, and two optical array probes (OAPs): a Stratton Park Engineering Company (SPEC) two-dimensional stereo (2D–S) probe and a DMT Precipitation Imaging Probe (PIP). The CDP–2 was mounted on the left-wing pylon, outboard position, on a canister nosecone. The 2D–S was mounted on the right-wing pylon, inboard position, and the PIP was mounted on the right-wing pylon, outboard position. All particle probes used antishattering tips to reduce measurements of shattered ice artifacts (Refs. 34 to 35).

Aerosol particles were sampled using a Particle Measuring Systems® (Particle Measuring Systems, Inc.) (PMS) Passive Cavity Aerosol Spectrometer Probe (PCASP–100X) mounted to the 62° viewport on the upper fuselage near fuselage station 440 and the University of Hawaii "Clarke" shrouded diffuser inlet (Ref. 36) mounted on the right side of the DC–8 at fuselage station 570. This inlet routed ambient air to a manifold within the aerosol instrument rack, where it was distributed to specific instrumentation and then exhausted through vent ports mounted to a right-side window near fuselage station 1290. A hand-operated gate valve was used to control the total flow rate through the air line to maintain isokinetic flow at the inlet. The primary aerosol instrumentation rack with specific instruments labeled is shown in Figure 8. CCN number concentration was measured with a dual-column DMT CCN–200 unit that was mounted in another rack just forward of the primary aerosol rack.

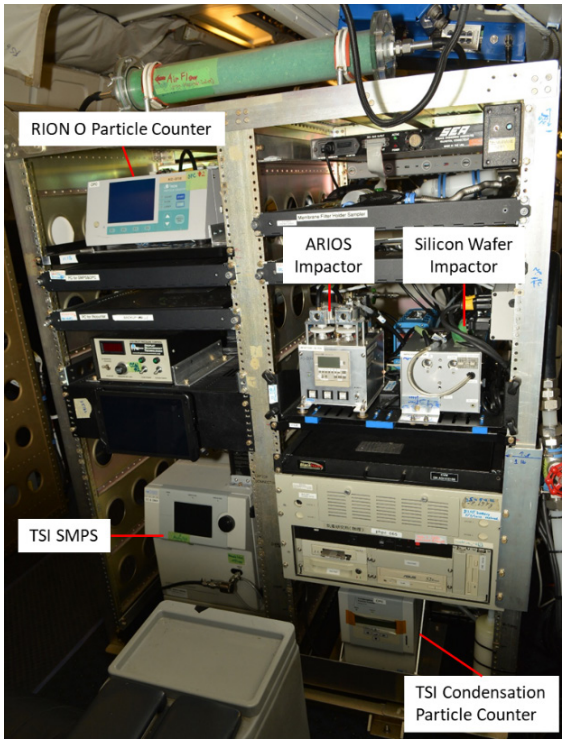

Figure 8.—Aerosol instrumentation rack with specific instruments identified.

During the flights, weather conditions were monitored by the pilots and researchers using the NASA Research RADAR. This system was developed cooperatively between the NASA Langley Research Center and Honeywell Aerospace (Redmond, Washington). The radar consisted of a modified Honeywell RDR–4000 and NASA signal and data processing hardware. The commercial product provided flight safety radar measurements traceable through FAA-certified radar technology, whereas the research product allowed flexible, customizable processing and displays and enabled recording of the fundamental radar measurements (in-phase and quadrature (I&Q) voltages) (Ref. 37). These radar recordings allowed a nearly unlimited examination of the radar echoes as if they were all being performed in flight. The availability of the radar on these flights enabled choosing specific flight paths that allowed encounters with HIWC and avoidance of high radar reflectivity factor (RRF) regions that could possibly contain hail.

Additional measurements were made to support the primary and ancillary analyses. For example, airspeed, air temperature (total and static), pressure altitude, and Global Positioning System (GPS) location were all provided by DC–8 standard systems such as the DC–8 pitot probes (Rosemount 0851CU–1.) A Rosemount pitot-TAT probe (model 102DG2U–2) was also mounted on the lower fuselage nose to provide total pressure to derive an auxiliary airspeed given that the DC–8 pitot probes had a history of pitot anomalies in high-IWC conditions. A research TAT 102LJ2AG probe was mounted on the fuselage nose near the SEA ICD to investigate localized ice concentration factors and the potential for TAT and pitot probe anomalies (Ref. 38). Ice accretion due to supercooled water drops was measured with a Goodrich Ice Detector (model 0871LM5) mounted on the nose near the DC–8 pitot probes. An L3 Communications WX–1000E Stormscope® (L3 Technologies, Inc.) was also integrated on the DC–8 to provide lightning detection range, bearing, and strike rate information to the flight crew and research team.

4.0 HIWC–2022 Flight Campaign Execution and Flight Summaries

The HIWC–2022 flight campaign was conducted from 2022-07-05 to 2022-08-01, based out of Cecil Airport (VQQ) near Jacksonville, Florida. During this time, 10 research flights were conducted. Only one flight (2022-07-30) was conducted near and in an MCS with high boundary-layer CCN aerosol concentrations. Seven of the flights were conducted near and in MCSs that were rooted in environments with low boundary-layer CCN aerosol concentrations. The levels of CCN aerosol for the 2022-07-27 flight were classified as potentially moderate. See Section 5.1 for a discussion on the relative aerosol, CCN, and droplet number concentrations associated with these low, moderate, and high aerosol designations. Lastly, one flight (2022-07-26) was dedicated to lower altitude measurements only (boundary-layer aerosol and TCu). Figure 9 displays the flight tracks for all 10 flights.

Counter to the climatology expectations, all flights were conducted during daytime hours. Longer range outlook weather forecasts indicated sufficient MCS opportunities would occur during the daytime hours, and switching to nighttime operations would have required additional downtime to adjust to a new operations schedule. The decision was made to maintain daytime operations to have more flight opportunities during the 27-day deployment.

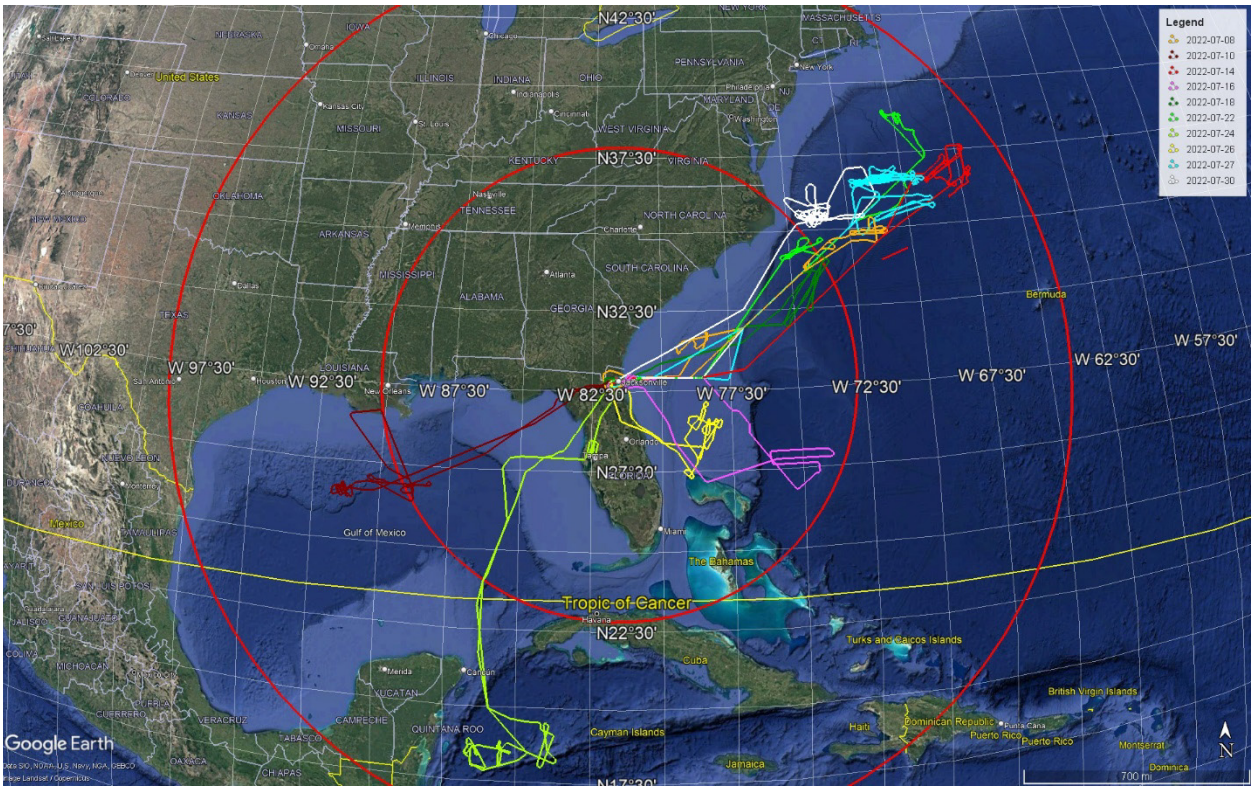

Figure 9.—Tracks of HIWC–2022 Flight Campaign. Red range rings indicate 450 and 900 Nm from Cecil Airport, Jacksonville, Florida.

Clearly, with only one case of an MCS with high CCN aerosol concentrations within the boundary layer, the HIWC–2022 objective of performing a convincing comparison of TWC subsets from cases of high and low CCN aerosol concentrations could not be reached. Section 5.5 nevertheless provides such comparisons for documentation. In Section 5.6, the additional flight data of HIWC RADAR II[4] and HIWC–2022 was used to determine whether these two campaigns would have significantly changed the data provided to ICIWG for Appendix D assessment had they been added to the original dataset. Section 6.0 discusses other efforts within HIWC–2022 to investigate the effect of aerosol concentrations on TWC levels, including a literature review, an analysis of the TCu measurements and their bearing on the HIWC–2022 first-order hypothesis, and a summary of predictions of IWC sensitivity to aerosol from two numerical cloud models.

4.1 Obstacles To Achieving Desired Flights in High-CCN-Aerosol Conditions

As written in Section 2.2, the science team set a goal of five flights in MCSs with high concentrations of CCN aerosol in the boundary layer and three flights in MCSs with low concentrations of CCN aerosol in the boundary layer to distinguish the impact of CCN aerosols on IWC levels in deep convection. Several unanticipated obstacles impeded the team from reaching that goal. The primary issue was that low concentrations of CCN aerosol conditions prevailed over much of the operational area during most of the campaign due to a high-pressure system centered near Bermuda. The clockwise circulation pattern at lower altitudes associated with the "Bermuda high" drew in air with relatively low concentrations of CCN aerosol from east of the Caribbean toward the east coast of the United States, and pushed high-CCN-aerosol air originating over the continental United States toward the north/northeast. The Bermuda high circulation's effect on the distribution of sulfate aerosols is illustrated in Figure 10.

The image in Figure 10 is from the NASA Global Modeling and Assimilation Office (GMAO) website, which provides global atmospheric composition forecast maps of various constituents, including sulfates and dust. The forecasts are based on aerosol predictions from a general circulation model coupled with emission inventories, chemical reactions, constituent advection and deposition, and satellite observations to provide map predictions of aerosol component concentrations with airflow vectors. As part of preflight forecasting and planning, the HIWC–2022 team examined sulfate maps at the 925-hPa level (approximately 2,500 ft pressure altitude) to help identify the region of interest for the flight.

Figure 10 illustrates how the Bermuda high circulation pattern pushed clean air toward the southeastern United States Atlantic coast that made a narrow corridor of high-sulfate air close to the U.S. coastline northeast of Georgia. This was a reoccurring observation during the campaign. Additionally burdensome, the airspace between the U.S. coastline and about 150 to 200 Nm seaward was often reserved for military special use (Figure 11), and the NASA DC–8 was usually not permitted to fly into that airspace. On multiple flight days, storms formed inside the special use airspace and were in regions forecasted to have the best and often only high-CCN-aerosol conditions. Unfortunately, these storms frequently decayed as they moved eastward beyond the special use airspace.

[4]The HIWC RADAR II flight campaign was conducted in August 2018 to collect validation data for the radar-derived IWC algorithm developed by NASA Langley (see Section 5.7). Flights into MCSs were based out of Fort Lauderdale, Florida; Palmdale, California; and Kona, Hawaii.

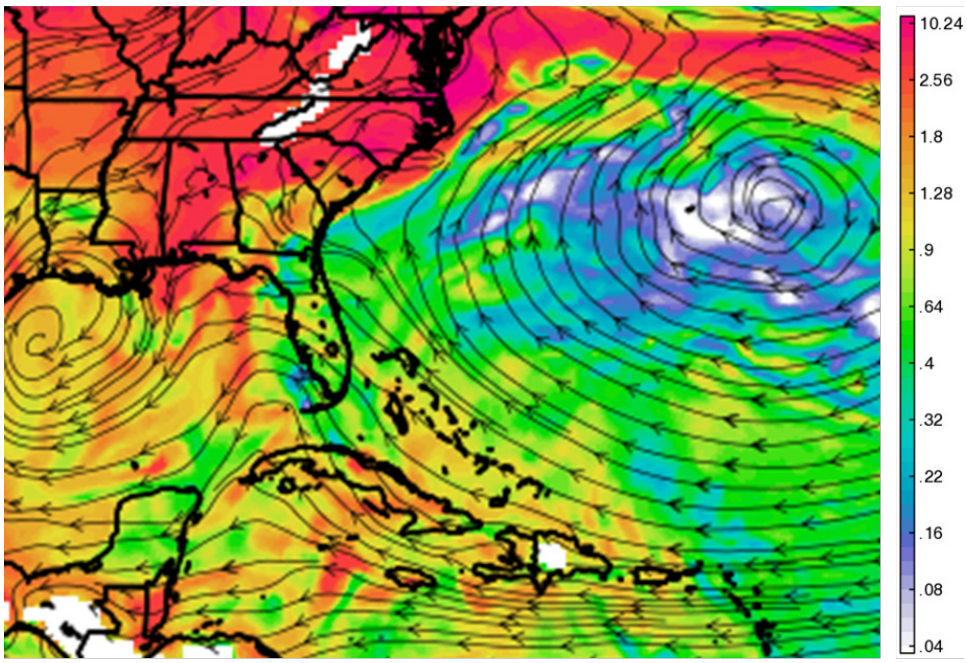

Figure 10.—NASA GMAO atmospheric composition forecast map of sulfate at 925 hPa for 2022-07-16.

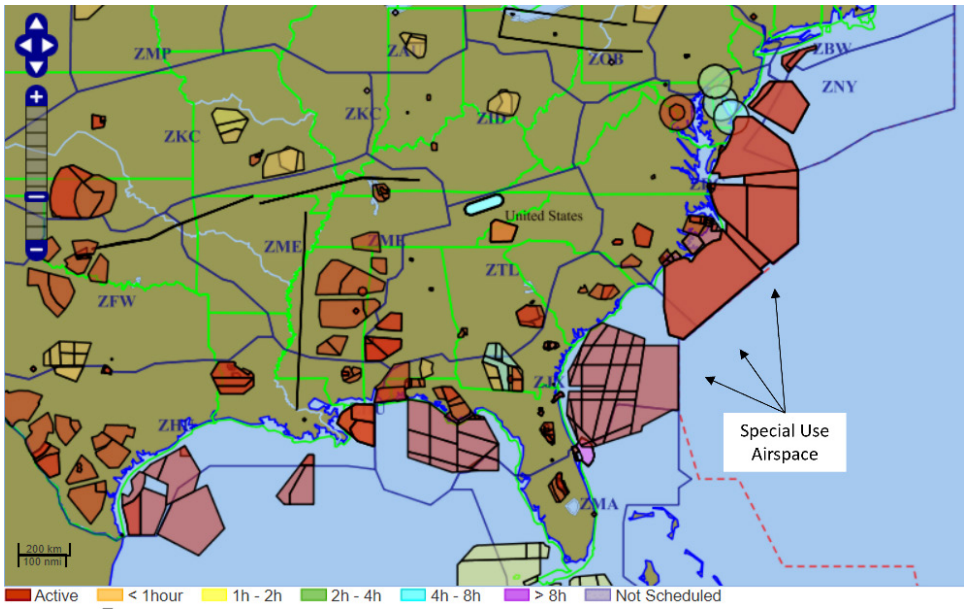

Figure 11.—FAA map of special use airspace. https://sua.faa.gov/sua/siteFrame.app

Lastly, three flights were terminated early, one due to a lightning strike on the DC–8 (2022-07-16) and two due to cabin pressurization control issues (2022-07-18 and 2022-07-30). In each case, incomplete or reduced datasets were collected. For the flights of 2022-07-16 and 2022-07-18, no low-altitude measurements were made to confirm boundary-layer aerosol concentrations, and both flights have been assumed to be low-CCN cases based on other data (Section 5.1.1). The flight on 2022-07-30 sampled the only MCS in a boundary layer with a confirmed high concentration of CCN aerosol. It was an ideal case of a large and long-lived active MCS, but only two high-level cloud traverses were performed due to the precautionary early return to base (RTB) because of a cabin pressure issue.

4.2 Preflight Planning/Plan of the Day

The 5-year climatology indicated that MCSs associated with moderate-to-high CCN aerosols in July occurred more frequently during the nighttime hours. As stated in Section 4.0, all flights in this campaign were conducted in daytime hours, primarily because the MCS options were similar to those at nighttime and the shift to night-time operations would require another down-day for the team to adjust to the new schedule. The climatology also indicated that the MCSs had lifecycles of approximately 6 h. The relatively brief duration of the MCSs required flight plans to be based on forecasts rather than nowcasts of active convective systems. Preflight plans started with a weather forecast team reviewing the National Oceanic and Atmospheric Administration (NOAA) High-Resolution Rapid Refresh (HRRR) and North American Mesoscale (NAM) operational weather model forecasts, NASA GMAO Atmospheric Composition (3D) Forecast Map of sulfate aerosols, IR and visible satellite imagery, NOAA Next Generation Weather Radar (NEXRAD), and other meteorological products to develop weather briefings. These briefings, which included proposed target areas for the flight of the day, were presented to the science team and a DC–8 navigator approximately 5.5 h before the proposed takeoff time. Discussion by the science team led to a final selection of target area and takeoff time, and a Go/Delay/No-Go decision was announced to the rest of the team about 4.5 h prior to takeoff. The DC–8 navigator then developed an aviation flight plan and submitted it to ATC. A second weather briefing was held at the airport base of operations approximately 2.5 h before the intended takeoff, and the target location and takeoff time were updated if needed. Concurrent with these activities, the DC–8 and research instruments were prepared for flight. Table 2 provides an example of the Plan of the Day.

TABLE 2.—PLAN OF THE DAY EXAMPLE

Thursday, 2022-07-14 – Science Flight 3		
	UTC	Local
Fuel load: 110,000 lb		
Flight crew rest begins (Wednesday, 2022-07-13):	23:30	19:30
Forecaster starts prepping weather (WX) brief:	07:00	03:00
Initial Weather brief (at hotel, Teams link in email):	08:30	04:30
Initial flight decision (at hotel); Maintenance team departs for VQQ:	09:30	05:30
Maintenance preflight start; Science team departs for VQQ:	10:30	06:30
2nd Weather brief start (B884, Teams link in email):	11:30	07:30
Start science instrument preflight:	11:30	07:30
Flight crew departs hotel (start of duty day):	11:30	07:30
File flight plan:	12:00	08:00
Preflight brief (B884)/Aircraft crew ready:	12:30	08:30
Door close:	13:30	09:30
Engine start:	13:35	09:35
Taxi:	13:50	09:50
Takeoff:	14:00	10:00
Land:	21:00	17:00
Flight crew duty day expires:	01:30	21:30

4.3 Flight Summaries

Table 3 provides the dates, times, general locations, basic information on the TWC and aerosol levels, and comments and observations for each of the 10 research flights.

Nomenclature is given in Appendix 1. Appendix 2 provides figures with flight tracks and time histories of altitude, temperature, MMD, and TWC for the 10 research flights. Annotations on the flight tracks indicate the general locations of the high-altitude (HA) traverses in the MCSs and low-altitude (LA) traverses for boundary-layer aerosol and TCu measurements. The IR satellite image in these figures is for a nominal time during the traverses through the MCSs and does not show the progression and decay of the storm during the flight. The cloud movement and evolution can be viewed at the NASA Langley satellite website (Ref. 39). The deepest convection was typically associated with the coldest cloud-top temperatures as indicated by the white and purple color levels. Time histories are limited to the periods in the clouds of interest and are annotated to indicate specific events such as pitot anomalies or lightning strikes.

Appendix 3 provides figures of the NASA GMAO model forecasts of aerosol sulfate (SO_4) and aerosol dust for each flight. The general location of the high-altitude and low-altitude traverses are annotated on these forecast maps. In each case, the model was initiated at 00:00 UTC for the flight date and the model validation time was consistent with the flight time.

TABLE 3.—FLIGHT DATES, TIME, AND RELEVANT INFORMATION

Flight date	Takeoff, UTC	Land, UTC	Flight time, h	Region	HIWC in MCSs	[a]Average aerosol, cm^{-3}	Comments and observations
2022-07-08	15:25	20:49	5.4	Off mid-Atlantic coast	8 runs at 34 kft (–41 °C) Peak IWC: 2.3 g/m^3 Time in cloud>1.0 g/m^3: 11.9 min	PCASP = 235 CCN = NA	One MCS well offshore; edges of MCS drifting out of military area. Air data computer 1 (ADC1) pitot anomalies at two time periods (17:22 and 17:30).
2022-07-10	16:10	22:18	6.1	Central Gulf	7 runs at 34 kft (–38 °C) 1 runs at 30 kft (–28 °C) Peak IWC: 3.5 g/m^3 Time in cloud>1.0 g/m^3: 25.1 min	PCASP = 160 CCN = NA	Two large MCSs; highest peak TWC of campaign. ADC1 and ADC2 pitot anomalies at two time periods (17:10 and 19:14). Lightning strike about 17:51. Graupel damage to ICDs (undetected).
2022-07-14	13:50	20:43	6.9	Off mid-Atlantic coast	9 runs at 34 kft (–41 °C) Peak IWC: 1.6 g/m^3 Time in cloud>1.0 g/m^3: 9.0 min	PCASP = 85 CCN = NA	MCS cells drifting rapidly out of special-use military area.
2022-07-16	14:02	18:21	4.3	North of Bahamas	4 runs at 30 kft (–33 °C) Peak IWC: 2.0 g/m^3 Time in cloud>1.0 g/m^3: 14.1 min	NA	Large MCS with multiple active areas. Lower altitude than previous flights due to ATC/air traffic. Lightning strike about 16:07. Flight terminated early. No low-level measurements.
2022-07-18	16:06	21:14	5.1	Off NC and SC coasts	7 runs at 34 kft (–41 °C) Peak IWC: 2.3 g/m^3 Time in cloud>1.0 g/m^3: 12.3 min	NA	MCS cells forming in special-use military area and drifting eastward. Worked cells outside special-use area. Flight terminated early due to cabin pressure control issue. No low-level measurements,
2022-07-22	12:01	18:36	6.6	Off NC and VA coasts	3 runs at 34 kft (–41 °C) 2 runs at 32 kft (–35 °C) Peak IWC: 2.6 g/m^3 Time in cloud>1.0 g/m^3: 16.4 min	PCASP = 109 CCN = 361	Low-altitude exploration of high-aerosol region well to northeast, then opportunistic sampling of nice MCS in special-use military area.
2022-07-24	11:35	18:59	7.4	East of Yucatan Peninsula/ south of Cuba	1 run at 35 kft (–44 °C) 1 run at 34 kft (–41 °C) 2 runs at 33 kft (–38 °C) 1 run at 30 kft (–30 °C) Peak IWC: 2.2 g/m^3 Time in cloud>1.0 g/m^3: 2.4 min	PCASP = 71 CCN = 174	Multiple medium-sized cumulonimbus clouds sampled, no large MCS.
2022-07-26	11:33	15:15	3.7	Off east coast of Florida	NA	PCASP = 77 CCN = 196	Dedicated flight for TCu and aerosol sampling. Could not get ATC clearance for lowest level aerosol and cloud base runs.
2022-07-27	9:58	19:10	9.2	Off coast of VA	9 runs at 34 kft (–41 °C) Peak IWC: 2.6 g/m^3 Time in cloud>1.0 g/m^3: 44.8 min	PCASP = 153 CCN = 741	Large MCS with multiple long traverses. High-altitude sampling before and after low-altitude sampling for aerosol and TCu. First high-level run directly over low altitude on north side of storm; second high-level run on south side.
2022-07-30	13:43	20:36	6.9	Off Carolina Coast	2 runs at 34 kft (–40 °C) Peak IWC: 2.0 g/m^3 Time in cloud>1.0 g/m^3: 12.7 min	PCASP = 840 CCN = 1,239	Large MCS, sole case with confirmed high boundary-layer aerosol concentrations. High- and low-altitude sampling, though high-altitude sampling terminated early. Attempted runs at 39 kft but could not maintain cabin pressure control. Flight terminated early.

[a]PCASP and CCN concentrations are average values in the boundary layer, typically over 30 min.

5.0 Results and Discussion

Data from the in situ and remote sensing instruments from these flights were processed and subsequently archived on the Earth Observation Laboratory (EOL) archive at the following website: https://www.eol.ucar.edu/field_projects/HIWC–2022. Datasets include aerosol measurements, TWC measurements from the IKP2, and water vapor data from the DLH in addition to cloud particle probe microphysics, pilot weather radar data, and GOES–16 satellite convective cloud products.

5.1 Aerosol Observations

5.1.1 Identifying Aerosol Levels of CCN and Dust for Each HIWC-2022 Flight

The following information was used to categorize the MCS measurements in each flight as being from low-, moderate-, or high-CCN boundary-layer aerosol conditions.

- Subjective assessments of concentrations from NASA GMAO maps of predicted 925-mb sulfate (Appendix 3).
- Average boundary-layer PCASP and 0.5-percent supersaturation CCN number concentrations from dedicated below-cloud-base runs, when available.
- Maximum CDP–2 cloud droplet concentrations in TCu clouds neighboring the MCS, when available.

Concentrations of dust, which are efficient ice nuclei, were also estimated, but solely from GMAO 925-mb maps. GMAO estimates of both sulfate and dust were estimated from their respective colors within the region of DC–8 low-altitude measurements near the MCS, or from the high-altitude region of measurements if low-altitude measurements were not made. These values are rough estimates due to the resolution of the map color bar.

Table 4 contains a flight-by-flight summary of these observations. Low-altitude in situ aerosol measurements were made on eight of the ten flights, providing a direct indication of whether the boundary layer near the MCS was considered to contain low, moderate, or high concentrations of CCN aerosol. CCN measurements were not available for three of these eight flights, and PCASP concentrations were used as surrogates for CCN concentrations. CDP–2 maximum 1-s (distance ~200 m) droplet concentrations were also considered for the eight flights when they were available. Generally, cases were classified as low-CCN cases if CCN concentrations were less than about 400 cm^{-3}, or when PCASP concentrations were less than about 300 cm^{-3} if CCN data were unavailable. Similarly, if maximum cloud droplet concentrations were less than about 350 cm^{-3}, the case was classified as a low-CCN case. Regions on GMAO sulfate maps were considered low, moderate, or high in CCN if low-altitude regions (or, if unavailable, the region where the high-altitude flight was conducted) were estimated to contain concentrations of <1 μgm^{-3} (low), 1 to 2 μgm^{-3} (moderate), or >2 μgm^{-3} (high). In situ low-altitude measurements superseded the GMAO predicted sulfate values when the former was available.

Based on these parameters, the following flights were concluded to have clearly sampled low-CCN-aerosol regions: 2022-07-08, 2022-07-10, 2022-07-14, 2022-07-16, 2022-07-24, and 2022-07-26. For the case of 2022-07-18, only GMAO information was available. The DC–8 high-altitude MCS measurements were taken in a patchy 0.5- to 1.5-μgm^{-3} region (i.e., possibly bordering on moderate), but without other supporting information, and given that the levels were marginal, the decision was made to also categorize this case as low-CCN.

The flight of 2022-07-22 was a more complex case. MCS measurements were unexpectedly taken in a special-use military area off the east coast of South Carolina and Georgia while returning from an aerosol investigation. A 100-Nm low-altitude traverse from southeast to northwest had been performed attempting to measure an increase in aerosol concentration predicted by GMAO along this track. The DC–8 in situ measurements did indeed reveal an approximate doubling in PCASP and CCN concentrations. While setting up for the high-altitude traverse, the closest low-altitude measurements to the later sampled MCS were taken about 235 Nm to the northeast and almost directly downwind, where PCASP and CCN values were relatively low at about 100 and 250 cm^{-3}, respectively. GMAO sulfate predictions in this region (see Figure 3.6 in Appendix 3) and the MCS region were both categorized as moderate to high. GMAO predictions were thus not consistent with the DC–8 low-altitude measurements. In fact, CCN concentrations exceeding 500 cm^{-3} were only found beyond 50 Nm to the northwest along the forementioned aerosol traverse, north of about 38.2 N latitude. Consequently, it was concluded that low-CCN aerosol levels likely existed in the vicinity of the MCS as well, and the case was therefore categorized as low-CCN, albeit with a greater degree of uncertainty due to the disagreement with GMAO. Interestingly, the cloud droplet measurements taken in cumulus clouds about 350 Nm to the northeast of the MCS reached 509 cm^{-3}, a value that could be considered moderate, but this was measured when returning along the forementioned gradient in aerosol and was possibly subject to the higher concentrations of CCN aerosol in the boundary layer.

Low-altitude measurements on 2022-07-27 were made in the vicinity of the MCS and revealed relatively low average PCASP concentrations (153 cm^{-3}) but moderate-CCN concentrations (741 cm^{-3}). The TCu measurements also revealed a maximum CDP–2 cloud droplet concentration of 423 cm^{-3}; this was higher than in most flights but was considered only moderate relative to polluted continental cases reported by others. The GMAO sulfate maps predicted that MCS measurements were in a transition region from low to high values, with a possible gradient across the front that was triggering the convection. The case was categorized as a moderate-CCN case due to the elevated CCN and moderate droplet concentrations.

Finally, 2022-07-30 was categorized as the only clear case of high-CCN aerosol. The DC–8 low- and high-altitude measurements were both taken in regions of predicted high GMAO sulfate. Average boundary-layer PCASP and CCN concentrations were the highest of all flights at 840 and 1,240 cm^{-3}, respectively. The maximum CDP–2 cloud droplet concentration of 715 cm^{-3} was also the highest, and while not extreme, it was approximately a factor of 2 to 3 higher than concentrations measured for the low-CCN flights. In comparison to heavily polluted cases, the boundary-layer CCN and CDP–2 droplet concentration in the continental TCu measurements of CAIPEEX over India reached 3,858 cm^{-3} (0.4-percent supersaturation) and 2,062 cm^{-3}, respectively (Ref. 40). However, for this study, the levels of 2022-07-30 were considered high enough that some signal of warm rain suppression via the HIWC–2022 first-order hypothesis might be detectable.

GMAO predictions of dust at 925 mb for the regions of the DC–8 measurements are also shown in Table 4. Dust from the African Sahara Desert was transported across the Atlantic in the easterly tropical trade winds. Such transport was clearly visible in animations of GMAO dust-prediction maps. For the purposes of this report, Table 4 categorizes relative dust levels for HIWC–2022 flights according to the following thresholds: <15 μgm^{-3} (low); 15 to 30 μgm^{-3} (moderate); and >30 μgm^{-3} (high). The table reveals that most of the HIWC–2022 flights were conducted in regions of >10 μgm^{-3} of GMAO-predicted dust and shows that some of those predictions exceeded 50 μgm^{-3}.

TABLE 4.—FLIGHT-BY-FLIGHT SUMMARY OF CCN AEROSOL AND DUST CONCENTRATIONS IN BOUNDARY LAYERS NEAR MCSS

Date	Region	Low-altitude in situ meas.?	[a]PCASP, cm^{-3}	[a]CCN, cm^{-3}	[b]CDP_{max} cm^{-3}	[c]Approx. GMAO, 925 mb		Comments	Conclusions	
						Sulfate, μgm^{-3}	Dust, μgm^{-3}		CCN	Dust
2022-07-08	East Coast	Yes, but distant to [d]HA	235	NA	294	~1.0–1.5	<30	[d]LA remote to MCS, but HA also in low GMAO sulfate	Low	Moderate
2022-07-10	G. Mexico	Yes	160	NA	313	<1.0	<25		Low	Moderate
2022-07-14	East Coast	Yes	85	NA	301	<1.0	<10	HA in higher GMAO sulfate region, but in situ confirms low aerosol	Low	Low
2022-07-16	Bahamas	No	NA	NA	NA	<1.0	~25–50	GMAO clean sulfate in HA region	Low	Moderate to high
2022-07-18	East Coast	No	NA	NA	NA	1.0–1.5	Broad ~30–50	GMAO HA sulfate <1.5 μgm^{-3}	Prob. low	Moderate to high
2022-07-22	East Coast	Yes, but distant to HA	109	361	509	>2.0	~25–50	LA remote from HA MCS, HA in military area, both with possible elevated GMAO sulfate. See text for further discussion.	Considered possibility of moderate to high, but concluded low for this report. See text discussion.	Moderate to high
2022-07-24	S. of Cuba	Yes	71	174	242	~1.0–2.0	~25–50	GMAO moderate sulfate at LA, but in situ indicates low. On edge of high dust episode S. of Cuba.	Low	Moderate to high
2022-07-26	E. of Florida	Yes	77	196	170	~1.0–1.5	~50–75	Substantial GMAO dust, but low GMAO sulfate	Low	High
2022-07-27	East Coast	Yes	153	741	423	~1.5–5.0	~10–25	HA MCS region in low GMAO sulfate	Possible moderate, based on CCN	Low to moderate
2022-07-30	East Coast	Yes	840	1,239	715	~2.0–5.0	~15–30	Both LA and HA in high GMAO sulfate. Broad dust plume just south of HA.	High	Moderate

[a]PCASP and CCN concentrations are average values from below-cloud-base, low-altitude runs.

[b]CDP_{max} is maximum droplet concentration <50 μm observed during TCu runs.

[c]GMAO sulfate and dust concentrations were estimated visually from color maps.

[d]HA and LA refer to the high-attitude and low-altitude regions of measurements during flights (Appendix 3).

Relative to the original intended oceanic project area east of east Asia, the following was found in the HIWC–2022 operating area: sulfate levels were low, organic and sea-salt aerosols were similar, but dust levels were very high. The global monthly averages of July 2022 sulfate and dust concentrations from the Japanese Spectral Radiation-Transport Model for Aerosol Species (SPRINTARS) (Refs. 41 to 43) are shown in Figure 12 and Figure 13, respectively. Other July maps for 2017 to 2021 showed similar results. Average dust concentrations in the Japan region in this period were typically lower than 2 μgm^{-3}. This

points out that there are differences in aerosol concentrations other than anthropogenic CCN that may regionally affect cloud microphysical properties.

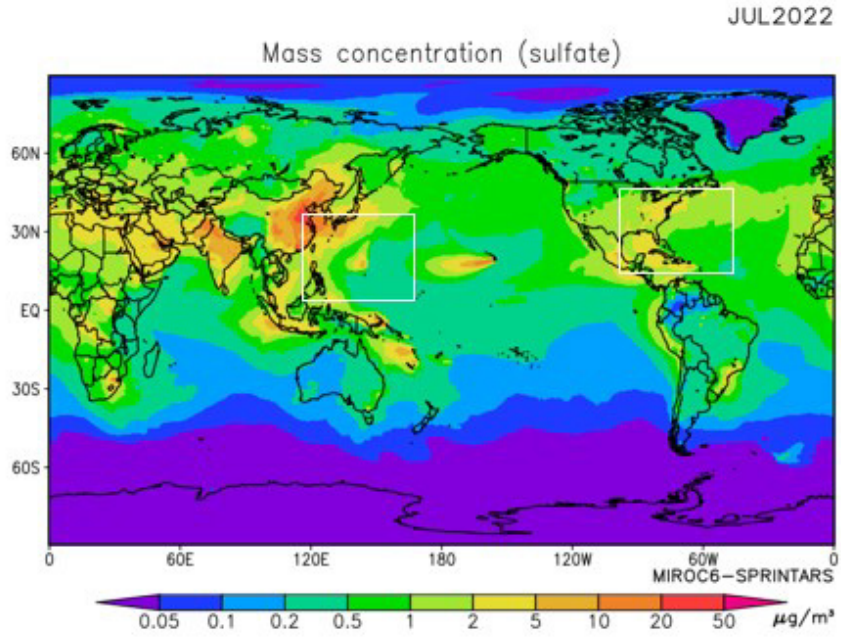

Figure 12.—July 2022 monthly average of sulfate concentration from SPRINTARS (Refs. 41 to 43).

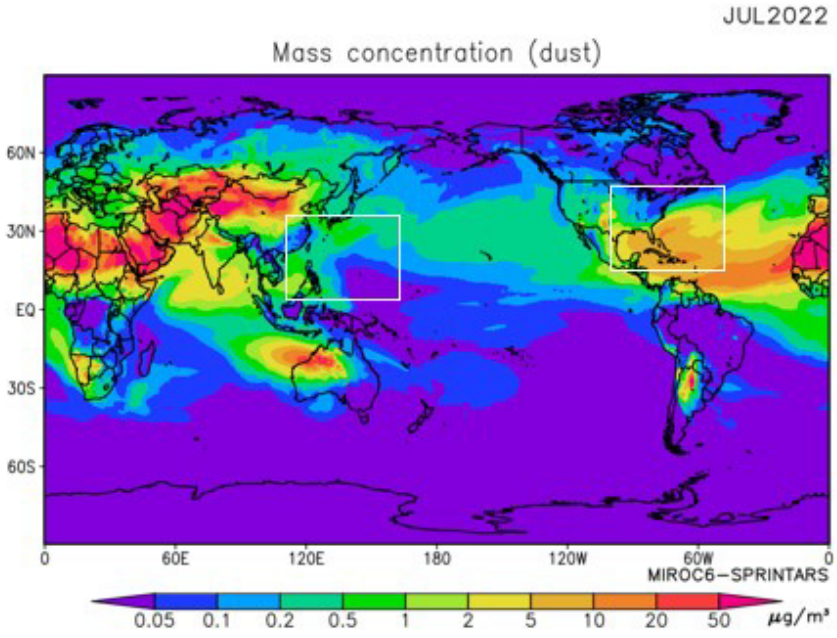

Figure 13.—July 2022 monthly average of dust concentration from SPRINTARS (Refs. 41 to 43).

5.1.2 Aerosol Processing and Analyses

CCN are a unique subset of aerosol particles that serve as nucleation sites for the formation and condensational growth of cloud droplets. Common CCN particles include dust, volcanic ash, factory and vehicle pollution, naturally emitted biological aerosols, and salt from ocean spray. CCN activate at a size that decreases with increasing supersaturation and is dependent on composition. For example, the typical activation size of marine aerosols in stratus clouds is about 0.025 to 0.030 μm at supersaturations with respect to water (SS_w) in the range of 0.5 to 1.0 percent. However, SS_w can exceed 0.5 percent, particularly in cumulus clouds with strong updraft velocities (Ref. 44). INPs are less common aerosol particles that facilitate the formation of ice particles in clouds. In contrast to CCN, the most effective INPs are hydrophobic. INP types can include desert dust, soot, organic matter, bacteria, fungal spores, and volcanic ash.

For the CCN property of atmospheric aerosols, the CCN number concentration was measured with the DMT CCN–200 counter. One humidifier column was fixed at 0.5 percent SS_w, and the other column was cyclically set at 0.1, 0.2, and 1.0 percent SS_w. Combined with the aerosol size distribution data, the hygroscopicity (kappa) was analyzed according to Petters and Kreidenweis (Ref. 45).

For the INP property and elemental composition of atmospheric aerosols, aerosol particles were processed using three methods: (1) aerosol sampler (AS) with two-stage impactor for transmission electron microscopy meshes (AS–TEM), (2) similar impactor for silicon wafer in water repellent coating (AS–SW), and (3) aerosol sampling holder fitted with a hydrophobic polytetrafluoroethylene (PTFE) membrane filter (MF) (Figure 14). Single-particle data were compiled based on each sampling mesh, wafer, or filter. The sampling duration onto these media typically ranged from 10 to 30 min. Aerosols were usually sampled on several meshes, wafers, and filters in each flight.

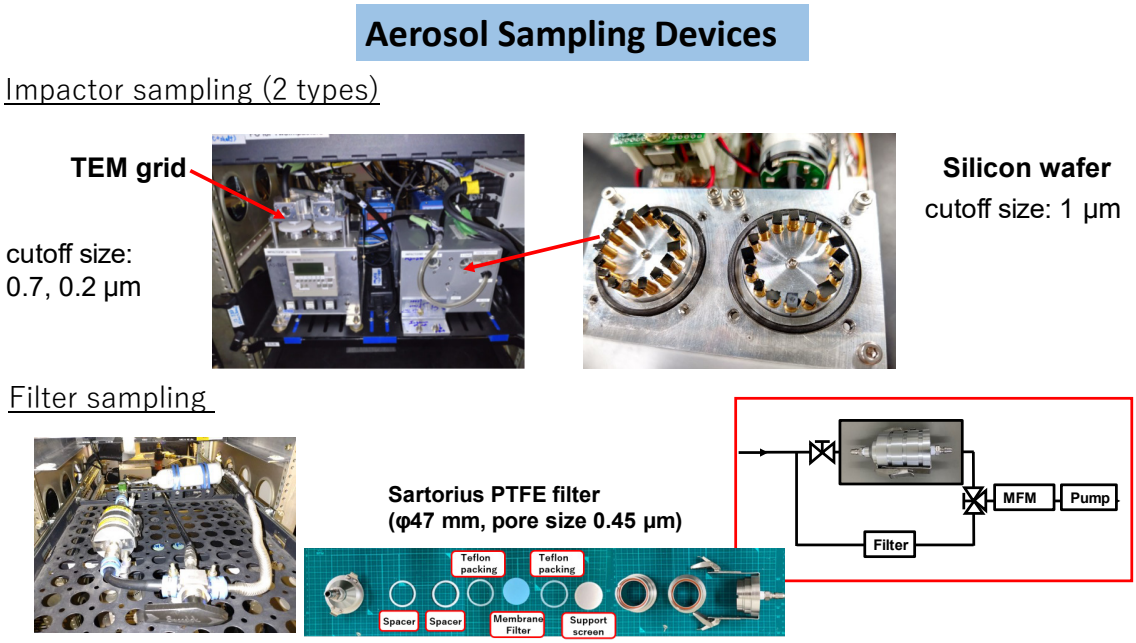

Figure 14.—Aerosol impactor sampling devices for transmission electron microscopy (AS–TEM) and silicon wafer (AS–SW) meshes. Membrane filter method, MFM.

For the AS–TEM aerosol data, individual particles were classified into eight categories (including "others") using TEM and scanning electron microscopy (SEM) and energy-dispersive X-ray analysis (EDX) according to Adachi et al. (Ref. 46). From the TEM analysis, each particle size was estimated by its equivalent circle diameter. INPs were identified by two methods. Identification (ID) Method 1 used a single-droplet freezing method developed in Reference 47 for the AS–SW aerosol data, followed by Raman and SEM–EDX spectroscopy analysis. ID Method 2, used for the MF aerosol data, was based on a droplet-freezing assay on filter (Ref. 48). ID Method 1 results provided the number of INPs identified in two processed temperature (T) regimes: $T \geq -22$ °C and -30 °C $< T < -22$ °C. The results of ID Method 2 included not only the estimated INP number concentration, but also the calculated ice nucleation active surface site (INAS) density as a function of T.

The data and results from ID Method 1 (using AS–SW with Raman and SEM–EDX spectroscopy) were provided by Kanazawa University in Japan. The data and results from ID Method 2 (using MF and AS–TEM) were provided by Meteorological Research Institute in Japan. More details on the processing and analyses can be found in Reference 49.

5.1.3 Aerosol Results

In general, a positive correlation was found at low altitudes between the number concentration of aerosols and CCN in the HIWC–2022 campaign. The CCN SS_w spectra ($N_{CCN} = C * SS_w{}^k$) were also analyzed for limited cases (2022-07-22, 2022-07-26, 2022-07-27, and 2022-07-30). The averaged CCN number concentration at low altitudes and, arbitrarily, the fifth-highest CDP-2 cloud droplet number concentrations near cloud base for these cases are shown in Figure 15.

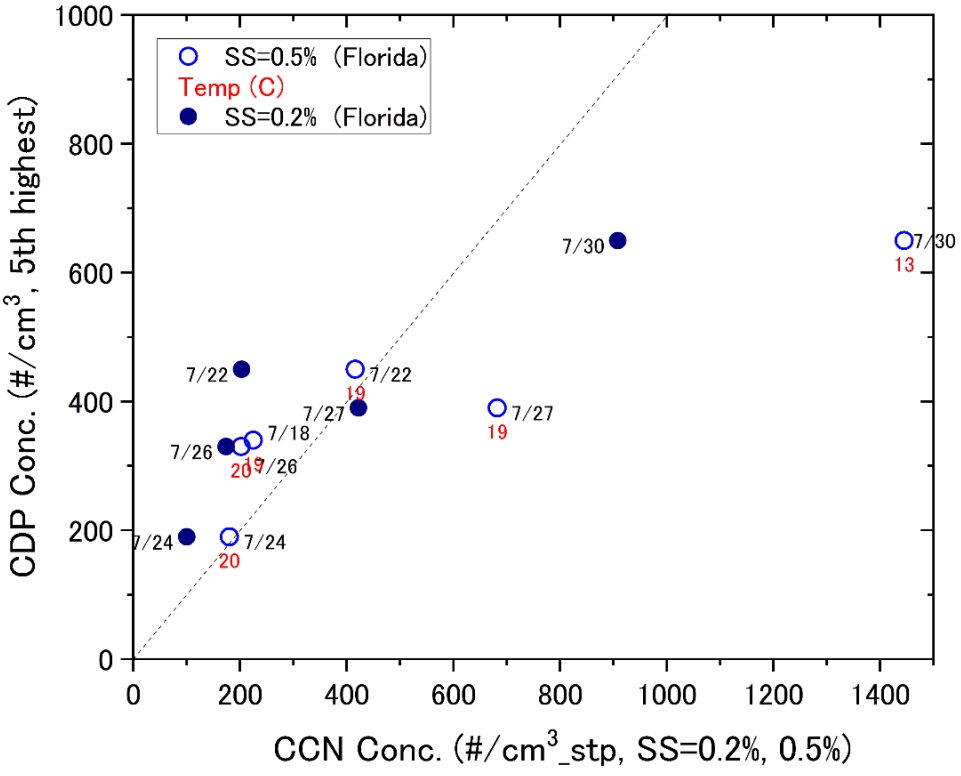

Figure 15.—CDP–2$_{(5th\ highest)}$ concentrations versus CCN concentrations at SS_w = 0.2 and 0.5 percent. Standard temperature and pressure, stp.

For the case of 2022-07-30, the coefficient C was relatively large, indicative of a high loading of aerosols, and the exponent k was small, indicative of a higher hygroscopicity and smaller critical diameter. The hygroscopicity kappa value at SS_w = 0.2 percent was about 0.1 to 0.2. This value is slightly lower than the land-based average values of 0.2 to 0.3 from previous studies (e.g., Andreae and Rosenfeld) (Ref. 50).

No clear correlation between the average aerosol number concentration at low altitudes and the highest number concentration of ice particles larger than 100 μm at higher altitudes was found from the flight observations. However, the highest ice concentrations were often measured at altitudes near –40 °C and sometimes at altitudes near –20 °C, so the difference in sampled height and freezing mechanism should be taken into consideration.

INP properties of aerosols obtained from ID Method 1 showed that out of approximately 46,000 particles, there were 15 and 32 particles acting as freezing nuclei in the warmer and colder temperature regimes, respectively. The low ratio of activating INPs to total aerosol particles is consistent with the literature. The aerosol particles acting as the warmer-temperature freezing nuclei were assumed to be bioaerosols from morphological observation and chemical composition. In addition, Na and Cl were also detected, so it is suggested that such particles acting as warmer-temperature freezing nuclei were internally mixed with sea-salt particles (Figure 16). From morphology, fluorescence, and from a composition that included Al and Fe, it appeared that mineral dust was dominant for particles acting as colder-temperature freezing nuclei (Figure 17). Based on NOAA's Hybrid Single-Particle Lagrangian Integrated Trajectory (HYSPLIT) back-trajectory analysis, it is suggested that the bioaerosol with high INP ability may have originated over the land.

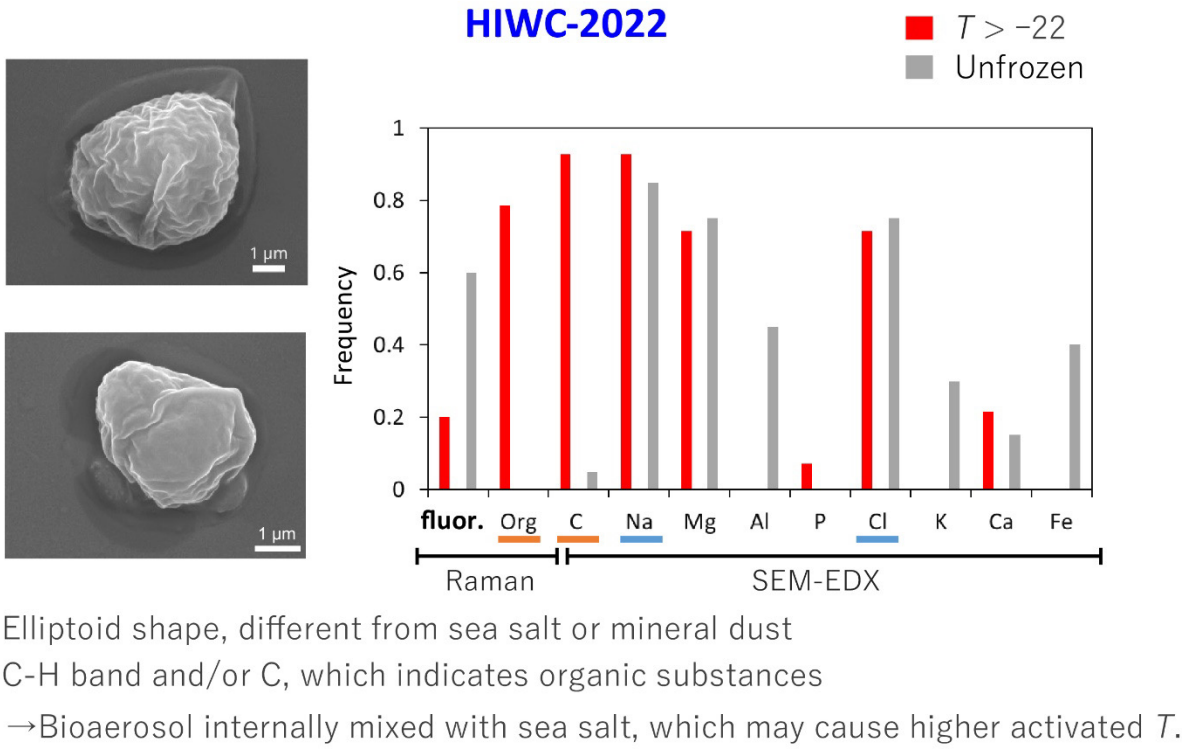

Figure 16.—INP ID Method 1 results at T > –22 °C.

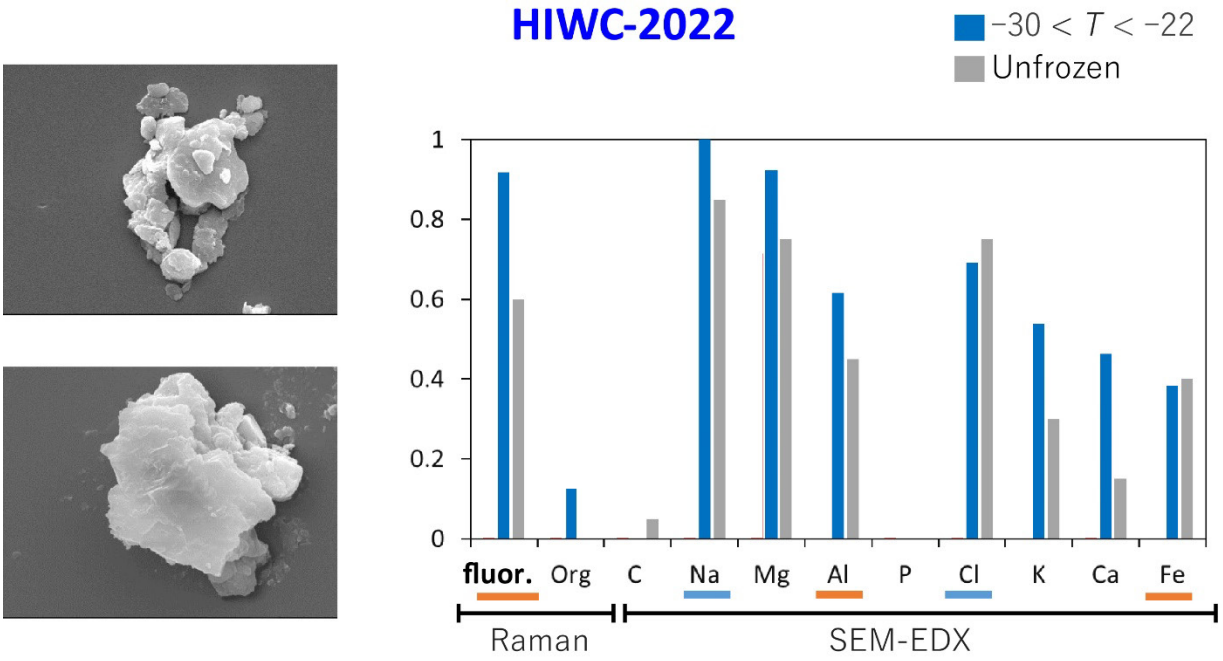

Figure 17.—INP ID Method 1 results at –30 °C < *T* < –22 °C.

The INP properties obtained from ID Method 2 indicated that estimated INP number concentrations ranged from approximately 0.4/L to 4.0/L at –15 °C and from 0.7/L to 19.5/L at –20 °C. Compared to a previous study by Petters and Wright (Ref. 51), higher INP concentrations over the temperature range from –5 to –20 °C were often observed in HIWC–2022. As for the INAS density, the variability covered 1 to 2 orders of magnitude for any specific temperature. If all aerosol particles were assumed to be mineral dust, HIWC–2022 INP concentrations or INAS densities estimated on the basis of the parameterization of previous studies were found to be consistent at temperatures colder than –20 °C. However, at temperatures warmer than –20 °C, estimated values were less than observed values. It is speculated here that such inconsistency in this warmer temperature range might be related to the presence of other aerosol types that are more effective INPs, or that the mineral dust particles are more effective INPs than those reported by previous studies.

The single-particle analysis from the TEM and SEM–EDX spectroscopy showed that sulfates were typically dominant over the submicron size range during HIWC–2022, whereas sea-salt particles and/or dust particles were dominant over the supermicron size range. The fractions of each particle type classification were diverse. The HIWC–2022 ternary diagram of elemental compositions combined with classified aerosol type information showed that the mineral dust internally mixed with sea-salt aerosols was often observed during HIWC–2022 (Figure 18). Further particle analysis showed that mineral dust particles were composed mainly of clay minerals. Additional studies are needed to determine what types of aerosol particles were effective INPs, especially at temperatures warmer than –20 °C. More details on these results can be found in Reference 49.

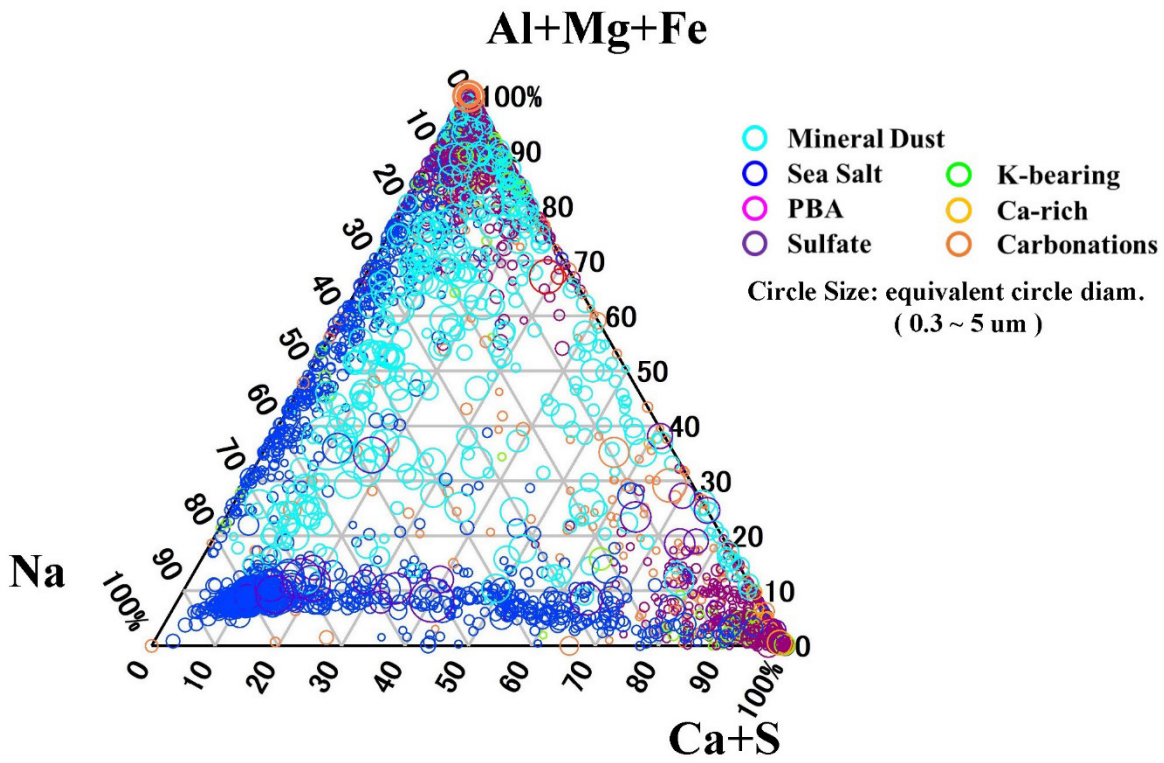

Figure 18.—Ternary diagram for weight–percent ratios.

5.2 Inventory of High-Altitude Data Collected

Table 5 shows general properties of the original datasets and the HIWC–2022 flight campaigns. Properties of the 2018 DC–8 HIWC RADAR II campaign are also shown for purposes of the discussion in Section 5.6. The contents of the table have also been reported in Reference 27. Row 5 shows composite results for the original datasets as provided to the ICIWG. Rows 6 and 7 display the data summaries for the new HIWC RADAR II and HIWC–2022 datasets, respectively. Rows 8, 9, and 10 show composite accumulations for the datasets identified in the first column.

In this section, the term “segment” is used to refer to a traverse or run across cloud that has been defined according to a specific set of rules for the Appendix D statistical data analysis. A segment must have been within an MCS. It must be approximately straight and level, with start and end points defined by a 0.1-gm^{-3} TWC threshold or a significant change in heading or altitude. Most segments have been derived from traverses across cloud, but some segments have been derived from shorter repositioning runs. Although segments are used in this section to be compatible with original Appendix D data analyses, the terms “run” and “traverse” may be used elsewhere throughout this report to more generally refer to a cloud pass or low-level aircraft track for aerosol collection.

The HIWC–2022 campaign added nine flights and approximately 25 clouds to the original dataset, increases of about 17 and 22 percent, respectively. The campaign added 80 cloud segments, increasing the original total by about 17 percent. Minimum and maximum segment lengths of the composite dataset were nearly unchanged. HIWC–2022 clouds were, on average, smaller than those of the original campaigns, with a 23-percent shorter average segment length of 48.8 Nm compared to 63.4 Nm. The average TWC of 0.57 gm^{-3} for HIWC–2022 clouds was 19 percent lower than the original TWC average of 0.70 gm^{-3}.

The HIWC RADAR II campaign added seven flights and approximately 19 clouds to the original dataset, increases of about 13 and 17 percent, respectively. The 98 additional cloud segments augmented

the original total by about 21 percent. Again, minimum and maximum segment lengths of the composite dataset were nearly unchanged. The average segment length of 60.5 Nm was about 5 percent shorter than the 63.4-Nm average of the original campaigns. HIWC RADAR II clouds had the lowest average TWC of all campaigns at 0.52 gm^{-3}, 26 percent lower than the original TWC average of 0.70 gm^{-3}. Strapp et al. (Ref. 27) speculated that the reason for this low average was that a high percentage of segments were in Tropical Storm/Hurricane Lane, where it was often not possible to penetrate the eyewall region with the suspected highest TWC due to high radar reflectivity. The highest campaign average TWC was observed in the Darwin–2014 dataset at 0.79 gm^{-3}. Further discussion of Table 5 will be provided in Section 5.6.

References 18 and 20 present TWC data statistics for all points across a cloud as a function of distance scale. For example, if a cloud segment were 174 Nm wide, 10 back-to-back 17.4-Nm data points, called Type 1 points, contributed for that segment to the statistical analysis of percentiles. Reference 21

TABLE 5.—INVENTORY OF DATA COLLECTED
[Includes summaries of data included in original dataset reported in Reference 18 (row 5), HIWC RADAR II (row 6), and HIWC–2022 (row 7), and new composite summaries created by adding new datasets (rows 8 to 10).]

Row No.	Campaign, location, and aircraft	No. of contributing flights	No. of clouds sampled (approx.)	No. of cloud segments	Avg. length of segments, Nm	Min. length of segments, Nm	Max. length of segments, Nm	Segment avg. TWC, gm^{-3}
1	HAIC–HIWC Darwin, AU Falcon–20	17	31	118	66.6	3.4	236.1	0.79
2	HAIC–HIWC Cayenne, GF Falcon–20	17	54	149	58.9	4.3	235.7	0.61
3	HAIC–HIWC Cayenne, GF Convair–580	10	30	76	45.7	2.5	175.8	0.78
4	HIWC RADAR I FL, US NASA DC8	10	21	127	75.6	7.9	159.9	0.66
5	Original dataset (All HAIC–HIWC datasets plus HIWC RADAR I)	54	115	470	63.4	2.5	236.1	0.70
6	HIWC RADAR II FL, CA, HI, US NASA DC8	7	19	98	60.5	1.9	237.8	0.52
7	HIWC–2022 FL, US NASA DC–8	9	25	80	48.8	1.5	158.3	0.57
8	Original dataset + HIWC–2022	63	140	550	61.3	1.5	236.1	0.68
9	Original dataset + HIWC RADAR II	61	134	568	62.9	1.9	237.8	0.67
10	Original dataset + HIWC RADAR II + HIWC–2022	70	159	648	61.1	1.5	237.8	0.66

reanalyzes the same original datasets, accepting only the maximum value of a distance window that progressed across the cloud at an interval of 0.1 Nm (i.e., not back-to-back averages but overlapping windows, contributing only one final point per cloud segment). Type 2 data points provided a more extreme statistic, with TWC_{99} values at 17.4 Nm—10 to 23 percent higher than Type 1 points, depending on the temperature interval. For simplicity, and because it represents the more conservative approach favored by the ICIWG, only Type 2 points were used in the analysis that follows.

Table 6 shows the breakdown of Type 2 data points by the 10 °C temperature intervals requested by the EHWG. Although the –20 °C temperature interval is shown, it was not a targeted interval and may not have followed the same flight strategies as the other intervals. During HIWC–2022, the sampling strategy emphasized the –40 °C temperature interval to better contrast the high-CCN-aerosol cloud segments of HIWC–2022 to the other campaigns by having a high fraction of all project points in that interval. This is reflected in a 53-percent increase in –40 °C data points from the original dataset to the original plus HIWC–2022 dataset.

TABLE 6.—BREAKDOWN OF TYPE 2 DATA POINTS COLLECTED IN 10° TEMPERATURE INTERVALS

Campaign, location, and aircraft	**Temperature interval**					
	–10 °C ($-15 < T \leq -5$)	**–20 °C ($-25 < T \leq -15$)**	**–30 °C ($-35 < T \leq -25$)**	**–40 °C ($-45 < T \leq -35$)**	**–50 °C ($-55 < T \leq -45$)**	**All temperature intervals**
HAIC–HIWC Darwin, AU Falcon–20	7	9	39	49	13	117
HAIC–HIWC Cayenne, GF Falcon–20	27	9	50	46	17	149
HAIC–HIWC Cayenne, GF Convair–580	76	0	0	0	0	76
HIWC RADAR I Florida, US NASA DC8	3	0	47	36	41	127
Original dataset (All HAIC–HIWC datasets plus HIWC RADAR I)	113	18	136	131	71	469
HIWC RADAR II FL, CA, HI (US) NASA DC8	0	17	23	45	13	98
HIWC–2022 Florida, US NASA DC–8	0	0	10	70	0	80
Original dataset + HIWC–2022	113	18	146	201	71	549
Original dataset + HIWC RADAR II	113	25	159	176	84	557
Original dataset + HIWC RADAR II + HIWC–2022	113	35	169	246	84	647

Comparisons of the original datasets to the new dataset properties of the HIWC RADAR II and HIWC–2022 campaigns are made is Section 5.6, and the effect of adding the new datasets to derive a full composite dataset is presented.

5.3 Occurrence of Graupel

The American Meteorological Society (AMS) Glossary of Meteorology defines graupel as "heavily rimed snow particles, often called snow pellets; often indistinguishable from very small soft hail except for the size convention that hail must have a diameter greater than 5 mm. Sometimes distinguished by shape into conical, hexagonal, and lump (irregular) graupel" (Ref. 52). During the HAIC–HIWC campaigns, it was concluded that episodes of graupel were rare, and their effects on MMD statistics were ignored. A cursory analysis of graupel episodes based on 2D OAP probe imagery suggested that graupel could be identified roughly 0.2 percent of the time for the original HAIC–HIWC Falcon–20 measurements. Graupel episodes were generally associated with high-IWC zones.

During the HIWC RADAR I and HIWC RADAR II campaigns, graupel episodes continued to be observed, but the subjective impression, without detailed analysis, continued to be that these episodes were rare. Relative to these previous flight campaigns, episodes of graupel and lightning strikes were frequently observed during the HIWC–2022 flights. As shown in Section 5.4, there was indeed a marked increase in lightning rate within the vicinity of the DC–8 during HIWC–2022, and the airplane was struck by lightning at least two times. Similarly, graupel was observed in flight by viewing images from the 2D–S and PIP and hearing the impacts on the fuselage. Figure 19 shows an example of the PIP imagery during one of the graupel episodes in HIWC–2022. In this figure, some large quasi-circular graupel particle images were present up to a maximum size of about 3 mm. A background population of more conventional smaller anvil ice particles was also present. The temperature was –39 °C and the TWC reached about 3.5 gm^{-3}.

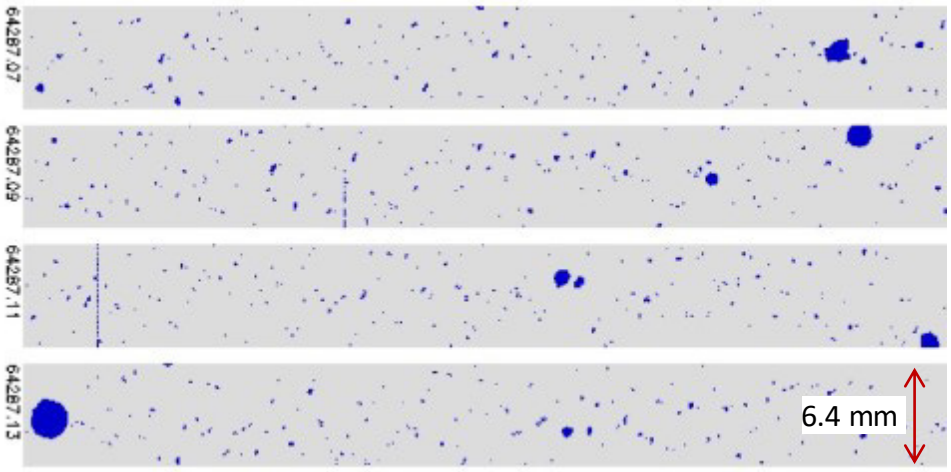

Figure 19.—Sample 60-ms period of PIP images during high-altitude traverse containing graupel on 2022-07-10 at 17:51:25 UTC. Width of each PIP image strip is 6.4 mm. Larger quasi-circular images are graupel. Copious smaller images represent general background of smaller particles.

As will be described in more detail in Section 5.6.4, the NCAR System for Optical Array Probe Data Analysis 2 (SODA–2) software package (Ref. 53) was used to calculate PSDs, mass size distributions (MSDs), and MMDs for the HIWC RADAR, HIWC RADAR II, and HIWC–2022 flight campaigns. A feature in SODA–2 calculates the area ratio of each particle (i.e., the ratio of area of shadowed pixels to the area of a circumscribed circle encompassing the shadowed particle). An area ratio of 1.0 would mean the shadowed particle was a perfect circle (implying a spherical particle), whereas column or needle ice particles would have much lower area ratios. SODA–2 was used to produce time histories of the PSD and area ratio distribution that enabled a visual/manual identification for graupel using criteria such as particle size >0.5 mm and area ratio >0.7. Figure 20 provides an example of this from the 2022-07-10 flight. The circled areas on this figure indicate two episodes when particles ranging in size from 0.5 to 3.0 mm with area ratios >0.7 were encountered. The PIP images shown in Figure 19 contributed to the PSD and area ratio shown in the later circled area on Figure 20.

The higher frequency of graupel observations during HIWC–2022 identified a potential issue in calculating the MSD by conventional means, that is, by using a mass-diameter relationship $m(D) = \alpha D^{\beta}$, where $m(D)$ is the mass of a particle of diameter D. This default conversion of PSD to MSD assumes, by definition, that the characteristics of an ensemble of particles in the basic time interval of 5 s were uniform, and it does not account for bifurcated particle populations, such as a background of typical anvil cirrus vapor-grown crystals and aggregates with a superimposition of large, high-density graupel.

To examine the potential effects of graupel particles on MSD, a hybrid mass estimation process was developed. In this process, mass estimation for bins of all sizes with an area ratio less than or equal to 0.6 followed the standard PSD-to-MSD calculation. However, if the average area ratio exceeded 0.6, the size bin was identified as a graupel bin, and particles were assigned a density of 0.91 gcm^{-3}. Although this diameter threshold and density scheme was somewhat arbitrary and was intended only as conjectural based on experience and intuition, it provided an objective examination for the effect of graupel on the flight campaign particle MSDs and MMDs.

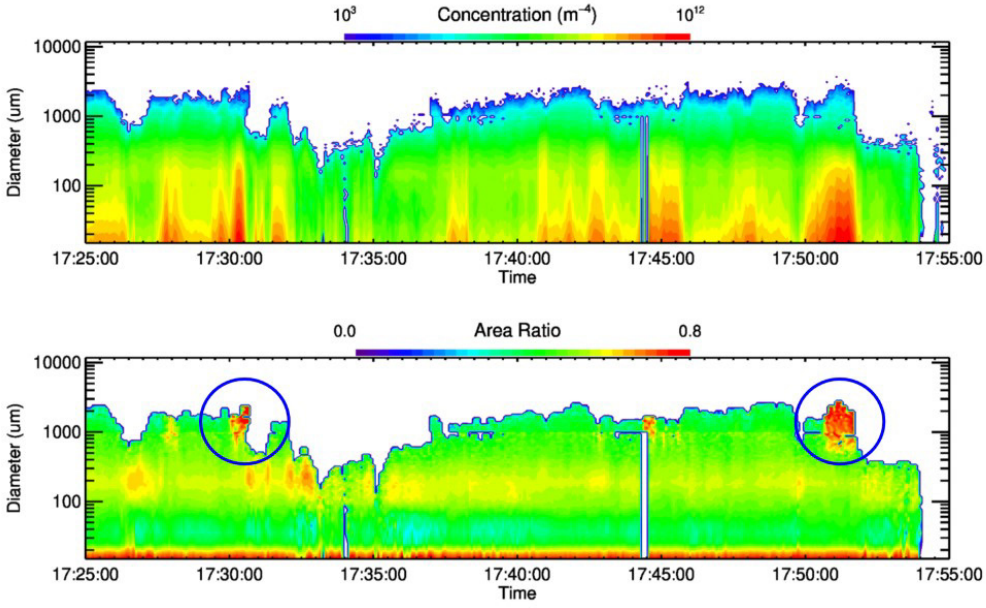

Figure 20.—30-min time series of PSD (top panel) and area ratio distribution (bottom panel) from 2022-07-10 flight. Areas of graupel in 0.5- to 3.0-mm size range visible in red/orange areas in bottom panel (circled).

An example of how this hybrid scheme might affect particle MSDs is given in Figure 21. The HIWC–2022 campaign dataset was used because it had the highest frequency of graupel and would display the greatest effect. The viewed area under each curve is proportional to TWC. The top plot shows mass distributions for all points within the specified TWC regimes, using solely the default $m(D) = \alpha D^{\beta}$ mass conversion scheme. The bottom plot shows the corresponding distributions where the hybrid process for graupel was used.

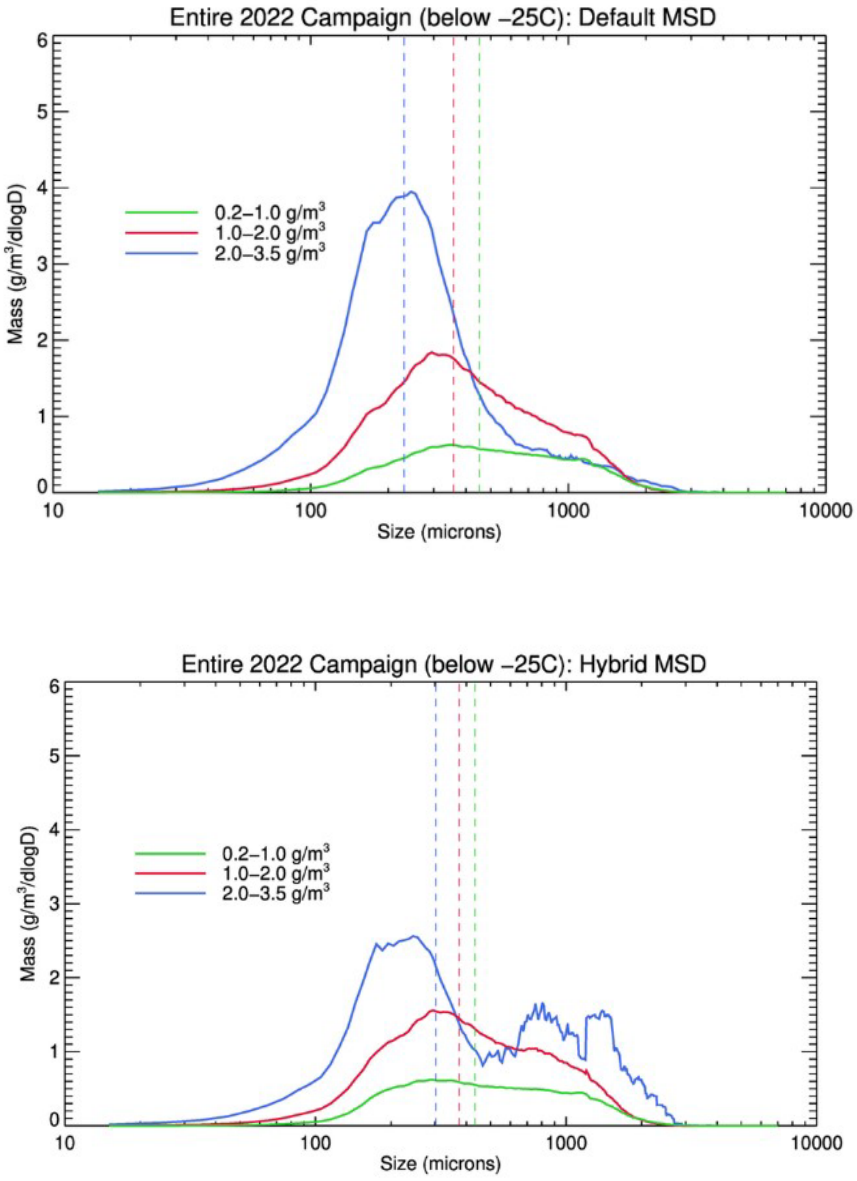

Figure 21.—Examples of composite mass distributions within different TWC regimes. Top plot shows mass distributions using simple $m(D) = \alpha D^{\beta}$ scheme. Bottom plot shows example of hybrid scheme used to exemplify possible effect of including higher densities to account for graupel particles. MMD for each distribution shown in vertical dashed lines.

When the hybrid treatment was used, a bimodality appeared in the mass distribution that was barely present in the default treatment. The effect on MMD was greatest for the TWC = 2- to 3.5-gm^{-3} regime, increasing from 238 to 300 μm. However, the real importance may not be in the change in MMD but in the appearance of the significant second mass mode larger than 1 mm. The presence of these graupel and frozen drop particles complicates the interpretation of mass-based cloud parameters such as MSD and MMD and should be considered carefully when using these results to compare with other field campaigns or to quantify the meteorology of the cloud encounters. In particular, the adjustment of the magnitude of the MSD to match the IKP2 measurement of condensed water content as used in the default $m(D) = \alpha D^{\beta}$ mass conversion scheme will result in an overestimate of the mass contained in the small-particle mode, given that a portion of that mass was actually contained in the larger graupel particles. Likewise, the bimodal nature of the MSD in the presence of graupel complicates the meaning of the MMD. A hybrid graupel/ice mass-size parameterization such as the one introduced here may improve the MSD and MMD retrievals, as may particle-shape-based mass estimation approaches that have been developed for other applications.

To look at the potential impact of graupel on the HIWC flight campaigns, a scheme was devised to objectively identify when the DC–8 was flying "in graupel." The scheme was based on the ratio of IWC derived from the hybrid MSD described above to the IWC from the default MSD. Graupel periods were identified when this ratio exceeded 1.5.

Applying this scheme, a first estimate of the percentage of distance in which graupel episodes occurred is given in Table 7 for HIWC RADAR I, HIWC RADAR II, and HIWC–2022. Considering all in-cloud periods with TWC <1 gm^{-3} (most of the data), the percentage of distance with graupel was less than 2 percent. But for high-TWC regions considered in the MMD analysis (i.e., ≥1 gm^{-3}), the percentage of distance with graupel increased with TWC in all three campaigns. As suspected, the frequency of graupel was highest in HIWC–2022, reaching 91 percent of the distance when TWC was 2.0 gm^{-3} or greater.

It should be noted that MSDs and cumulative mass distributions (CMDs) presented to the ARAC ICIWG and reported in Reference 27 were based on the default MSD treatment and are subject to inaccuracies during the short high-TWC graupel episodes previously discussed. In these regions, MMDs were likely somewhat underestimated but, more importantly, true mass distributions were likely bimodal with a potentially significant contribution of mass at millimeter sizes. The hybrid MSD calculation method is exploratory, with some arbitrary assumptions, and more work would be needed to develop a new processing approach. Furthermore, reprocessing the original PSD dataset is currently impractical due to the level of effort required, and access to the original raw datasets has not been investigated. These graupel results have been brought to the attention of the ARAC engine and probe representatives, and to date, no further action has been requested by ARAC. Consequently, there are no current plans to reprocess the PSD dataset. Although aircraft engines may be insensitive to mass at large particle sizes due to breakup in the forward stages, other components—air data probes, for example—may be more impacted.

TABLE 7.—OCCURRENCE OF SUSPECTED GRAUPEL IN THREE HIWC FLIGHT CAMPAIGNS AS FUNCTION OF IN-CLOUD DISTANCE

TWC regime	HIWC RADAR I	HIWC RADAR II	HIWC–2022
<1.0 gm^{-3}	<2%	<2%	<2%
1.0 to 2.0 gm^{-3}	19%	14%	12%
2.0 to 3.5 gm^{-3}	57%	40%	91%

5.4 Lightning

According to the AMS Glossary of Meteorology, “natural lightning arises from the strong electric fields that exist between separate regions of thunderstorm (cumulonimbus) clouds whose hydrometeors have a surplus of either positive or negative electric charge…. Lightning serves to neutralize the charge imbalances that build up in thunderstorms over time” (Ref. 54). The electrical discharges associated with lightning radiate electromagnetic signals in all directions.

During the HIWC RADAR flight campaigns in 2015 and 2018 and the HIWC–2022 campaign, the WX1000E Stormscope® onboard avionics system detected lightning discharges up to 200 Nm away from the DC–8 and informed pilots of the locations of the discharges. The lighting discharge rate, range distance, and bearing with respect to the DC–8 heading were recorded during the HIWC flight campaigns. In 2015, the lightning detection data were unusable, perhaps due to P-static discharges near several of the DC–8 viewport hatch plates. The issues were resolved for the 2018 and 2022 campaigns, and the lightning detection data from these flights were analyzed to provide comparisons between the two test campaigns.

The recorded lightning discharge rate ranged from 0 to 63 discharges per minute (63/min was the WX1000 system maximum limit). Figure 22 shows a time history of the discharge rate (purple line) and the pressure altitude (black line) from the flight on 2022-07-10. The vertical dashed lines indicate the time period when flying near or in MCSs. Although electrical discharges were detected throughout the flight, the rate was typically less than 20 discharges/min. However, the discharge rate exceeded 40/min during several periods when flying in and near MCSs. During postflight discussions, it was determined that lightning struck the DC–8 at approximately 17:51 during a graupel episode with particle sizes of 0.8 to 3 mm and a lightning discharge rate of 63/min. The DC–8 was struck again during the 2022-07-16 during flight in an MCS with 1- to 2-mm graupel and a lightning discharge rate at 63/min. A protocol was established for subsequent flights to divert from convective cells when the graupel was observed on the particle imaging probes and the lightning discharge rate exceeded 50/min.

Lightning discharge rate data for each flight in 2018 and 2022 were averaged for the time periods when flights were in or near deep convective storms. The maximum discharge rate was also identified for the same time periods. Figure 23 shows the average discharge rates (solid bars) and the maximum discharge rates (hatched bars) for each flight while in MCSs. Comparing these results, the average lightning discharge rates during the five flights in Tropical Storm/Hurricane Lane (2018) were significantly less than those of any other flights. Interestingly, even the maximum discharge rates during those flights were less than most of the other flights in MCSs in 2018 and 2022.

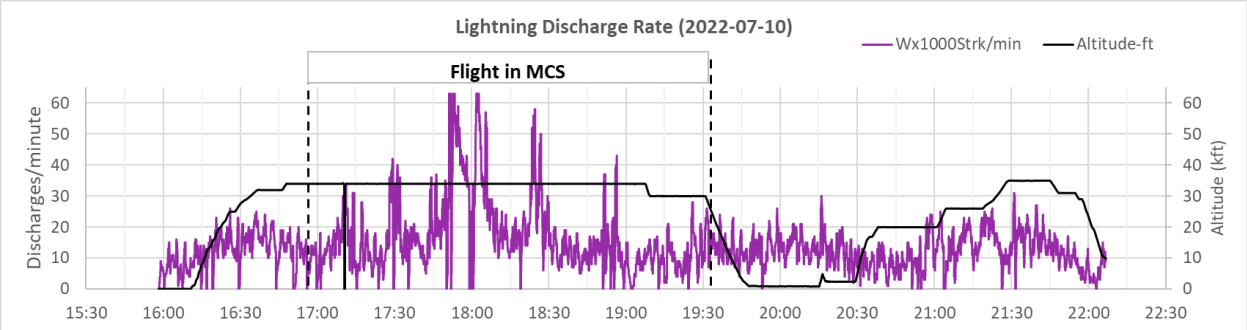

Figure 22.—Time history of lightning discharge rate measured by WX1000E on 2022-07-10.

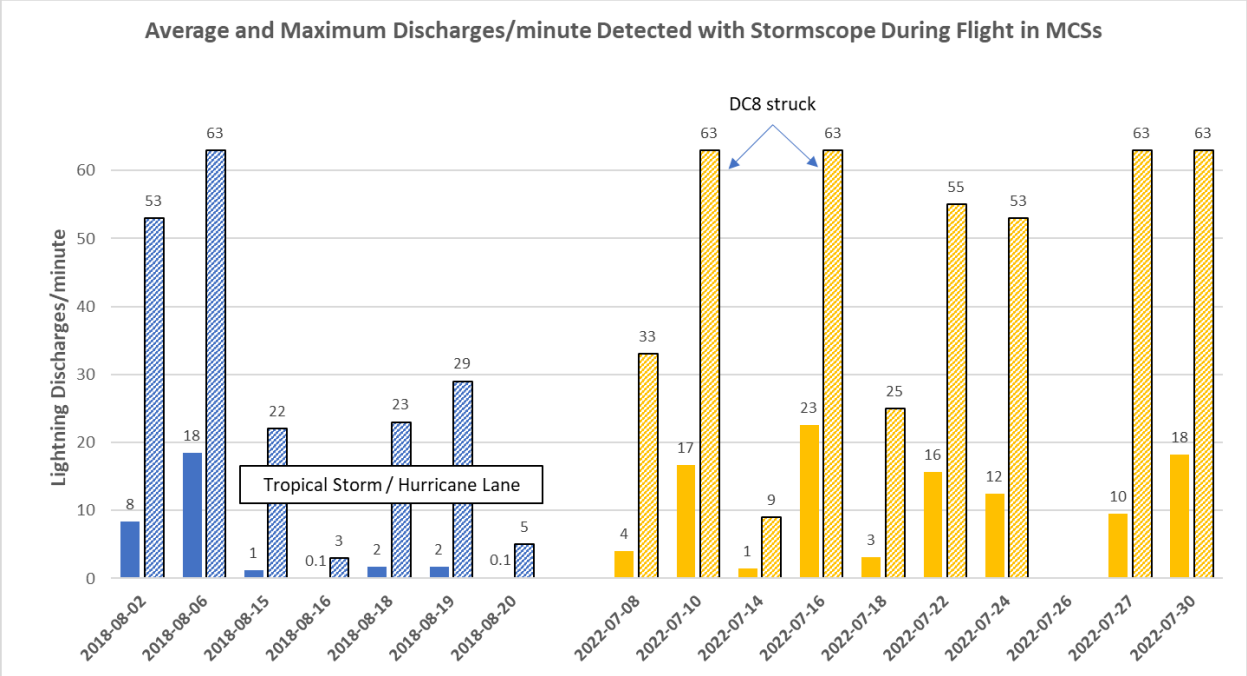

Figure 23.—Average (solid) and maximum (hatched) lightning discharge rates during flight in MCSs as recorded during HIWC RADAR II (blue) and HIWC–2022 (yellow).

In general, the lightning discharge rates recorded during the 2022 flight campaign were greater than those from the 2018 campaign. An exception was the 2018-08-06 flight; an oceanic MCS in the southern Gulf of Mexico had lightning rates comparable to the flights in 2022 when the DC–8 was struck by lightning. The greater discharge rates and the higher frequency of graupel episodes in 2022 provide an indicator that the MCSs were more vigorous during HIWC–2022 than during HIWC RADAR II campaign (2018).

5.5 Limited Comparison of Low- and High-CCN-Aerosol MCS Data in HIWC–2022

As per the opinion of the HAIC–HIWC science team and as reported in Reference 18, it is contended here that all original datasets were collected in MCSs embedded in relatively unpolluted atmospheres, that is, atmospheres with relatively low levels of CCN aerosol. The same is likely true for the data from the HIWC RADAR II campaign. In all those campaigns, there was no attempt to target days or locations with possible high concentrations of CCN aerosol, and the remote locations and season of the measurements were generally conducive to clean conditions. As experience in HIWC–2022 off the east coast of the United States would show, targeting high CCN aerosol co-located with an MCS proved difficult.

As discussed in Section 2.2, the intention was to target five of a projected eight flights with MCSs having high-CCN boundary-layer aerosol concentrations. However, due to a number of circumstances described in Section 4.1, only one flight included in the HIWC–2022 data collection was categorized as high-CCN (2022-07-30), and only one flight was categorized as moderate-CCN (2022-07-27). (See Section 5.1.2 for categorization criteria.) Both flights collected high-altitude data in the MCS only in the –40 °C temperature interval. The resulting amounts of data for the following dataset pairs are compared in Sections 5.5.1 and 5.5.2 and summarized in Table 8. TWC comparisons are from Type 2 TWC data points and MMD comparisons are based on 5-s PSDs in regions with TWC ≥1.0 gm^{-3}.

TABLE 8.—NUMBER OF TWC AND MMD DATA POINTS AT –40 °C: HIGH CCN VERSUS LOW AND MODERATE CCN; MODERATE AND HIGH CCN VERSUS LOW CCN

High CCN aerosol (2022-07-30) versus low and moderate CCN aerosol (all other flights)			
	TWC data points at 0.5-Nm distance scale	**TWC data points at 17.4-Nm distance scale**	**MMD data points based on 5-s PSDs with TWC ≥1.0 gm^{-3}**
High CCN	2	2	139
Low and moderate CCN	68	57	1,234
Moderate and high CCN aerosol (2022-07-30 and 2022-07-27) versus low CCN aerosol (all other flights)			
	TWC data points at 0.5-Nm distance scale	**TWC data points at 17.4-Nm distance scale**	**MMD data points based on 5-s PSDs with TWC ≥1.0 gm^{-3}**
Moderate and high CCN	15	12	671
Low CCN	55	47	702

It is important to note that only small numbers of high-CCN TWC data points were collected for comparisons. Successful testing for a statistically significant difference between, for example, 2 high-CCN and 68 low- and moderate-CCN TWC points at 0.5 Nm seemed highly unlikely based on simple intuition, unless the former TWC values lay well outside the range of the latter (e.g., maximum total water content TWC_{max} of the two cloud segments in high-CCN conditions was substantially higher than that of the 68 cloud segments in low- and moderate-CCN conditions). For higher percentiles and maxima, determination from a smaller number of samples would tend to yield lower values. Nevertheless, comparisons are presented in the following sections for documentation.

It is also important to note that many of the flights experienced high levels of Saharan desert dust (Table 4), which may have affected cloud microphysical properties in addition to any anthropogenic CCN effects.

5.5.1 Comparison of TWC Values

Due to the small number of high-CCN TWC points, the maximum and higher percentiles derived from such a subset were expected to be lower than for the larger subset of lower CCN data points, simply because the probability of sampling the more extreme values decreased as the number of samples decreased. So, in an attempt to determine if the lower and higher CCN TWC datasets were significantly different, the lower CCN dataset was subsampled 10,000 times with replacement, taking a small number of samples each time corresponding to the number of higher CCN data points collected in the campaign. For example, the 68 lower CCN TWC data points at 0.5 Nm were subsampled two at a time, TWC_{max} for each subsample was calculated, and then the average of the resulting 10,000 TWC_{max} values was calculated along with its 95-percent confidence interval. This procedure is called bootstrapping. If the observed TWC_{max} of the higher CCN dataset was greater than the upper 95-percent confidence interval of the bootstrap, this would represent a statistically significant result at the 95-percent confidence level.

The 0.5-Nm and 17.4-Nm TWC_{max} values for the two HIWC–2022 high-CCN segments of 2022-07-30 were 2.02 and 1.55 gm^{-3}, respectively. The corresponding maxima for the 68 low-to-moderate-CCN segments of the remaining flights were higher at 3.55 and 1.97 gm^{-3}, respectively. Using the bootstrapping procedure, and subsampling the 68 values two at a time, the mean TWC_{max} value for the 0.5-Nm distance scale was 2.22 gm^{-3}, with a 95-percent confidence interval of 0.46 to 3.53 gm^{-3}. For 17.4 Nm, 2 high-CCN and 57 low-to-moderate-CCN segments were collected. The two-sample bootstrapping returned an expected average TWC_{max} of 0.99 gm^{-3}, with a 95-percent confidence of 0.24 to 1.96 gm^{-3}. Clearly, selecting two samples to estimate TWC_{max} from the population of HIWC–2022 TWC data

resulted in very wide 95-percent confidence intervals. Although the high-CCN TWC_{max} value of 1.55 gm^{-3} was higher than the mean TWC_{max} from the bootstrapping at 17.4 Nm, differences were not significant at the 95-percent confidence level at either distance scale.

Similarly, there were 15 and 12 moderate-to-high-CCN points at 0.5 and 17.4 Nm, respectively, from 2022-07-27 and 2022-07-30. Bootstrap subsampling of 15 and 12 points from the remaining 55 0.5-Nm and 47 17.4-Nm low-CCN points yielded the following. The mean bootstrapped TWC_{max} for the 0.5-Nm dataset was 2.83 gm^{-3} with a 95-percent confidence interval of 1.87 to 3.53 gm^{-3}. The TWC_{max} value of the 15 moderate-to-high-CCN points was lower at 2.31 gm^{-3}, but within the 95-percent confidence interval. The mean bootstrapped TWC_{max} value at 17.4 Nm was 1.54 gm^{-3} with a 95-percent confidence interval of 1.15 to 1.72 gm^{-3}. This time, the moderate-to-high-CCN TWC_{max} was higher at 1.97 gm^{-3}, and higher than the upper 95-percent confidence interval. Therefore, at the 17.4-Nm distance scale, the combined data of 2022-07-27 and 2022-07-30 produced a TWC_{max} value statistically different from the other flights, possibly due to having higher CCN values. But this could alternatively be due to the fact that the MCS of 2022-07-27 was larger, with longer cloud segments, thereby being more likely to produce higher 17.4-Nm TWC_{max} values, regardless of CCN aerosol levels.

A similar bootstrapping analysis was not performed for TWC_{99} values. Calculating TWC_{99} from two samples is highly dubious, and is also quite sensitive to the percentile calculation algorithm. Since TWC_{99} estimates would have been similar to TWC_{max} values, it is contended that similar conclusions would have been reached.

5.5.2 Comparison of MMD Values

The MMD of the aggregate of all 5-s (~0.5-Nm) PSD points with IWC ≥1 gm^{-3} was calculated for the lower and higher CCN flights of HIWC–2022. The total number of 5-s points for the two high-CCN and 68 low-to-moderate-CCN segments were 139 and 1234 respectively. The MMDs for each subset were calculated in the same manner as the original datasets, by accumulating all 5-s values into a single spectrum and then calculating the MMD of the accumulation. The low-to-moderate-CCN and high-CCN MMDs were 331 and 309 μm, respectively, with high-CCN being about 7 percent lower.

A corresponding analysis was performed to compare the MMD obtained from the moderate-to-high-CCN flights of 2022-07-27 and 2022-07-30 to that obtained from the remaining low-CCN flights. MMD for the moderate-to-high-CCN flights was 351 μm versus 311 μm for the low-CCN flights, this time with the moderate-to-high-CCN flights being 13 percent higher. The apparent direction of influence of increased CCN was inconsistent. However, on closer inspection, the high-CCN flight's MMD of 309 μm was very close to the low-CCN flight's MMD of 311 μm. The moderate-CCN flight of 2022-07-27 was the outlier at 363 μm. Consequently, no conclusion on the effect of elevated CCN on MMD was proposed, other than that the observations suggested that if such an effect were present in the data, it affected MMD by less than 13 percent.

5.5.3 Mixed-Phase Results

No mixed-phase regions were identified in any high-altitude MCS segments, and therefore no mixed-phase differences between low-CCN and high-CCN regions were observed. Mixed-phase regions were identified using an analysis of a combination of instruments, including ice accretions detected on the Goodrich Ice Detector, and a signature of poor overlap between the CDP–2 and 2D–S particle probes in glaciated conditions. Appendix 4 of Reference 18 describes in more detail similar analysis techniques used to identify mixed phase in the original dataset.

5.6 Addition of HIWC RADAR II and HIWC–2022 Data to Original Datasets

Section 5.5 revealed that due to the small number of high-CCN data segments in HIWC–2022, a comparison of the two high-CCN segments to the 68 low-CCN segments had limited significance. However, in the context of the original datasets delivered to the ARAC ICIWG, HIWC–2022 and HIWC RADAR II provided a significant amount of new data collected in a manner compatible with the original datasets and in MCSs that were somewhat different than the original. The question then arises as to whether the data would have been sufficiently different to change ongoing ICIWG deliberations on Appendix D modifications, had the two new datasets been included. This is the subject of the article by Strapp et al. (Ref. 27), and is summarized below and in the following sections.

The HIWC RADAR II campaign collected data in a new location in the eastern north tropical Pacific approaching Hawaii. As discussed earlier, this campaign contributed the only data in a hurricane, and the lower measured average TWC (Table 5) may have resulted from avoidance of the areas of highest expected TWC in the eyewall due to NASA's mission rules for avoiding high radar reflectivity at flight level to 5,000 ft below flight level. HIWC–2022, although conducted in the same general area as the original HIWC RADAR I campaign, contributed data from smaller MCSs (Table 5) with a larger amount of lightning and graupel. Therefore, it is contended that the diversity of the high-IWC MCS dataset is increased when adding HIWC RADAR II and HIWC–2022.

5.6.1 Effect on Maximum Total Water Content

Table 6 displayed the amount of Type 2 data added by the HIWC RADAR II and HIWC–2022 datasets in each temperature interval. Collectively, adding these two datasets to the original increased the number of points by about 38 percent. The largest increase of 88 percent, excluding the nontargeted –20 °C interval, was at –40 °C due to HIWC–2022 focusing on that interval.

The effects of adding these two campaigns to the original campaigns on TWC_{max} at 0.5 and 17.4 Nm are shown in Table 9 (0.5 Nm) and Table 10 (17.4 Nm). The HAIC–HIWC Cayenne and Darwin datasets provided the highest TWC_{max} values at 0.5 Nm, whereas HIWC RADAR I contributed the highest TWC_{max} value at 17.4 Nm and –50 °C due to its long traverses in the tropical storms. The new HIWC RADAR II and HIWC–2022 campaigns generally provided lower TWC_{max} values, particularly at 17.4 Nm. It was speculated that lower values in HIWC RADAR II were due to avoidance of high reflectivity in the Pacific tropical storm/hurricane and that lower values in HIWC–2022 were due to the MCSs generally being smaller. Lower values may also have resulted from the smaller number of samples in the new datasets; the probability of reaching similarly high TWC_{max} values in an identical population would decrease with a decreasing number of samples. However, the HIWC–2022 TWC_{max} value of 3.55 gm^{-3} at 0.5 Nm and –40 °C did almost reach the original campaign value of 3.66 gm^{-3} measured in Cayenne. In the end, the composite of original-plus-new dataset TWC_{max} values (row 10 values in Table 9 and Table 10) were unchanged from those of the original datasets alone (row 5 values in same tables). More information on TWC_{max} can be found in Strapp et al. (Ref. 27), where individual plots of TWC_{max} versus distance scale are provided. The addition of the two new datasets did not increase TWC_{max} values at any distance scale relative to the original dataset.

TABLE 9.—TYPE 2 MAXIMUM TWC VALUES MEASURED AT 0.5-NM-DISTANCE SCALE BY DIFFERENT CAMPAIGNS IN MCSs IN FOUR TARGETED TEMPERATURE INTERVALS

[Composite results for original campaigns shown in row 5; final composites including all campaigns shown in row 10.]

Row no.	Dataset	–50 °C		–40 °C		–30 °C		–10 °C	
		No. of cloud segments	TWC_{max}, gm^{-3}	No. of cloud segments	TWC_{max}, gm^{-3}	No. of cloud segments	TWC_{max}, gm^{-3}	No. of cloud segments	TWC_{max}, gm^{-3}
1	HAIC–HIWC Darwin, AU; F20	13	2.65	49	3.63	39	3.69	7	3.40
2	HAIC–HIWC Cayenne, GF; F20	17	2.49	46	3.66	50	4.17	27	4.14
3	HAIC–HIWC Cayenne, GF; CV580	---	---	---	---	---	---	76	3.14
4	HIWC RADAR I FL, US; DC–8	41	2.55	36	2.38	47	3.32	3	2.62
5	Original dataset (All HAIC–HIWC datasets plus HIWC RADAR I)	71	2.65	131	3.66	136	4.17	113	4.14
6	HIWC RADAR II FL, CA, HI, US; DC–8	13	2.15	45	2.86	23	3.79	---	---
7	HIWC–2022	---	---	70	3.55	10	3.22	---	---
8	Original dataset + HIWC RADAR II	84	2.65	176	3.66	159	4.17	113	4.14
9	Original dataset + HIWC–2022	71	2.65	201	3.66	146	4.17	113	4.14
10	Original dataset + HIWC RADAR II +HIWC–2022	84	2.65	246	3.66	169	4.17	113	4.14

TABLE 10.—TYPE 2 MAXIMUM TWC VALUES MEASURED AT 17.4-NM-DISTANCE SCALE BY DIFFERENT CAMPAIGNS IN MCSs IN FOUR TARGETED TEMPERATURE INTERVALS
[Composite results for original campaigns shown in row 5;
final composites including all campaigns shown in row 10.]

Row no.	Dataset	–50 °C		–40 °C		–30 °C		–10 °C	
		No. of cloud segments	TWC_{max}, gm^{-3}	No. of cloud segments	TWC_{max}, gm^{-3}	No. of cloud segments	TWC_{max}, gm^{-3}	No. of cloud segments	TWC_{max}, gm^{-3}
1	HAIC–HIWC Darwin, AU; F20	11	1.75	49	2.85	32	2.75	78	3.06
2	HAIC–HIWC Cayenne, GF; F20	16	1.31	44	2.38	42	2.40	24	3.06
3	HAIC–HIWC Cayenne, GF; CV580	---	---	---	---	---	---	49	2.43
4	HIWC RADAR I FL, US; DC–8	37	2.07	33	1.85	43	2.74	NA	NA
5	Original dataset (All HAIC–HIWC datasets plus HIWC RADAR I)	65	2.07	126	2.85	117	2.75	78	3.06
6	HIWC RADAR II FL, CA, HI, US; DC–8	8	1.38	37	1.91	21	2.31	---	---
7	HIWC–2022	---	---	59	1.97	7	1.91	---	---
8	Original dataset + HIWC RADAR II	73	2.07	163	2.85	138	2.75	78	3.06
9	Original dataset + HIWC–2022	65	2.07	185	2.85	124	2.75	78	3.06
10	Original dataset + HIWC RADAR II + HIWC–2022	73	2.07	222	2.85	145	2.75	78	3.06

5.6.2 Effect on 99th-Percentile Total Water Content

The primary TWC statistic requested by the EHWG was TWC_{99} at a reference distance of 17.4 Nm. Flight plans approved by the EHWG defined the environment for which this statistic pertains. It is conditional on the aircraft being in an MCS, ideally similar to MCSs that have been documented in engine events, and ideally within 20 Nm of a heavy precipitation area below the aircraft. The absolute probability of encountering the TWC_{99} level is therefore much more remote than the 1 in 100 suggested by the 99th percentile.

Comparisons of Type 2 TWC_{99} values at the 0.5- and 17.4-Nm distance scales in the four targeted temperature intervals are shown in Table 11 and Table 12, respectively. The number of data points for each entry is the same as shown in Table 9 and Table 10. Reference 27 provides a more detailed description of the derivation of these values and sampling uncertainties. The final effects of adding the new campaign data to the original are shown in the comparisons of the row 3 and row 4 values and in the final percent differences in row 5. There was a small change in the –10 °C interval TWC_{99} statistics (–0.2 and –0.3 percent, respectively) even though no additional points were added. This is because the

bootstrapping procedure returns slightly different mean values and uncertainty each time due to its random subsampling. The –50 °C and –30 °C intervals showed small decreases from the original composites (e.g., –1.6 and –1.2 percent at 17.4 Nm, respectively), partially due to the modest increase in the number of points (about 18 and 24 percent, respectively). Given that the new campaigns tended to have lower TWC_{max} values (Table 9) and that TWC_{99} values were typically driven by the few highest TWC points, the addition of a small number of lower TWC points from the new campaigns had little influence on TWC_{99}. Naturally, lower percentiles (not shown) were more affected. The largest change due to the addition of the new campaign points was in the –40 °C interval at 17.4 Nm (–5.9 percent), where the original composite dataset number of points was augmented by 88 percent. Further information on TWC_{99} versus distance can be found in Reference 27, which provides individual plots of TWC_{99} versus distance for the composite original and composite original-plus-new datasets.

TABLE 11.—TYPE 2 TWC_{99} VALUES MEASURED AT 0.5-NM-DISTANCE SCALE FOR TWO NEW HIWC RADAR II AND HIWC–2022 CAMPAIGNS, COMPOSITE OF ORIGINAL CAMPAIGNS, AND COMPOSITE OF ORIGINAL PLUS NEW CAMPAIGNS
[Values in rows 1 to 4 are gm^{-3}; uncertainties (±2σ) provided from bootstrapping with replacement.]

Row no.	Dataset	–50 °C	–40 °C	–30 °C	–10 °C
1	HIWC RADAR II FL, CA, HI, US NASA DC8	2.34±0.50	2.75±0.46	3.61±1.05	---------
2	HIWC–2022 Florida, US NASA DC–8	---------	3.29±0.67	3.09±1.35	---------
3	Original dataset	2.66±0.10	3.59±0.23	3.75±0.46	3.91±0.42
4	Original dataset + HIWC RADAR II + HIWC–2022	2.63±0.12	3.54±0.24	3.72±0.32	3.90±0.40
5	Difference	–1.0%	–1.4%	–0.8%	–0.2%

TABLE 12.—TYPE 2 TWC_{99} VALUES MEASURED AT 17.4-NM-DISTANCE SCALE FOR TWO NEW HIWC RADAR II AND HIWC–2022 CAMPAIGNS, COMPOSITE OF ORIGINAL CAMPAIGNS, AND COMPOSITE OF ORIGINAL PLUS NEW CAMPAIGNS
[Values in rows 1 to 4 are gm^{-3}; uncertainties (±2σ) provided from bootstrapping with replacement.]

Row no.	Dataset	–50 °C	–40 °C	–30 °C	–10 °C
1	HIWC RADAR II FL, CA, HI, US NASA DC8	1.58±0.25	1.64±0.58	2.36±0.48	---------
2	HIWC–2022 FL, US NASA DC–8	---------	1.93±0.19	2.04±0.69	---------
3	Original dataset	2.02±0.17	2.60±0.39	2.72±0.15	3.07±0.20
4	Original dataset + HIWC RADAR II + HIWC–2022	1.99±0.17	2.45±0.35	2.69±0.18	3.06±0.19
5	Difference	–1.6%	–5.9%	–1.2%	–0.3%

Due to the small percent changes, it is contended that there is insufficient justification for updating the original dataset for the ARAC ICIWG. The original campaigns provide the more conservative TWC dataset for regulatory purposes. The uncertainty bars for the two individual new campaigns were quite large due to the small number of data points in each temperature interval, reaching, for example, about 21 percent for HIWC RADAR II in the –50 °C interval at 0.5 Nm (13 points). This underscores the problem of collecting an adequate dataset for TWC_{99} estimation from a single campaign. When combining the original dataset plus the two new campaigns (i.e., six datasets), the 17.4 Nm ±2σ sampling uncertainties were ±6.2, ±6.7, ±14.3, and ±8.5 percent for the –10, –30, –40, and –50 °C intervals, respectively.

5.6.3 Effect on TWC_{99} Distance Factor

Following the method of Reference 20 for Type 1 data points, Reference 21 derived a Type 2 distance factor for the original campaign dataset. This method combined the data from all temperature intervals and calculated the distance factor relative to the value at 17.4 Nm by fitting a polynomial through the individual values of TWC_{99}(dNm)/TWC_{99}(17.4 Nm). Here, the same method was applied to the composite original-plus-new datasets and compared to that of the original composite dataset. Figure 24 displays the comparisons. By definition, the distance factor must be unity at 17.4 Nm, but the curve fit results in a small offset at 17.4 Nm, so a small adjustment was made to the best-fit polynomial to force it to unity at 17.4 Nm. A table of the old and new distance factors is included in Figure 24 for convenience. The addition of the new datasets had negligible effect on distance factors greater than about 10 Nm. However, for shorter distance scales, the distance factor increased slightly. For example, at 0.5 Nm, the distance factor increased from 1.312 to 1.347. The polynomial equation describing the composite old-plus-new dataset distance factor is as follows:

$$df = 1.2736 - 0.22354Z + 0.051396Z^2 - 0.039464Z^3$$

where df is the distance factor and Z is log10(d(Nm)).

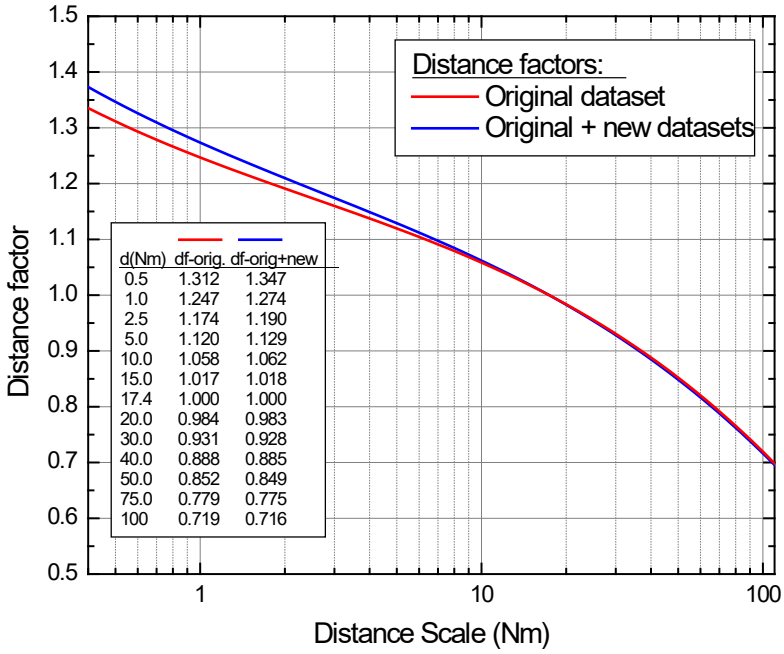

d(Nm)	df-orig.	df-orig+new
0.5	1.312	1.347
1.0	1.247	1.274
2.5	1.174	1.190
5.0	1.120	1.129
10.0	1.058	1.062
15.0	1.017	1.018
17.4	1.000	1.000
20.0	0.984	0.983
30.0	0.931	0.928
40.0	0.888	0.885
50.0	0.852	0.849
75.0	0.779	0.775
100	0.719	0.716

Figure 24.—Type 2 TWC_{99} distance factor, relative to 17.4 Nm, for composite HAIC–HIWC and HIWC RADAR I datasets (original) and after adding new HIWC RADAR II and HIWC–2022 datasets.

5.6.4 Effect on Particle CMDs and MMDs

Processing of mass distributions from particle number size distributions is complex. Procedures used in the processing and filtering of the original campaign high-IWC PSD data (5-s glaciated points with IWC ≥ 1.0 gm^{-3}) has been provided by References 14 and 20. Reference 27 describes the adaptation of the NCAR SODA–2 OAP analysis software to maximize compatibility with the original PSD processing, the filtering of erroneous PSD data from the new campaigns, and the integration of the single aircraft CMDs and MMDs of the original dataset into one single CMD for each of the four temperature intervals. These discussions will not be repeated here.

The original method to produce CMDs was to accumulate all valid high-IWC 5-s PSDs together into a single spectrum and then produce the cumulate normalized spectrum. The same procedure was applied when adding the new campaign datasets. Figure 25 displays original CMDs as well as CMDs for the original-plus-new datasets. The differences resulting from adding the new datasets are barely perceptible using the logarithmic diameter axis. The additional number of points and the MMD differences are shown in Table 13.

For the –10 and –50 °C intervals, the differences of the original-plus-new dataset MMDs were small at 0.0 and 0.6 percent, respectively, because the number of points was increased only by 0.7 and 7.2 percent. There was a more substantial MMD decrease of 3.1 and 5.0 percent in the –30 and –40 °C intervals, respectively, where the number of points was augmented by 19.7 and 43.2 percent. These differences were considered to be within the overall MMD uncertainty.

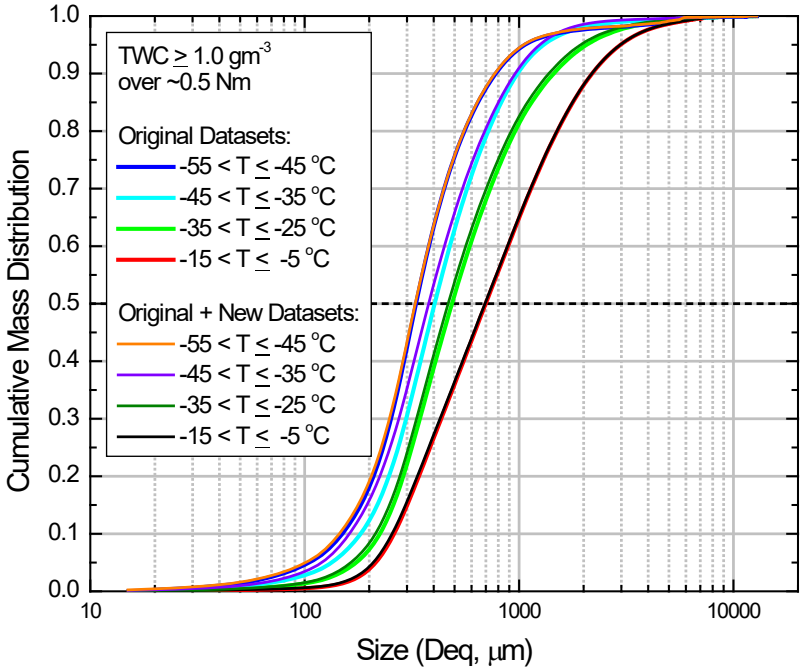

Figure 25.—CMDs of original datasets and CMDs from original-plus-new datasets. See Table 13 for MMDs and numbers of additional points.

TABLE 13.—MEDIAN MASS DIAMETERS AND NUMBER OF POINTS FOR ORIGINAL DATASET, NEW HIWC RADAR II DATASET, NEW HIWC–2022 DATASET, AND COMPOSITE OF ORIGINAL PLUS NEW DATASETS

	Original dataset (This report)		**HIWC RADAR II**		**HIWC–2022**		**Original plus new datasets**		**Percent difference between original plus new and original datasets**	
	Points	MMD, μm	Points	MMD, μm	Points	MMD, μm	Points	MMD, μm	Points	MMD
–50 °C	1,508	331	109	404	0	NA	1,617	333	7.20%	0.6%
–40 °C	3,769	404	518	361	1,373	329	5,398	384	43.20%	–5.0%
–30 °C	4,122	487	635	414	225	400	4,935	472	19.70%	–3.1%
–10 °C	4,087	699	0	NA	4	641	4,091	699	0.09%	0.0%

5.7 Radar-Derived Ice Water Content

Radar-derived ice water content (RIWC) is the NASA-derived product that was developed as a possible means to remotely detect and enable avoidance of potentially hazardous high-IWC conditions. The motivation for this effort was outlined in the HIWC Science Plan (Ref. 12). RIWC has been demonstrated to remotely identify regions of high IWC and estimate ice particle concentrations out to 60 Nm ahead of the airplane (Ref. 37). The range limit reported was set by the data acquisition subsystem rather than by radar observables or scattering physics. Consequently, the actual range limit for the RIWC is not known but is at least 60 Nm.

Using the NASA Research RADAR, the HIWC researchers were able to provide guidance to the NASA DC–8 flight crew on high-IWC regions of interest while maintaining safety and avoiding severe weather conditions that often occur in the vicinity of the high-IWC encounters. The radar was not expected to observe CCN aerosol concentrations, but it was able to observe and measure the general meteorological environment and the convective cells that were spawned in these environments. An example of the research display is shown in Figure 26. The upper left quadrant shows the radar reflectivity factor (RRF) at flight level; the lower left quadrant shows the RRF at 5,000 ft below the flight level. The upper right quadrant shows RIWC at flight level. The lower right quadrant shows the radar-derived turbulence at flight level.

The RRF rendering in this display uses more colors than a typical commercial weather radar, but the bright-green, yellow, red, and magenta colors match the colors and RRF bands used in commercial weather radars. The additional colors were used to portray the RRF measurements that exist in a commercial radar but are suppressed to minimize visual clutter. Lastly, whereas typical commercial radar displays only show only one scan and one measurement (e.g., RRF), the NASA display was developed to allow immediate visualization of all the radar measurements that were needed to establish safe flying conditions for this aircraft and these missions.

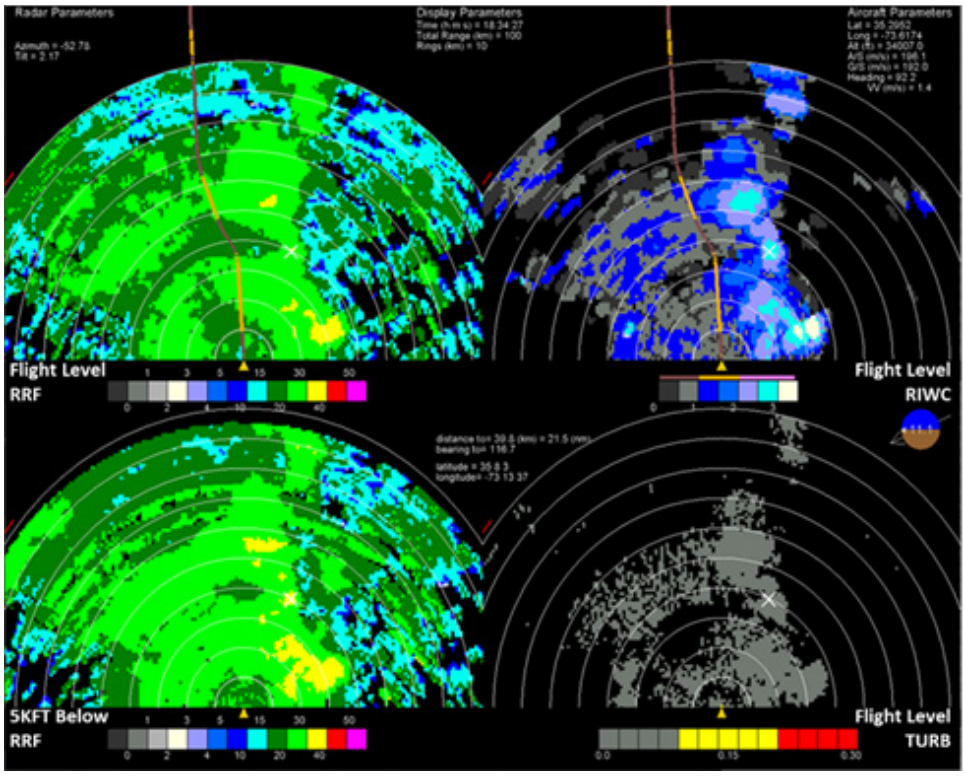

Figure 26.—NASA Research RADAR display used for weather and radar research and demonstration of new and noncertified measurements and observables.

One of the secondary objectives for this flight campaign was the assessment of any aerosol concentration dependencies on the previously developed NASA algorithm for RIWC. The NASA algorithm had been empirically derived from previous flight data without regard to aerosol concentrations (Ref. 37). The NASA Radar team looked at the various scaling parameters within the algorithm to see if there were any dependencies on aerosol concentrations that might require a modification to the algorithm. It was concluded that no change to the algorithm was needed to account for aerosol concentrations. This result was not surprising given that the radar (by means of the RIWC algorithm) responds to the concentration of ice particles that were observed without knowledge of whether the ice particles were more abundant than would have been produced under other aerosol conditions. Simply stated, the radar (by means of the RIWC algorithm) measured the ice particle concentrations it observed; if higher aerosol concentrations resulted in an increased concentration of ice particles, then the radar would observe this higher ice particle concentration and report the concentration it observed.

RIWC estimates were remotely sensed approximately 70 Nm ahead of the DC–8 (about 10 min prior to the actual encounter) to less than 0.5 Nm (about 5 s) before the DC–8 flew into that volume of air and cloud. Multiple RIWC estimates were produced as the aircraft approached each area of interest (latitude, longitude, and altitude). The RIWC values reported are the time-averaged value of these individual, position-based estimates and were limited to only those observations within 1,000 ft of the aircraft's altitude; this removes RIWC observations well below the aircraft's altitude and potentially in much warmer conditions.

Figure 27 shows a scatter plot of remotely sensed RIWC versus in situ IWC measured by the IKP2 probe for the flights through MCSs at –40 °C or colder during the HIWC–2022 campaign. The values for RIWC in this plot were generated by averaging raw RIWC measurements over 0.5 Nm so they would be commensurate with the 5-s averaged IKP2 measurements. The data in this figure are from locations at –40 °C or colder, as they typify the in-flight SAT conditions experienced during commercial cruise operations. These results show fundamental performance estimates for the RIWC process; however, care was taken not to manipulate these measurements to show the "best possible" performance of the radar or the RIWC process, as those additional filtering and human-factor processes would alter the fundamental measurements, hiding any differences between the radar observations.

To see general trends in the scatter plot, the RIWC data were parsed into 0.2-g/m^3 bins of IKP2, and the mean and standard deviations of the RIWC were computed for each bin. This process was applied to the RIWC and IKP2 data with SAT ≤ –40 °C from the HIWC RADAR I (2015), HIWC RADAR II (2018), and the HIWC–2022 datasets. The results are shown in Figure 28. The symbols are staggered slightly in the x-axis for better visualization. The number of points in each bin is shown next to the RIWC mean value, and the whiskers indicate one standard deviation. This figure shows the agreement and variability of the RIWC estimates versus the IWC measurements observed during each of the three NASA HIWC Flight Campaigns.

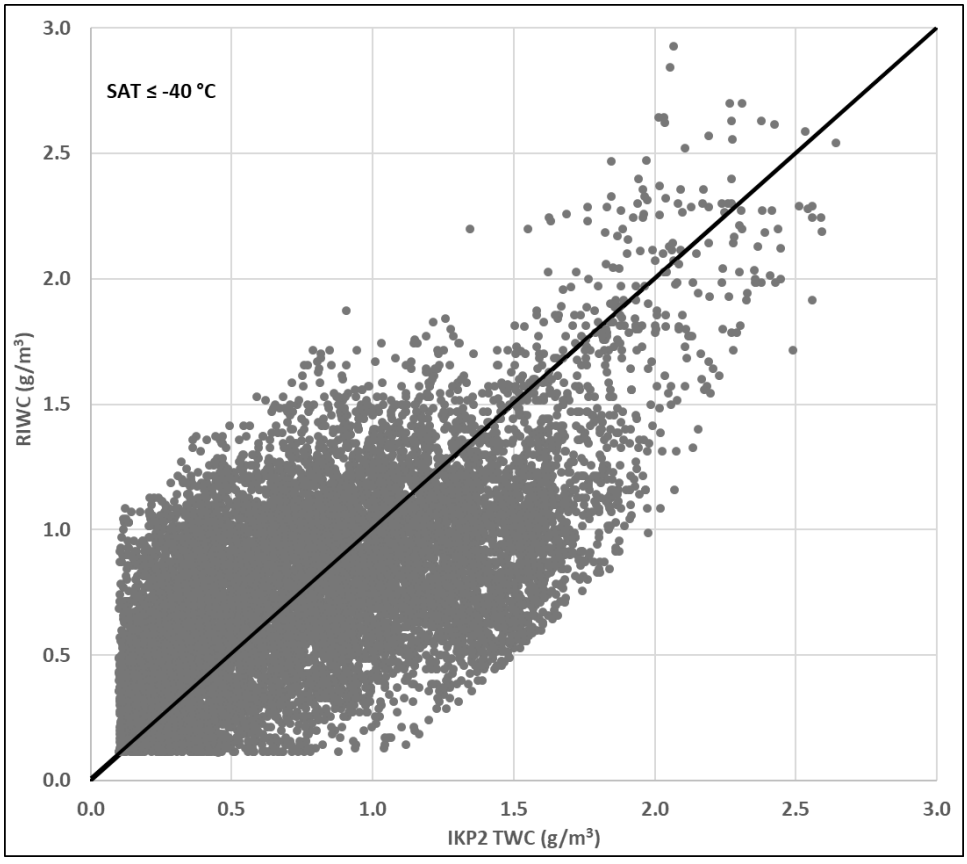

Figure 27.—Scatter plot of RIWC versus IWC measurements for all flights through MCSs with SAT ≤ –40 °C in HIWC–2022. Measurements less than 0.1 g/m^3 were suppressed as extraneous.

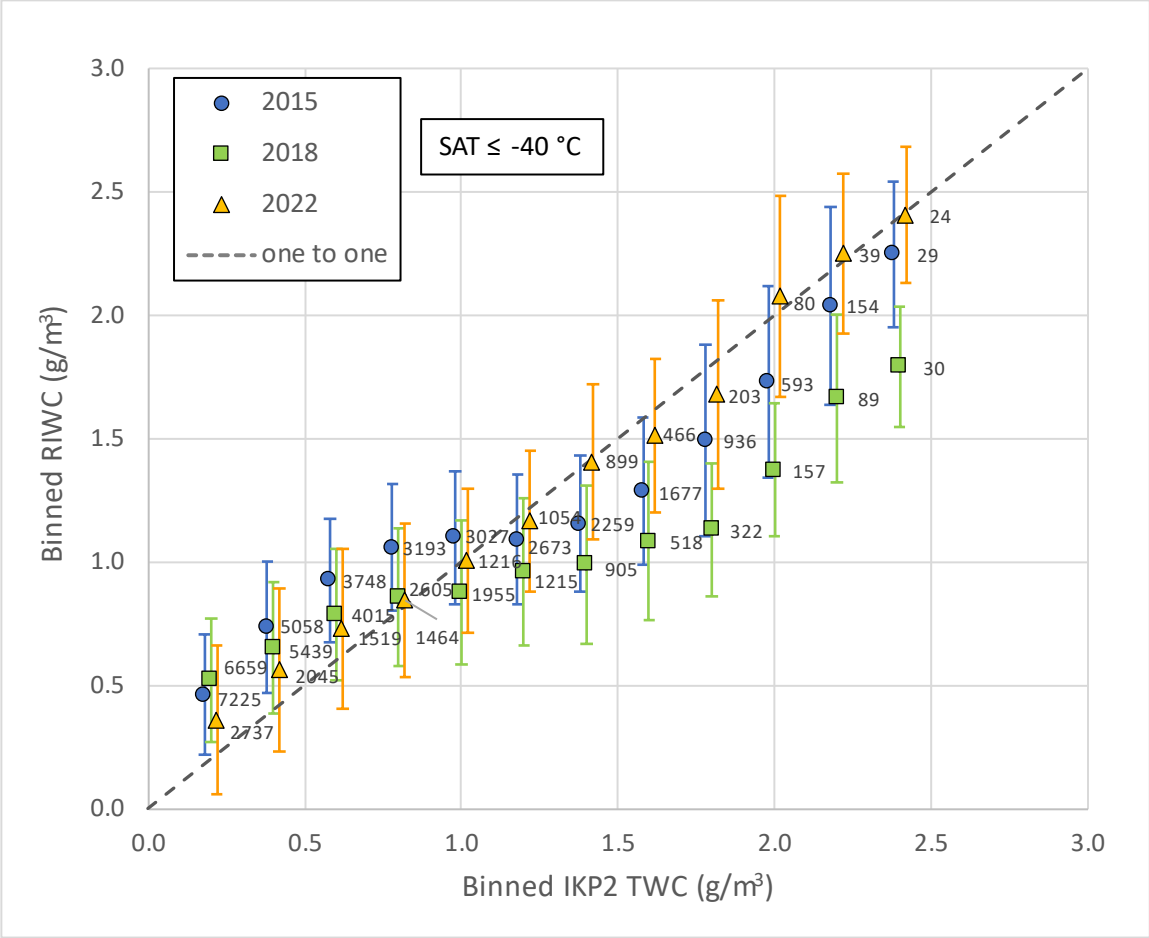

Figure 28.—Mean values of RIWC with ±1σ standard deviation in 0.2 g/m^3 bins of IKP2 TWC for all flights through MCSs with SAT ≤ –40 °C in HIWC RADAR I (2015), HIWC RADAR II (2018), and HIWC–2022. Symbols staggered in x-axis for better visualization. Data labels indicate number of points in each bin. Measurements less than 0.1 g/m^3 were suppressed as extraneous.

In general, the trends are roughly the same over all three flight campaigns and the mean values from year to year are typically within the 1σ standard deviations (typically about 0.3 g/m^3). However, for IKP TWC > 1.0 g/m^3, the 2018 RIWC results trend lower than the 2015 and 2022 results. It is speculated that this may be due to the high percentage of data points from HIWC RADAR II (2018) that were made in Tropical Storm/Hurricane Lane. As pointed out in Section 5.2, during the flights into Lane, the regions of expected highest TWC near the eyewall were avoided due to NASA mission rules against flying through high radar reflectivity. It was also pointed out in Section 5.4 that the lightning discharge rates during the flights into Tropical Storm/Hurricane Lane were significantly less than those measured in HIWC–2022. As such, the statistics from 2018 may be driven by some unique aspects of the data from the HIWC RADAR II flight campaign. Nevertheless, given that the median RIWC values from HIWC–2022 were consistent with those observed in HIWC RADAR I (2015), and to a lesser degree with those observed in HIWC RADAR II, the conclusion is that RIWC did not provide evidence to support a change in the TWC_{99} due to higher boundary-layer aerosols.

6.0 Discussion on Effects of Aerosols on High-Altitude IWC in Deep Convection

6.1 Brief Description of Processes That Create Precipitation in Cloud

It is commonly accepted that clouds with tops warmer than 0 °C can produce rain without the presence of the ice phase. This is particularly true in marine tropical clouds but has also been observed to be common in tropical continental clouds. This mode of precipitation development is called the warm rain process. Droplets nucleate in an updraft on CCN grown by vapor diffusion and eventually become large enough to further grow through collision and coalescence to raindrop sizes.

For clouds with tops that rise above the freezing level, ice particles will eventually form through homogenous nucleation at temperatures near –40 °C. However, by about –15 °C, ice crystals are usually observed in clouds. The primary formation pathways other than homogeneous freezing are through interactions with ice nuclei in the atmosphere: heterogeneous freezing, or direct deposition to ice particles bypassing the water droplet stage; condensation freezing, initiated by ice nuclei contained during the liquid drop nucleation; contact freezing, when supercooled drops immediately freeze on contact with an INP in the surrounding atmosphere; and immersion freezing, when a water droplet contacts and absorbs an INP and subsequently freezes during its evolution. After ice particles have formed, they grow rapidly by diffusion in cloud regions that are supersaturated with respect to ice and at the expense of any liquid droplets in cloud (due to ice having a lower saturation vapor pressure than liquid water). Once reaching a few hundred microns in size, ice particles can further grow through collisions with water droplets (accretion) and through collision and aggregation with other ice crystals. Precipitation formation through the ice phase dominates higher latitude clouds, particularly in the winter, and tends to glaciate mixed-phase clouds once sufficient ice concentrations have been established.

Observations have shown that the concentration of ice particles in growing clouds often greatly exceeds the concentrations of available ice nuclei, indicating the presence of a secondary ice production (SIP) mechanism. Evidence for SIP in HIWC–2022 TCu clouds is discussed in Section 6.3.3. The development of precipitation is also affected by cloud dynamics, which determine the thermodynamic environment in which particles grow and the redistribution of particles through their fall velocities and cloud updrafts and downdrafts. The overall process is rife with complex interactions.

Further details and references on these fundamental cloud precipitation development processes can be found in Pruppacher and Klett (Ref. 55); Rogers and Yau (Ref. 56); and Lamb and Verlinde (Ref. 57).

6.2 Literature Review of Warm Rain Process

The HIWC–2022 first-order hypothesis contends that the suppression of warm rain in a high-CCN-aerosol environment may result in more condensate reaching higher altitudes (i.e., higher TWC). A limited review of the cloud physics literature was performed to investigate studies related to the effects of CCN concentration on warm rain production. A total of 21 articles published between 1982 and 2017 were reviewed. The objective of the literature review was to help identify what is already known and to note points of disagreement. Both observational and modeling studies were reviewed. The modeling articles include a complicated combination of model types, cloud types, and varied levels of microphysics simulation, all of which is best understood by a cloud modeler. Interpretation of articles documenting observations were more straightforward. The approach taken in this review was to identify the level of agreement on the effect of CCN on warm rain development, and any additional effects that might counteract a suppression effect (e.g., giant nuclei (GN), on high water content).

Early investigations of the warm rain process were reported in the late 1930s to the 1950s. Some examples are Houghton (1938) (Ref. 58); Bowen (1950) (Ref. 59); Ludlam (1951) (Ref. 60); and Telford (1955) (Ref. 61). These researchers established that droplets formed by the activation of aerosols, whereafter they grew by diffusional growth as vapor condensed in an updraft. Diffusional growth alone led to an increasingly narrow drop spectrum that required an unrealistically long time to evolve into precipitation-sized particles. They established that collision and coalescence of droplets was additionally required to develop precipitation-sized raindrops. Still, observations showed that tropical clouds could develop rain in less than 20 min, much shorter than predicted from early calculations of condensation and coalescence. Calculations required that a sufficient number of drops with diameters greater than 40 to 50 μm be formed in order to get rapid formation of rain drops. Although stochastic coalescence accelerated precipitation formation to more reasonable time frames, the rapid development of rain in short time frames remained an unresolved issue for decades and continues to be a matter of debate. The proper simulation of warm rain is an important problem in cloud physics for numerical prediction of weather and for climate change prediction scenarios produced by complex models incorporating weather processes.

For several decades thereafter, researchers focused on explaining the rapid onset of warm rain using calculations and numerical models. Three main mechanisms were proposed for the early production of large droplets that would start the rapid acceleration of droplet growth: (1) the activation of giant cloud condensation nuclei (GCCN), defined as aerosols with diameters 2 μm $\leq d <$ 20 μm, and ultra-giant CCN (UGCCN), defined as aerosols with diameters $d \geq$ 20 μm; (2) entrainment and mixing, which would locally decrease droplet concentrations, thereby allowing more growth per droplet; and (3) turbulent enhancement of collision efficiencies. Most of the work since about 1980 has focused on (1) and (2).

6.2.1 Origin of HIWC–2022 First-Order Hypothesis

Anthropogenic aerosols produced by industrial and other human activities (e.g., fossil fuel burning and biomass burning) cause increases in CCN concentrations in the regions where the aerosols are produced. Increasing CCN concentration will increase the number of cloud droplets and decrease the droplet sizes compared to a cloud with the same LWC, but lower CCN. This decrease in droplet size results in a higher cloud albedo (Twomey 1977) (Ref. 62) and a suppression of warm rain due to the decrease in concentration of larger drops that would accelerate the coalescence process. Much interest in this effect within the atmospheric science community has focused on higher albedo clouds and their contribution to global climate change by reflecting more incoming solar radiation. Still, the overall effect of aerosols on climate is a complex interplay of multiple processes (Myhre et al. 2013) (Ref. 63).

Rosenfeld (1999) (Ref. 22) discussed the suppression of warm rain by high CCN concentrations. Rosenfeld et al. (2008) (Ref. 23) contended that in cases of heavy forest fire smoke, the warm rain process could be practically shut down, and that increasing CCN concentration delayed the formation of warm rain "so that more water can ascend to altitudes where the temperature is colder than 0 °C." This formed the basis of the HIWC–2022 first-order hypothesis that high-CCN-aerosol regions could contain higher TWC levels aloft than were measured in the original dataset, as outlined in Section 1.2.

6.2.2 Giant and Ultra-Giant Cloud Condensation Nuclei

Although increased anthropogenic CCN could inhibit the development of 40- to 50-μm droplets that would initiate the warm rain process, observations suggested that GCCN and UGCCN could independently provide coalescence embryos directly from the drop nucleation process. This was first pointed out by Houghton (1938) (Ref. 58), who noted that sea-salt aerosol (SSA) created by breaking waves was an abundant source of GCCN over the oceans. By the early 1980s, Johnson (1982) (Ref. 64) had noted that measurements of aerosol over the ocean from the 1950s (Woodcock 1953) (Ref. 65)

showed the existence of UGCCN up to 200 μm. As summarized by Johnson (1982) (Ref. 64), "big aerosols make big drops." Given that all the HAIC–HIWC, HIWC–RADAR, and HIWC–2022 campaign flights sampled clouds over the oceans, this could be an important counteracting influence on the HIWC–2022 first-order hypothesis.

6.2.3 Relevant Flight Campaigns That Have Studied Development of Warm Rain and Ice in Convective Clouds

Several observational campaigns have been performed to study the warm rain process in warm tropical oceanic clouds. The Joint Hawaiian Warm Rain Project (JHWRP) was conducted in 1985, followed by the Hawaii Rainfall Project (HaRP) in 1990. Both projects employed research radars and aircraft to collect datasets characterizing clouds around Hawaii. Two articles by Beard, Johnson, and Baumgardner (1986) (Ref. 66) and Rauber, Beard, and Andrews (1991) (Ref. 67) describe the existence of very large raindrops (4 to 8 mm in diameter) that were unexpected according to conventional knowledge on drop breakup due to collisions in rain shafts.

The Small Cumulus Microphysics Study (SCMS) was conducted in the summer of 1995 near Cape Canaveral, Florida. Aircraft measurements were made of small cumuli with tops below the freezing level to attempt to trace warm rain evolution of single clouds through their lifecycle. A sensitive dual-wavelength ground-based radar was used to monitor the clouds and to define the first radar echo >0 dBZ as the start of warm rain. The objective was to help fill the gaps in understanding of the warm rain process and the apparent unexplained rapid development of rain in relatively shallow tropical clouds.

The Rain In shallow Cumulus over the Ocean (RICO) experiment was conducted during November 2004 to January 2005 in the Caribbean near Antigua and Barbuda, as reported by Rauber et al. (2007) (Ref. 68). Three aircraft were deployed to collect in situ cloud and aerosol data within an S- and K- band radar domain. The emphasis of this campaign was on the understanding of the entire cloud domain of small cumulus clouds, rather than sampling individual clouds through their lifecycle. A more statistical sampling strategy was employed in which multiple clouds were sampled at one altitude before proceeding to subsequent altitudes. RICO had many of the same objectives as SCMS, namely, identifying the processes governing warm rain development in such clouds, investigating the effects of entrainment and mixing, and investigating more macro characteristics—for example, quantifying the amount of rain produced by the cloud field. RICO also took advantage of new measurement technologies not available for SCMS.

The Cloud Aerosol Interaction and Precipitation Enhancement Experiment (CAIPEEX) was conducted in 2009 to 2010 over the Indian subcontinent, the Bay of Bengal, and the Arabian Sea, with an emphasis on the development of microphysical properties of different stages of growing continental TCu clouds. The types of measurements and objectives were similar to the TCu experiments of the HIWC–2022 campaigns. The effect of increasing CCN concentrations on the initiation of warm rain was explored in several articles (Khain et al. (2013) (Ref. 69); Konwar et al. (2010) (Ref. 40); and Konwar et al. (2012) (Ref. 70)) and is further discussed here and in Section 6.3.4.

The flight campaign known as ACRIDICON–CHUVA (Aerosol, Cloud, Precipitation, and Radiation Interaction and Dynamics of CONvective Cloud Systems – Cloud Processes of the Main Precipitation Systems in Brazil: A Contribution to Cloud Resolving Modeling and to the Global Precipitation Measurement) was conducted mainly over continental Brazil in the austral spring of 2014 (Wendisch et al. (2016) (Ref. 71)). The German Aerospace Center (DLR) High Altitude and LOng Range (HALO) research aircraft was used to make in situ measurements of growing continental TCu, again in a manner similar to the HIWC–2022 and CAIPEEX measurements. Emphasis was on the microphysical development of such convective clouds and, in particular, the development of warm rain and the initiation

of ice precipitation. Two articles provide details of the TCu measurements: Braga et al. (2017a) (Ref. 72) and Braga et al. (2017b) (Ref. 73)). These articles are further discussed here and in Section 6.3.4.

6.2.4 Summary of Articles on Effects of CCN Concentrations on Warm Rain

The following modeling articles supported the hypothesis that increased CCN concentrations delayed the onset of warm rain: Feingold et al. (1999) (Ref. 74); Yin et al. (2000) (Ref. 75); Rosenfeld et al. (2002) (Ref. 76); Lu and Seinfeld (2005) (Ref. 77); Teller and Levin (2006) (Ref. 78); Jensen and Lee (2008) (Ref. 79); Cheng et al. (2009) (Ref. 80); and Dagan, Koren, and Altaratz (2015) (Ref. 81). The following observational articles also supported the effect: Konwar et al. (2012) (Ref. 70); Braga et al. (2017a) (Ref. 72); and Hudson and Yum (2001) (Ref. 82). There was a general claim that high CCN concentrations increased the height above cloud base at which warm rain was first observed, and some claimed that drizzle/warm rain was completely suppressed by high CCN concentration. There were no articles that contradicted this effect directly.

No information was found in the modeling studies as to whether high CCN concentrations completely suppressed warm rain, although such information may have been overlooked. Several observational studies demonstrated complete suppression of warm rain in high CCN concentrations: Rosenfeld (1999) (Ref. 22); Konwar et al. (2010) (Ref. 40); Konwar et al. (2012) (Ref. 70); and Braga et al. (2017a) (Ref. 73).

6.2.5 Summary of Articles on Effects of GCCN and UGCCN on Warm Rain

Several studies have established the existence of giant SSA over the ocean up to 200 μm in diameter, e.g., Woodcock (1953) (Ref. 65). Giant aerosol can also exist over the land in the form of industrial by-products and soil components. If aerosols are sufficiently large, they do not need to be hygroscopic to act as coalescence embryos.

The following modeling articles suggested that the existence of GCCN was potentially important to warm rain development: Ochs and Semonin (1979) (Ref. 83); Johnson (1982) (Ref. 64); Beard and Ochs (1993) (Ref. 84); Szumowski, Rauber, and Ochs (1999) (Ref. 85); Lasher-Trapp, Knight, and Straka (2001) (Ref. 86); Rosenfeld et al. (2002) (Ref. 76); Blyth et al. (2003) (Ref. 87); Jensen and Lee (2008) (Ref. 79); Cheng et al. (2009) (Ref. 80); Lowenstein, Blyth, and Lawson (2010) (Ref. 88); Kogan, Mechem, and Choi (2012) (Ref. 89); Cooper, Lasher-Trapp, and Blyth (2013) (Ref. 90); Dagan, Koren, and Altaratz (2015) (Ref. 81); and Jensen and Nugent (2017) (Ref. 91). The following modeling articles suggested the importance of GCCN was limited to conditions of high concentrations of small CCN: Feingold et al. (1999) (Ref. 74); Yin et al. (2000) (Ref. 76); Hudson and Yum (2001) (Ref. 82); Lu and Seinfeld (2005) (Ref. 77); Teller and Levin (2006) (Ref. 78); and Gerber and Frick (2012) (Ref. 92). The ACRIDICON–CHUVA measurements showed that GCCN and UGCCN were only important when high background CCN concentrations were present. Konwar et al. (2012) (Ref. 70) pointed out that in very low background aerosol concentrations, the warm rain process was already very efficient, so that the effects of GCCN and UGCCN would be difficult to detect.

The following modeling studies claimed that GCCN and UGCCN had minor or no importance to warm rain development: Khain et al. (2000) (Ref. 93); Zhang, Michelangeli, and Taylor (2006) (Ref. 94); Goke, Ochs, and Rauber (2007) (Ref. 95); Reiche and Lasher-Trapp (2010) (Ref. 96); Blyth et al. (2013) (Ref. 97); and Dziekan et al. (2021) (Ref. 98). GCCN were not discussed in detail in the observational study of Braga et al. (2017a) (Ref. 72), but the absence of such a discussion seemed to indicate the lack of importance. Two of the listed authors had earlier articles suggesting the importance of GCCN, illustrating the evolution of opinions on the subject.

There did appear to be a greater number of modeling studies supporting the importance of GCCN in warm rain production, at least in clouds with high background concentrations of conventional CCN. The

reason for the varied conclusions from the modeling studies was not clear, although it is reasonable to assume that it may be at least partially due to differing scales of clouds and microphysical treatments. Several of the studies were for quite specific conditions. The definition of high CCN concentrations also varied considerably. As to applicability to the HIWC–2022 study, the observational studies of Konwar et al. (2012) (Ref. 70), supporting the importance of GCCN when background CCN concentration is high, are arguably the most convincing and relevant to the HIWC–2022 first-order hypothesis.

6.2.6 Summary of Articles Suggesting Importance of High LWC in Development of Warm Rain

In early calculations of warm rain development by condensation coalescence, Twomey (1966) (Ref. 99) pointed out that warm rain could develop much faster if the LWC were high. The modeling study of Blyth et al. (2013) (Ref. 97) also showed that large drops could form in high-LWC zones without the presence of large drop embryos. Cooper, Lasher-Trapp, and Blyth (2013) (Ref. 90) showed that a small amount of warm rain could develop in SCMS clouds over short time frames if their trajectories cycled them from entrainment zones back into high-LWC zones. Szumowski, Rauber, and Ochs (1999) (Ref. 85) argued that "giant" drops (4 to 8 mm in diameter) observed in Hawaii clouds could form by way of smaller drops recycling back into the main high-LWC updraft. Khain et al. (2013) (Ref. 69) showed that clouds with a high cloud water path (vertically integrated LWC) developed warm rain earlier. The common thread here was the potential importance of high-LWC zones in the cloud. This seemed eminently logical based on the fact that collection growth is proportional to the available LWC and drop diameter, and thus a "snowballing" growth effect would be more significant if LWC were high. Maritime airmasses would tend to have higher condensation rates than continental airmasses due to higher surface dewpoints. In this regard, maritime clouds may already be more likely to form early warm rain than continental clouds formed in drier airmasses.

6.2.7 Giant Drops

Reports in the literature from the JHWRP and HaRP campaigns (e.g., Beard, Johnson, and Baumgarder (1986) (Ref. 66) and Rauber, Beard, and Andrews (1991) (Ref. 67)) documented the existence of giant drops (4 to 8 mm). Earlier experimentation and calculations had predicted a limit to the maximum drop size of about 2 to 3 mm due to collision-induced drop breakup processes in rain shafts (e.g., List and Gillespie (1976) (Ref. 100); Gillespie and List (1978) (Ref. 101); and Low and List (1982) (Ref. 102)). Rauber, Beard, and Andrews (1991) (Ref. 67) argued that recirculation of drops falling in downdrafts could insert them back into lower updraft regions favorable for large drop growth. Szumowski, Rauber, and Ochs (1999) (Ref. 85) performed calculations to show how high-reflectivity cores could be produced by simple collection growth of a small concentration of 1- to 2-mm raindrops falling from cloud top, producing much larger drops lower in the cloud in an area less sensitive to breakup, presumably due to their low concentrations. Although these giant drops may have no clear connection to the issue of aerosol effects on cloud, it is worth noting that large drops up to approximately 5 mm were also observed in the HIWC–2022 towering cumulus (TCu) cloud measurements (Appendix 4.5).

6.3 HIWC–2022 Cloud Microphysics Investigations

MCSs evolve from individual deep convective cells that develop into a conglomerate producing a precipitation field larger than 100 km. At the mature stage of an MCS, such individual building blocks can be observed in the form of isolated cumulus and TCu clouds in the vicinity or edges of the MCS, at different stages (depths) of their evolution. These TCu clouds provide a simpler environment to study the early evolution of precipitation in an isolated quasi-Lagrangian environment before the mature stage. As described in the following sections, the HIWC–2022 TCu data were analyzed to identify any observations

supporting the HIWC–2022 first-order hypothesis about warm rain suppression early in the cloud evolution, as well as to help generally understand the microphysical evolution of precipitation in this maritime convective environment.

6.3.1 General TCu Observations

During HIWC–2022, a substantial number of flight hours were devoted to below-cloud-base aerosol sampling and in-cloud measurements in TCu clouds in the vicinity of the targeted MCSs. Penetrations across TCu clouds of various depths were made to investigate the development of warm rain and the initiation of ice in clouds formed in the MCS environment. Initially, the main purpose for these measurements was to support the numerical cloud modeling efforts of Nagoya University and to establish the aerosol composition and loading of the MCS environment. However, during the campaign, interest in the TCu measurements increased, and the target number of cloud levels and sampling time was expanded. Finding and sampling suitable TCu within available flight time was challenging. The TCu measurements decreased time available for the primary high-altitude, high-TWC sampling in the MCSs. In rough terms, about 48 percent of the flight hours were spent in transit to and from a cloud area, 33 percent in high-altitude high-TWC sampling, and 19 percent in below-cloud-base and TCu sampling. On reflection, it is now evident that the HIWC–2022 TCu dataset is incomplete and would have been better executed using a second aircraft. Furthermore, analysis of the data is time consuming, and only a fraction could be fully examined for this report. However, the analysis described in this section does provide important insights into the processes that were active in the earliest stages of maritime deep convective cloud development in the geographical region identified in Section 4.0.

The HIWC–2022 TCu measurements were made in a similar manner to those of CAIPEEX and ACRIDICON–CHUVA (Section 6.2), that is, at a series of different levels above cloud base and near cloud top. Rather than following a single cloud, the measurements were taken over a field of TCu. In HIWC–2022, clouds were chosen such that the target temperature levels were about 1,000 ft below cloud top. The five temperature levels were approximately 21 °C (~1,000 ft above cloud base); 14 and 5 °C (below freezing-level altitude); and –9 and –19 °C (above freezing-level altitude) (Figure 29). Note that the assumption here was that the clouds were growing, and measurements near the top represented the time evolution of precipitation development in a rising air parcel. Forward video taken on the NASA DC–8 documented the location of the cloud penetration and the visual characteristics of the clouds. Although the intention was to perform such runs for each HIWC–2022 flight, various operational problems resulted in acceptable TCu measurements being taken in only six of the ten flights.

Table 14 summarizes the final inventory of runs across TCu clouds, filtered as follows. Runs where the cloud top was obscured on the DC–8 video were excluded, as were runs that were clearly not TCu clouds. Runs less than 5 s (~0.5 Nm) were also excluded. The table shows runs separated into the five temperature levels. A total of 79 filtered runs were identified: 22 cloud base runs, 9 runs at ~14 °C, 11 runs in the 4 to 7 °C (5 °C) temperature interval, 24 runs near –9 °C, and 13 runs near –19 °C. The average cloud width was about 1.9 Nm.

A detailed analysis of all 79 runs of Table 14 was impractical given the resources available for this report. Instead, a subset of representative runs was analyzed for each day with TCu data, with details provided in Appendix 4. Each analysis included documentation of cloud base PSDs and identification of coalescence embryos (larger droplets), a frame from the DC–8 forward video showing the point of entry into the cloud and proximity to cloud top, OAP imagery at each of the levels above base and below the freezing level identifying large droplets, and PSDs and MSDs at those levels to quantify warm rain development. When runs above the freezing level also displayed liquid-only conditions, the same analysis was included to continue the assessment of warm rain development.

Levels Sampled *(Ideally 1000 ft below cloud top)* :

- SAT= -19 C, Press Alt=25 kft
- SAT= -9 C, Press Alt=19 kft
- SAT= +4 to 7 C, Press Alt=12 kft
- SAT= +14 C, Press Alt= 7 kft
- SAT= + 21 C, 1000 ft above cloud base

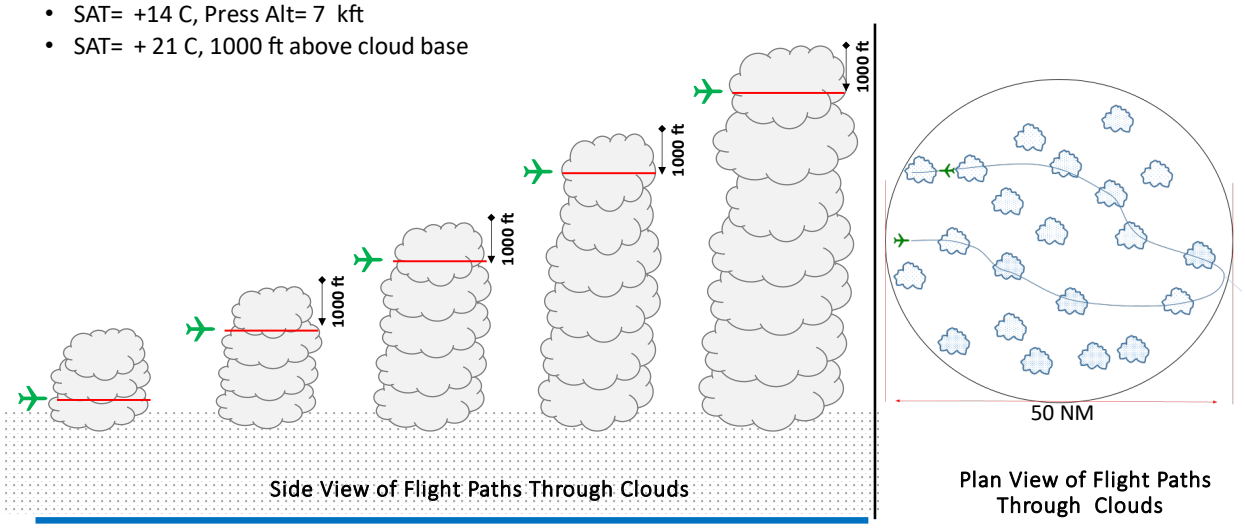

Figure 29.—HIWC–2022 sampling locations and flight path for TCu measurements.

TABLE 14.—SUMMARY OF FILTERED TCU RUNS IN HIWC–2022

	Above cloud base, approx. 21 °C		**Below freezing-level alt., approx. 14 °C**		**Below freezing-level alt., approx. 4 to 7 °C**		**Above freezing-level alt., approx. –9 °C**		**Above freezing-level alt., approx. –19 °C**	
Flight date	**No. of runs**	***SAT*$_{avg}$, °C**	**No. of runs**	***SAT*$_{avg}$, °C**	**No. of runs**	***SAT*$_{avg}$, °C**	**No. of runs**	***SAT*$_{avg}$, °C**	**No. of runs**	***SAT*$_{avg}$, °C**
2022-07-08	0	23.7								
2022-07-10	5	22.7					4	–8.5	0	–19.1
2022-07-14	3	23.0								
2022-07-16										
2022-07-18										
2022-07-22	2	20.6								
2022-07-24	4	20.9			2	4.7	5	–9.4	4	–18.1
2022-07-26			5	13.7	4	4.1	5	–9.6	6	–19.8
2022-07-27	3	21.3			5	7.0	5	–8.0		
2022-07-30	5	21.6	4	14.5			5	–9.9	3	–18.4
	22		9		11		24		13	
Total runs	79									

A cursory analysis of all 79 runs was also performed from simple visual inspection of the data to subjectively track the development of warm rain and the production of ice crystals with height. The following bulleted list summarizes the results of this cursory inspection. A more detailed version of this summary is provided in Reference 103.

- All cloud base runs in shallow clouds, at about 21 °C, contained coalescence embryos (i.e., cloud droplets with diameters larger than about 50 μm).
- By ~14 °C, the PSDs had started to develop a broader small-droplet spectrum, with occasional large drops to ~1 mm diameter.
- In the 4 to 7 °C interval, all 3 days and 11 runs displayed warm rain developing or having developed. There was no evidence of melting ice falling from above.
- At the –9 °C level:
  - 4 of the 24 runs were essentially liquid only, with supercooled large drops (SLDs) and drops exceeding 1 mm in maximum diameter.
  - 18 runs were mixed-phase runs, 12 of which were dominated by droplets and graupel, and 6 of which were sometimes dominated by glaciated zones of small ice particles.
  - 2 of the 24 runs were mostly glaciated, with little evidence of graupel and high concentrations of small ice.
- At the –19 °C level:
  - 8 of the 13 runs were glaciated, and 3 were substantially mixed phase. Two were mixed phase with only a trace of LWC.
  - At least 2 of the glaciated runs had obvious graupel images.
  - 3 of the 4 substantially mixed-phase runs were from 2022-07-30, the only high-CCN case.
  - The dominant observation was a mixture of small-to-medium-sized ice particles and graupel.

These observations led to questions as to the effect of aerosol on precipitation development. Did the warm rain observed in the 4 to 7 °C temperature range significantly deplete TWC aloft (i.e., were rainfall rates significant)? Was it possible to see a difference in warm rain production between the low-CCN cases and the single high-CCN case? Were natural ice nuclei in sufficient numbers to account for the ice observed in the sub-0 °C runs? Could the known SIP processes explain the sudden appearance of glaciating small ice? Does the existence of large drops coming up through the freezing level affect the development of ice in the cloud? To help address these questions, Section 6.3.2 provides a summary of the detailed warm rain observations of Appendix 4; Section 6.3.3 provides evidence of SIP from observations in the HIWC-2022 TCu clouds; and Section 6.3.4 provides comparisons to the corresponding measurements in CAIPEEX and ACRIDICON–CHUVA experiments.

6.3.2 Summary of Detailed TCu Warm Rain Case Studies in Appendix 4

Table 15 contains detailed microphysical observations of warm rain for a subset of runs from Table 14 that are described in detail in Appendix 4. The below-cloud-base PCASP aerosol and CCN concentrations identify the aerosol loading that day. The size of coalescence nuclei at cloud base, the cloud droplet concentrations, the total LWC and LWC ≥ 49.5 μm, and the PSD rainfall rate are included in the table.

The analyses of the PSDs revealed that the PIP probe data were often compromised, likely due to fogging of cold-soaked optics during descending runs through cloud. In retrospect, this problem may have been avoided by performing the below-cloud-base runs first, followed by ascending runs through the TCu clouds. Although the PIP data, when reliable, did appear to close the tail of the LWC spectrum, the 2D–S tail was usually truncated due to the short traverses, its relatively small sample volume, and its 1,408-μm

upper size limit. When PIP data were unreliable, the estimates of the warm rain mode from the CDP and 2D–S alone likely underestimated LWCs and rainfall rates. These cases are so identified in Table 15, and LWCs and rainfall rates are given as estimated minimum values (i.e., greater than or equal to measured value) due to the 2D–S truncation.

As previously discussed, all cloud base runs contained coalescence embryos at an adequate size to initiate warm rain. Table 15 shows that droplets with diameters up to about 110 μm were observed. These are speculated to result from nucleation of large SSAs. Indications of bimodal LWC spectra, with a condensation mode in the sub-50-μm size range and a warm rain mode at millimeter sizes, were present in average PSD measurements at 5 °C, where between 55 percent and >94 percent of the total LWC was present in the warm rain mode. PSD rainfall rates were substantial at this temperature, ≥9.8 mm/h and up to 23.2 mm/h, raising the question of whether TWC levels passing through the freezing level were significantly depleted by such rainfall rates. The answer is not obvious, and it depends on the balance between the rate of supply of condensate in updrafts and the losses due to rain fallout and other processes such as dry air entrainment. This in turn is dependent on the cloud dynamics and would be best explored using a cloud model. Taking the 2022-07-27 measurements as an example, the 23.2 mm/h at 5 °C is equivalent to 0.92 gm^{-3} falling at the 7-ms^{-1} terminal velocity of its modal size of 2 mm, which would appear on the surface to be quite significant.

Of the four flights with measurements at –9 °C, each flight experienced one run that appeared to be liquid only, which was appropriate for further examination of evolution of supercooled warm rain past the freezing level. The data of Table 15 reveal that during each of these runs, more than 50 percent of the LWC was contained in the warm rain mode. Average rainfall rates varied from 1.5 to ≥13.4 mm/h. Still, by –9 °C, the majority of runs were in mixed-phase conditions, which will be discussed separately in Section 6.3.4.

Having performed the detailed warm rain analysis of Table 15, it became apparent that measurements at 5 °C were particularly important in identifying warm rain, as this level was the highest available to approximate its maximum development before ice processes started to affect and eventually dominate precipitation. In this regard, it is unfortunate that measurements at 5 °C were not taken on 2022-07-30, the one day identified as the only high-CCN case. Below-cloud-base PCASP and CCN concentrations averaged 840 and 1,239 cm^{-3}, respectively, the highest of the campaign. At 14 °C, the maximum cloud droplet concentration reached 790 cm^{-3}, which would be considered moderately high even for a continental cumulus cloud. There was some indication in this case of more dominance of small droplets over coalescence embryos in the cloud base runs, although such embryos were nevertheless present. The sole evidence of the development of warm rain available in this case was at the –9 °C level, where about 64 percent of the LWC was in the warm rain mode and the computed rainfall rate was about 6.3 mm/h. Based on the other days, one could speculate that rainfall rates would have been higher at 5 °C. Despite the limited amount of data in this case, it can be concluded that warm rain clearly developed in an initially high droplet concentration environment, likely due to the presence of giant SSA.

TABLE 15.—DETAILED MEASUREMENTS OF WARM RAIN DEVELOPMENT
IN SELECTED TCU RUNS DURING HIWC–2022
[Runs filtered as per Table 14.]

	Measured data	2022-07-10 flight	2022-07-24 flight	2022-07-26 flight	2022-07-27 flight	2022-07-30 flight	
	Aerosol level	Low	Low	Low	Moderate	High	
	Below-base PCASP, cm^{-3}	160	71.3	77	153	840	
	Below-base CCN, cm^{-3}	NA	174	196	741	1,239	
Cloud base runs	Number of filtered runs	5	4	0	3	5	
	Chosen run time, UTC	20:28:28 to 20:28:59	14:47:13 to 14:47:21	----	14:36:55 to 14:37:09	17:03:36 to 17:04:04	
	CDP_{max} chosen run (<50 μm), cm^{-3}	254	136	----	344	715	
	CDP_{max} all runs, cm^{-3}	313	242	----	423	715	
	Max. size coalescence embryos, μm	~77	~66	----	~110	~77	
	PSD rainfall rate, mm/h	Negligible	Negligible	----	Negligible	Negligible	
14 °C runs	Number of filtered runs	0	0	5	0	4	
	Chosen run time	----	----	13:44:36 to 13:45:04	----	16:32:13 to 16:32:36	16:34:56 to 16:35:17
	CDP_{max} chosen run (<50 μm), cm^{-3}	----	----	170	----	790	385
	CDP_{max} all runs, cm^{-3}	----	----	175	----	790	790
	PSD LWC, gm^{-3}	----	----	1.05	----	0.84	0.34
	% LWC ≥49.5 μm	----	----	31%	----	5%	23%
	PSD rainfall rate, mm/h	----	----	3.0	----	0.4	1.2
5 °C runs	Number of filtered runs	0	2	4	5	0	
	Chosen run time	----	14:28:07 to 14:28:25	13:20:27 to 13:20:54	15:21:00 to 15:21:13	----	
	CDP_{max}, chosen run (<50 μm), cm^{-3}	----	71	77	414	----	
	CDP_{max}, all runs, cm^{-3}	----	101	83	414	----	
	PSD LWC, gm^{-3}	----	>1.5	>2.5	2.0	----	
	% LWC ≥49.5 μm	----	>81	>94	55	----	
	PSD rainfall rate, mm/h	----	>16	>9.8	23.2	----	
–9 °C, non mixed-phase runs	Number of filtered runs	1	0	1	1	1	
	Chosen run time	20:52:29 to 20:52:43	----	12:55:22 to 12:55:37	14:10:13 to 14:10:24	16:09:40 to 16:09:54	
	CDP_{max}, chosen run (<50 μm), cm^{-3}	70.1	----	105	46	114	
	CDP_{max}, all runs, cm^{-3}			105	46	114	
	PSD LWC, gm^{-3}	0.93	----	>0.79	0.42	0.62	
	% LWC ≥49.5 μm	78	----	>84	52	72	
	PSD rainfall rate, mm/h	13.4	----	>10.6	1.5	6.3	
Comments			Bad PIP data, PSD from CDP and 2D–S	Bad PIP data, PSD from CDP and 2D–S			

6.3.3 Ice Production

A brief overview of processes creating warm rain and ice precipitation in cloud has been given in Section 6.1. Traditionally, the primary process for production of ice particles is through the action of INPs, whose activation efficiencies increase with decreasing temperature and composition. If ice concentrations were due to primary INP activation alone, the concentration of ice particles in cloud would be determined by the activation spectra of measured INPs. INP concentrations versus temperature, measured by flight during the HIWC–2022 campaign, are shown in Figure 30. At the two nominal HIWC–2022 TCu subfreezing run levels of –9 and –19 °C, INP concentrations varied from about 0.04/L to 0.6/L and 0.6/L to 10/L, respectively. The day-to-day differences in INP concentrations were likely influenced by Saharan dust incursions, which provide a transient source of abundant INPs over background levels in this region.

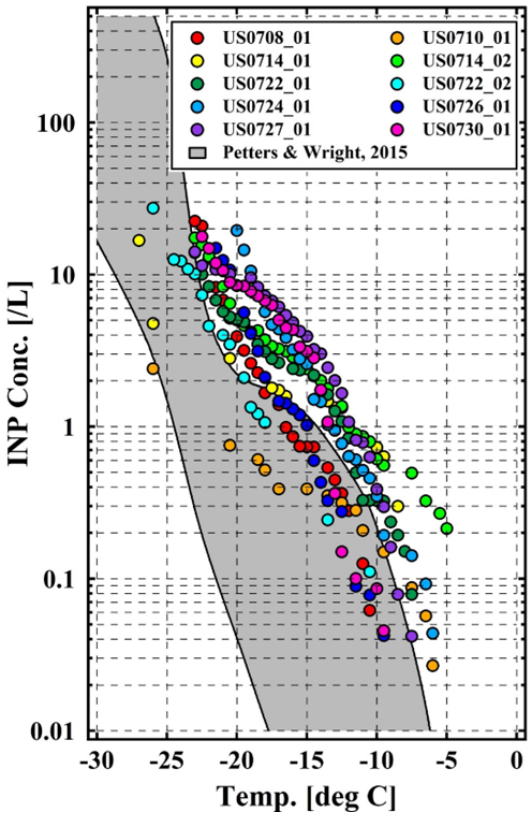

Figure 30.—INP concentrations measured each flight by Nagoya University during HIWC–2022. Legend USmmdd_0*x* refers to flight of 2022-mm-dd, sample number 0*x*. Petters and Wright (Ref. 51) data show ranges of INPs detected at various locations in cloud water, rain water, sleet, snow, and hail samples.

However, the number of ice particles measured in clouds often exceeds the number of INPs available in the atmosphere. This discrepancy can exceed several orders of magnitude and is thought to be the result of a variety of SIP processes that can occur in clouds during the course of their development. The most well-known process was described in 1974 by Hallett and Mossop (Ref. 104), where secondary ice particles generated in a laboratory chamber were found in the –3 to –8 °C temperature range, presumably due to ice fragments produced during the riming process. In natural clouds, this process would require the presence of relatively large droplets (greater than about 25 μm in diameter) and an accreting hydrometeor such as a large ice particle (e.g., frozen drop or graupel). Other laboratory experiments, for example, Takahashi (Ref. 105) and Wildeman et al. (Ref. 106) have demonstrated SIP through the physical stresses that arise inside a freezing drop, such as fragmentation of the freezing ice shell, development and fragmentation of spicules, or fragmentation of the entire drop itself. These processes have been found to be most productive for relatively large drops (at least 80 μm in diameter) in a temperature range of –10 to –20 °C. Other proposed SIP mechanisms include mechanical fragmentation due to particle collisions, breakup through sublimation, and thermal shock during particle collisions of supercooled liquid droplets and ice, as discussed in recent review articles by Field et al. (Ref. 107); Korolev and Leisner (Ref. 108); and Korolev et al. (Ref. 109).

In this section, evidence of SIP in the HIWC–2022 TCu runs is investigated. Observed ice number concentrations in the –7 to –21 °C temperature range often significantly exceeded INP concentrations. Fragmented frozen drops were found in many cloud particle images recorded by the 2D–S (Figure 31), pointing toward frozen drop breakup as a possible active mechanism for the observed high ice concentrations. Drizzle drops and raindrops were also present in many of the clouds; these have been shown to promote ice initiation (Ref. 110) and productive fragmentation upon freezing (Ref. 111). Additionally, frozen drops and/or graupel were frequently observed to coexist with drizzle, providing conditions favorable for the rime-splintering mechanism of Hallett and Mossop (Ref. 104). Similar microphysical conditions were observed in the marine TCu observations reported by Lawson et al. (Ref. 112), who attributed the high measured ice concentrations to the previously noted droplet breakup processes during freezing while indicating that these conditions are not typically present in continental clouds with higher CCN concentrations.

Table 14 provided a general summary of HIWC–2022 TCu cloud runs, subjectively filtered to include only runs at least 5 s in duration, for which the DC–8 forward video showed that the cloud was clearly a TCu cloud and that the cloud top was visible and not otherwise obscured. In Section 6.3.1, the –7 to –11 °C and –17 to –21 °C intervals have been termed the –9 °C and –19 °C intervals, respectively. The runs examined here for SIP typically lasted for 10 to 60 s. For each cloud run, the total particle number concentration (N_{t100}) was computed at 1-Hz resolution, using a lower particle size threshold of 100 μm to minimize the uncertainties in determining concentrations of small particles with OAPs such as the 2D–S. N_{t50} and N_{t200} were also calculated for the discussions that follow here.

All the –9 °C cloud runs contained supercooled liquid water, either exclusively or mixed with various quantities of small ice and graupel, which tended to coexist in areas of high ice concentration. Given that ice particles up to several hundred microns can be indistinguishable from equivalently sized water droplets due to OAP image distortions, it is difficult to convincingly separate ice total number concentrations from water drops, which can occur in comparable concentrations. Therefore, for the purposes of demonstrating possible regions of SIP, it was necessary to restrict analysis to runs or run sections that were clearly glaciated. Such sections were identified as having no detectable supercooled liquid in the 2D–S imagery, a characteristic CDP–2 distribution shape and overlap characteristics with the 2D–S, and/or a lack of an icing signal in the Goodrich Ice Detector time series. There were a few such sections at –9 °C, typically near the cloud edge, that appeared to be fully glaciated and where N_{t100} would be unaffected by the presence of supercooled drizzle and raindrops. 2D–S images from one such section on the flight of 2022-07-26 are shown in Figure 32 with an N_{t100} of 36/L.

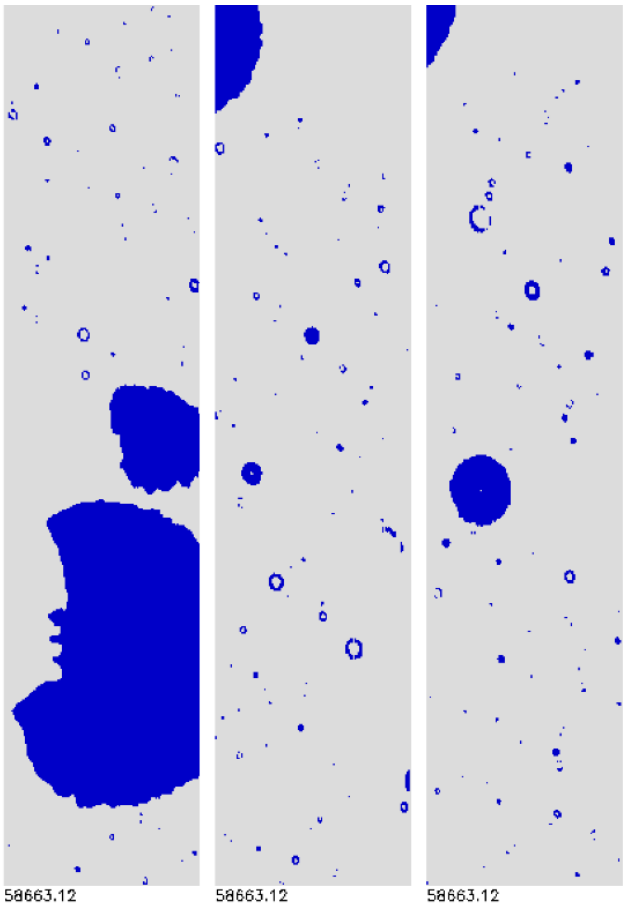

Figure 31.—Large fragmented frozen drop (left panel, bottom) with diameter of ~1.5 mm measured at –9 °C on 2022-07-24. Width of 2D–S image frame is 1.28 mm.

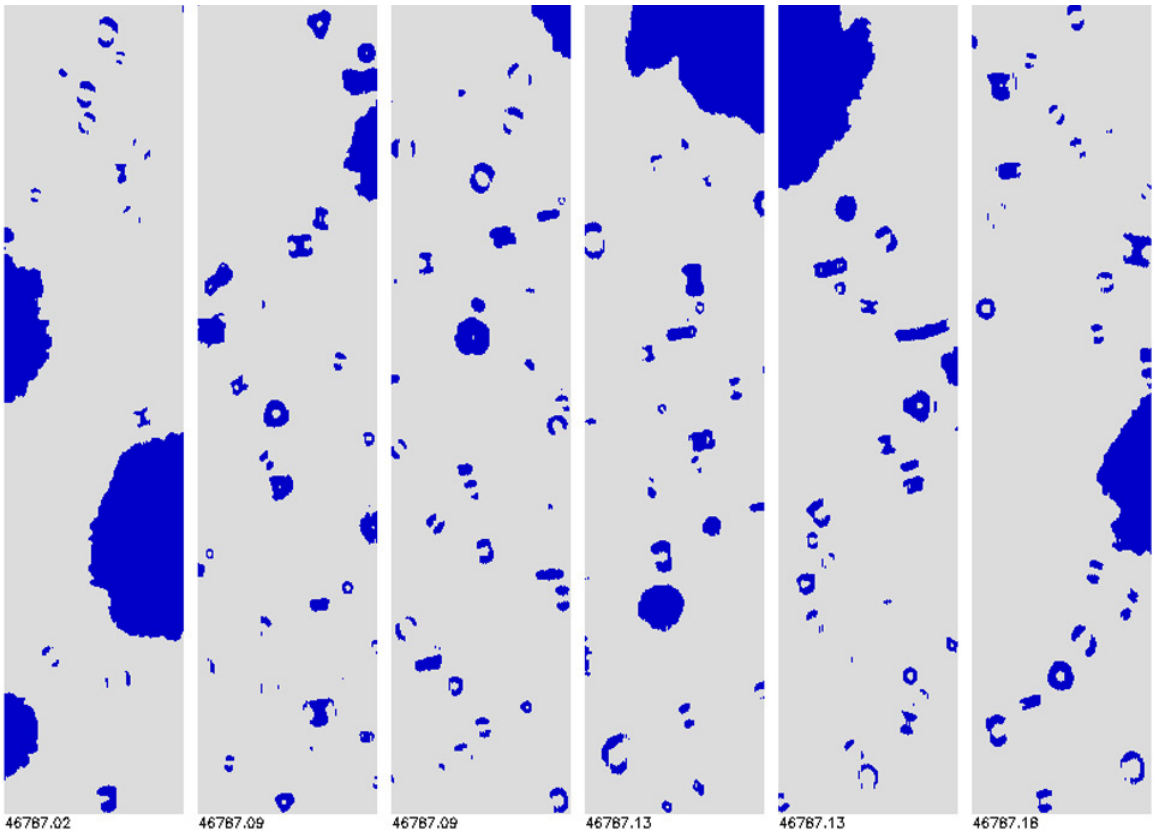

Figure 32.—Cloud particle images from 2D–S in fully glaciated section of cloud run on 2022-07-26.

There were several other –9 °C TCu runs where all the liquid drops were smaller than 100 μm and thus would not interfere with the ice N_{t100} concentration measurements. N_{t100} could be very high in these clouds, often exceeding 100/L (e.g., 2022-07-27, 14:09:22 at 103/L and 14:24:41 at 395/L), where ice was largely composed of columnar crystals. However, these measurements occurred in TCu that appeared to be less active, as opposed to the vigorously building TCu that would be expected to carry the ice upward to colder temperatures, and where graupel and fragmented ice particles were more frequently observed. In this regard, it is speculated that during the growth to –9 °C, in lower updraft velocities rather than more vigorous cells, high ice concentrations may have resulted from a longer time frame for SIP to have been active, possibly from Hallett–Mossop rime splintering in the –3 to –8 °C temperature window.

In the –19 °C interval, eight runs clearly met the glaciation measurement criteria noted previously. An example from 2022-07-24 is shown in Figure 33, with N_{t100} (blue line) consistently above 200/L and peaking at 1,121/L. The very conservative measurement of N_{t200} peaked at 768/L, which exceeded the Figure 30 –19 °C INP measurement estimate of 10/L by a factor of 77. The cloud particle images show that a wide variety of ice particles were present at the time of peak concentration, including pristine columns, aggregates, rimed ice, and graupel.

Measurements of maximum N_{t100} and N_{t200} from all eight glaciated cloud runs at –19 °C are shown in Table 16, with peak ice concentrations ranging from 132/L to 1,121/L on 2022-07-24, and from 63/L to 622/L on 2022-07-26.

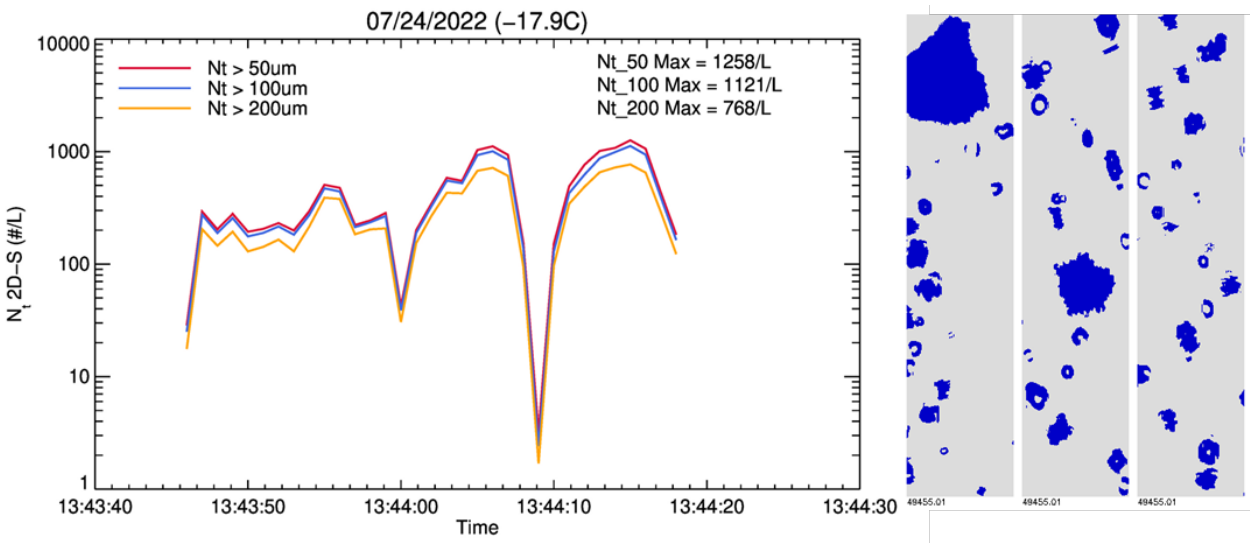

Figure 33.—Time series of N_{t50}, N_{t100}, and N_{t200} through cloud run on 2022-07-24 and 2D–S particle images during peak ice concentration measurement at 13:44:15.

TABLE 16.—PEAK ICE PARTICLE NUMBER CONCENTRATIONS FOR FULLY GLACIATED CLOUD RUNS AT –19 °C AND CORRESPONDING INPs AT –19 °C

Date; Time	Max N_{t100}, no./L	Max N_{t200}, no./L	Meas. INP est. at –19 °C, no./L
2022-07-24; 13:34:45	132	108	10
2022-07-24; 13:39:25	481	388	10
2022-07-24; 13:43:45	1121	768	10
2022-07-24; 13:49:45	951	650	10
2022-07-26; 11:50:35	63	53	4
2022-07-26; 11:53:45	145	105	4
2022-07-26; 12:46:35	360	250	4
2022-07-26; 12:48:00	622	460	4

These peak ice concentrations at –19 °C are comparable to the peak concentrations measured at high altitude in HIWC–2022 MCS clouds at –40 °C. Assuming that these TCu clouds can be considered precursor clouds to the nearby marine MCSs, this suggests that ice production may be complete at relatively warm temperatures in embedded growing convective cells of MCSs, well before reaching the homogeneous freezing level of –40 °C, and that SIP could be an important mechanism in generating the high ice-particle concentrations observed in marine HIWC events. Recent modeling efforts have also suggested that SIP may be responsible for high ice concentrations measured in TCu and in broader cloud systems. For example, Lawson et al. (Ref. 113) used a simplified 1D model to show how droplet breakup during freezing can account for their observations of rapid glaciation in TCu; Yano et al. (Ref. 114) similarly used an idealized model to highlight how efficiently various SIP processes can operate after just a few primary ice nucleation events; and Phillips et al. (Ref. 115) extended SIP modeling efforts to full cloud models.

In summary, evidence of SIP was found in glaciated regions of HIWC–2022 TCu at approximately –9 and –19 °C, where ice concentrations peaked more than 2 orders of magnitude higher than measured INP

concentrations at those temperatures. Drizzle, warm rain, frozen and fractured drops, and graupel provided conditions favorable for known SIP mechanisms to operate.

6.3.4 Evidence of Warm Rain and Secondary Ice Production Suppression in CAIPEEX, ACRIDICON–CHUVA, and HIWC–2022 TCu Measurements

As discussed in Section 6.2, two other previous campaigns made airborne in situ measurements in TCu clouds at different altitudes to investigate the evolution of warm rain and the development of ice. The CAIPEEX experiment made extensive measurements, mostly over continental India, with some limited measurements over the Bay of Bengal. CCN concentrations were high for all continental cases, exceeding 650 cm^{-3} and reaching over 10,000 cm^{-3}. The limited oceanic cases exhibited much lower CCN concentrations between about 50 and 360 cm^{-3}. ACRIDICON–CHUVA made measurements over the Amazon continental basin, with some limited measurements over the Brazil Atlantic coast. Again, aerosol concentrations were usually moderate to high. Braga et al. (Ref. 72) provided a surrogate CCN indicator in the form of a calculated adiabatic droplet number concentration, which in their dataset varied from about 276 cm^{-3} in the one maritime case and from 566 to 1,080 cm^{-3} in the remaining continental cases. In this regard, the HIWC–2022 measurements, with the exception of 2022-07-30, represented a lower CCN aerosol regime than CAIPEEX and ACRIDICON–CHUVA.

Some important common results were obtained from the CAIPEEX and ACIRDON–CHUVA observations. Increasing CCN concentration pushed the first development of warm rain to higher levels in the cloud. In continental cases with moderate to high CCN, warm rain was initiated above the freezing level, and in the most highly polluted cases, warm rain was suppressed. In contrast, warm rain development was ubiquitous in the HIWC–2022 TCu measurements, and no evidence of suppression was found, likely due to the contribution of GCCN in the form of SSAs. The CAIPEEX results showed that the counteracting effect of GCCN was significant for high CCN concentrations, but this effect was postulated to be minor for the few clean maritime airmass cases because warm rain processes were already efficient in the low maritime droplet concentrations.

ACRIDICON–CHUVA found that the development of ice particles was delayed in polluted clouds, which was attributed to the limiting of the Hallet–Mossop SIP mechanism (Ref. 104) through the suppression of the necessary larger supercooled droplets. A consequence of this could be higher TWCs aloft due to the delay in precipitation development. No support was found in the single HIWC–2022 high-CCN case of 2022-07-30. Substantial warm rain was observed in TCu at –9 °C, along with substantial small ice initiation. At the –19 °C level, ice concentrations were difficult to estimate due to the persistence of mixed phase. Nevertheless, the lack of a suppression of warm rain was clear.

6.4 Numerical Cloud Model Simulations To Assess Sensitivity to Aerosol Concentration

Over the last few decades, the atmospheric science community has developed cloud simulation models that numerically solve the equations of fluid flow, thermodynamics, and water substance, including hydrometeor evolution and transport. Models have specialized in simulating different cloud types, atmospheric environments, and scales of interest and have been used in the past to study the importance of processes and interactions that affect cloud evolution. In the case of this report, the effect of concentrations of aerosols feeding the cloud on levels of IWC aloft are of primary interest. Three-dimensional models with increasingly finer spatial resolution and ever-improving simulation of microphysical processes have evolved with increases in computing power. Due to the numerical complexity of these models, parameterizations have been developed to simplify certain model processes, including for cloud microphysics. Primary uncertainties in such models result from the inaccuracy of parameterizations and the application and simplification of initial conditions. The spatial resolution of the model may also affect simulations.

The Nagoya University HIWC–2022 original objectives included assessment of predictions of their numerical cloud model through comparisons to DC–8 in situ measurements, and sensitivity testing of the model hydrometeor fields to different initial conditions, such as the concentration of aerosols. Due to the scarcity of high-CCN-aerosol MCS in situ data from HIWC–2022, the desired statistical comparison of 99th-percentile high-CCN-aerosol TWC values to previous campaigns' low-CCN-aerosol TWC values was not possible, and the interest in model simulations of aerosol effect on MCS IWC aloft increased. As a result, a second model study was supported by NASA and the FAA to simulate HIWC–2022 cases with a large eddy simulation (LES) cloud model. For both models, by adjusting aerosol loadings, simulations could be run to contrast TWCs predicted under polluted and clean conditions.

6.4.1 Results of Large Eddy Simulation Modeling

An LES cloud model simulates the growth and evolution of clouds and captures turbulence and other scales of motion that can be resolved by the assumed grid resolution. The AMS Glossary of Meteorology defines the LES as "a three-dimensional numerical simulation of turbulent flow in which large eddies (with scales smaller than the overall dimension of the problem in question) are resolved and the effects of subgrid-scale eddies, which tend to be more isotropic and homogeneous, are parameterized" (Ref. 116). Atmospheric flow is numerically solved using the Navier Stokes equations, equations for mass continuity of air and water substances, and thermodynamic energy formulations, all which account for the transportation and phase transformations for the water in the atmosphere. Cloud and precipitation development is simplified using parameterizations.

The LES model used for this study was the NASA Langley Terminal Area Simulation System (TASS). The theoretical details of the model can be found in Proctor (Ref. 117), and the application to the modeling of high-IWC conditions in deep convective clouds is described in Proctor and Switzer (Ref. 118) and Proctor et al. (Ref. 119). In short, the 3D TASS model includes prognostic equations for pressure deviation, potential temperature, water vapor, cloud droplet water, cloud ice crystals, rain, snow, and graupel. Cloud and precipitation growth are simulated using over 60 bulk microphysical submodels, including autoconversion of cloud water to rain, and the formation and growth of ice into categories of small ice crystals, snow, and graupel. More detail has been provided in Reference 118.

Two HIWC–2022 case studies were chosen for study of the sensitivity of LES model predictions of IWC to initial aerosol concentrations: 2022-07-30 and 2022-07-10. Both were offshore oceanic MCSs, the former off the Virginia coast and the latter in the Gulf of Mexico. The 2022-07-30 case had the highest boundary-layer aerosol concentrations of the campaign, where PCASP and CCN concentrations averaged 840 and 1,239 cm^{-3}, respectively. The boundary-layer average PCASP concentration for the 2022-07-10 case was low at about 160 cm^{-3}; the CCN concentrations were not measured. In both cases, in situ properties of neighboring TCu clouds and high-altitude high-IWC regions within the MCSs were measured. During the 2022-07-10 case, the highest high-altitude peak TWC of the campaign was measured in situ by the DC–8 at about 3.5 gm^{-3} over 0.5 Nm.

Past studies of the TASS high-IWC and RRF fields have shown general agreement with aircraft observations in terms of spatial distributions and peak values, including Proctor and Switzer (Ref. 118) and Proctor et al. (Ref. 120). The same level of agreement was observed in the two case studies herein, and the demonstration of such will not be repeated here for brevity.

6.4.1.1 TASS Model Simulation of 2022-07-30

The MCS on this day consisted of a line of convective cells along an offshore front. A color-enhanced IR satellite picture is shown in Figure 34 along with the location chosen for the 30- by 120-km TASS domain. The lateral and vertical grid spacing was 150 m. The model was initialized with an unstable

environment using a North American Mesoscale (NAM) model sounding located at 36.58° N 69.90° W, within the inflow region just ahead of the line of convective cells. The sounding tropopause was approximately –71 °C, surface-based convective available potential energy (CAPE) was about 3,169 J/kg, and precipitable water was 58.7 mm. Convection was triggered with a thermal impulse (a warm bubble of 2 °C). The MCS reached a mature stage at 150 to 180 min, at which time the system possessed a persistent cirrus canopy that extended to the tropopause at 15 km elevation. At this time, the maximum integrated condensed water volume was reached, and the simulations were terminated. A cross section of RRF at 160 min and at X position of 25.8 km is shown in Figure 35. The model produced a cloud with a structure very similar to the MCS conceptual model of Houze et al. (Ref. 121). The model also produced IWCs and RRF fields aloft that were in general agreement with airborne TWC measurements from the IKP2 probe and the NASA Research RADAR (not shown).

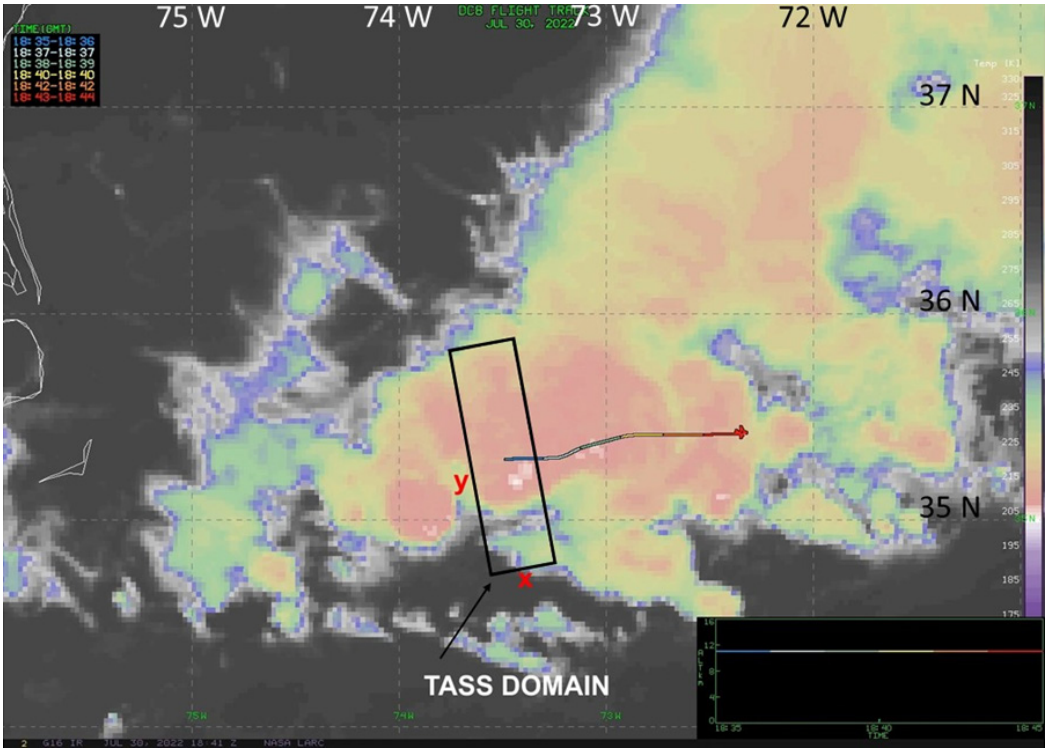

Figure 34.—Color-enhanced satellite IR image at 18:41 UTC on 2022-07-30. TASS model domain shown over MCS.

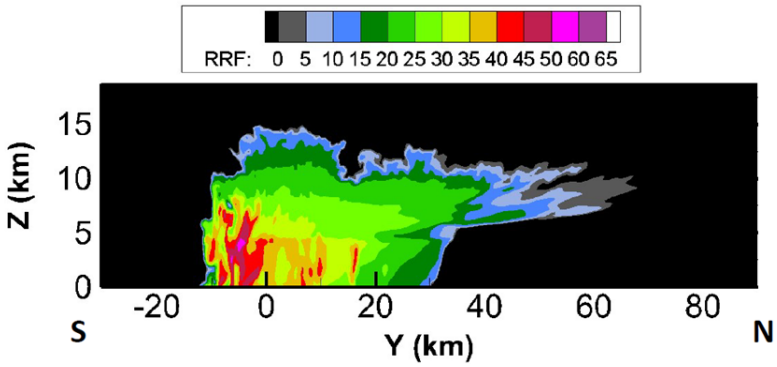

Figure 35.—Model-simulated RRF cross section at time of 168 min and at domain X position of 25.8 km.

Past studies have shown that in early updraft stages, cloud droplet number concentration (referred to herein as *ncc*) is positively correlated to the CCN concentration of aerosols feeding a cloud. Model aerosol sensitivity tests were therefore performed by changing the initial *ncc* using the following nominal values: 50 cm^{-3} (very clean), 275 cm^{-3} (typical of most HIWC–2022 cases), 650 cm^{-3} (chosen as representative for 2022-07-30), and 1,000 cm^{-3} (very polluted). One challenge in interpreting model sensitivity tests is the complexity of the 3D interactions. After discussion with the HIWC–2022 science team, the total area within the model domain of *IWC* >1 gm^{-3} was chosen as one appropriate metric of aerosol effect on high IWC. Figure 36 shows such results as a function of altitude and time. There was a clear aerosol effect, but it was in the direction opposite to that suggested by the HIWC–2022 first-order hypothesis. The total area of *IWC* >1 gm^{-3} (designated as IAR10 in Figure 36) actually seemed to decrease with increasing aerosol loading (higher *ncc*), especially in the most intense maximum in the 8- to 10-km altitude band. Spatial variation in IWC at 160 min at 9.5 km inside this band is shown in Figure 37. The highest IWCs associated with the small cells were present in the *ncc* = 275 cm^{-3} frame Figure 37 (b), reaching over 4 gm^{-3}. Still, there did appear to be a general decrease in integrated IWC from *ncc* = 50 cm^{-3} to *ncc* = 1,000 cm^{-3}. Note for example the decrease in the area of *IWC* ≥1.5 gm^{-3} (yellow shades and warmer).

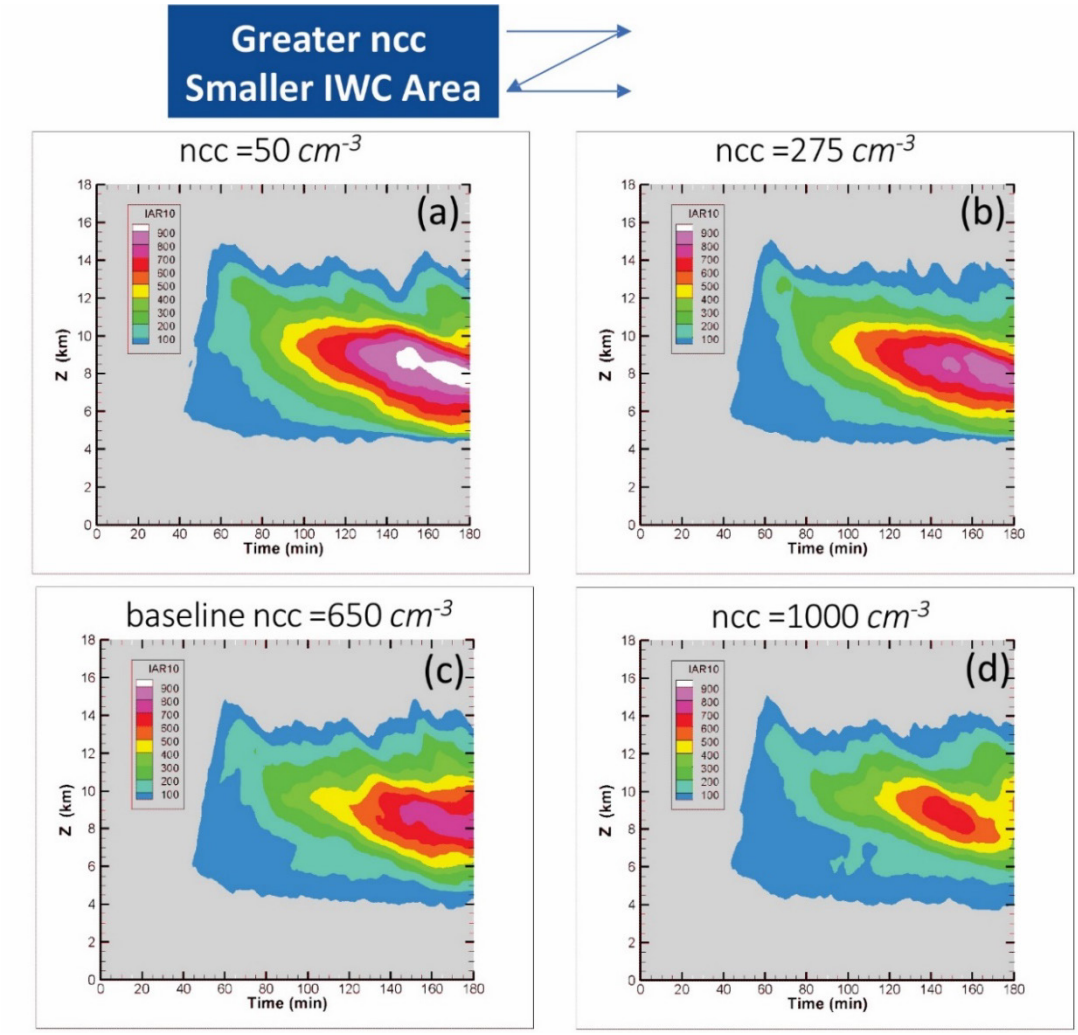

Figure 36.—TASS model aerosol sensitivity tests for 2022-07-30 with various input initial droplet number concentrations (*ncc*). Plotted field (IAR10) is total horizontal area with *IWC* >1 gm^{-3} shown as function of altitude and time.

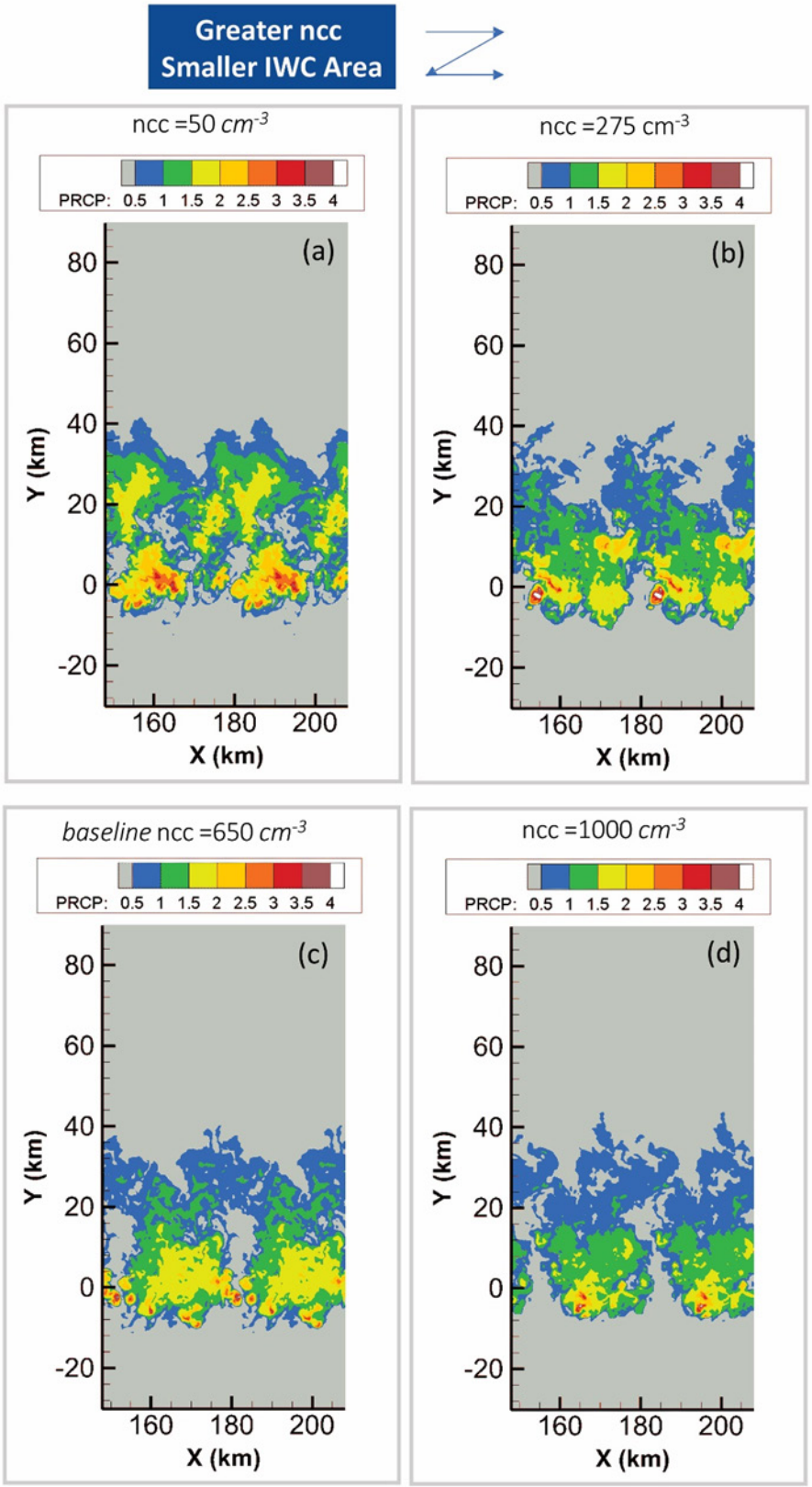

Figure 37.—IWC at 9.5 km elevation for varying aerosol levels of Figure 36. Precipitation (PRCP) levels are equivalent to IWC in gm^{-3}.

Two additional metrics were chosen for evaluation of net aerosol effects: the total volume of integrated ice in the domain, and the time- and space-integrated surface precipitation. Results for these simulations are shown in Figure 38(a) and (b), respectively. Given that liquid water above the freezing level was negligible except in small updraft cells (not shown), the integrated ice approximately represented the integrated TWC above the freezing level. The lowest aerosol simulation (Figure 38(a), *ncc* = 50 cm^{-3}, red line) showed the fastest evolution of domain-integrated IWC with highest values. The highest aerosol case (Figure 38(a), *ncc* = 1,000 cm^{-3}, magenta line) showed the lowest integrated IWC values with the intermediate aerosol cases in between, although not in a strictly ordered manner. At 150 min, the domain-integrated IWC was about 45 percent higher for the simulation of *ncc* = 50 cm^{-3} than that for *ncc* = 1,000 cm^{-3}. There was some convergence of all simulations by 180 min. The time-integrated surface precipitation (Figure 38(b)) showed only a small difference with increasing aerosol, indicating that all simulations produced nearly the same domain-integrated precipitation. When combined with Figure 38(a), this indicated that the lower aerosol case must have produced more condensate, with more of it remaining above the freezing level. Again, this result was opposite to what would be predicted from the HIWC–2022 first-order aerosol hypothesis.

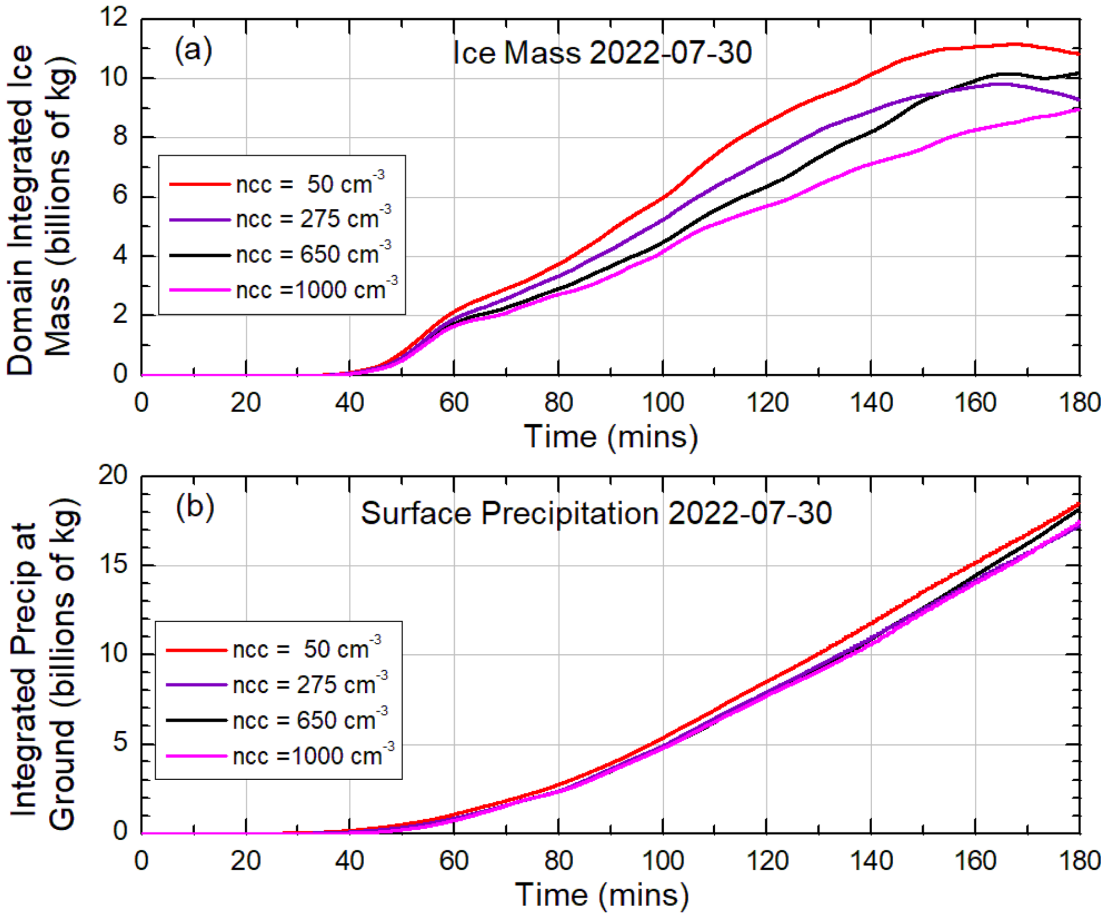

Figure 38.—Domain volume integrated IWC (top) and domain surface integrated precipitation (bottom) for simulation of 2022-07-30.

6.4.1.2 TASS Model Simulation of 2022-07-10

Two MCSs were observed in the Gulf of Mexico on 2022-07-10, the first in the middle of the Gulf near 27° N 89° W, and the second on the Louisiana coast centered near 29° N 101° W. The latter was more vigorous in terms of high reflectivity at altitude, lightning, and hail and was sampled to a lesser extent, with sampling performed more on the periphery of the most active areas. The TASS domain for this day was centered on the first MCS, at about 27° N 89° W. The chosen TASS domain size was 30 by 100 km, with a maximum vertical extent of 20 km and lateral and vertical grid spacings of 175 and 150 m, respectively. Figure 39 shows a color-enhanced IR satellite image at 18:21 UTC and indicates the location of the TASS domain. The transition from warmer pink to colder white colors in this color scheme occurs at approximately –66 °C. The second, more vigorous MCS is partially visible at the top left of the figure. The model environment was initialized with a NAM sounding from 18:00 UTC at 28° N 91° W. The sounding showed a tropopause of about –73 °C, with a surface-based CAPE of 3,416 J/kg, a little higher than the case of 2022-07-30. Precipitable water was about the same at 58.8 mm. Convection was again initiated with a thermal impulse (a warm bubble of 2 °C). In this case, the simulation reached its maximum domain-integrated IWC at about 120 min and declined slowly thereafter. Simulations were terminated at 180 min.

Aerosol sensitivity tests were performed for the same nominal initial *ncc* values as the 2022-07-30 simulation. Time histories of the domain average area of IWC as a function of altitude, this time for IWC exceeding 1.5 gm^{-3}, are shown in Figure 40. This case showed a very clear and monotonic decrease in the integrated high-IWC area aloft with increasing *ncc*, again in the opposite direction as expected from the HIWC–2022 first-order hypothesis. The altitude zone of highest IWC was again in the 8- to 10-km range. Figure 41 shows the simulated IWC fields at 130 min at an elevation of 9.5 km, the approximate period

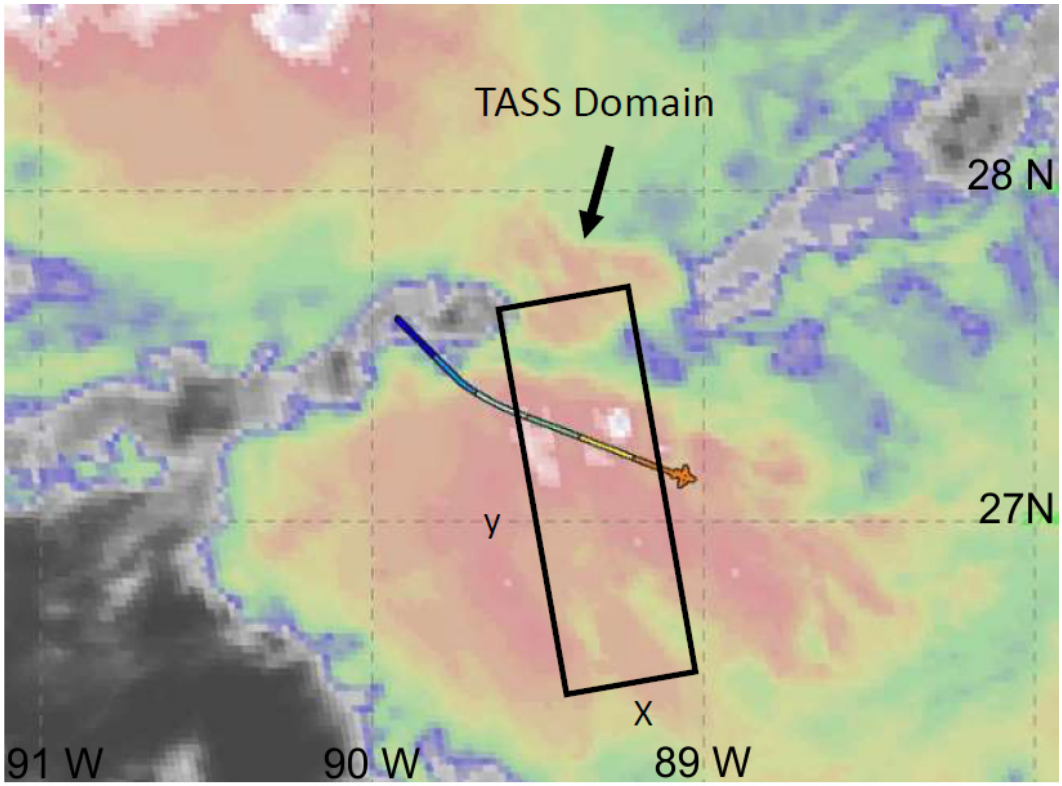

Figure 39.—Color-enhanced satellite IR image at 18:21 UTC on 22-07-10; TASS domain shown over modeled MCS.

and altitude of maximum IWC. Simulated IWC exceeded 3 gm^{-3} in small cells, similar to the DC–8 in situ observations. Areas for all the IWC levels above 1.5 gm^{-3} progressively decreased from the cleanest to the most polluted simulations. Figure 42(a) shows the domain-integrated IWC versus time for the four aerosol simulations. As explained in the 2022-07-30 case study, due to the lack of LWC above the freezing level, this is an estimate of the total IWC above the freezing level. The figure shows that the simulations at the peak of the lifecycle produced more IWC overall in a clean environment than in a polluted one. The integrated IWC difference at 120 min between *ncc* = 50 cm^{-3} and 1,000 cm^{-3} was about 25 percent. As in the case of 2022-07-30, the different aerosol simulations started to converge after the peak in the lifecycle. Surface precipitation (Figure 42(b)) was highest for the most polluted case, unlike the simulation of 2022-07-30.

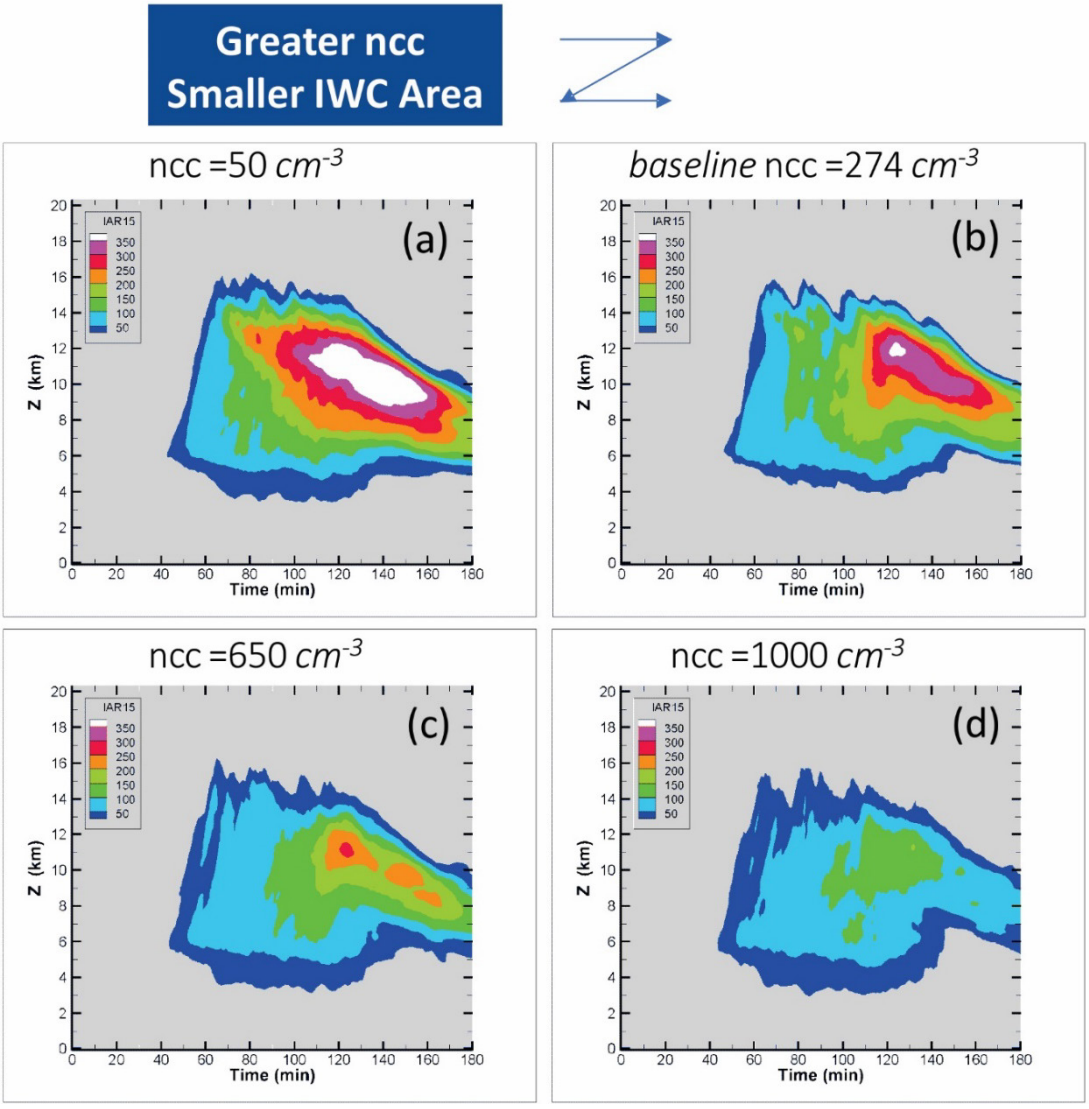

Figure 40.—TASS model aerosol sensitivity tests for 2022-07-10 with varying input initial droplet number concentrations (*ncc*). Plotted field (IAR15) is total horizontal area with *IWC* >1.5 gm^{-3} shown as function of altitude and time.

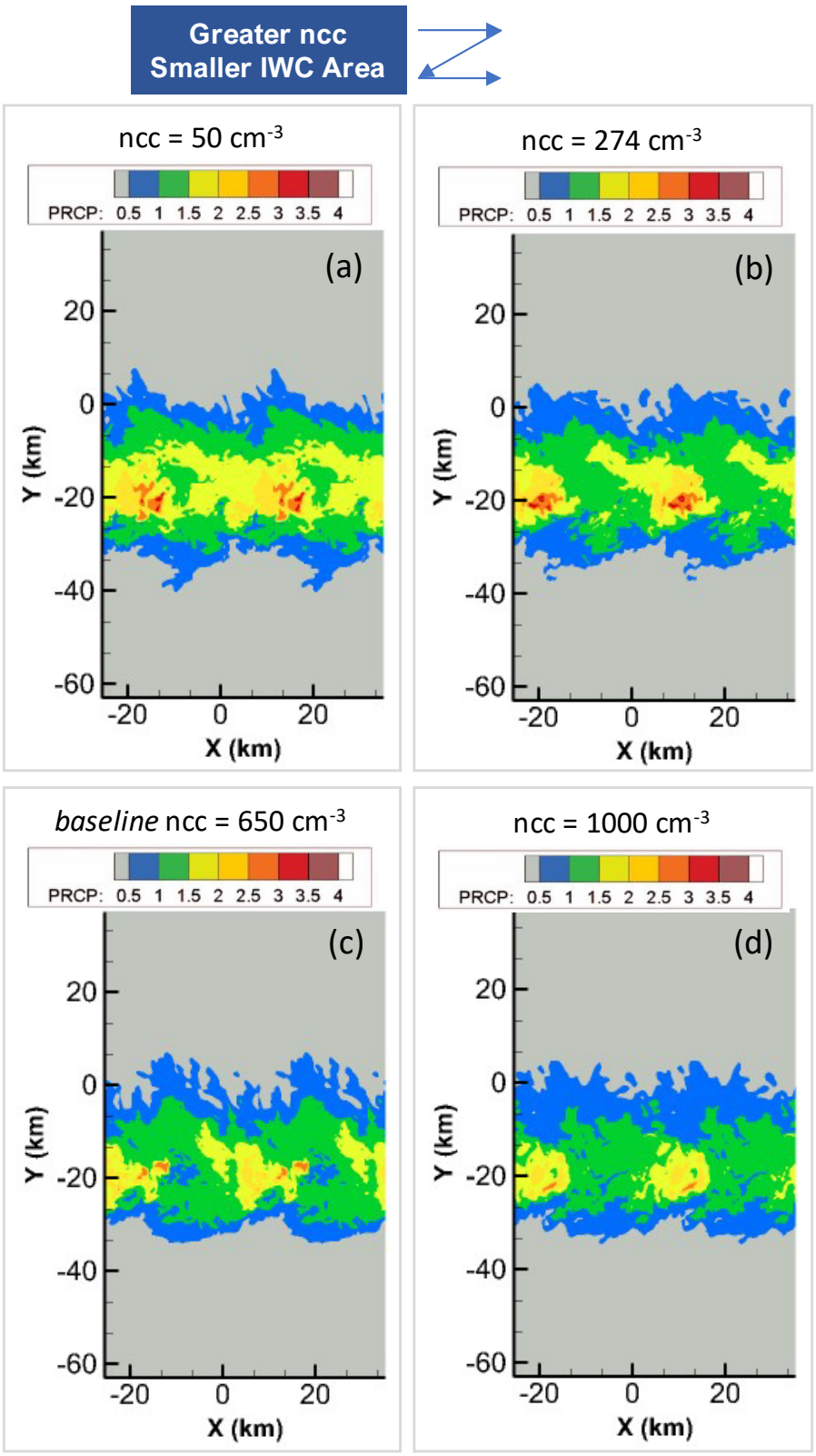

Figure 41.—TASS-simulated field of IWC at 130 min and 9.5-km elevation at approximate time and altitude of maximum domain-integrated IWC. Panels represent simulation for cleanest simulation (top left) to most polluted simulation (bottom right). PRCP levels are equivalent to IWC in gm^{-3}.

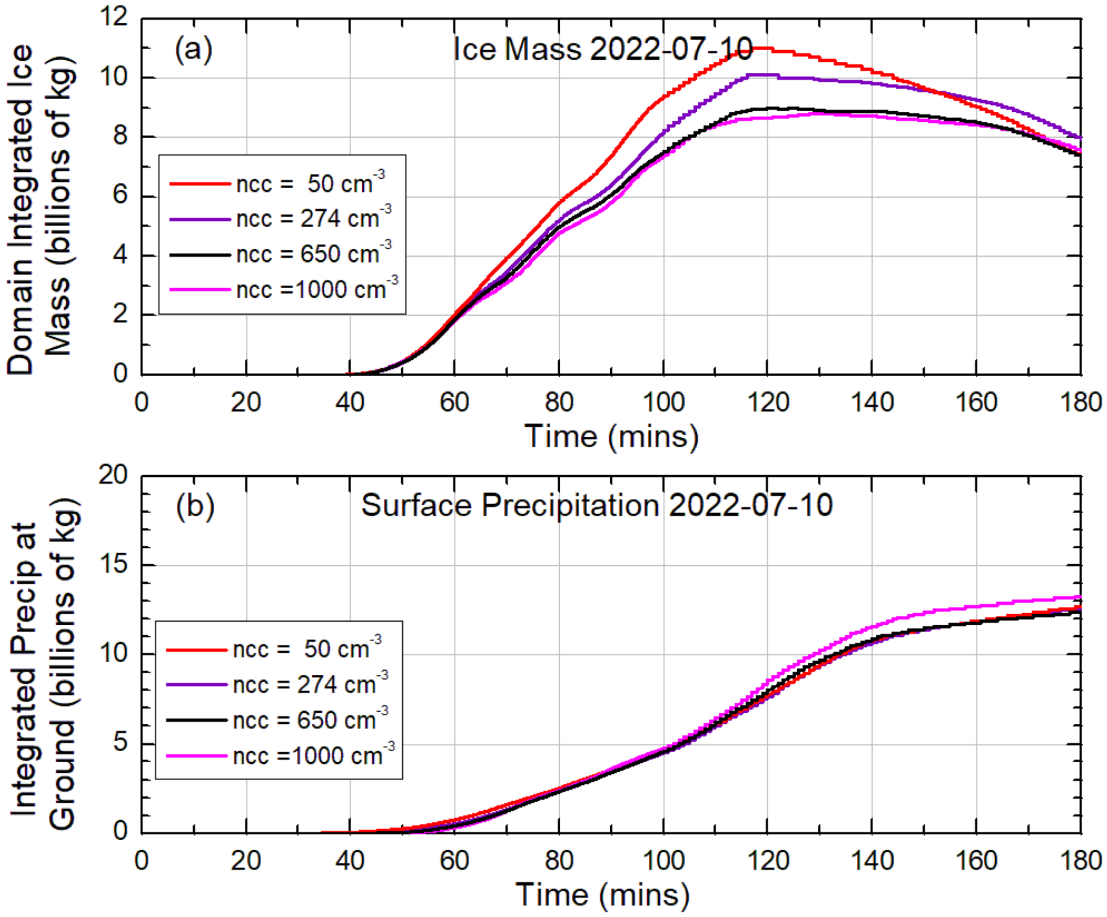

Figure 42.—Domain volume-integrated IWC (top) and domain surface-integrated precipitation (bottom) as function of time for simulation of 2022-07-10.

6.4.1.3 TASS Model Sensitivity to Cloud Droplet Dispersion and Ice Production Rate

The HIWC–2022 TCu observations of Section 6.3.1 and Section 6.3.2 revealed that coalescence embryos larger than 50 μm in diameter were always present at cloud base, possibly due to the action of GCCN in the form of SSA nuclei. Drizzle and warm rain developed quickly above cloud base. The TASS simulations were performed using initial cloud droplet spectra with a dispersion (σ) of 0.3, a value close to that reported by Simpson and Wiggert (Ref. 122) as appropriate for maritime clouds. To test the sensitivity of the model to the spread of the droplet distribution, simulations were also performed with narrower initial cloud droplet spectra with σ of 0.15, closer to the continental values reported for Colorado High Plains clouds by Knight et al. (Ref. 123).

For all previous model runs, a constant INP concentration was used for both clean and polluted simulations. The question then arose as to whether a more polluted atmosphere with higher CCN and higher initial *ncc* may also have proportionately higher INP concentrations. Support for this claim in the literature was not investigated, and it is known that INP concentrations can he highly influenced by events such as desert dust episodes that are not associated with high-CCN anthropogenic pollution events. Nevertheless, the idea prompted interest in assessing sensitivity of model simulations to INP concentration. Furthermore, ice crystal concentrations in natural clouds have often been shown to exceed primary INP concentrations (see Section 6.3.3) and SIP mechanisms have been identified that are not included in TASS. Section 6.3.3 showed that SIP was most likely active in HIWC–2022 TCu clouds,

sometimes producing peak ice concentrations more than 2 orders of magnitude higher than expected from INP concentrations measured during HIWC–2022. For these reasons, it was concluded that the sensitivity of simulations to ice production should be investigated. The simplest way to increase ice production rate was to increase the INP concentration. An increase of a factor of 10 over the baseline was chosen as a benchmark.

Results of the droplet dispersion sensitivity tests are given in Figure 43, where the total area in the domain with *IWC* >1.5 gm^{-3} is plotted versus altitude and time. The sensitivity to drop dispersion was minor. Further assessment will be provided below in Figure 44.

The effect of increasing INP concentration by a factor of 10 for the baseline case of *ncc* = 274 cm^{-3} is shown in Figure 44(a) and (c). The effect was substantial during the lifecycle maximum period from about 120 to 160 min. This perhaps could be explained by production of higher concentrations of smaller ice crystals, which were less prone to fallout. The effect of this increase in INP concentration for the most polluted case is shown in Figure 44(b) and (d) and was arguably even more pronounced. Finally, the simulations of Figure 44(a) and (d) represent a combined effect of simultaneously increasing CCN and INPs, which in this case more or less canceled each other out and provided similar end results.

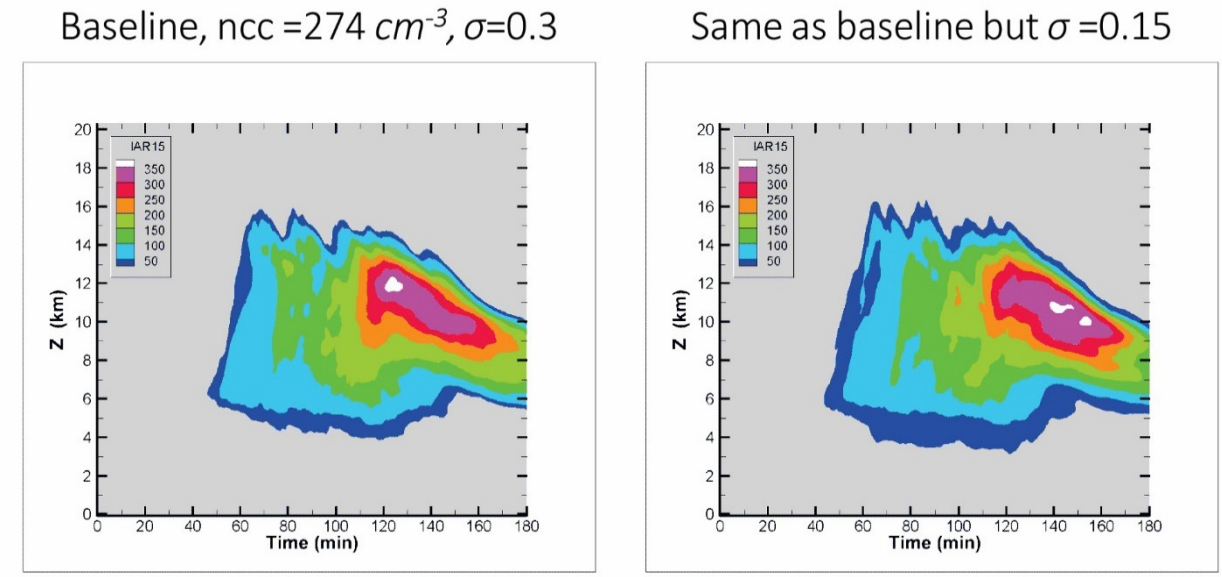

Figure 43.—TASS model sensitivity to initial droplet spectrum dispersion (σ). Plotted field is total horizontal area with *IWC* >1.5 gm^{-3}.

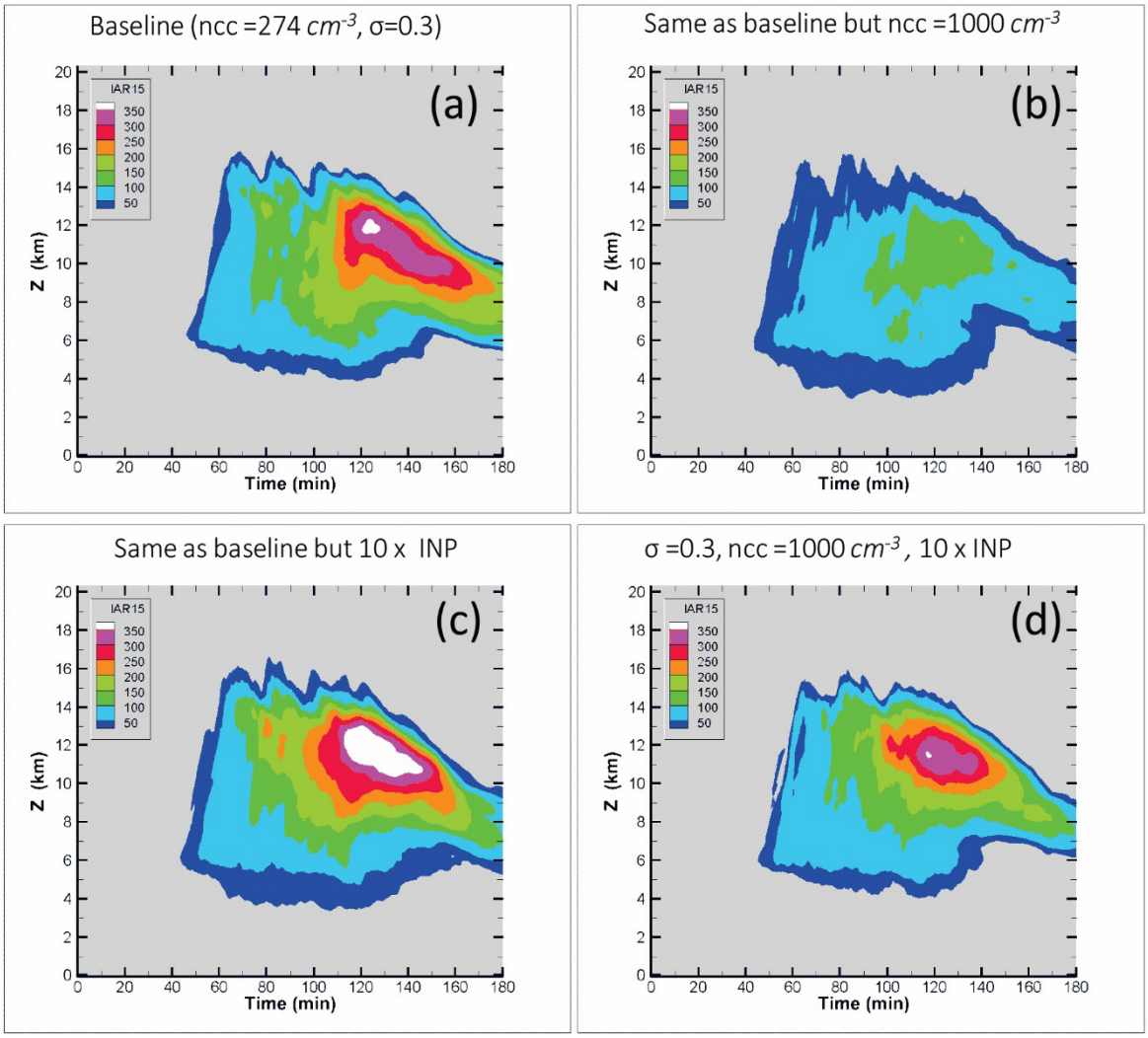

Figure 44.—TASS model sensitivity showing effect of increasing INP concentration by factor of 10. Plotted field is total horizontal area with *IWC* >1.5 gm^{-3}.

Figure 45(a) shows the domain-integrated IWC as a function of time for further comparison of the simulation sensitivity runs. Comparing first the baseline case, with drop dispersions of 0.3 (violet line), to the drop dispersion of 0.15 (green line), there was very little difference, as already observed in Figure 43. Comparison of the baseline *ncc* and INP case (violet line) to the baseline *ncc* with 10 times higher INP concentration (orange line) revealed about 10 to 15 percent more domain-integrated IWC for the latter after 120 min. Finally, comparison of the baseline *ncc* and INP case (violet line) to the high-CCN-aerosol simulation (*ncc* = 1,000 cm^{-3}) with 10 times the INP concentration (blue line) revealed nearly equivalent domain-integrated IWC at the apparent lifecycle peak at 120 min, although the two values diverged at later times, with the latter exceeding the former. Figure 45(b) shows the surface-level domain-integrated precipitation. Although all lines showed similar time histories, there was some indication that the simulations with baseline *ncc* and 10 times the INP concentration had lower precipitation rates from the lifecycle peak to the end of the simulation, consistent with more IWC remaining suspended aloft.

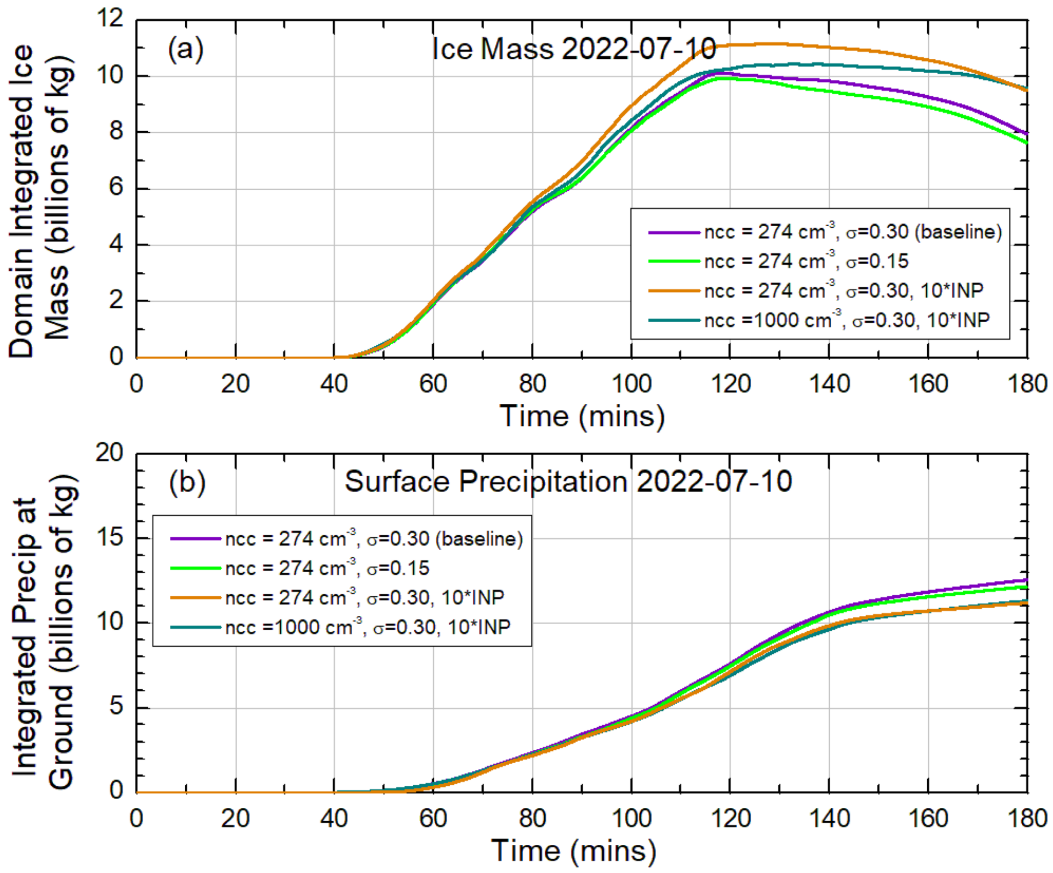

Figure 45.—Ice mass and precipitation versus time for drop dispersion (σ) sensitivity and ice nucleus sensitivity tests of Figure 43 and Figure 44 for model simulations of 2022-07-10. (a) Domain volume-integrated IWC versus time. (b) Surface domain-integrated precipitation versus time.

6.4.1.4 Additional Results

One additional case study was performed on an MCS from the HIWC RADAR I campaign and will only be summarized briefly here. Details on this MCS, sampled on the Louisiana coast on 2015-08-19, can be found in Proctor et al. (Ref. 120). As in all other TASS simulations of high-IWC regions of sampled MCSs, the levels of reflectivity and IWC were generally well reproduced by the simulations. For the current report, aerosol sensitivity tests were again performed, this time for the following *ncc* and cloud droplet dispersion combinations: *ncc* = 50 cm^{-3}, σ = 0.37; *ncc* = 500 cm^{-3}, σ = 0.30; and *ncc* = 1,000 cm^{-3}, σ = 0.15. The main results were qualitatively the same as for the case studies of 2022-07-30 and 2022-07-10. The domain-integrated high-IWC areas (*IWC* >1.5 gm^{-3}) were highest for the lowest *ncc* case. However, domain total rainfall at the surface was highest for the lowest *ncc* case.

6.4.2 Results of Cloud-Resolving Model Simulations

6.4.2.1 Overview of CReSS

The Cloud Resolving Storm Simulator (CReSS) is a cloud-resolving model that has been developed by the Japanese research community for real-time forecasts and research of weather systems from small-scale thunderstorms to large-scale typhoons. The model uses a nonhydrostatic compressible equation system. Bulk parameterizations are used to simplify cloud microphysical processes defining transformations of water vapor and cloud hydrometeors. A full description of the model is given in the CReSS User's Guide (Ref. 124).

For HIWC–2022, new bulk parameterizations, 4ICE–CCN and 4ICE–AEROSOL, were developed and incorporated into CReSS. 4ICE–CCN has six types of hydrometeors: cloud water, cloud ice, snow, rain water, graupel, and hail, each being represented as double-moment gamma-size distributions. 4ICE–CCN employs a simplified CCN treatment with a new CCN activation scheme. CCN were assumed to be uniform in the domain, but the ability to implement a vertical profile of CCN activation spectra was included.

4ICE–AEROSOL can have up to 20 types of aerosols in the air and in the six types of hydrometeors. Each type of aerosol is represented by a double-moment log-normal size distribution. Two double-moment log-normal distributions are included for sea salt and dust, and one each for submicron and supermicron size ranges. Each aerosol species is characterized by its CCN ability (hygroscopicity) and INP ability (INAS density) Processes related to aerosols include the following:

- Advection, diffusion, and sedimentation
- Precipitation scavenging (by cloud water; Brownian and turbulent diffusion, phoretic effects, and others; and Brownian diffusion, interception, and impaction)
- Nucleation scavenging
- Ice nucleation (homogeneous, immersion/condensation, and contact freezing; and deposition nucleation)
- Aerosol regeneration during hydrometeors' evaporation/sublimation
- Aerosol transport associated with interaction among hydrometeors

A description of the six aerosol types used in CRESS–4ICE–AEROSOL for the current simulations is given in Table 17. Columns 2 to 4 describe the aerosol distribution parameterizations. CCN hygroscopicity is shown column 5. Columns 6 to 9 describe the ice nucleation parameterizations, where INAS densities as a function of temperature are as follows:

- Immersion/condensation INAS(T) = bb $e^{(aa\ T)}$
- Contact INAS(T) = bb $e^{(aa\ (T-4))}$
- Deposition INAS(T) = dd $e^{(cc\ SSi)}$, where SS_i is the supersaturation temperature with respect to ice

TABLE 17.—AEROSOL TYPES USED IN CRESS–4ICE–AEROSOL
[See text for explanation of INAS ice-nucleating parameterizations.]

Aerosol type	Size dist.	Initial mode radius, μm	Density, gcm^{-3}	Hygro-scopicity	INAS aa	INAS bb	INAS cc	INAS dd
Sea-salt aerosol (SSA)	Log normal, σ = 2.0	NA	2.2	1.2	0	0	0	0
Sulphate ($SO_4^{=}$)	Log normal, σ = 2.0	0.0695	1.8	0.68	0	0	0	0
Organic carbon (OC)	Log normal, σ = 2.0	0.1	1.3	0.1	0	0	0	0
Black carbon (BC)	Log normal, σ = 2.0	0.1	0.3	0.01	–0.517	7.86×10^{3}	5.20×10^{-1}	1.81×10^{3}
OC, BC mixture	Log normal, σ = 2.0	0.2	1.3	0.1	–0.517	7.86×10^{3}	5.20×10^{-1}	1.81×10^{3}
Mineral dust	Log normal, σ = 2.0	NA	2.6	0.03	–0.517	7.86×10^{3}	5.20×10^{-1}	1.81×10^{3}

All particle types act as CCN, although black carbon and mineral dust are very weakly hygroscopic. Only black carbon, mixtures of black carbon and organic carbon, and mineral dust act as ice nuclei, and their INAS densities are the same with temperature.

6.4.2.2 Idealized Aerosol Sensitivity Experiments

For this study, CReSS–4ICE–AEROSOL was first run in an idealized experiment of a single supercell thunderstorm. The model was run in a domain measuring 50 by 50 by 20 km with resolution of 250 by 250 by 250 m. An initial atmospheric sounding was used to initialize the model, one that was typical for summertime MCS formation off the east cost of the United States. The sounding had a surface temperature of about 25 °C, lifting condensation level of 24.1 °C, CAPE value of 2765 J/kg, and tropopause of about 12 km (–73 °C). The model was initiated with a warm bubble and was run for 2 h.

The CReSS–4ICE–AEROSOL was initialized with vertical profiles of the six aerosol types, using monthly SPRINTARS averages from 2022-07-08 to 2022-07-30 for the east coast of the United States, within the window 15° to 40° N and 65° to 95° W. SPRINTARS is a global aerosol model coupled with a general circulation model. SPRINTARS aerosol initialization is derived from aerosol and gas emission source data. Aerosol transport processes of emission, advection, diffusion, and deposition, simplified aerosol-cloud-precipitation interactions, and trace gas chemical reaction are calculated to derive forecasts of global 3D mass mixing ratios of species. Results have been assessed through comparison of optical thickness from NOAA Advanced Very High Resolution Radiometer (AVHRR) satellite data. Details have been provided by Takemura (Ref. 41).

In the list of model output parameters, individual hydrometeor mass mixing ratios are defined as follows: *qc* = cloud water, *qi* = cloud ice, *qr* = rain, *qs* = snow, *qg* = graupel, and *qh* = hail. The combined ice mass is *qisgh* and will be considered an end product for evaluation of the HIWC–2022 first-order hypothesis. The model maximum *qisgh* values in gm^{-3} were found at about 60 min and at an altitude of about 11.6 km. The dominant ice types produced by the model in mass mixing ratio were snow and graupel, with the cloud ice category representing the smallest fraction. Figure 46 shows a horizontal cut of *qisgh* through the storm at 60 min and 11.6 km, at its peak time and altitude, using the control aerosol settings. The maximum *qisgh* value of 1 to 3 gm^{-3} was reached in a small area (red) next to the updraft area. A large area of 0.3 to 1.0 gm^{-3} (orange) was produced.

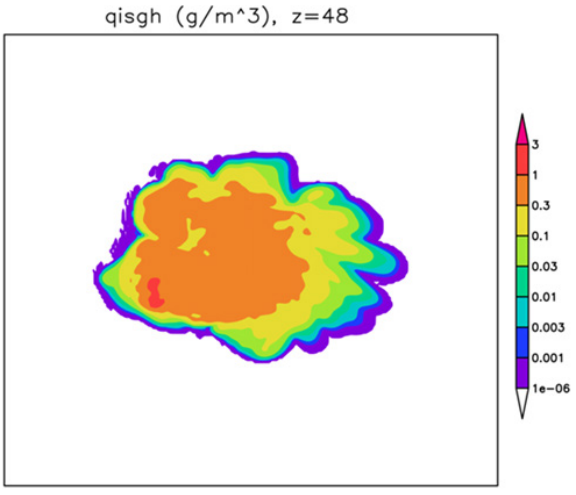

Figure 46.—Horizontal cut of total IWC (*qisgh*) produced by model at 60 min and 11.6 km, peak time and altitude of idealized simulation.

Low, control (medium), and high CCN (organic carbon and sulphate) and INP (dust and black carbon) settings were used for the sensitivity comparisons. Results of model cloud droplet number concentration (*ncc*) response are given in Figure 47. The effect of increasing CCN for low, control, and high INPs is illustrated by comparing the lowest to the highest figure in each column. For example, for the control INP settings, Figure 47(h), (e), and (b) returned maximum *ncc* values of about 40, 300, and 3,000 cm^{-3}. It is clear that the highest CCN concentrations created the highest *ncc* values for each INP choice; this illustrates the Twomey effect (Ref. 62) and is consistent with the HIWC–2022 first-order hypothesis. The effect of increasing INP concentrations, for which dust particles also act as CCN, increased *ncc* values. This effect is most noticeable for the lowest CCN choice (e.g., Figure 47(g) to (i), along the bottom row), where dust CCN were added to a low background *ncc* from conventional CCNs.

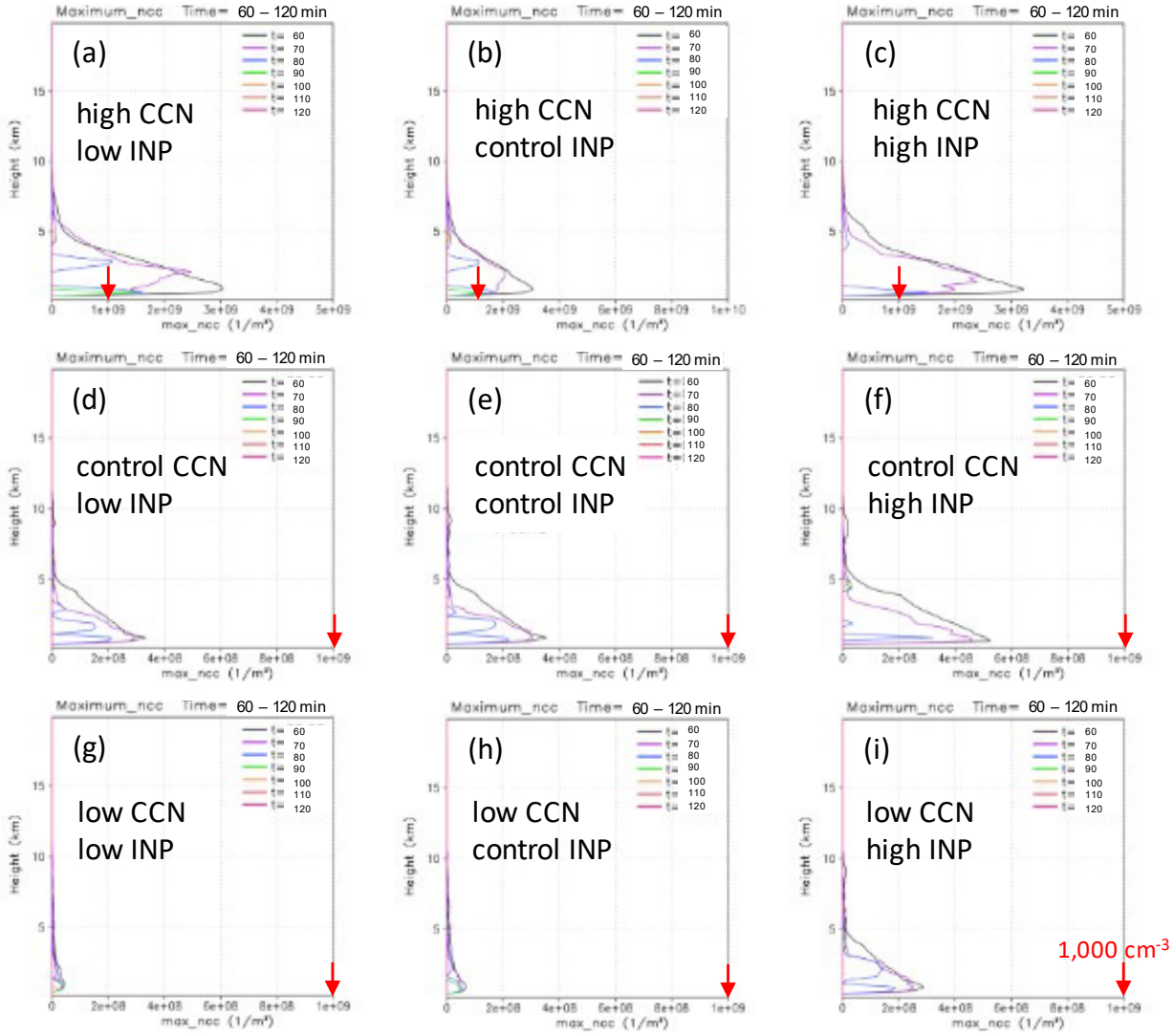

Figure 47.—Vertical profiles of domain maximum cloud droplet concentration (*ncc*) for low, control, and high CCN and INP initial concentrations. Results shown for time scales between 60 and 120 min in model time frame; x scale not static. Red arrow points to common value of 1,000 cm^{-3}.

Figure 48 displays the same sensitivity tests as in Figure 47, but for the effect of CCN and INP on *qisgh*. Due to the complexity of the time series of 3D fields of TWC in model simulations, the domain-average total IWC, *ave_qisgh* at system maturity (i.e., at its maximum value), was chosen as the metric for assessing simulation sensitivity to aerosol inputs and is termed here $IWC_{Da.}$ This value is analogous to the maximum domain-integrated IWC in TASS simulations in Section 6.4.1.1.

The first column of Figure 48—(a), (d), and (g)—shows the effect of increasing CCN at low INP settings. The level average *qisgh*, maximizing at about 60 min and 11.6 km, increased roughly 40 percent from ~0.035 gm^{-3} to ~0.05 gm^{-3} with increasing CCN. The corresponding IWC_{Da} values did not change substantially for the control and high INP settings. For all CCN settings, IWC_{Da} increased with increasing INP, for example, by about 35 percent for the control CCN between the low and high INP except for the decrease of IWC_{Da} from low to control INP for high CCN.

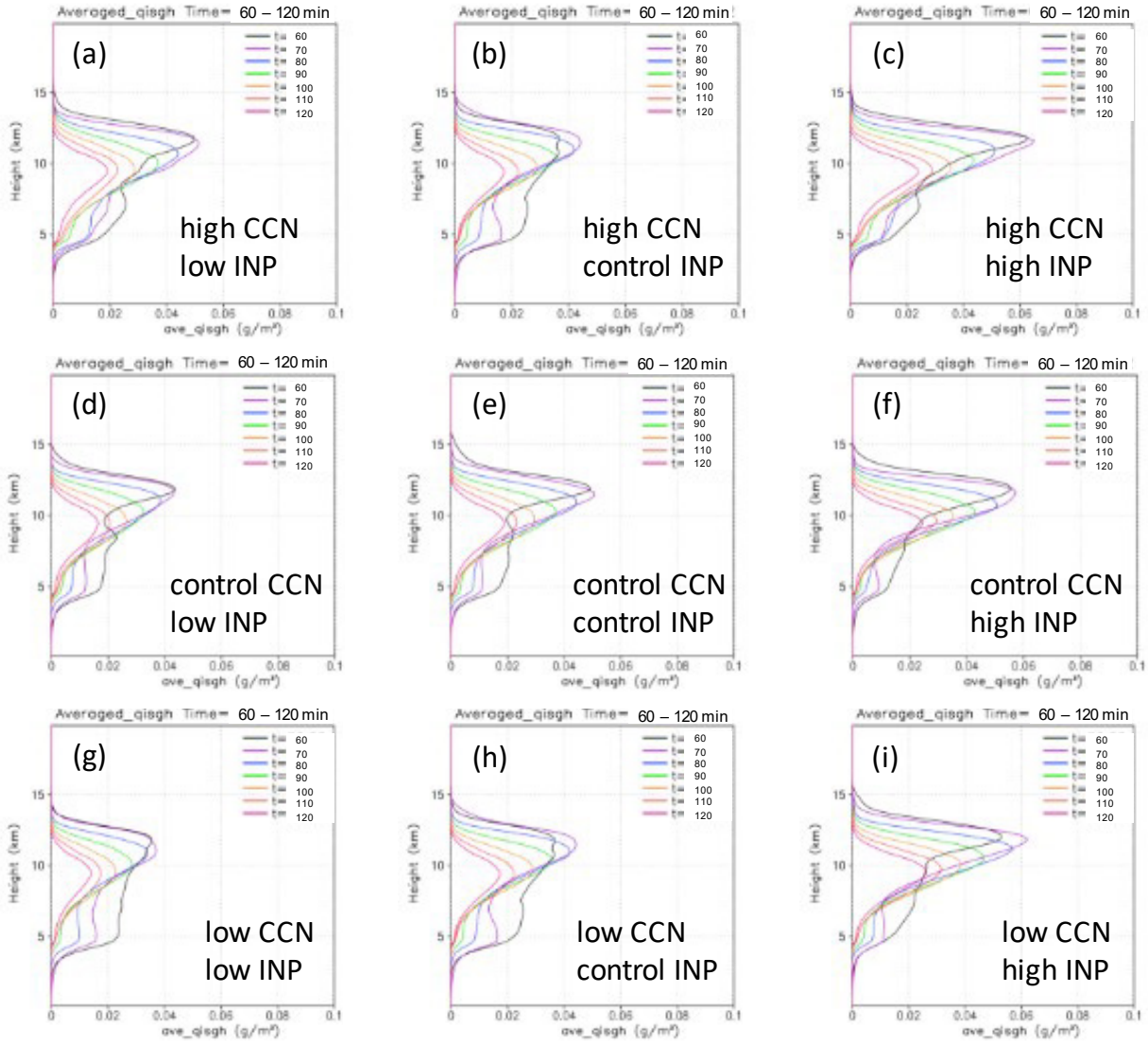

Figure 48.—Vertical profiles for model domain-average total ice mass mixing ratio (*ave_qisgh*) for low, control, and high CCN and INP initial concentrations. Results shown for time scales between 60 and 120 min in model time frame.

Nagoya University qualitatively estimated the level CCN and INP settings used here relative to an East Asian maritime environment. East Asian CCN concentrations were generally higher, with U.S. low, medium, and high CCN corresponding to very low, low, and normal for East Asia. For INP, the U.S. concentrations were higher than for East Asia mainly due to the influence of transport of Saharan dust. U.S. low, medium, and high INP concentrations corresponded to high, high, and very high in East Asia. This implies that single-cell model simulations for maritime East Asia would show an increased IWC_{Da} with increasing CCN throughout the entire range of expected INP values, whereas this would only be true at the U.S. location if not significantly influenced by African dust.

6.4.2.3 CReSS–4ICE Simulation of 2022-07-30

A larger scale multiple-cell simulation was run with the CReSS–4ICE–CCN model for the case of 2022-07-30, the only HIWC–2022 case that was judged to have formed in a high-CCN-aerosol environment. Figure 49 displays the NOAA HRRR model forecast of IR brightness temperature for 16:00 UTC. The HRRR model developed a line of cells along a front offshore of North Carolina, similar to what was actually observed. This case was also simulated using the TASS model, as discussed in Section 6.4.1.1, where a IR satellite picture is shown (Figure 34). A dust episode originating over the Saharan Desert had been tracked across the Atlantic by the Composition Field component of the NASA Goddard Earth Observing System model (GEOS–CF), and it was visible from the aircraft as a distinct haze layer on the flights of 2022-07-27 and 2022-07-30. Aerosol components were roughly characterized by Nagoya University from SPRINTARS data on 2022-07-30 at 15:00 UTC and 925 mb as follows: sulphate low, organic carbon about average, and dust very high. The CCN components on this day were estimated at about 50 percent organic carbon, 30 percent sulphate, and 20 percent dust.

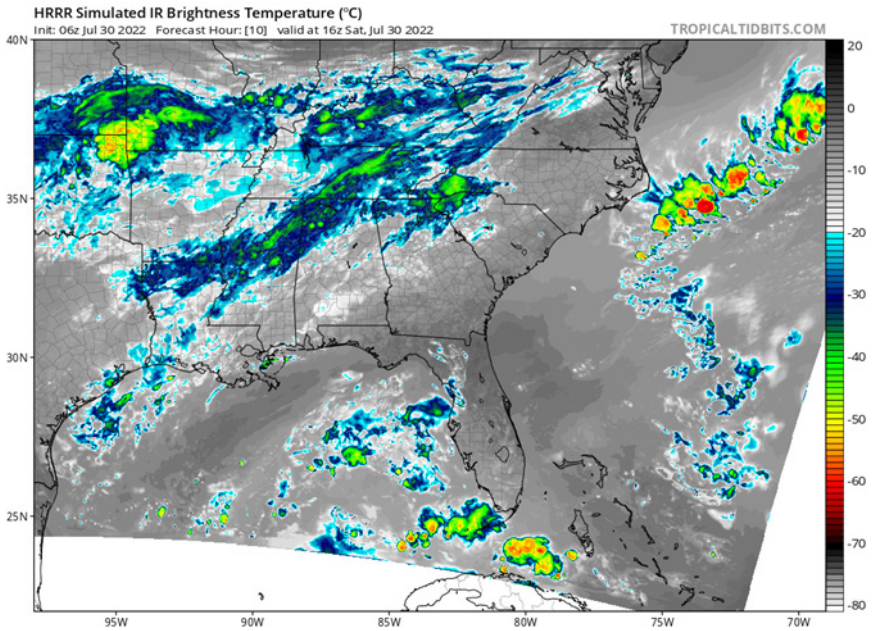

Figure 49.—NOAA HRRR forecast of IR brightness temperature for 16:00 UTC on 2022-07-30 showing convective cells developing along offshore front off east coast of United States. Image courtesy of https://tropicaltidbits.com.

The model was run with horizontal resolution of 1 by 1 km and with 50 unevenly spaced layers in the vertical. The geographical window was approximately bounded by 32° to 40° N and 67° to 77° W. Due to problems with the CReSS–4ICE–AEROSOL model that were unresolved at the time of this report, only simulations for CCN concentration sensitivity were conducted. Again, three levels of CCN were run: low, control, and high. Unlike the idealized model run (Section 6.4.2.2), due to the multiple convective cells, new cells developed under the influence of already precipitating clouds, which poses a complicating factor for interpretation.

Figure 50 shows the time evolution of the CReSS–4ICE–CCN simulation of surface precipitation rate from 18:00 to 21:00 UTC using the control CCN settings (CCN = 500). The model produced a line of cells basically consistent with the HRRR model prediction of Figure 49 that had reached a maximum extent by about 20:00 UTC. There was little difference in the precipitation rate simulated with the other two CCN levels (not shown). A time series of vertical profiles of domain-maximum *ncc* is given in Figure 51. Maximum *ncc* profiles reached a near steady state by about 60 min into the simulation (lower row of plots, black line). There was a clear increase in maximum *ncc* with increasing CCN concentration from about 80 cm^{-3} for low CCN to about 2,400 cm^{-3} for high CCN. Figure 52 displays the domain-averaged total ice mass *qisgh* (in units of kilograms of water per cubic meter of air). Values of *qisgh* increased with time and were still increasing at the last plotted vertical profile (100 min, lower row). IWC_{Da} values reached a peak at an altitude of about 11.2 km. Values of *qisgh* generally decreased with increasing CCN concentration after about 70 min, by up to about 40 percent in the last profile.

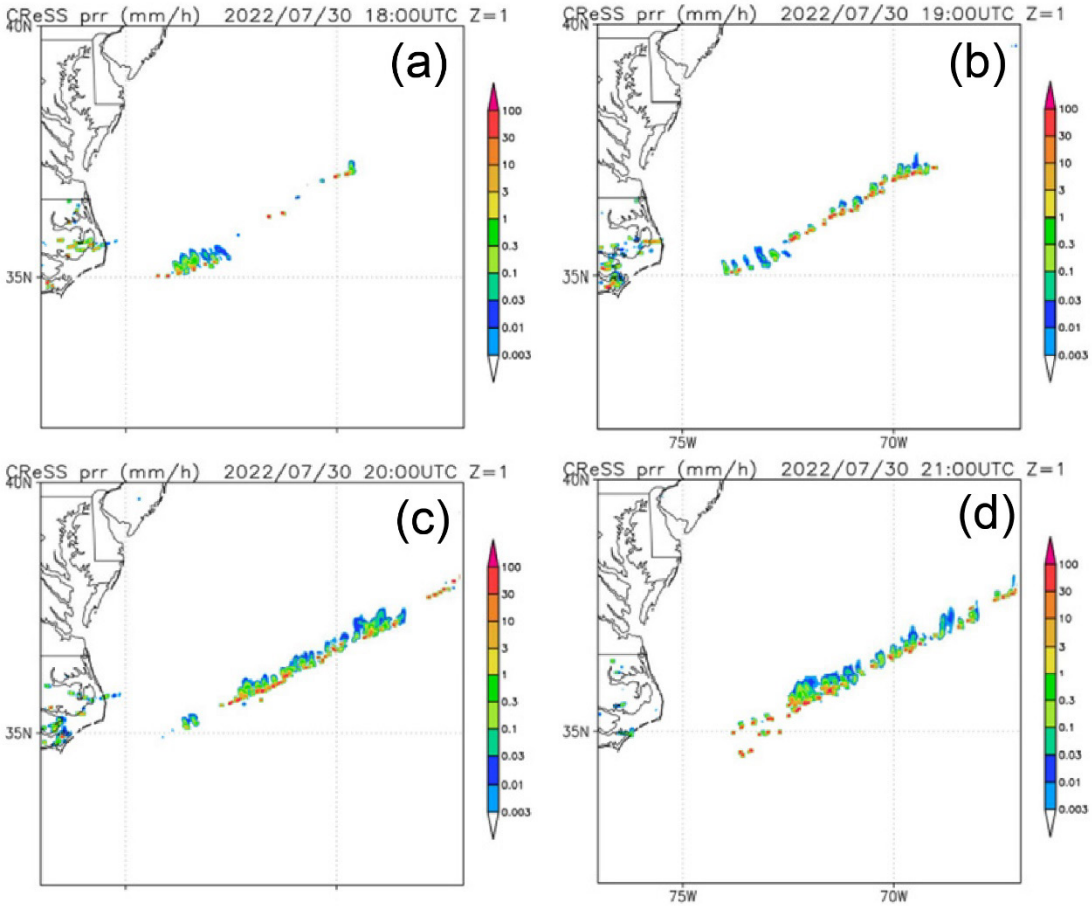

Figure 50.—CReSS model evolution of surface precipitation rate (mm/h) from 18:00 to 21:00 UTC on 2022-07-30 using control values of CCN and INP.

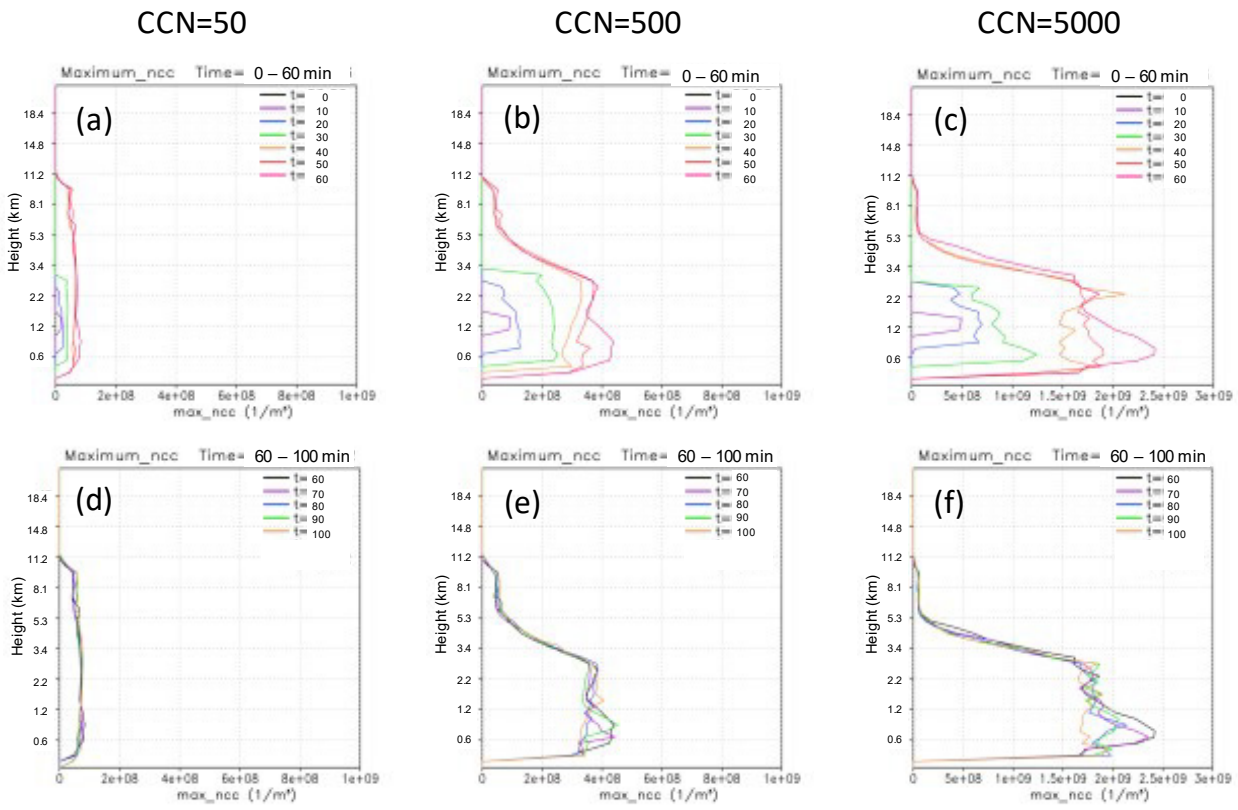

Figure 51.—Vertical profiles of domain-maximum droplet concentration (*ncc*) for low CCN (left column, (a) and (d)), control CCN (center column, (b) and (e)), and high CCN (right column, (c) and (f)). CCN = 50 means C = 50 in CCN activation spectrum: $N_{CCN} = C \times SS_w^{0.63}$.

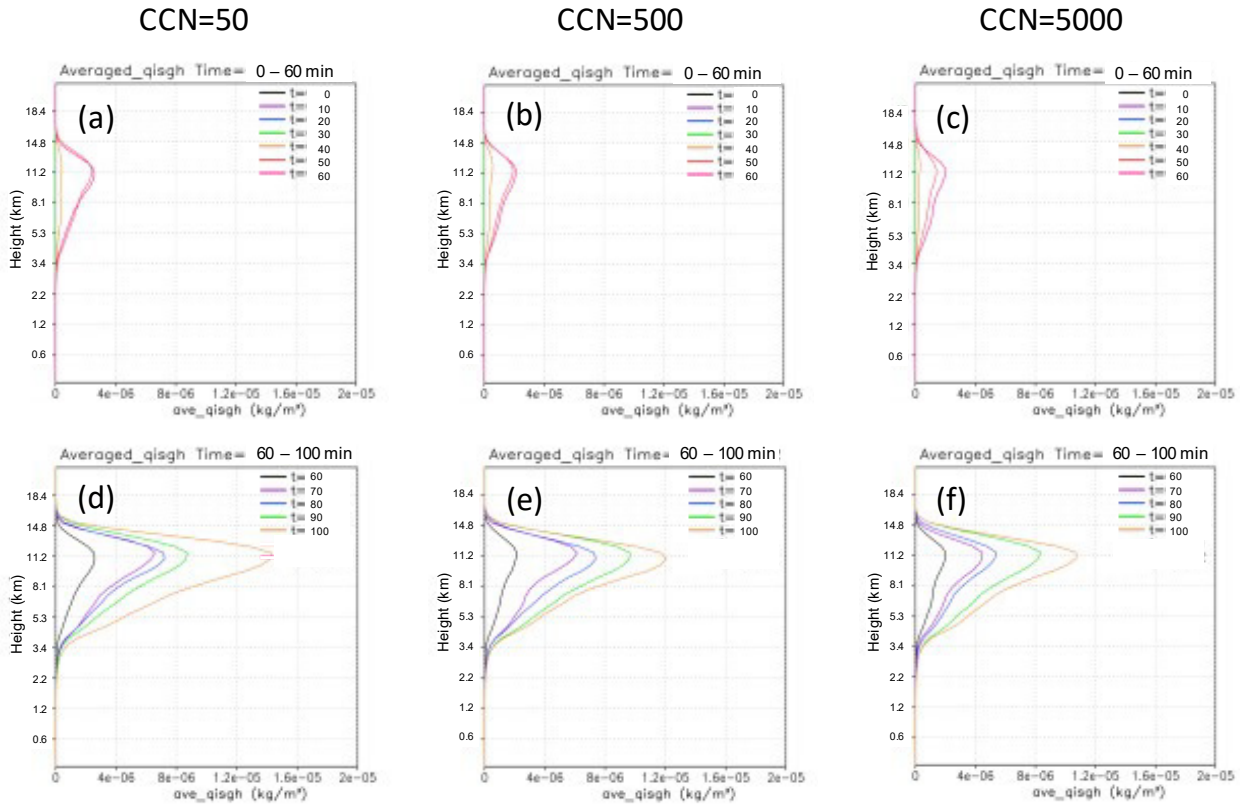

Figure 52.—Vertical profiles of domain-averaged total ice mass (*qisgh*) for low CCN (left column, (a) and (d)), control CCN (center column, (b) and (e)), and high CCN (right column, (c) and (f)). CCN = 50 means C = 50 in CCN activation spectrum: $N_{CCN} = C \times SS_w^{0.63}$.

6.5 Discussion on Implications of Literature Review, TCu Studies, and Modeling Studies

In this section, the information from the literature review, TCu studies, and numerical cloud model simulations is integrated to form an opinion on what can be currently concluded from these sources about the effect of elevated CCN levels on MCS high-altitude, high-TWC levels. The two effects considered that could increase TWC aloft were the suppression of warm rain as per Rosenfeld (Ref. 23) (i.e., the HIWC–2022 first-order hypothesis) and the delay in ice initiation suggested by Braga et al. (Ref. 72).

The TCu studies provided information on the evolution of microphysics in isolated clouds from cloud base to the –19 °C level, including the development of warm rain and ice precipitation that would deplete the TWC reaching flight levels. The TCu studies represent oversimplified behavior within active cells within an MCS at the mature stage, and it is important to note that the interaction of the MCS on the environment and the transport of ice from aloft likely modifies that behavior. The model studies of Sections 6.4.1 and 6.4.2 provide some insight into TWC levels aloft under the more complex environment, subject to the model assumptions.

Regarding the development of warm rain in continental TCu, the CAIPEEX and ACRIDICON–CHUVA experiments showed observational evidence of complete warm rain suppression in “very polluted” atmospheres. Warm rain suppression was identified by the absence of large droplets in OAP imagery by about the freezing level. In the case of CAIPEEX, the CCN and CDP maximum cloud droplet concentrations in very polluted atmospheres were typically in excess of 1,000 cm^{-3} (Ref. 40). For

ACRIDICON–CHUVA, CCN concentrations were not available, but conditions were classified as very polluted when adiabatic cloud droplet concentrations, deduced from the slope of adiabatic LWC calculations and measured droplet volume with height, exceeded about 900 cm^{-3}. Based on these classification thresholds the maritime HIWC–2022 case of 2022-07-30 (Table 4) came very close to meeting the bottom threshold of CAIPEEX very polluted cases and for the sake of this discussion will be referred to as such. The other HIWC–2022 cases could accordingly be considered clean as per the ACRIDICON–CHUVA categorization, with the exception of 2022-07-27, which may have reached that campaign's "polluted" threshold. In all of the HIWC–2022 cases for which relevant maritime TCu data were available, coalescence embryos (droplet larger than 50 μm) were observed at cloud base, and warm rain had developed at higher altitudes. Coalescence embryos were attributed to large SSAs (GN). The lack of suppression of warm rain in the single HIWC–2022 very polluted case was attributed to SSAs counteracting the effect of higher concentrations of smaller droplets predicted in the high-CCN-concentration environment. The majority of articles included in the literature review support the importance of SSAs to warm rain development, although some studies suggest the effect was irrelevant for lower CCN cases, where warm rain was already efficient. It is then suggested that in a very high CCN maritime environment where sufficiently high SSA concentrations are also present, coalescence embryos will be formed at cloud base, and warm rain could still develop. The SSAs could counteract the suppression of warm rain by high CCN concentrations and thus suppress the potential increase in IWC aloft.

Regarding the development of ice precipitation in continental TCu, ACRIDICON–CHUVA detected a delay in the initiation of ice to higher levels in cloud in very polluted conditions, attributed to the suppression of drizzle and thereby the Hallet–Mossop SIP that has been reported to be active in the –5 to –8 °C temperature range. In the HIWC–2022 maritime cases, drizzle and/or large drops were commonly observed at the –9 °C level, even in the very polluted case of 2022-07-30. In runs at –19 °C, glaciated regions with peak concentrations reaching over 1,000/L were observed, about 2 orders of magnitude higher than INP concentrations measured during HIWC–2022, signaling active SIP. The graupel and drizzle commonly observed in mixed-phase runs provided conditions favorable for SIP via drop freezing and/or the Hallet–Mossop mechanism on all days, probably explaining why the ACRIDICON–CHUVA delay of ice formation was not observed in the single HIWC–2022 high-CCN case. Again, the difference may have been due to the influence of SSAs and possibly high concentrations of dust particles internally mixed with SSAs in encouraging drizzle formation, even in a high-CCN environment. Therefore, the HIWC–2022 data, although limited, did not support the hypothesis of higher levels of TWC aloft due to the suppression of SIP.

A Nagoya University CReSS model simulation examined the sensitivity of IWC_{Da} of a simple single-cell system at the mature stage to CCN and INP concentrations at a much later stage of development than the TCu studies did. Cloud droplet concentrations increased with increasing CCN as predicted, but IWC_{Da} increased with increasing CCN only for the lowest INP concentrations; in other words, the primary HIWC–2022 hypothesis was observed but was sensitive to INP concentration.

Due to the lack of in situ MCS data collected at high altitude in very polluted conditions, the TASS and CReSS model simulations provided the only estimations of the CCN and INP effects of IWC_{Da} in large MCSs. The two TASS LES simulations of HIWC–2022 cases showed that domain-integrated IWC (the non-averaged but corresponding version of the CReSS–4ICE–CCN IWC_{Da}) decreased with increasing CCN regardless of INP concentrations. These results were in the opposite direction to the HIWC–2022 first-order hypothesis. INP concentration increases acted in the opposite direction of CCN increases. If both CCN and INP concentrations were increased from baseline to higher pollution levels, an approximate net-neutral effect was found in IWC_{Da}. The CReSS multicell simulation sensitivity tests have been performed only for CCN to date. There was a net decrease in IWC_{Da} with increasing CCN, again in

the opposite direction of the HIWC–2022 first-order hypothesis. Nagoya University suggested that this may be due to storm kinematics and interactions between mature and growing regions in multicell systems overriding any simple CCN single-cell effect. Based on these model findings, it is also suggested here that INP effects on IWC_{Da} may dominate over CCN effects, and the two must be considered together.

In final summary, warm rain and efficient early SIP were observed in HIWC–2022 TCu clouds, even in the single more-polluted case. There were no clear signals of high CCN suppressing warm rain or delaying ice development, although it would have been desirable to have obtained more very polluted cases and cases reaching more extreme CCN levels. For complex multicell MCS simulations, the TASS and CReSS models displayed a signal in the opposite direction of the HIWC–2022 first-order hypothesis and pointed out that both CCN and INP concentrations may affect IWC aloft, possibly working in opposite directions. Other modeling studies of MCS in the literature have focused on the sensitivity of the surface precipitation produced, which can be conjectured to be connected to IWC aloft, to aerosol concentrations and other parameters. The results from these other studies underscore the complexity of such simulations and the sensitivity to parameters such as CAPE and wind shear (Ref. 125). The results of the simulations within this report may thus be specific to their particular atmospheric environments.

7.0 Conclusions

The primary objective of the NASA/Federal Aviation Administration (FAA) High Ice Water Content and Aerosols Flight Campaign (HIWC–2022) was to collect total condensed water content (TWC) data in high-altitude, mesoscale convective systems (MCSs) that formed in regions with high concentrations of anthropogenic aerosols for comparisons to TWC data from correspondingly low-aerosol regions. The purpose was to address a potential gap in the in situ cloud data set that was collected through three flight campaigns in 2014 and 2015; these flight campaigns were concluded to be within low concentrations of aerosols. To meet that objective, the intention of HIWC–2022 was to collect data from five flights with upwards of 50 high-altitude cloud traverses from MCSs within high boundary-layer cloud condensation nuclei (CCN) concentrations for comparison to the original low-CCN dataset. The original datasets had been collected in Darwin, Australia; Cayenne, French Guiana; and Florida. In the end, HIWC–2022 only had one confirmed high-CCN flight, with only two cloud traverses, and thus only two Type 2 TWC data points were collected. This was insufficient to form a meaningful comparison between the high- and low-CCN cases of HIWC–2022 in order to test the HIWC first-order hypothesis.

The HIWC–2022 data, along with that from the HIWC RADAR II campaign, nevertheless provided important additional information for Appendix D assessment. These campaigns provided up to 40 percent additional data, again from Florida, but also from a new location in the east Pacific. Both campaigns also contained data from somewhat different clouds than the original datasets and thus contributed to a more diverse composite dataset. In this report, the HIWC–2022 and HIWC RADAR II campaign data were added to the original dataset to determine if significant differences would have been found had all campaign data been included in the original analysis provided to the Aviation Rulemaking Advisory Committee (ARAC). The TWC_{max}, TWC_{99}, TWC_{99} distance factor, and ice particle cumulative mass distribution (CMD) and median mass diameter (MMD) changes were minor, and are concluded in this report to be of little significance to ARAC. Measurements did also point out that short episodes of relatively large graupel with high bulk density, coexistent with a background of conventional smaller ice crystals, were not uncommon in HIWC–2022. Such episodes were less frequent in previous campaigns but were nevertheless present. An exploratory analysis of the effect of graupel density on CMDs and MMDs during graupel episodes suggested that a second mass mode above about 1 mm was likely, although changes in MMD were relatively small. None of the CMD and MMD analyses provided in the

original report submitted to the Ice Crystal Icing Working Group (ICIWG) accounted for these short graupel episodes. It would be both premature and impractical to reprocess the data. The issue has been brought to the attention of the ICIWG, with no return request for further action.

As a result of the lack of HIWC–2022 high-altitude MCS data collected in high-CCN-aerosol environments, it was decided to undertake extra efforts to expand the literature review, the analysis of TCu data taken in the vicinity of the HIWC–2022 MCSs, and modeling efforts that were already underway, in order to determine if anything further could be contributed regarding the effect of high CCN levels on TWC aloft. It was found that whereas complete suppression of warm rain in simple single-cell continental convective clouds in high-CCN-aerosol cases was observed in the CAIPEEX and ACRIDICON–CHUVA flight campaigns,[5] it was not observed in the oceanic clouds of HIWC–2022. It was concluded that sea-salt aerosols could enable warm rain production even in the presence of high concentrations of CCN aerosol, and the importance of such aerosols was supported in the majority of articles reviewed for this report. This in turn implied that in very polluted maritime regions, such as off the coast of east Asia, the same effect could be present. Regarding the suppression of secondary ice production (SIP) observed in the ACRIDICON–CHUVA campaign, which could also increase TWC levels aloft, the existence of warm rain and SIP in TCu at the –9 °C level in HIWC–2022, even in its single high-CCN flight, indicated that the secondary ice suppression effects observed in ACRIDICON–CHUVA campaign were not active in HIWC–2022.

In the absence of adequate high-altitude, high-CCN-aerosol in situ MCS TWC data, the Terminal Area Simulation System (TASS) and Cloud Resolving Storm Simulator four-ice (CReSS–4ICE) cloud models provided the only guidance on effects of CCN on high-altitude TWC levels in large multicelled mature systems. Both models showed that increasing CCN actually decreased the domain-averaged ice water content (IWC_{Da}) at system maturity, in the opposite direction of the HIWC–2022 first-order hypothesis. An increase in ice nucleus particle concentrations was found to act in the opposite direction of an increase in CCN. It was suggested that storm kinematics and interactions between mature and growing regions in multicell MCSs could result in much more complex outcomes relative to single-cell isolated clouds and/or the HIWC–2022 first-order hypothesis. Furthermore, levels of ice nucleus particles should be considered in tandem with CCN concentrations. For example, the east coast of the United States is subject to much higher levels of desert-dust ice nucleus particles than the coast of east Asia, while both are subject to high-CCN-aerosol concentrations. Potential aerosol-driven differences in TWC levels aloft may result from aerosols of multiple types and may thus vary regionally due to distinct mixes of aerosols. Finally, other modeling studies have shown that factors such as convective available potential energy (CAPE) and wind shear may also affect results, indicating that the results of this report may be particular to the specific environment in which the clouds evolved.

Little can be concluded in this report about high TWC levels in continental MCSs, an additional gap in the original dataset noted by the High Altitude Ice Crystal and High Ice Water Content (HAIC–HIWC) science team. The complete suppression of warm rain in high-CCN-aerosol cases in continental CAIPEEX and ACRIDICON–CHUVA TCu clouds suggests that in the absence of giant nuclei such as sea-salt aerosols, higher TWC aloft may initially be found in young, growing continental clouds, but there is no information of such at the mature MCS stage. Furthermore, the high turbulence, lightning, and high radar reflectivity of the highest-expected-TWC areas of continental clouds may lead to pilot avoidance, and thereby to a decreased aviation threat.

[5]CAIPEEX stands for Cloud Aerosol Interaction and Precipitation Enhancement Experiment, and the ACRIDICON–CHUVA acronym is derived from the full name of the campaign: Aerosol, Cloud, Precipitation, and Radiation Interaction and Dynamics of CONvective Cloud Systems – Cloud Processes of the Main Precipitation Systems in Brazil: A Contribution to Cloud Resolving Modeling and to the Global Precipitation Measurement.

While numerical cloud models provide insight into CCN effects, there is a lack of rigorous validation of levels of TWC data aloft to provide full confidence in their predictions of sensitivity to aerosols. Ultimately, the most defensible product for the ARAC ICIWG would be the comparison of large in situ datasets collected in MCSs formed in high- and low-CCN-aerosol environments, as originally intended for the HIWC–2022 campaign. Experience in HIWC–2022 revealed the formidable challenges for a Government agency to achieve success in such a campaign. Such challenges include securing a suitable aircraft with a high ceiling and long flight duration during a period of maximum MCS frequency, soliciting collaboration from multiple agencies for expertise and instrumentation, securing access and freedom of flight into prime high-pollution regions often restricted by foreign governments and/or for military use, establishing diplomatic agreements if required, and budgeting sufficient time and funds to catch conditions when and where high pollution and MCS coexist. Due to the decommissioning of the NASA DC–8 aircraft, securing and outfitting an aircraft for compatible high TWC measurements would be the first major challenge. There are no current plans within NASA or the FAA to pursue a follow-up flight campaign. Accordingly, the authors recommend a periodic review of new in situ datasets and modeling results from the atmospheric science and aviation communities to identify any new relevant information. For in situ datasets, it is important to consider the large uncertainty of most available high-TWC measurement devices and the considerable effort expended to develop the IKP2 instrument for adequate accuracy and reliability. Furthermore, for comparison of the statistics of new and past results, a compatible cloud sampling strategy is essential.

Appendix 1.—Nomenclature

2D–S	2-dimensional stereo imaging probe (SPEC)
4ICE	four ice (cloud ice, snow, graupel, and hail modeling scheme)
AC	Advisory Circular
ACRIDICON–CHUVA	Aerosol, Cloud, Precipitation, and Radiation Interaction and Dynamics of CONvective Cloud Systems – Cloud Processes of the Main Precipitation Systems in Brazil: A Contribution to Cloud Resolving Modeling and to the Global Precipitation Measurement (flight campaign)
ADC	air data computer
ADIZ	Air Defense Identification Zone
AMS	American Meteorological Society
AOD	aerosol optical depth
ARAC	Aviation Rulemaking Advisory Committee (FAA)
AS	aerosol sampler
AS–SW	aerosol sampler–silicon wafer
AS–TEM	aerosol sampler–transmission electron microscopy
ATC	air traffic control
AVHRR	Advanced Very High Resolution Radiometer
BC	black carbon
BHS	background humidity system
BWV	background water vapor
CAIPEEX	Cloud Aerosol Interaction and Precipitation Enhancement Experiment
CAPE	convective available potential energy
CCN	cloud condensation nuclei
CCN–200	Cloud Condensation Nuclei Counter, dual-column version (DMT)
CDP–2	Cloud Droplet Probe 2 (DMT)
CFR	Code of Federal Regulations
CMD	cumulative mass distribution
CPC	Condensation Particle Counter
CPEX–CV	Convective Processes Experiment–Cabo Verde
CReSS	Cloud Resolving Storm Simulator
CS	Certification Specification
DLH	Diode Laser Hygrometer
DLR	German Aerospace Center (Deutsches Zentrum Für Luft- Und Raumfahrt)
DMT	Droplet Measurement Technologies®
EASA	European Union Aviation Safety Agency
EDX	energy-dispersive X-ray analysis
EHWG	Engine Harmonization Working Group
EM	electron microscopy
FAA	Federal Aviation Administration
GCCN	giant cloud condensation nuclei
GEOS–CF	Goddard Earth Observing System–Composition Field
GMAO	Global Modeling and Assimilation Office
GN	giant nuclei
GOES	Geostationary Operational Environmental Satellite

GPS	Global Positioning System
HA	high altitude
HAIC	High Altitude Ice Crystal
HALO	High Altitude and LOng Range (aircraft, DLR)
HaRP	Hawaii Rainfall Project
HIWC	High Ice Water Content
HRRR	High-Resolution Rapid Refresh model
HYSPLIT	Hybrid Single-Particle Lagrangian Integrated Trajectory
I&Q	in-phase and quadrature
ICD	Ice Crystal Detector (SEA)
ICI	ice crystal icing
ICIWG	Ice Crystal Icing Working Group
IKP2	Isokinetic Probe 2 (SEA)
INAS	ice nucleation active surface site
INP	ice-nucleating particle
IPHWG	Ice Protection Harmonization Working Group
IR	infrared
IWC	ice water content
IWC_{Da}	ice water content domain-average
JHWRP	Joint Hawaiian Warm Rain Project
LA	low altitude
LES	large eddy simulation
LWC	liquid water content
MCS	mesoscale convective system
MF	membrane filter
MFM	membrane filter method
MLIT	Ministry of Land, Infrastructure, Transportation and Tourism
MMD	median mass diameter (μm)
MRI	Meteorological Research Institute
MSD	mass size distribution
NAAPS	Navy Aerosol Analysis and Prediction System
NAM	North American Mesoscale (weather prediction model)
NCAR	National Center for Atmospheric Research
ncc	cloud droplet number concentration
NEXRAD	Next Generation Weather Radar
NOAA	National Oceanic and Atmospheric Administration
NRC	National Research Council of Canada
NRL	Naval Research Laboratory
NU	Nagoya University
OAP	optical array probe
OC	organic carbon
OIIR	Office of International and Interagency Relations Mission
OPC	optical particle counter (RION)
PCASP	passive cavity aerosol spectrometer probe (DMT)
PIP	Precipitation Imaging Probe (DMT)
PMS	Particle Measuring Systems®

PPIHWG	Power Plant Installation Harmonization Working Group
PRCP	precipitation
PSD	particle size distribution
PTFE	polytetrafluoroethylene
RADAR	radio detection and ranging
RAE	Royal Aircraft Establishment
RH	relative humidity
RICO	Rain In shallow Cumulus over the Ocean
RIWC	radar-derived ice water content
RRF	radar reflectivity factor
RTB	return to base
SAFIRE	Service des Avions Français Instrumentés pour la Recherche en Environnement
SAT	static air temperature
SCMS	Small Cumulus Microphysics Study
SEA	Science Engineering Associates
SEM	scanning electron microscopy
SIP	secondary ice production
SLD	supercooled large drop
SMPS	scanning mobility particle sizer (TSI Inc)
SODA	System for Optical Array Probe Data Analysis
SPEC	Stratton Park Engineering Company
SPRINTARS	Spectral Radiation-Transport Model for Aerosol Species
SS_i	supersaturation with respect to ice
SS_w	supersaturation with respect to water
SSA	sea-salt aerosol
TASS	Terminal Area Simulation System
TAT	total air temperature
TCu	towering cumulus
TEM	transmission electron microscopy
TWC	total condensed water content
TWC_{99}	99th percentile value of TWC dataset for given distance scale-length
TWC_{max}	maximum total water content
UGCCN	ultra giant cloud condensation nuclei
UTC	Coordinated Universal Time
VQQ	Cecil Airport code
WVSS–II	Water Vapor Sensing System, 2nd generation (SpectraSensors)
WX	weather

Appendix 2.—Flight Summary Figures

Figure 2.1 to Figure 2.10 show flight tracks and time histories of altitude, temperature, median mass diameter (MMD), and total water content (TWC) for the 10 research flights. Data sources are shown in parentheses. The source for pressure altitude was the Interagency Working Group 1 (IWG1) standard data available on the DC–8. Annotations on the flight tracks indicate the general locations of the high-altitude traverses in the MCSs and low-altitude traverses for boundary-layer aerosol and towering cumulus (TCu) measurements. The infrared (IR) satellite image in these figures is for a nominal time during the traverses through the MCSs and does not show the progression and decay of the storm during the flight. Time histories are limited to the periods in the clouds of interest and are annotated to indicate specific events such as pitot anomalies or lightning strikes.

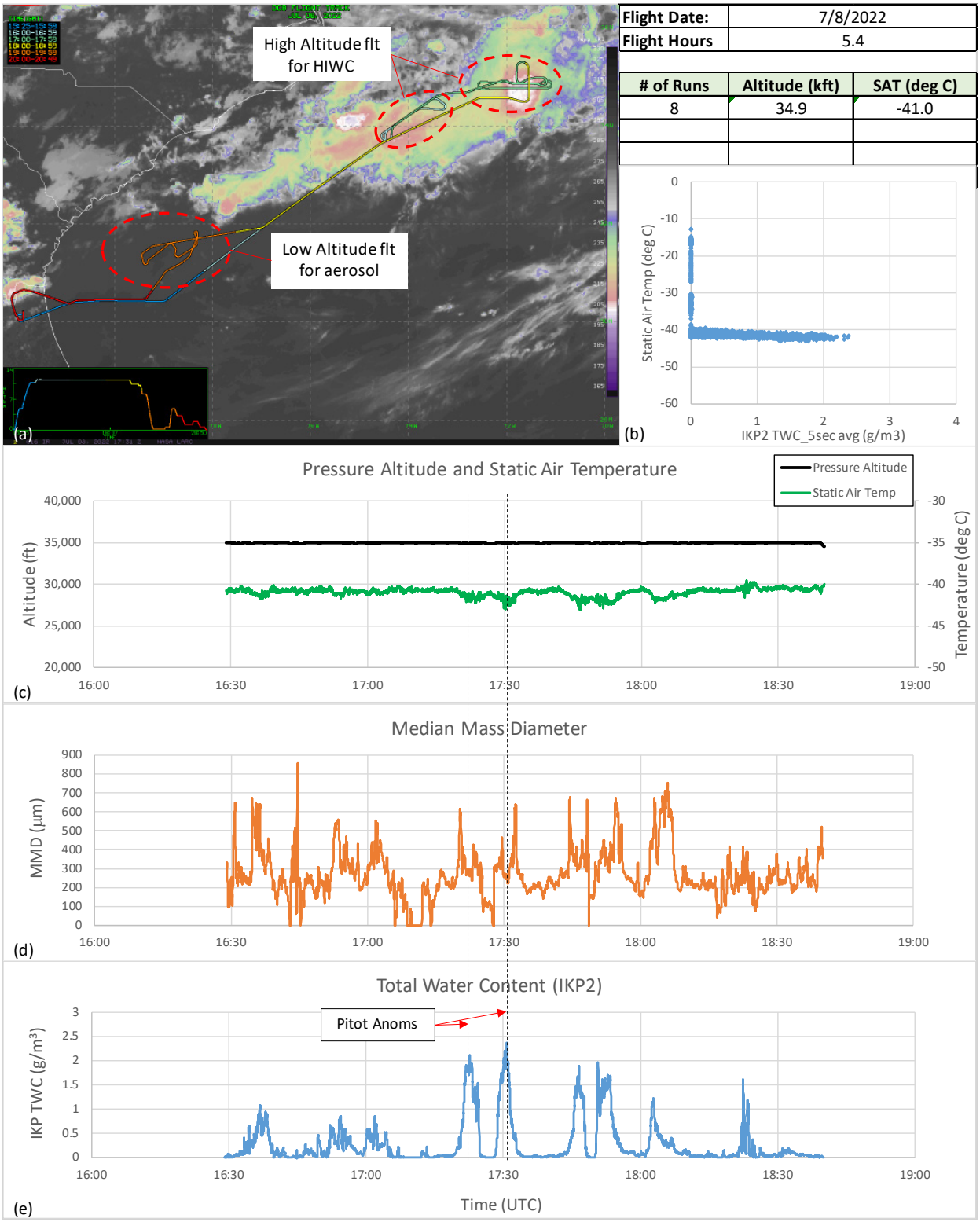

Figure 2.1.—Flight track overlay IR satellite image and select time histories for 2022-07-08. (a) DC–8 flight track. (b) Static air temperature (SAT) versus Isokinetic Probe 2 (IKP2) total water content (TWC) 5-s average. (c) Pressure altitude (IWG1) and SAT (Goodrich 102LJ total air temperature (TAT)). (d) MMD. (e) IKP2 TWC with pitot anomaly times noted.

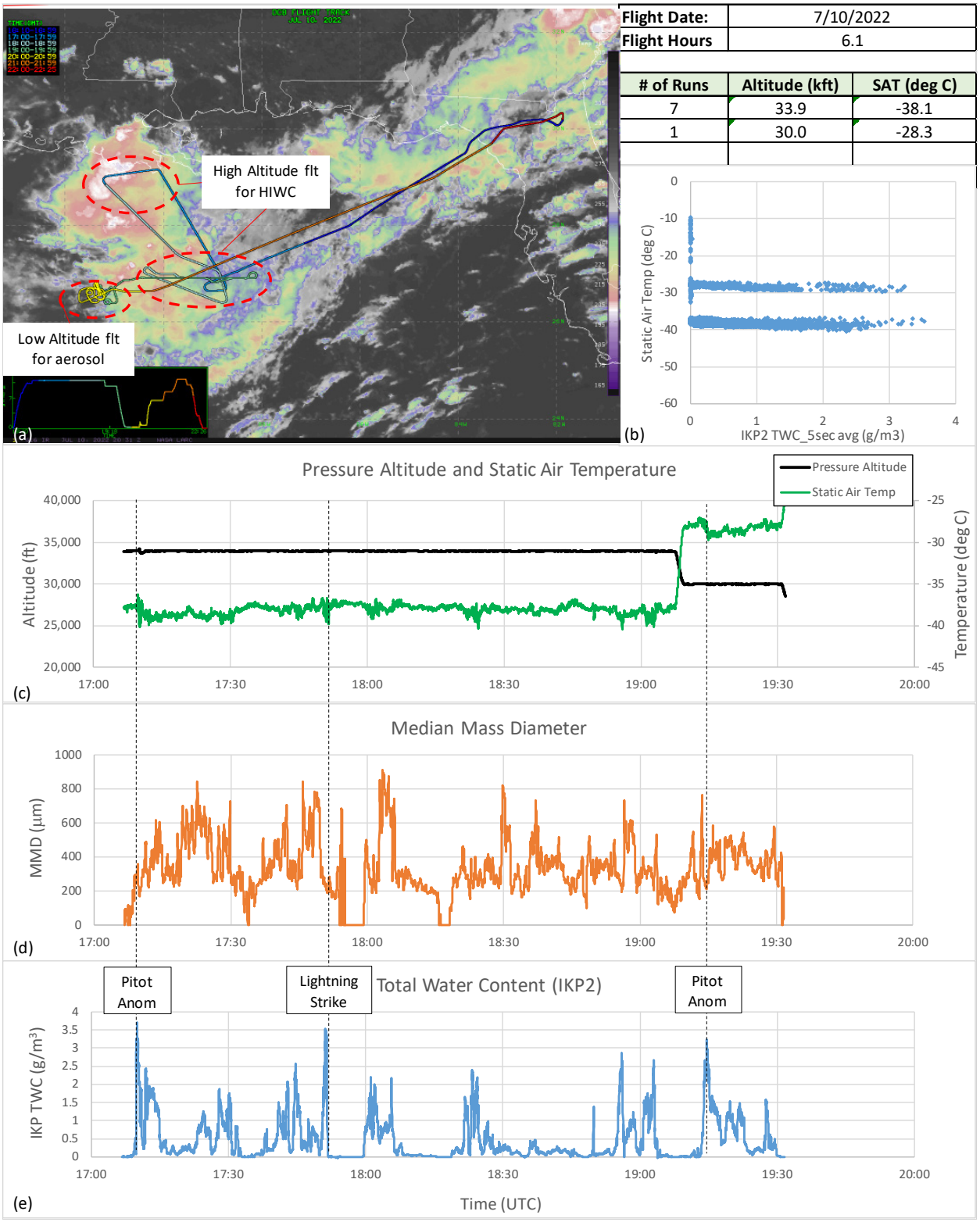

Flight Date:	7/10/2022
Flight Hours	6.1

# of Runs	Altitude (kft)	SAT (deg C)
7	33.9	-38.1
1	30.0	-28.3

Figure 2.2.—Flight track overlay on IR satellite image and select time histories for 2022-07-10. (a) DC–8 flight track. (b) SAT versus IKP2 TWC 5-s average. (c) Pressure altitude (IWG1) and SAT (Goodrich 102LJ TAT). (d) MMD. (e) IKP2 TWC with pitot anomaly and lightning strike times noted.

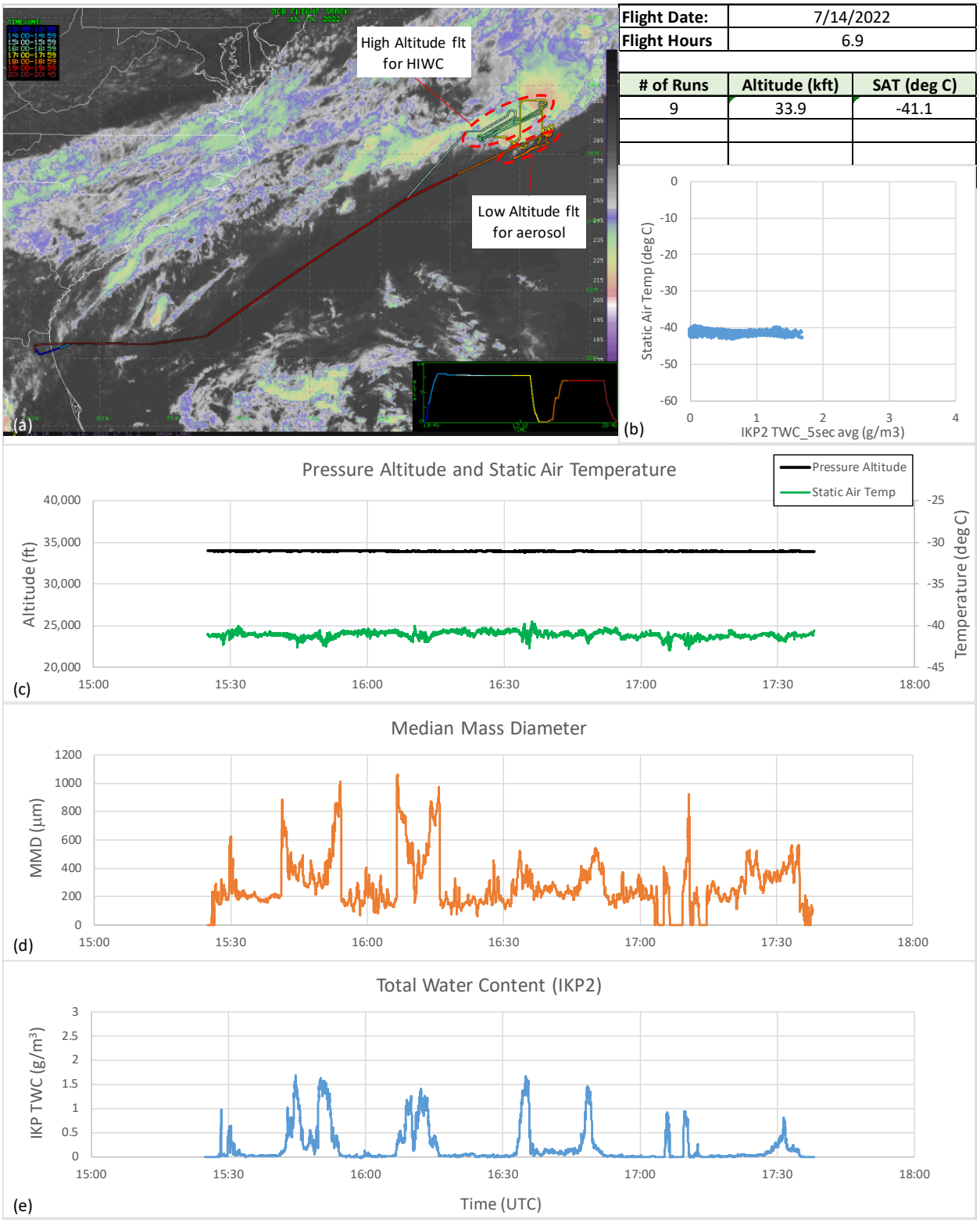

Flight Date:	7/14/2022
Flight Hours	6.9

# of Runs	Altitude (kft)	SAT (deg C)
9	33.9	-41.1

Figure 2.3.—Flight track overlay on IR satellite image and select time histories for 2022-07-14. (a) DC–8 flight track. (b) SAT versus IKP2 TWC 5-s average. (c) Pressure altitude (IWG1) and SAT (Goodrich 102LJ TAT). (d) MMD. (e) IKP2 TWC.

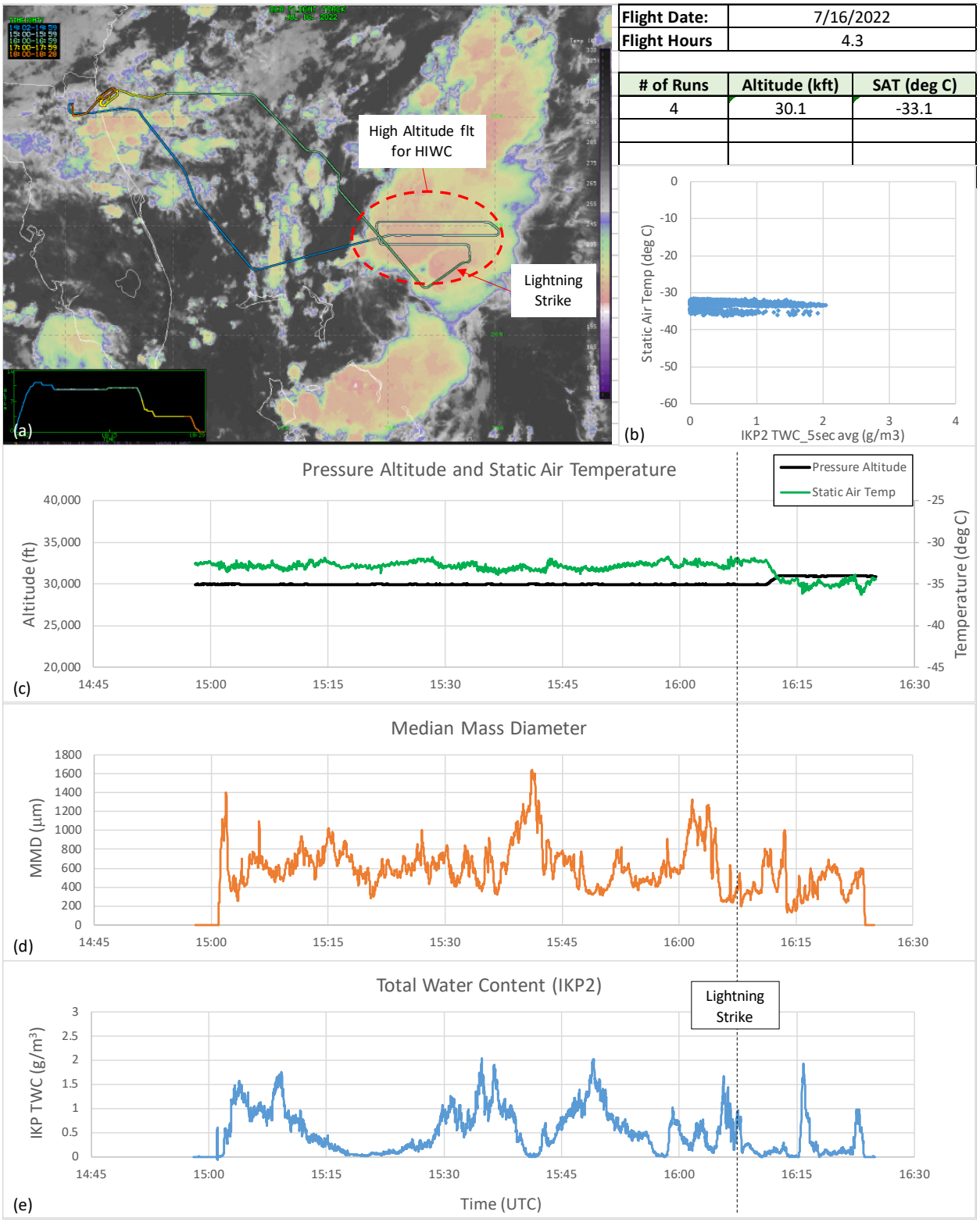

Figure 2.4.—Flight track overlay on IR satellite image and select time histories for 2022-07-16. (a) DC–8 flight track. (b) SAT versus IKP2 TWC 5-s average. (c) Pressure altitude (IWG1) and SAT (Goodrich 102LJ TAT). (d) MMD. (e) IKP2 TWC with lightning strike time noted.

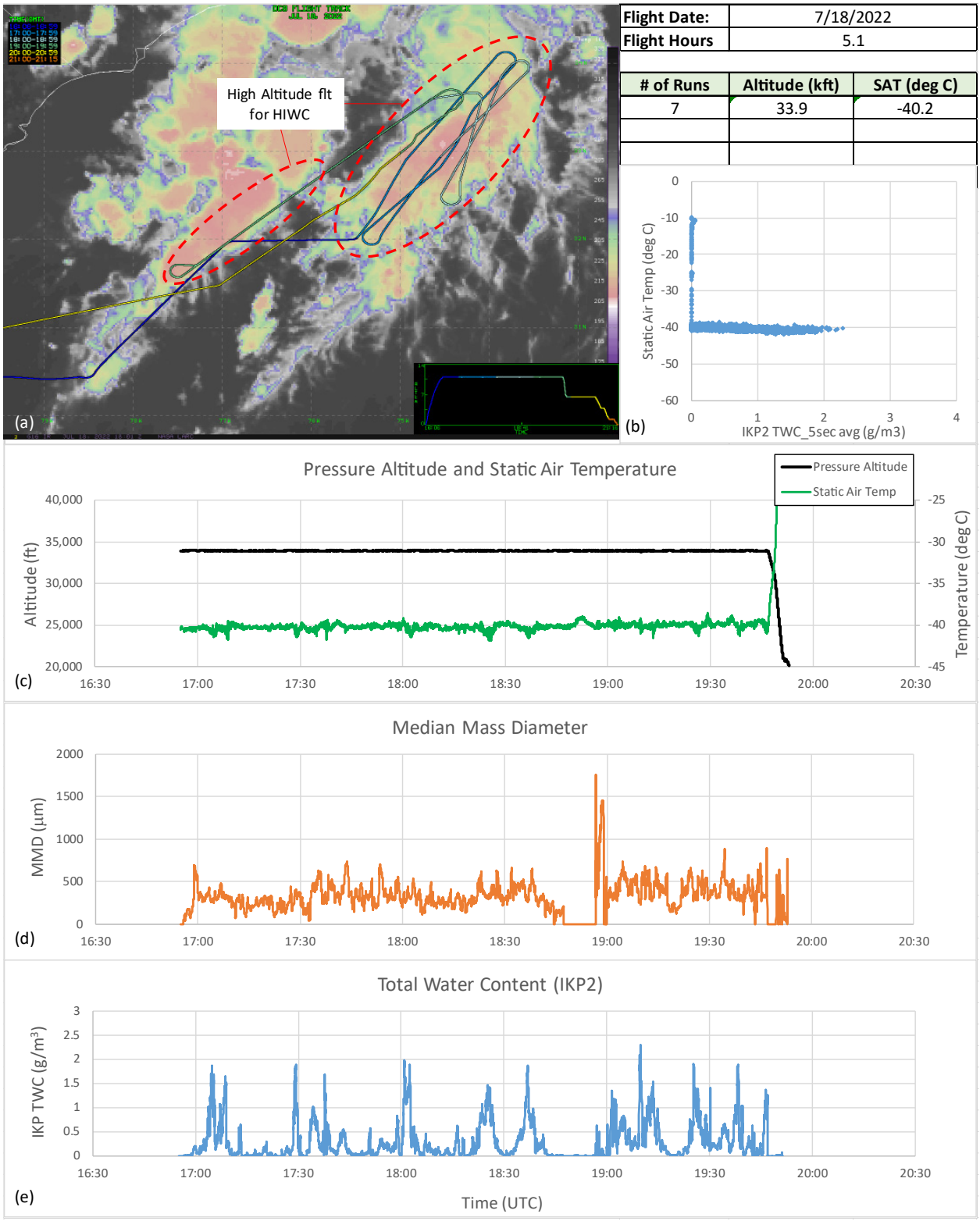

Figure 2.5.—Flight track overlay on IR satellite image and select time histories for 2022-07-18. (a) DC–8 flight track. (b) SAT versus IKP2 TWC 5-s average. (c) Pressure altitude (IWG1) and SAT (Goodrich 102LJ TAT). (d) MMD. (e) IKP2 TWC.

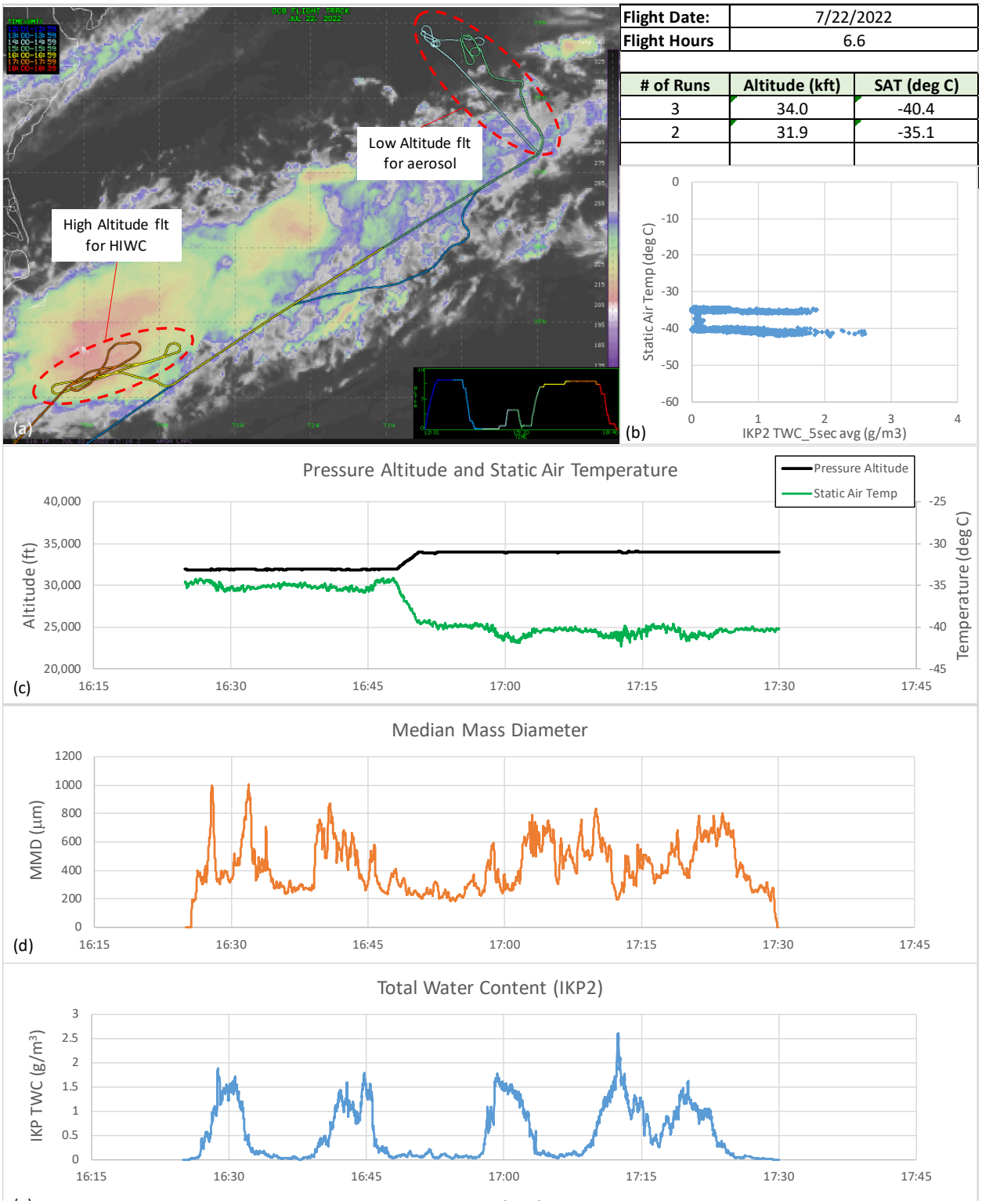

Flight Date:	7/22/2022
Flight Hours	6.6

# of Runs	Altitude (kft)	SAT (deg C)
3	34.0	-40.4
2	31.9	-35.1

Figure 2.6.—Flight track overlay on IR satellite image and select time histories for 2022-07-22. (a) DC–8 flight track. (b) SAT versus IKP2 TWC 5-s average. (c) Pressure altitude (IWG1) and SAT (Goodrich 102LJ TAT). (d) MMD. (e) IKP2 TWC.

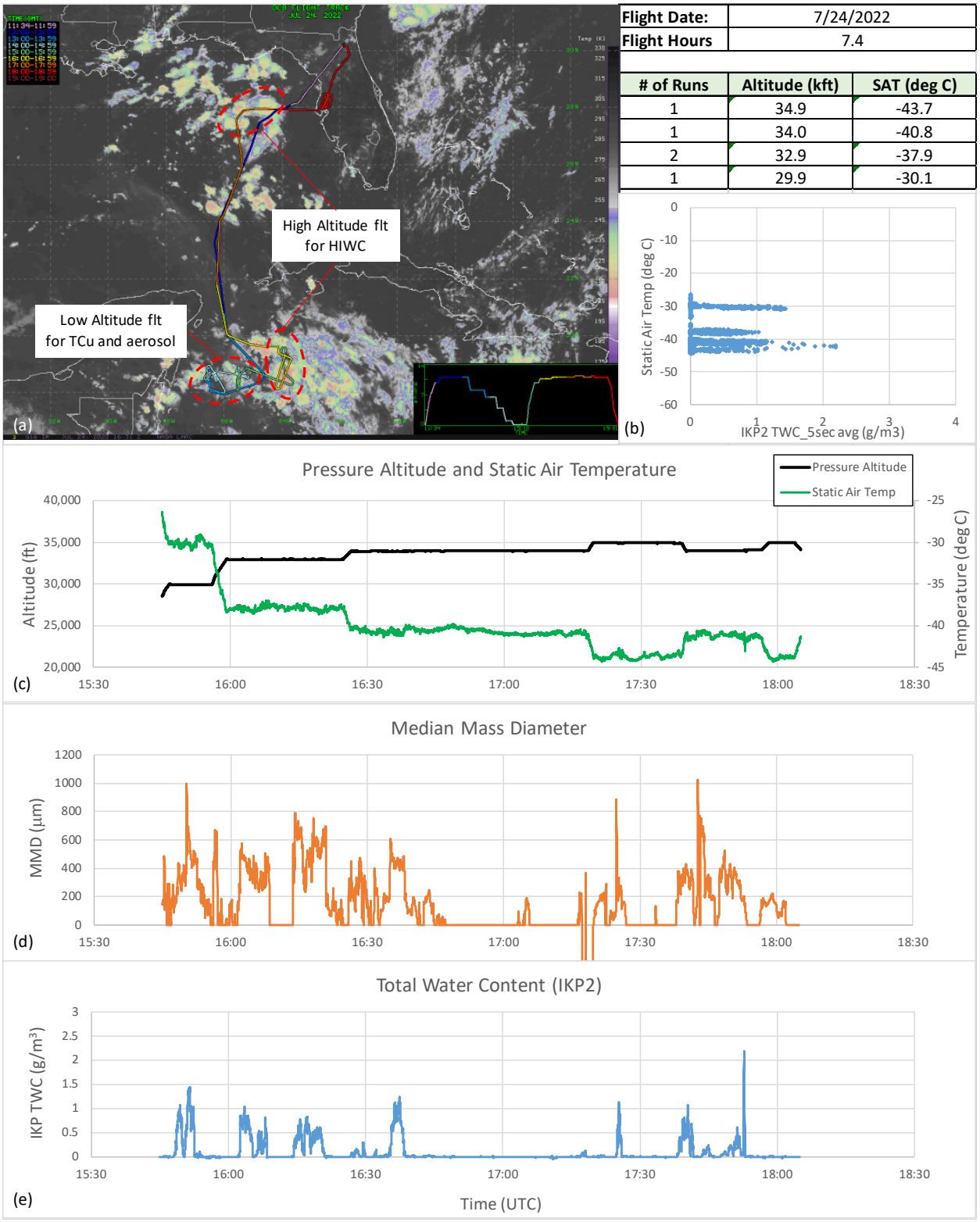

Flight Date:	7/24/2022
Flight Hours	7.4

# of Runs	Altitude (kft)	SAT (deg C)
1	34.9	-43.7
1	34.0	-40.8
2	32.9	-37.9
1	29.9	-30.1

Figure 2.7.—Flight track overlay on IR satellite image and select time histories for 2022-07-24. (a) DC–8 flight track. (b) SAT versus IKP2 TWC 5-s average. (c) Pressure altitude (IWG1) and SAT (Goodrich 102LJ TAT). (d) MMD. (e) IKP2 TWC.

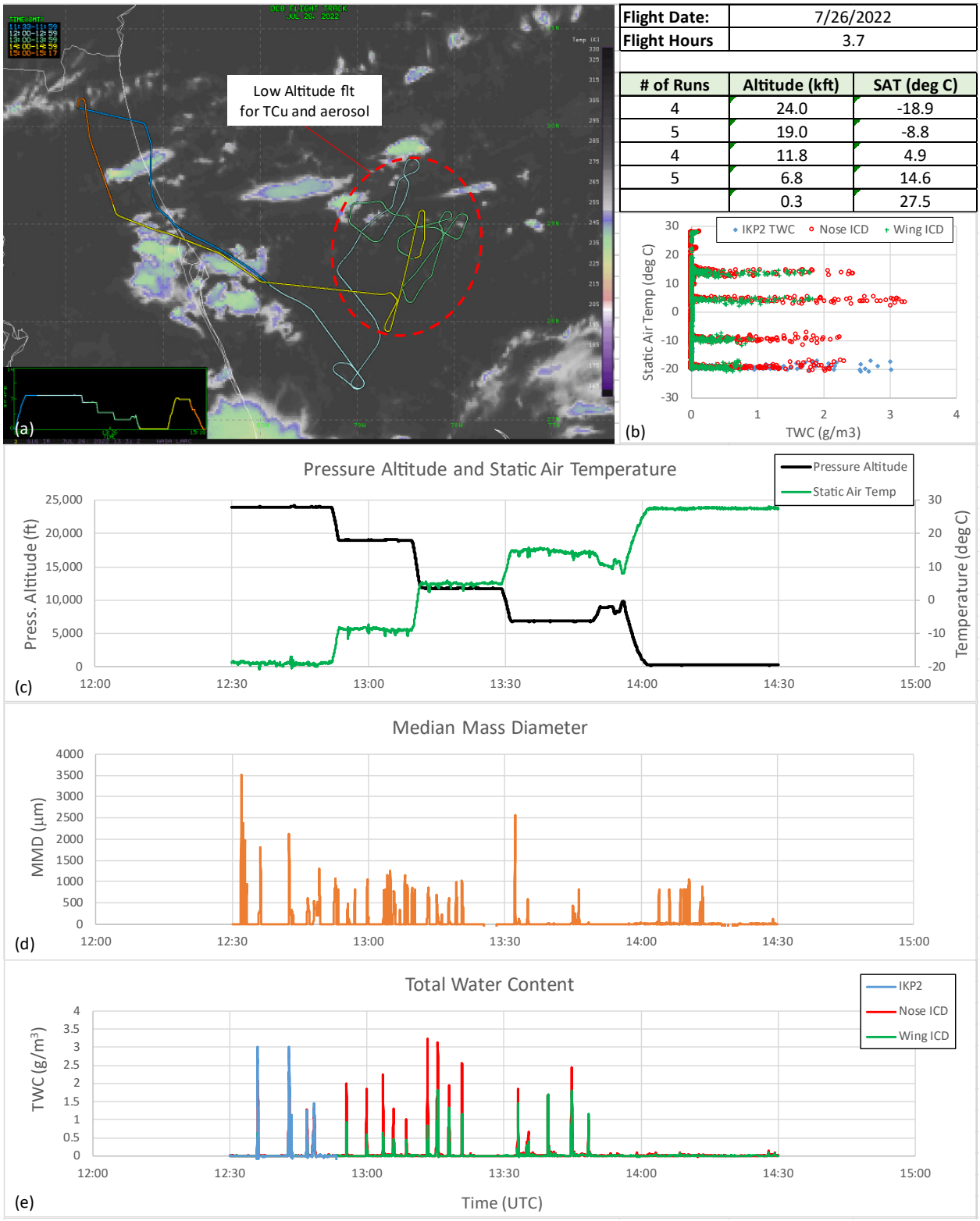

Figure 2.8.—Flight track overlay on IR satellite image and select time histories for 2022-07-26. (a) DC–8 flight track. (b) TWC versus SAT. (c) Pressure altitude (IWG1) and SAT (Goodrich 102LJ TAT). (d) MMD. (e) IKP2 TWC, nose ICD TWC, wing ICD TWC.

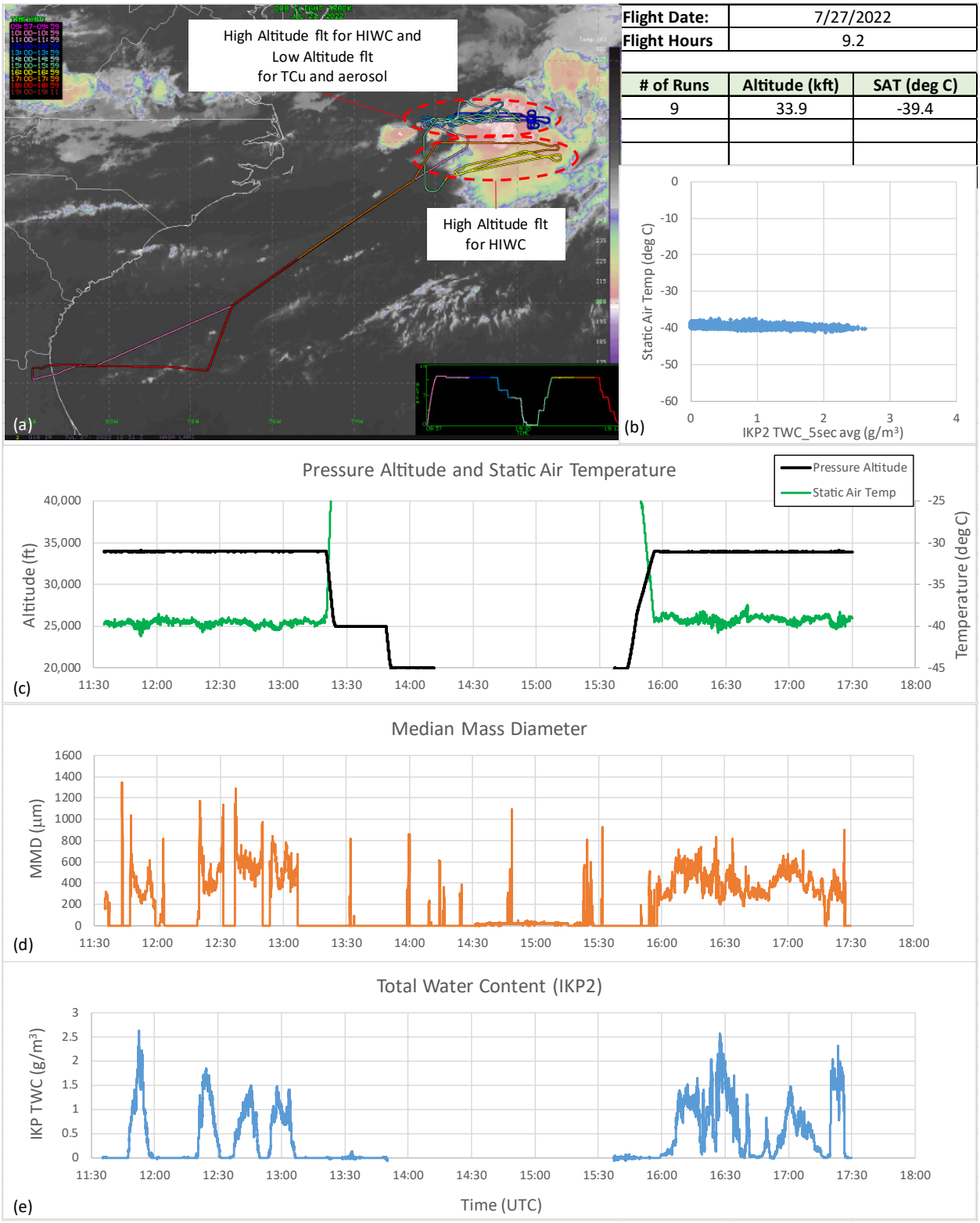

Figure 2.9.—Flight track overlay on IR satellite image and select time histories for 2022-07-27. (a) DC–8 flight track. (b) SAT versus IKP2 TWC 5-s average. (c) Pressure altitude (IWG1) and SAT (Goodrich 102LJ TAT). (d) MMD. (e) IKP2 TWC.

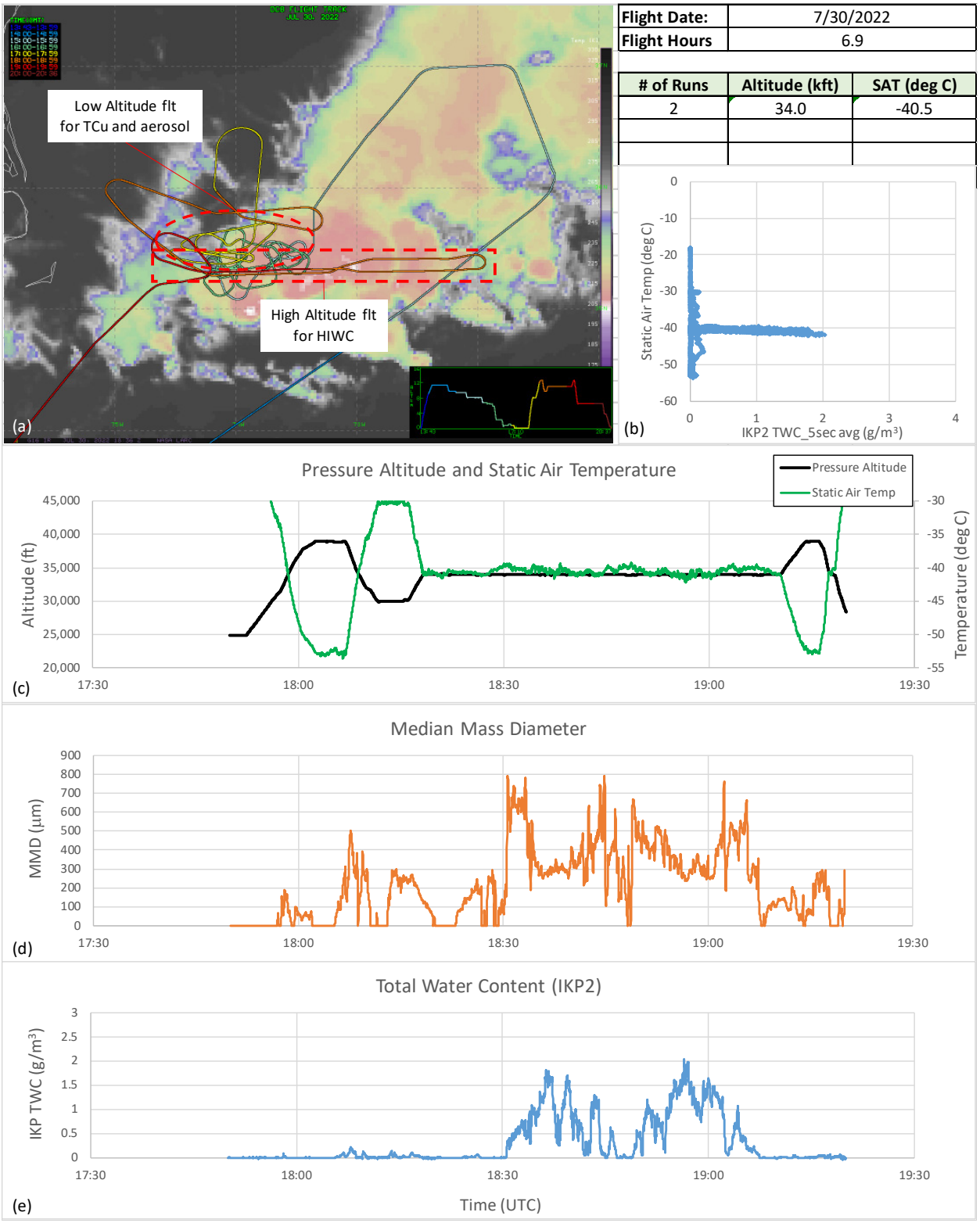

Figure 2.10.—Flight track overlay on IR satellite image and select time histories for 2022-07-30. (a) DC–8 flight track. (b) SAT versus IKP2 TWC 5-s average. (c) Pressure altitude (IWG1) and SAT (Goodrich 102LJ TAT). (d) MMD. (e) IKP2 TWC.

Appendix 3.—NASA Global Modeling and Assimilation Office Model Forecast of Atmospheric Composition Maps

Figure 3.1 to Figure 3.10 show aerosol forecast maps for sulfate and dust for the 10 research flights.

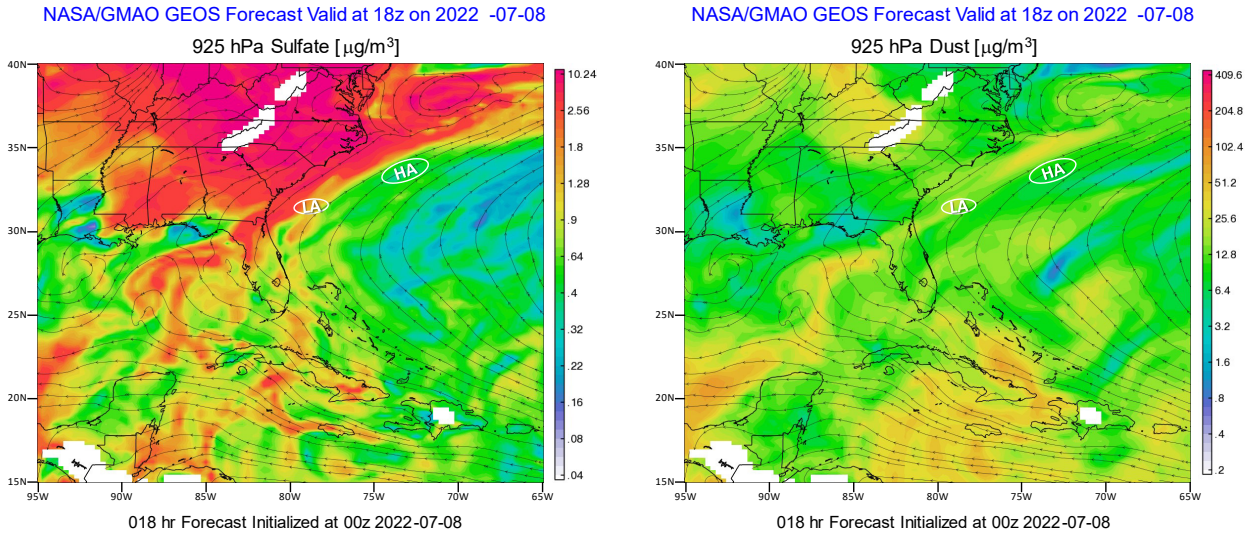

Figure 3.1.—Aerosol forecast for sulfate (left) and dust (right) at 925 hPa on 2022-07-08.

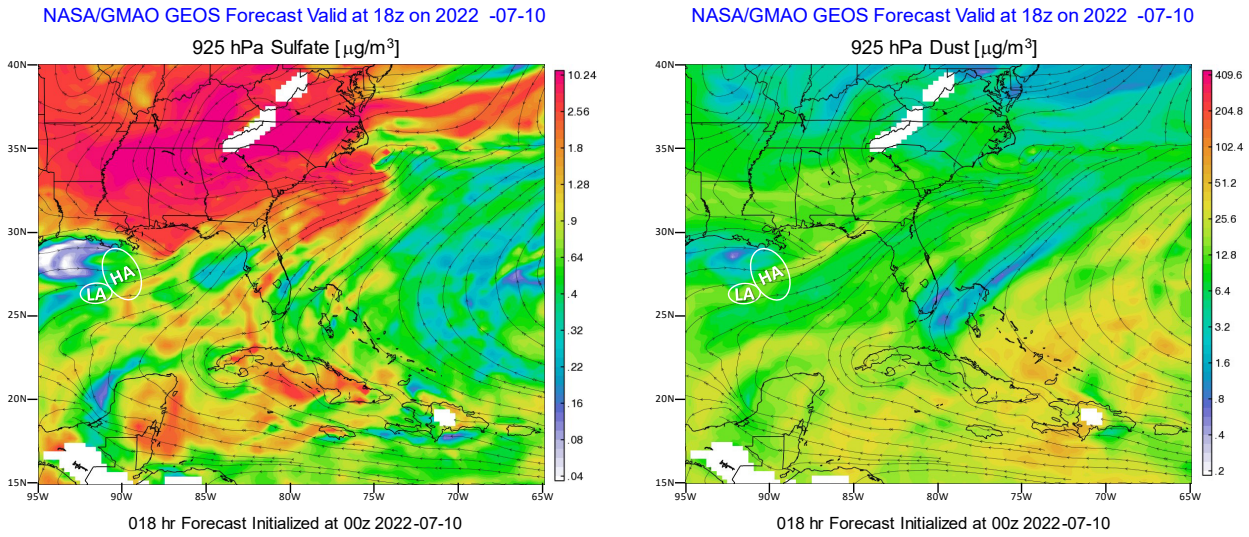

Figure 3.2.—Aerosol forecast for sulfate (left) and dust (right) at 925 hPa on 2022-07-10.

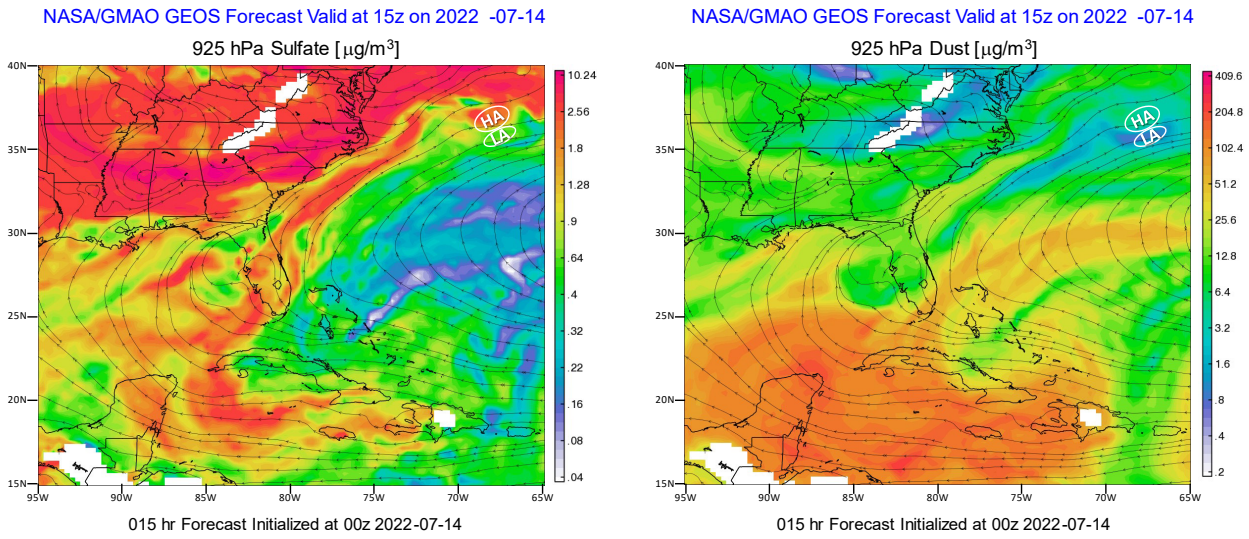

Figure 3.3.—Aerosol forecast for sulfate (left) and dust (right) at 925 hPa on 2022-07-14.

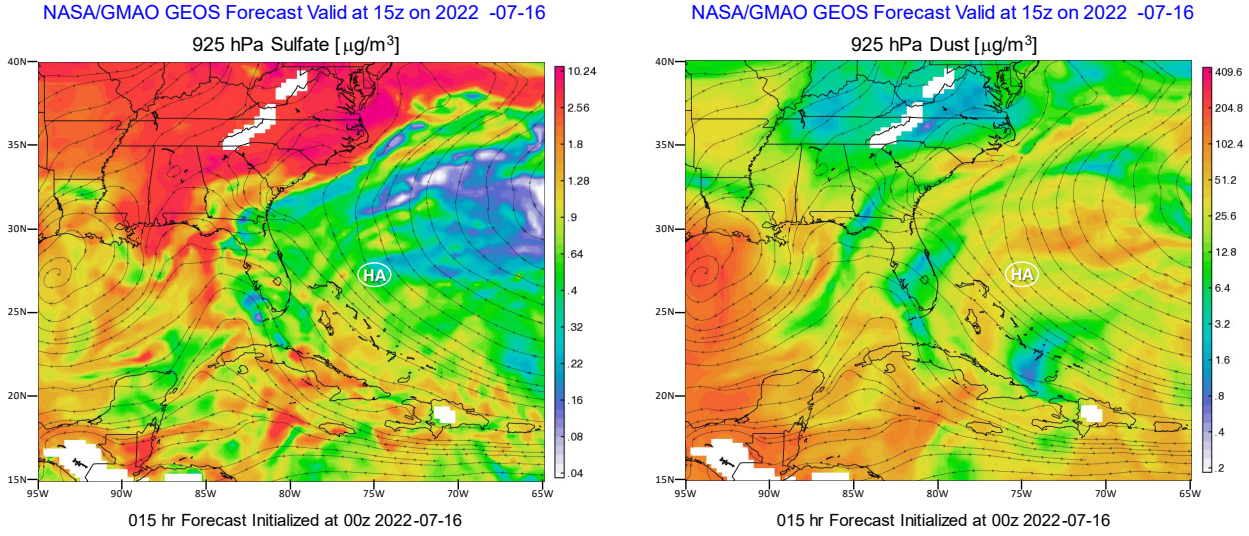

Figure 3.4.—Aerosol forecast for sulfate (left) and dust (right) at 925 hPa on 2022-07-16.

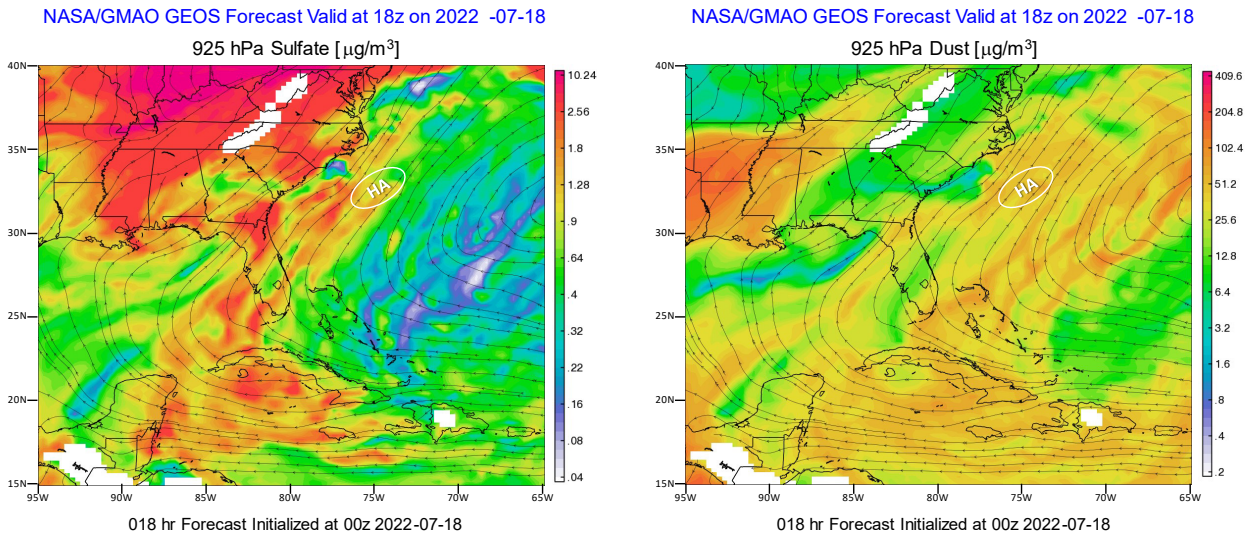

Figure 3.5.—Aerosol forecast for sulfate (left) and dust (right) at 925 hPa on 2022-07-18.

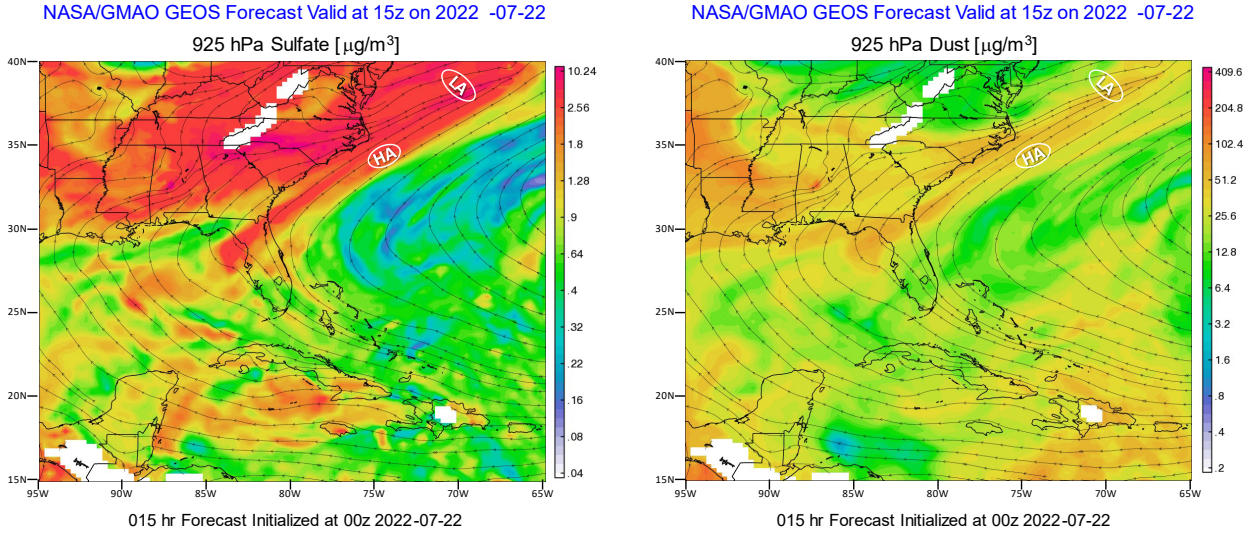

Figure 3.6.—Aerosol forecast for sulfate (left) and dust (right) at 925 hPa on 2022-07-22.

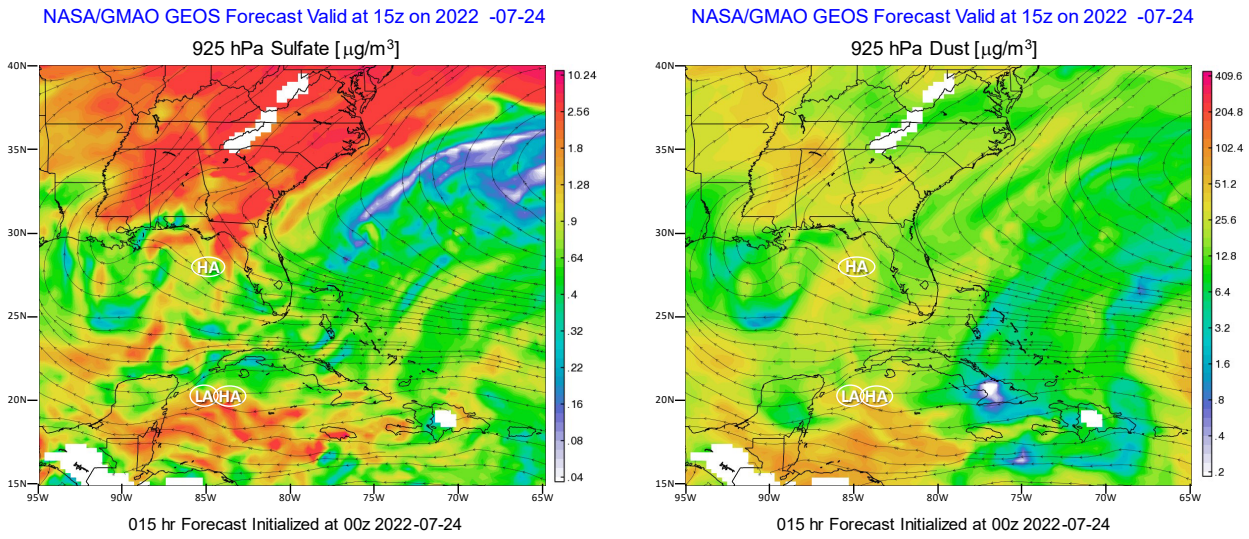

Figure 3.7.—Aerosol forecast for sulfate (left) and dust (right) at 925 hPa on 2022-07-24.

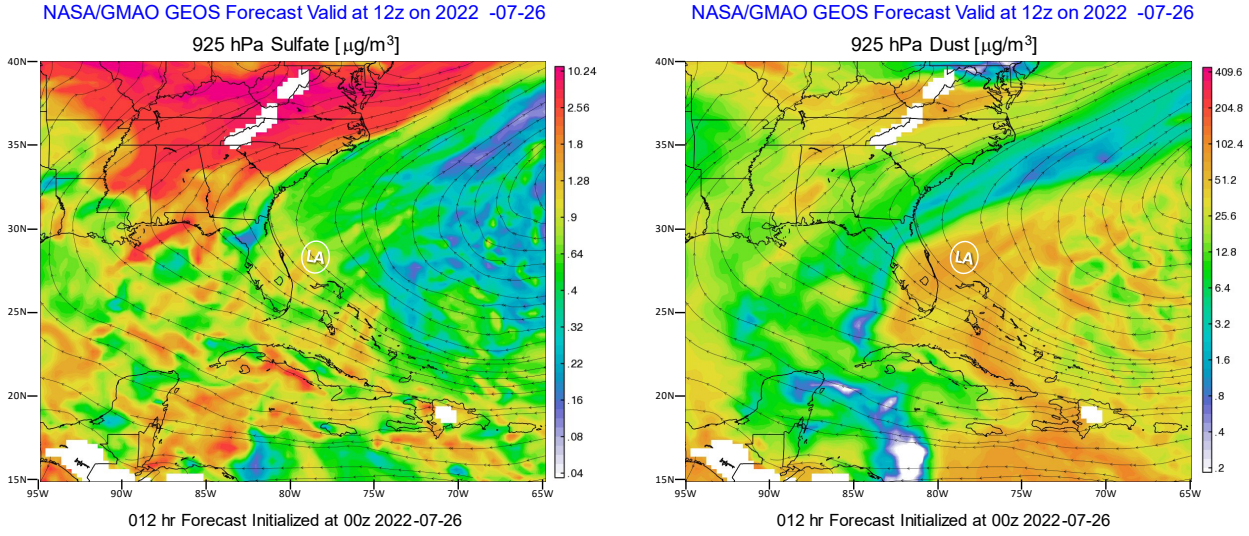

Figure 3.8.—Aerosol forecast for sulfate (left) and dust (right) at 925 hPa on 2022-07-26.

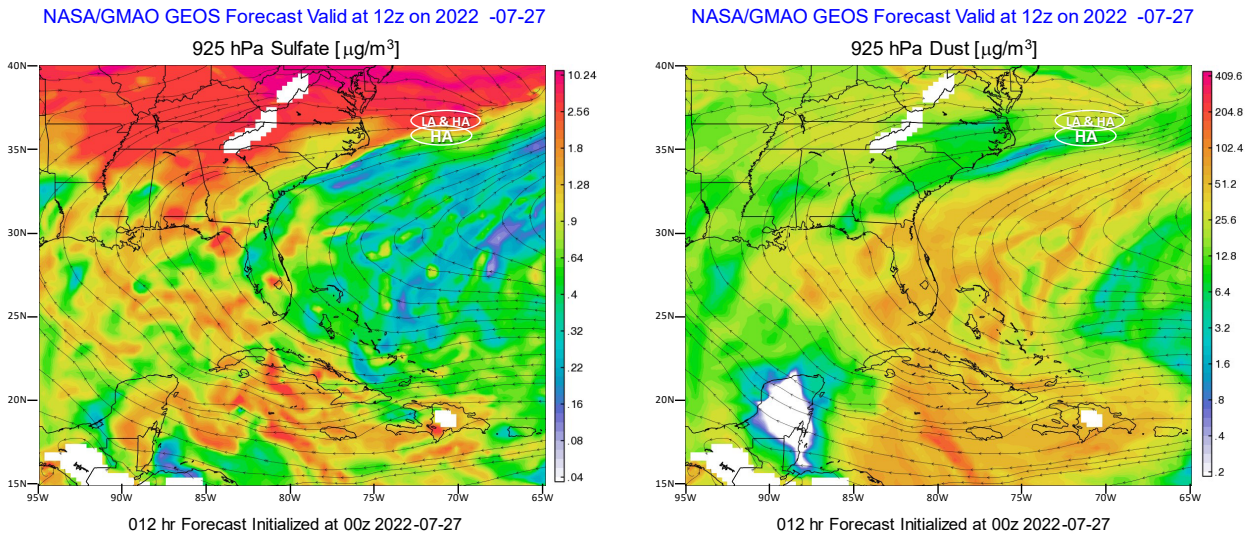

Figure 3.9.—Aerosol forecast for sulfate and dust at 925 hPa on 2022-07-27.

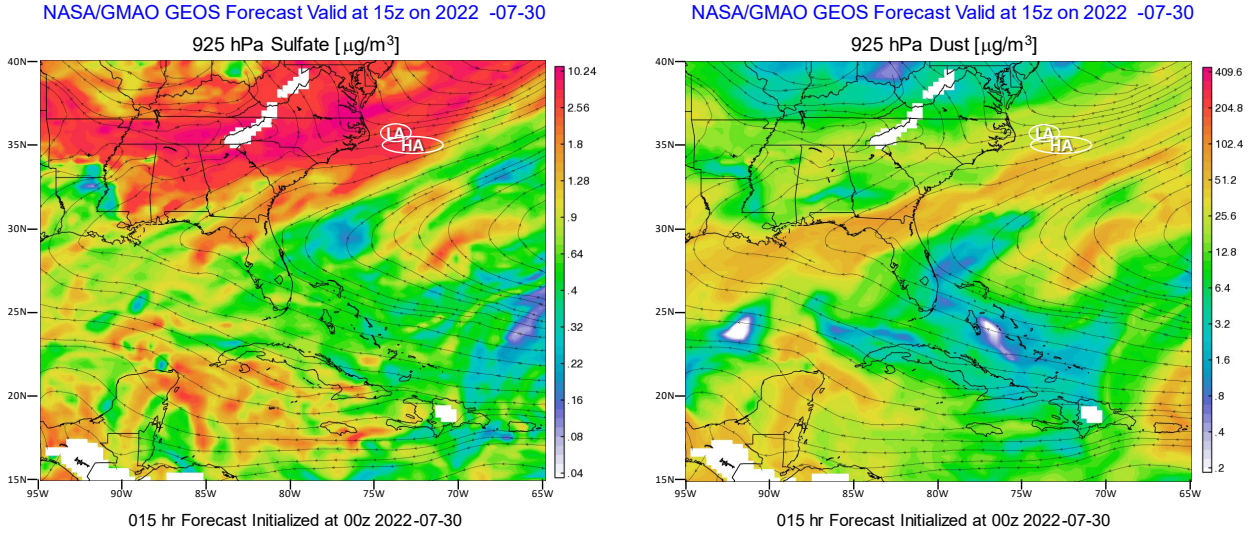

Figure 3.10.—Aerosol forecast for sulfate and dust at 925 hPa on 2022-07-30.

Appendix 4.—TCu Case Studies of Warm Rain Development

4.1 Introduction

Table 14 revealed that a full set of measurements at all levels was not available for any of the cases, but a concept of cloud microphysical development could be formed by combining the results from the individual days. This appendix provides towering cumulus (TCu) data relevant to the development of warm rain for each flight day, when available. More information can be found in Reference 126.

The following information is included. Frames from the forward video on the DC–8 are provided to show an image of the cloud a moment before entry, with a red X marking the approximate point of entry. Average particle size distributions (PSDs) across the cloud are provided; they are calculated using the System for Optical Array Probe (OAP) Data Analysis 2 (SODA–2) software, employing the "all-in" and "water" options. Average liquid water content (LWC) distributions are also provided. The SODA all-in filter limits the maximum size of the 2-dimensional stereo imaging probe (2D–S) to about 1,408 μm and also results in a quickly decreasing sample volume with size. This could result in a noisy 2D–S LWC spectrum tail, requiring the use of the Precipitation Imaging Probe (PIP) data to adequately close the LWC spectrum. When the Cloud Droplet Probe 2 (CDP–2), 2D–S, and PIP were all available, a composite spectrum was calculated, switching to the 2D–S above 49.5 μm and, due to 2D–S sample volume, to the PIP at 450 μm. Unfortunately, PIP data were often unusable, likely due to fogging of cold-soaked optics when descending into a warmer moist environment. In such cases, the PSDs were calculated only using the CDP–2 and 2D–S, which likely resulted in underestimation of rainfall rates. PSD analysis was not performed for all runs due to limited resources for analysis. When multiple runs were available at the same level, the one that exhibited the most advanced warm rain development was chosen for illustration in the following sections.

4.2 2022-07-27

The aerosol levels this day were concluded to be moderate. Although below-base passive cavity aerosol spectrometer probe (PCASP) average concentration was relatively low at 153 cm^{-3}, the average cloud condensation nuclei (CCN) concentration was moderate at 741 cm^{-3}, indicating that CCN were activated below the minimum size of the PCASP. The inventory of "good" TCu runs for this day included three cloud base runs, five runs at 7 °C, and five runs at about –9 °C. There was no sampling at 14 °C or –19 °C this day. One run was selected as representative from each level—cloud base (21 °C), 7 °C, and –9 °C—to track the evolution of warm rain. Each run will be described in detail. Three –9 °C runs were estimated to be mixed-phase runs, and one was liquid only. The latter was selected as most appropriate for warm rain tracking in the following analysis.

Figure 4.1 shows sample 2D–S (11 to 1,408 μm, 11-μm resolution) OAP images for a cloud base run at 2,440-ft pressure altitude and 21.4 °C. Note the background of very small images associated with the main droplet condensation mode, but also the occasional larger droplet. Figure 4.2 shows the average number concentration PSD for this run as measured by the CDP–2 (red) and 2D–S (blue-green) probes. The average and 1-s maximum CDP–2 droplet concentrations were 126 and 344 cm^{-3}, respectively. The maximum size of the CDP–2 (49.5 μm) is chosen here as an arbitrary threshold to the start of warm rain. The LWC at sizes ≥49.5 μm was negligible (see figure inset), but some large droplets were evident in the 2D–S imagery to at least 55 μm or so and in the computed average PSD of Figure 4.2 to at least 110 μm.[6] The literature claims that droplets above about 50 μm are required to start the coalescence process (hereafter called coalescence embryos), and they were indeed present.

[6]Note that the SODA image processing corrected 2D–S sizes in Figure 4.2 for out-of-focus oversizing, for example, the largest droplet with a central hole (Poisson spot) on the bottom right of the first frame of Figure 4.1.

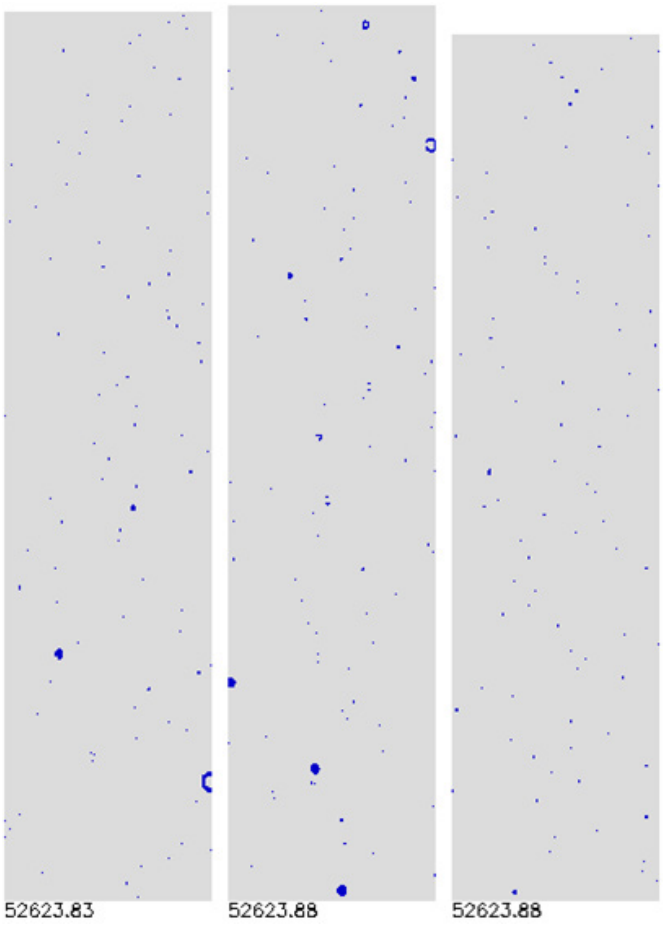

Figure 4.1.—Sample 2D–S OAP images of droplets from cloud base run on 2022-07-27. Width of each image strip is 1,408 µm. Length of cloud run was 15 s.

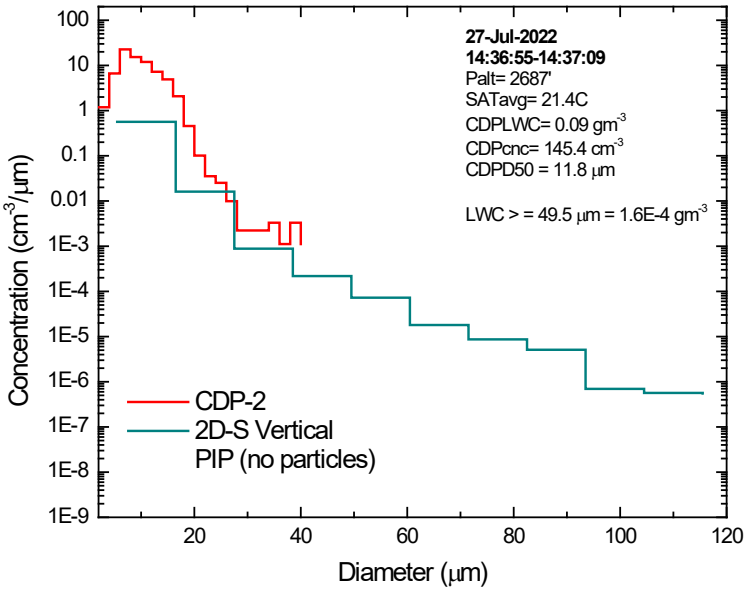

Figure 4.2.—Average PSD across cloud base run on 2022-07-27.

Figure 4.3.—Frame from DC–8 forward video before entry into cloud of 2022-07-27 at 7.4 °C. Red X is approximate location of entry.

Figure 4.3 shows a frame from the DC–8 video prior to entry in a cloud at 7.4 °C and 10,820-ft pressure altitude. The location of entry was at a good location with respect to the top and was near the center of the cloud. The cloud appeared to be growing, and there was no cloud above. Figure 4.4 shows sample 2D–S and PIP (100 to 6,400 μm) OAP particle imagery from this run. The 2D–S probe imagery was dominated by small condensation mode droplets, and only the occasional large drop was recorded. The PIP probe was more clearly dominated by large drops up to about 1.5 mm due to its insensitivity to the small condensation mode droplets. On close inspection, the perimeters of the PIP images were often quite rough. It is contended that the cloud was growing and thus had not reached the freezing level in its lifetime, and graupel particles could not exist at this temperature in any event. Figure 4.4 therefore shows that irregular PIP drop perimeters of circular drops could be expected due to coarse resolution and digitization, and graupel would be best identified using the higher resolution 2D–S imagery. Figure 4.5 and Figure 4.6 show the average PSD number concentration and LWC distributions, respectively, for the 7.4 °C run. The normalization of the LWC spectrum (dLWC/dlog$D$) provides a display where the area under the curve is proportional to LWC. A composite LWC spectrum (gray line) of the CDP–2 forward scatter probe (2 to 47 μm, ~1-μm resolution), 2D–S, and PIP probes was constructed with probe crossover points at 49.5 and 450 μm. The average and maximum droplet concentrations were 164 and 414 cm^{-3}, respectively. There were now distinct condensation and warm rain LWC modes, the former centered at about 30 μm and the latter at about 2 mm. The calculated fraction of LWC above 49.5 μm was 55 percent. The PSD LWC and the best estimate of the Isokinetic Probe 2 (IKP2) LWC were 2.00 and 1.79 gm^{-3}, respectively. The rainfall rate was substantial at 23.2 mm/h. The 2D–S did not adequately close the LWC spectrum due to the short interval in cloud and low sample volume, but the PIP did appear to do so.

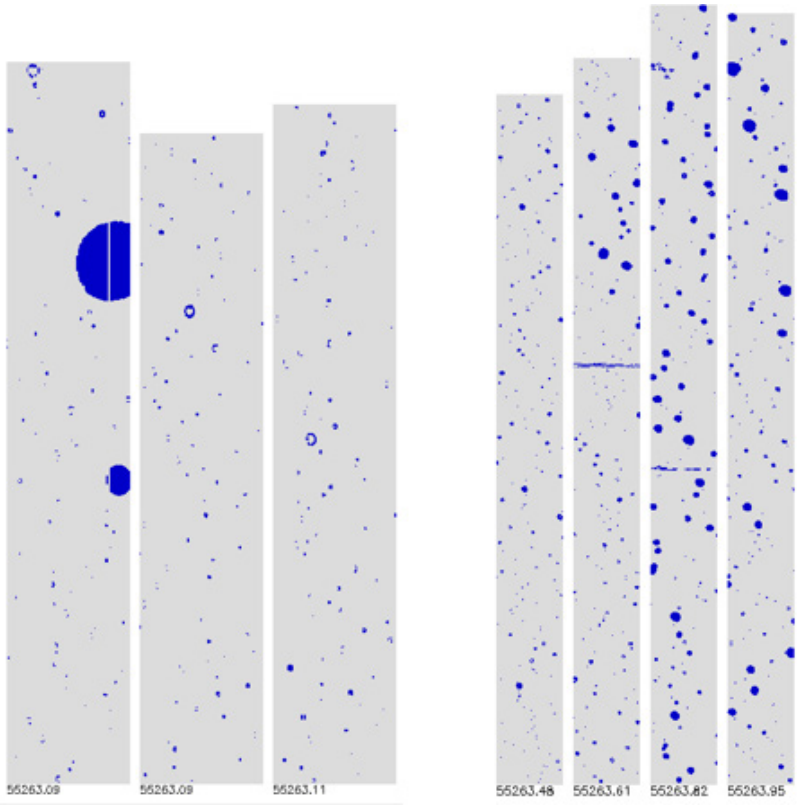

Figure 4.4.—Sample 2D–S (left) and PIP images (right) of droplets from run on 2022-07-27 at 7.4 °C. Width of each 2D–S image strip is 1,408 µm. Width of each PIP image strip is 6,400 µm.

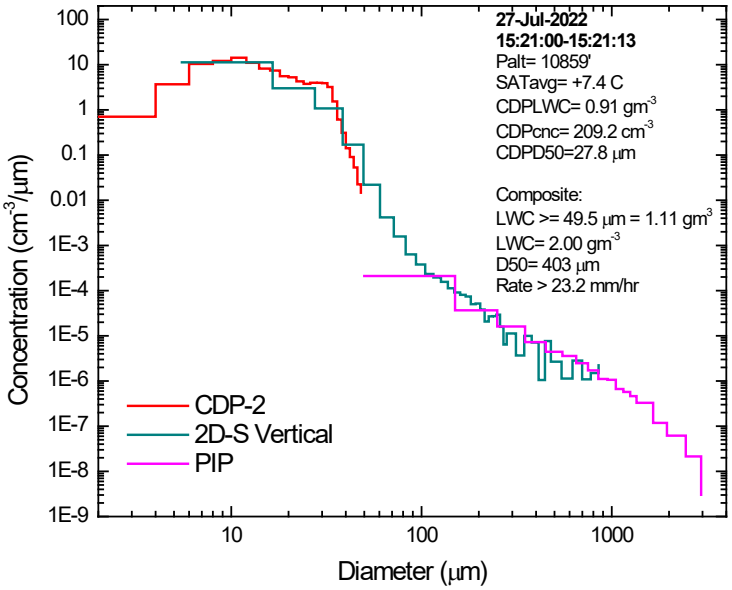

Figure 4.5.—Average PSD for 7.4 °C run of cloud on 2022-07-27.

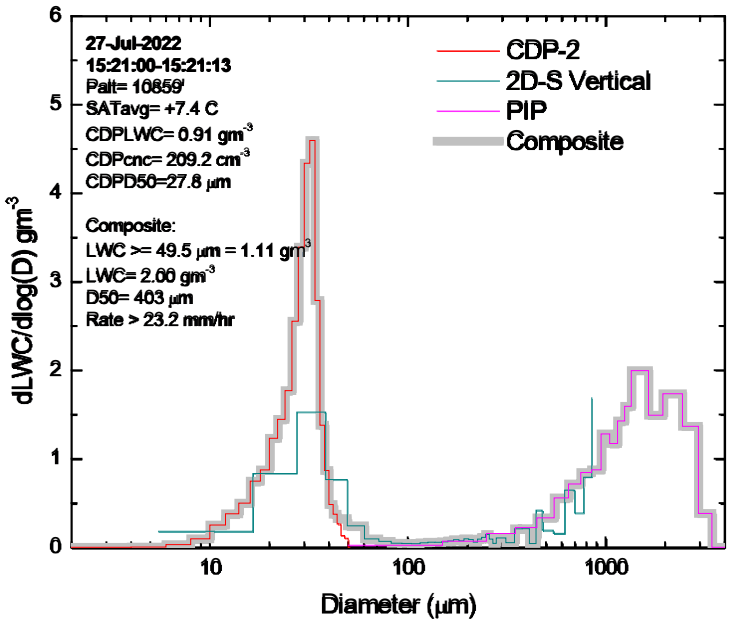

Figure 4.6.—Corresponding LWC distribution for 7.4 °C run on 2022-07-27. LWC spectrum normalized to logarithm of diameters (d*LWC*/dlog*D*). Visible area under curve is proportional to LWC in this presentation.

Figure 4.7 shows a DC–8 forward video frame prior to the liquid-only cloud run at –8.6 °C and 20,030-ft pressure altitude. The aircraft was turning to the right to set up the run (note the horizon). The penetration level was again near the cloud top, and the cloud appeared to be growing. Figure 4.8 shows sample 2D–S and PIP imagery. The 2D–S imagery exhibited mainly drizzle droplets with a less pronounced small droplet condensation mode, and the PIP imagery showed drops up to a few hundred microns. Figure 4.9 and Figure 4.10 show the average PSD number concentration and LWC distributions across the run. The composite LWC spectrum is again shown in gray. The average and maximum CDP–2 concentrations were 17 and 46 cm^{-3}, respectively. The offset between the 2D–S and PIP in this case, particularly for the LWC distribution, was larger than other cases, but the reason for this was not further investigated. The condensation and warm rain modes of the composite spectra had nearly equal LWCs, the latter comprising 52 percent of the total. The PSD and IKP2 LWCs were 0.42 and 0.49 gm^{-3}, respectively. The PSD rainfall rate was 1.5 mm/h.

Figure 4.7.—Frame from DC–8 forward video before entry into cloud of 2022-07-27 at –8.6 °C. Red X is approximate location of entry. In-cloud time was 12 s.

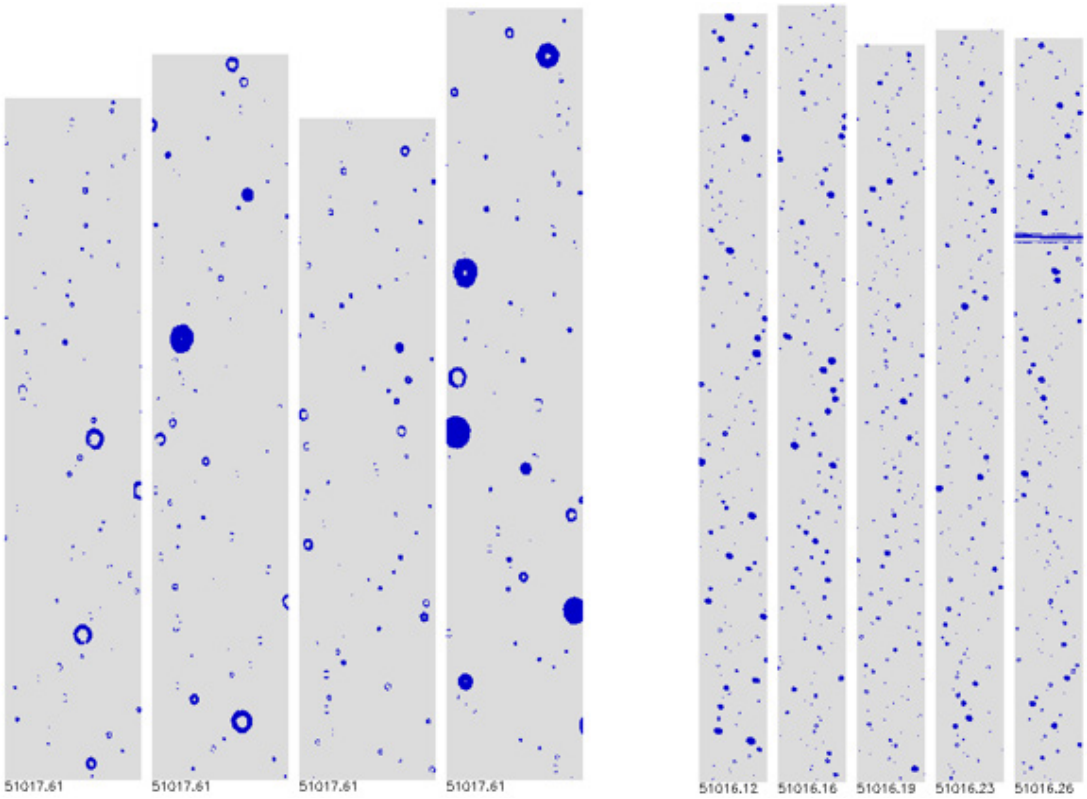

Figure 4.8.—Sample 2D–S (left) and PIP images (right) of droplets from run on 2022-07-27 at –8.6 °C. Width of each 2D–S and PIP image strip is 1,408 µm and 6,400 µm, respectively.

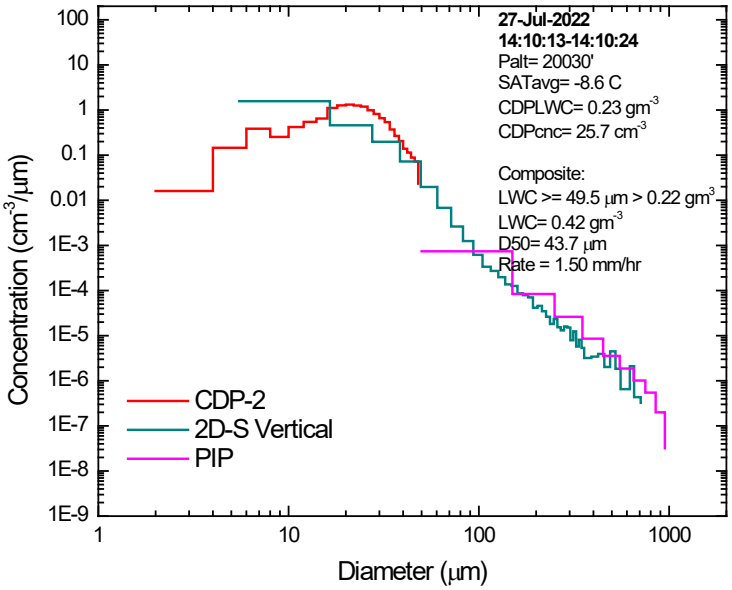

Figure 4.9.—Average PSD for –8.6 °C run on 2022-07-27.

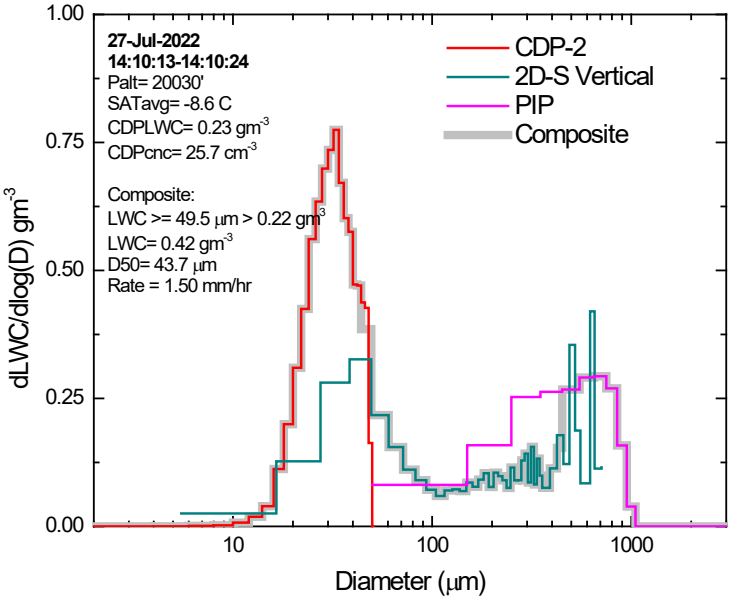

Figure 4.10.—Corresponding LWC distribution for –8.6 °C run on 2022-07-27.

In summary, on this day, coalescence embryos were present at the cloud base at a size adequate to initiate a warm rain process. Substantial warm rain (23.2 mm/h) was observed at 7.4 °C and, to a lesser degree, at –8.6 °C. It is important to note that each level was sampled in a different cloud, so that changes with height cannot be directly interpreted in a Lagrangian sense but may result from cloud-to-cloud variability. Even the location of the run within the cloud, whether through the center or off to one side, could contribute to different results. The most important takeaway is the existence of cloud-base coalescence embryos, likely from giant cloud condensation nuclei (GCCN) in the form of sea-salt aerosol (SSA) that were adequately large to initiate a warm rain process. The existence of warm rain at both altitudes may in fact be due to the influence of these GCCN.

The other runs at –9 °C exhibited mixed-phase characteristics and a switch from the dominance of warm rain to ice processes in precipitation development. The characteristics of the ice production are discussed separately in Section 6.3.3.

4.3 2022-07-10

Only two cloud levels were sampled on this day. Five runs were performed at ~22 °C, and four at about –9 °C (Table 14). The development of warm rain must be inferred from the –9 °C level only. At –9 °C, only one of the four runs was estimated to be liquid-only, and that run was chosen for the following analysis as most suitable for tracking warm rain evolution.

Figure 4.11 shows sample 2D–S imagery at 22.5 °C from one of the cloud base runs. Small images associated with the main condensation mode dominated the imagery. There were also occasional droplet images larger than 44 μm in the frame. There were no useful PIP images. Figure 4.12 shows the average number concentration spectrum. There was negligible LWC above 49.5 μm, but the important point is that the spectrum extended out to at least 77 μm. Coalescence embryos were thus present at sufficient size to initiate the warm rain process.

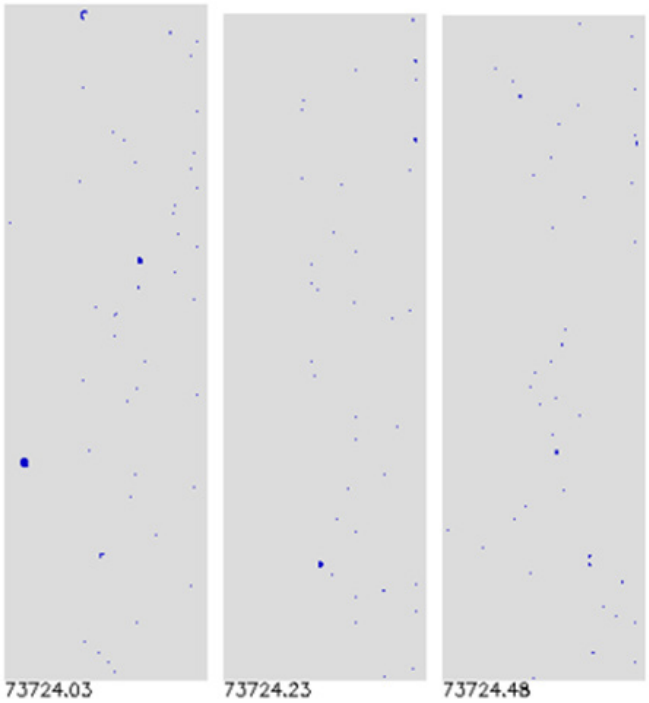

Figure 4.11.—Sample 2D–S OAP images of droplets from cloud base run of 2022-07-10. Width of each image strip is 1,408 μm. Length of cloud run was 32 s.

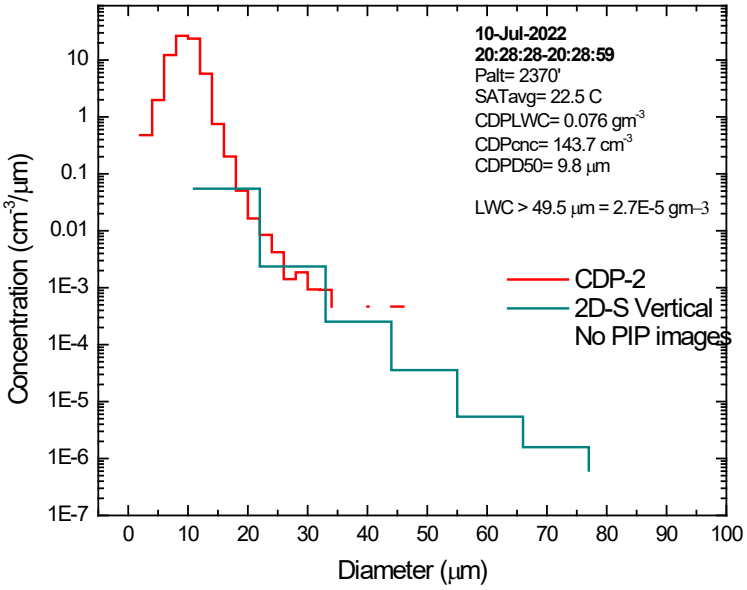

Figure 4.12.—Average PSD across cloud base run on 2022-07-10.

The next measurements are from the sole liquid-only run at –8.4 °C and 19,950-ft pressure altitude. Figure 4.13 shows a frame from the DC–8 forward video camera. Note that the aircraft passed through the edge of the cloud rather than through the center, but reasonably close to the cloud top. Figure 4.14 contains sample 2D–S and PIP imagery during the run. The 2D–S image (left) shows an abundance of small condensation mode particles extending into the drizzle size range and the occasional large drop, up to about 700 µm in the frame. As usual, the PIP probe was not sensitive to the smaller droplets and therefore provided a more selective sampling of the larger particles. The images were mostly round. Close inspection may have shown a few particles with rough perimeters, as might be expected for graupel, but this could also be explained by the coarse resolution of the probe. There are no indications of graupel particles on the 2D–S image, which has much finer resolution. The vast majority of PIP particles are likely water drops. The average and maximum CDP–2 concentrations were 23 and 70.1 cm^{-3} respectively. Figure 4.15 and Figure 4.16 show average number concentration and LWC spectra calculated using SODA–2. The composite LWC spectrum showed the condensation mode at small sizes and a warm rain mode at about 1 mm. The warm rain mode was dominant, with 76 percent of the LWC ≥49.5 µm. The composite PSD and IKP2 TWCs were 0.93 and 1.08 gm^{-3}. The PSD rainfall rate was 13.4 mm/h.

In summary, on this day coalescence embryos were present at cloud base. At –8.4 °C, in a run where ice had not yet formed, warm rain dominated the LWC distribution with a substantial rainfall rate.

Figure 4.13.—Frame from DC–8 forward video before entry into cloud of 2022-07-10 at –8.4 °C. Red X is approximate location of entry. In-cloud time was approximately 15 s.

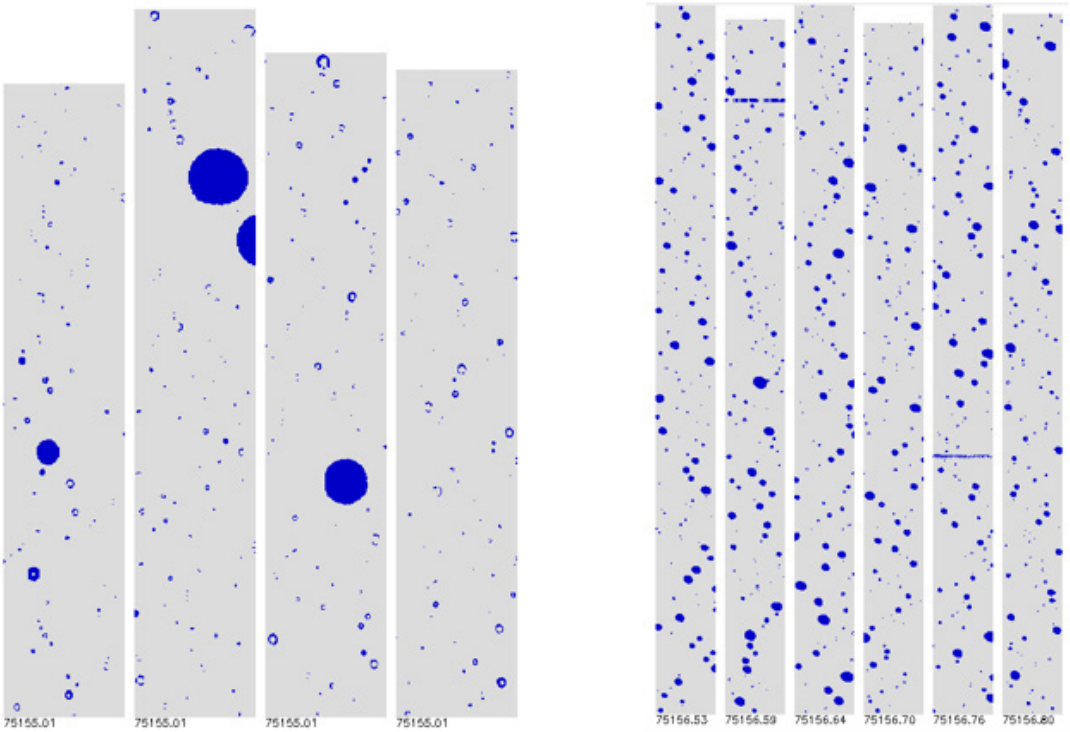

Figure 4.14.—Sample 2D–S (left) and PIP (right) imagery from cloud of 2022-07-10 at approximately –8.4 °C. Width of each 2D–S image strip is 1,408 µm. Width of each PIP image strip is 6,400 µm.

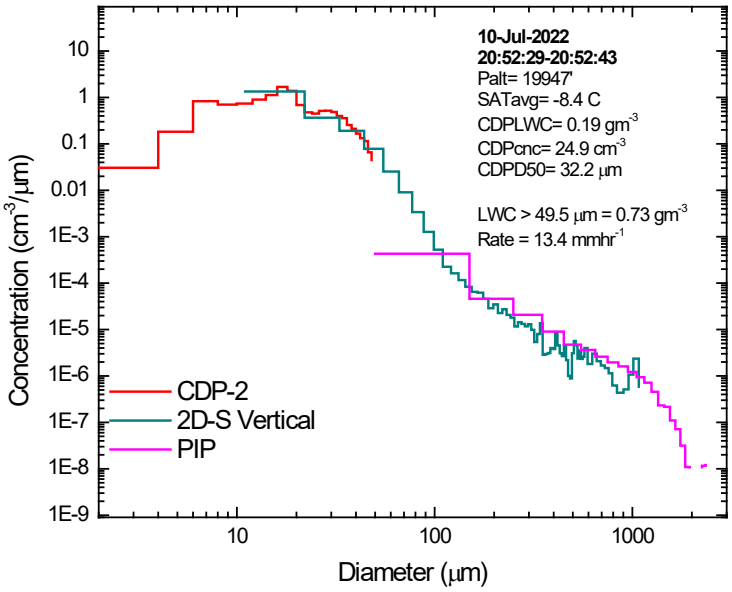

Figure 4.15.—Average PSD number concentrations for –8.4 °C run on 2022-07-10.

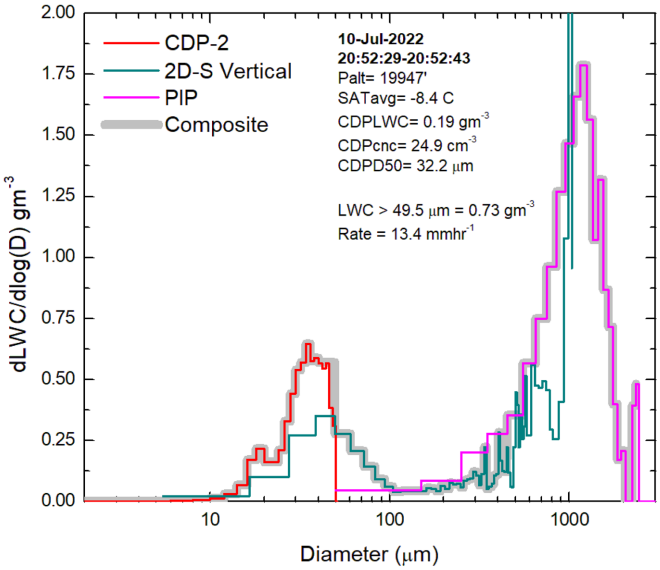

Figure 4.16.—Corresponding LWC distribution for –8.4 °C run on 2022-07-10.

4.4 2022-07-24

Four cloud base runs were performed on this day. Figure 4.17 shows sample particle images from the 2D–S OAP from the 10-s cloud base run starting at about 14:47:12 UTC. The imagery showed a background of very small images from the main condensation mode of the PSD and, for this image block, a single larger particle contributing to the tail of the spectrum. Other 2D–S image buffers showed similar occasional larger particles. Figure 4.18 shows the PSDs from the CDP–2 and 2D–S probes. The estimated LWC from the CDP–2 was about 0.1 gm^{-3}, and the average and maximum 1-s concentrations were 42 and 136 cm^{-3}. There was negligible LWC above 50 µm. Of interest here is the tail of the 2D–S spectrum, which reached 66 µm and confirmed that coalescence embryos were again present at cloud base.

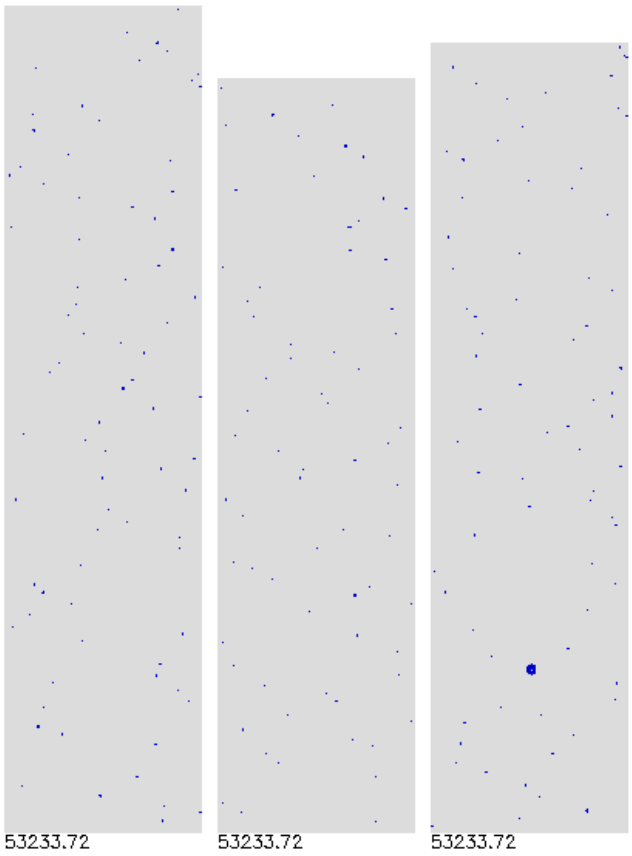

Figure 4.17.—Sample 2D–S OAP images of droplets from cloud base run of 2022-07-24. Width of each image strip is 1,408 µm.

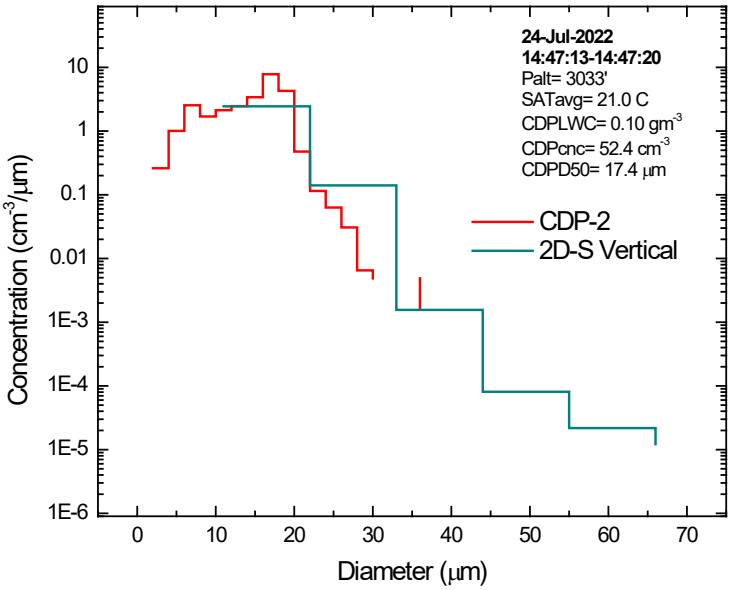

Figure 4.18.—Average PSD across cloud base run on 2022-07-24.

Two clouds were sampled this day at about 5 °C. Figure 4.19 shows the cloud discussed here, as seen on the DC–8 forward video. The red X marks the approximate location of the DC–8 entry into cloud. Figure 4.20 shows sample imagery from the 2D–S and PIP OAPs. Unfortunately, the PIP imagery was unusable due to apparent fogging. The 2D–S imagery was good and showed well-developed drizzle and warm rain, with drops visible in this image frame to at least 600 µm. Figure 4.21 and Figure 4.22 show the number concentration and LWC spectra, respectively. The CDP–2 average and maximum concentrations were about 21 and 71 cm^{-3}, respectively, about half of that observed in the cloud base run. The average CDP–2 LWC was 0.30 gm^{-3}. The tail of the composite LWC spectrum displayed increasing noise approaching the maximum nominal size of the 2D–S, where the contribution of LWC appeared to be still rising; the analysis was unable to close the LWC spectrum due to the failure of the PIP probe. Still, some estimates were made. The PSD average LWC was at least 1.24 gm^{-3}. The IKP2 TWC was estimated at 1.94 gm^{-3}, but accuracy was low due to the background water vapor (BWV) level being around 7 gm^{-3}. The rainfall rate was estimated to be at least 16 mm/h.

Figure 4.19.—Frame from DC–8 forward video before entry into cloud of 2022-07-24 at approximately 4.7 °C. Red X is approximate location of entry.

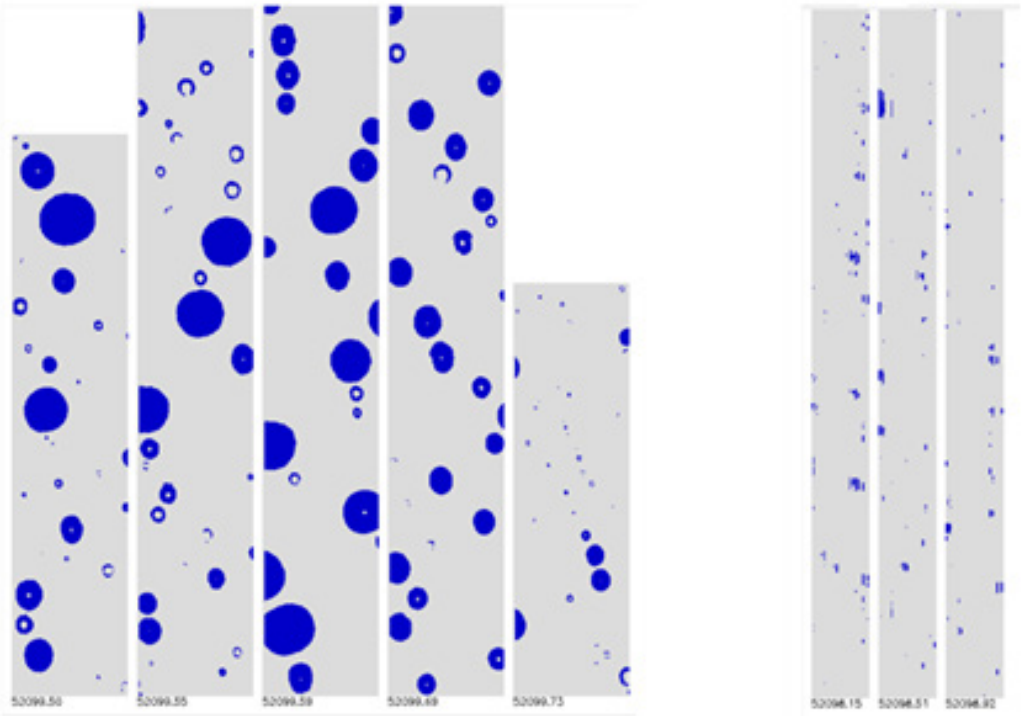

Figure 4.20.—Sample 2D–S (left) and PIP (right) imagery from cloud of 2022-07-24 at approximately 4.7 °C. Width of each 2D–S image strip is 1,408 µm. Width of each PIP image strip is 6,400 µm.

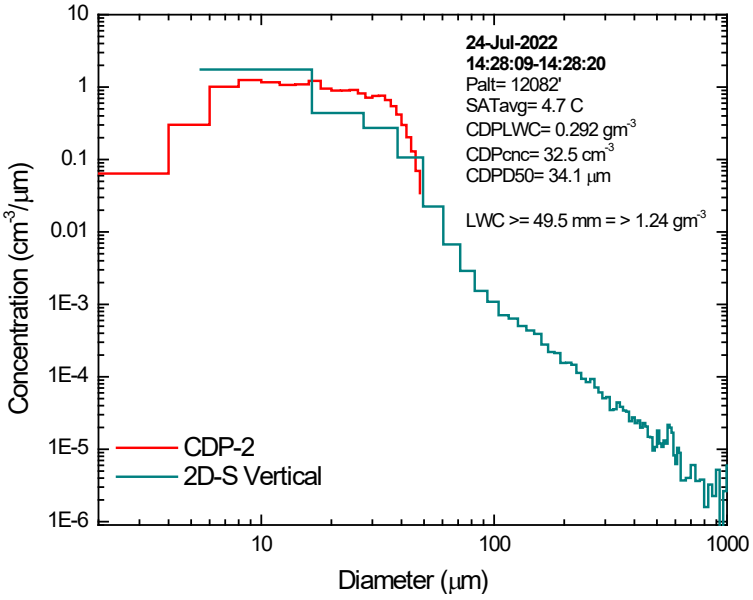

Figure 4.21.—PSD for 4.7 °C run on 2022-07-24.

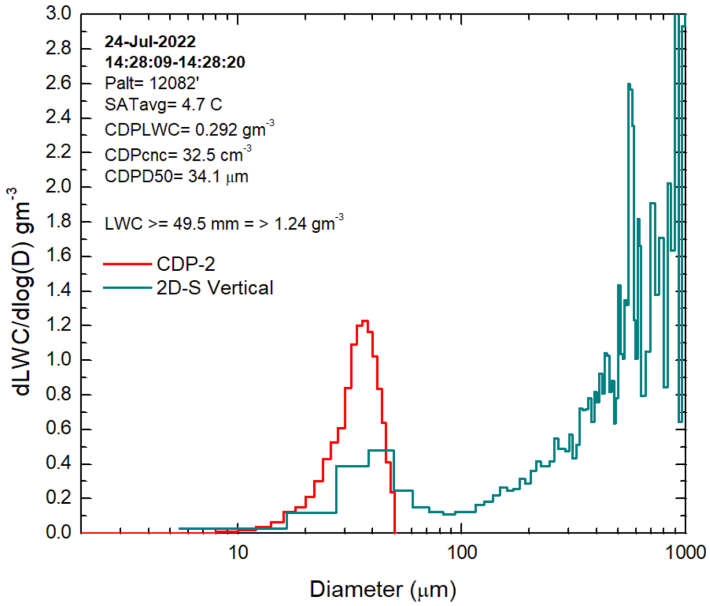

Figure 4.22.—Corresponding LWC distribution for 4.7 °C run on 2022-07-24.

All five cloud runs at about –9.5 °C were mixed-phase or glaciated, so no estimates of warm rain could be produced.

In summary, on this day coalescence embryos were present at cloud base, and well-developed warm rain was present at 4.7 °C. The other two unanalyzed runs at 4.7 °C also showed warm rain by visual inspection of 2D–S imagery.

4.5 2022-07-26

Five runs were performed at approximately 14 °C, four at 4 °C, five at about –9 °C, and six at approximately –19 °C (Table 14). No cloud base runs were performed. This section will examine analysis of one run at 13.7 °C, one at 4 °C, and one at –9 °C. At –9 °C, only one of the five runs was estimated to be liquid-only, and that run was chosen for the following analysis as the most suitable for tracking warm rain evolution.

Figure 4.23 shows a frame from the DC–8 forward video before entry into the cloud at 13.7 °C. In this case, the distance below the top may have been greater than in typical runs, and it should be considered that the measurements could reflect falling particles from a colder temperature level than usual. Figure 4.24 shows sample 2D–S and PIP imagery from this run. The 2D–S imagery was dominated by small droplets in the main condensation mode, which also dominated the probe active-sampling time and made detection of large particles in a small number of image frames more difficult. In Figure 4.24, the largest 2D–S image is approximately 150 μm. The PIP imagery was unfortunately compromised by apparent fogging, but it did show some very large drops (“giant”) reaching about 5 mm, similar to the observations of Hawaiian clouds during the Joint Hawaiian Warm Rain Project (JHWRP) and the Hawaii Rainfall Project (HaRP); see Section 6.2.3. Figure 4.25 and Figure 4.26 show the PSD and normalized LWC spectra. The CDP–2 average and maximum concentrations were ~80 and 170 cm^{-3}, respectively. Note that in spite of the questionable PIP imagery, the PSD looked continuous, and the LWC spectra looked reasonable, apart from the abrupt cutoff of the spectrum at about 4 mm. In this case, the integrated PSD average LWC was 1.05 gm^{-3}. The IKP2 data were not estimated due to the very high BWV of approximately 12 gm^{-3}. The PSD rainfall rate was about 3 mm/h. The condensation mode still dominated the LWC spectrum, but the development of the warm rain mode was unmistakable.

Figure 4.23.—Frame from DC–8 forward video before entry into cloud of 2022-07-26 at 13.7 °C. Red X is approximate location of entry. In-cloud time was 29 s.

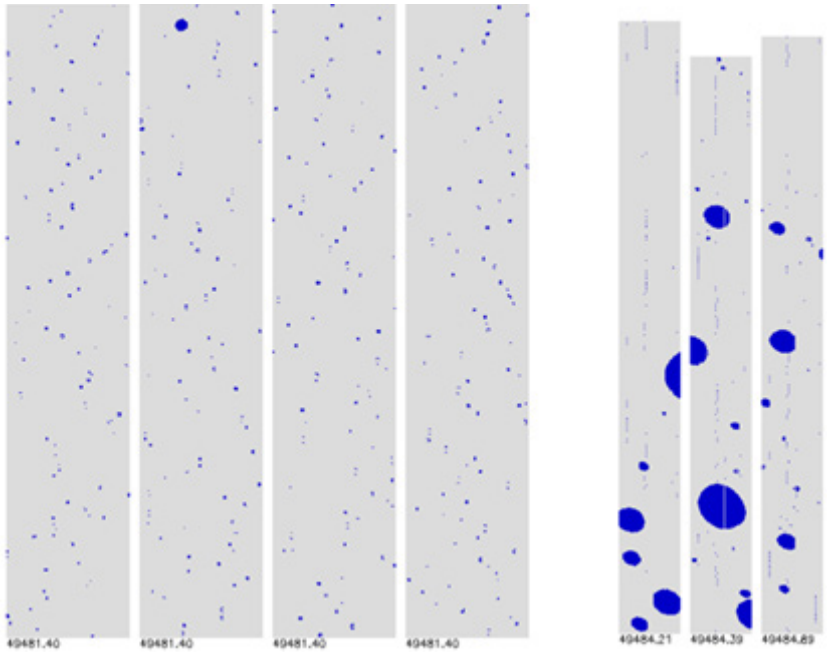

Figure 4.24.—Sample 2D–S (left) and PIP (right) imagery from cloud of 2022-07-26 at approximately 13.7 °C. Width of each 2D–S image strip is 1,408 µm. Width of each PIP image strip is 6,400 µm. PIP imagery shows evidence of fogging.

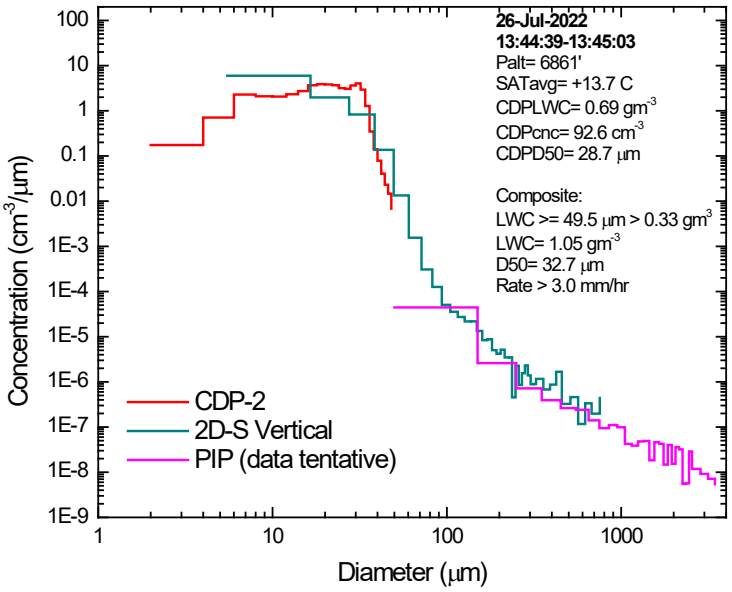

Figure 4.25.—PSD for 13.7 °C run of cloud on 2022-07-26.

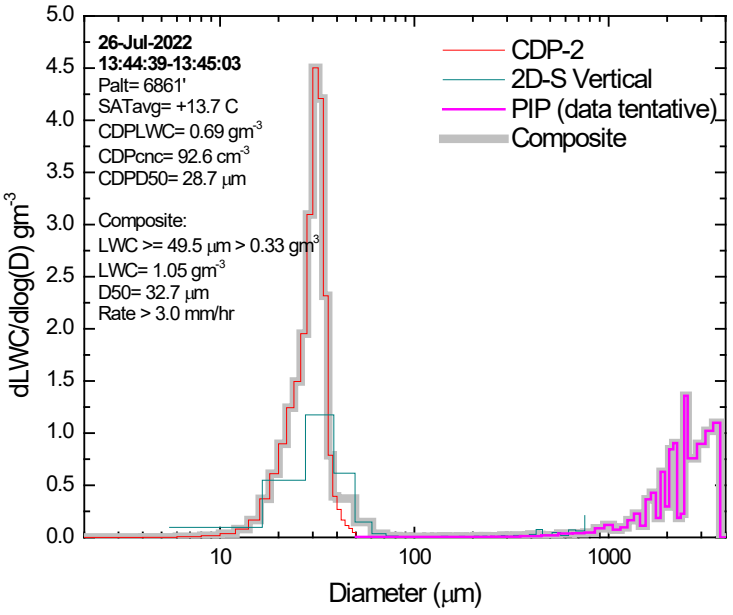

Figure 4.26.—Corresponding LWC distribution for 13.7 °C run of cloud on 2022-07-26.

The next level sampled was approximately 3.8 °C. Figure 4.27 shows a frame from the DC–8 forward video before entry into the cloud. Figure 4.28 shows sample 2D–S and PIP imagery. The PIP was unfortunately quite fogged, and data could not be accurately processed, but it could be estimated visually that drop sizes reached about 3 mm. The 2D–S showed a small droplet condensation mode with a drizzle background, with drops in the frame reaching about 900 µm. Figure 4.29 and Figure 4.30 show the average number concentrations and normalized LWC spectra for this cloud run. Although the PIP PSD calculations are shown, they are unreliable. The average and maximum CDP concentrations were about 22 and 77 cm^{-3}. The 2D–S LWC contribution was still climbing at its maximum drop size, and thus the LWC spectrum was not closed without the PIP. Therefore, assuming that PIP would have added additional LWC at the tail, one can conclude that the average PSD LWC was at least the 2.32 gm^{-3} contributed by the CDP and 2D–S. The LWC estimated by the IKP2 was 2.79 gm^{-3}. The rainfall rate was at least 9.8 mm/h. So, by 3.8 °C, the cloud LWC was now dominated by the warm rain mode, and the rainfall rate was substantial.

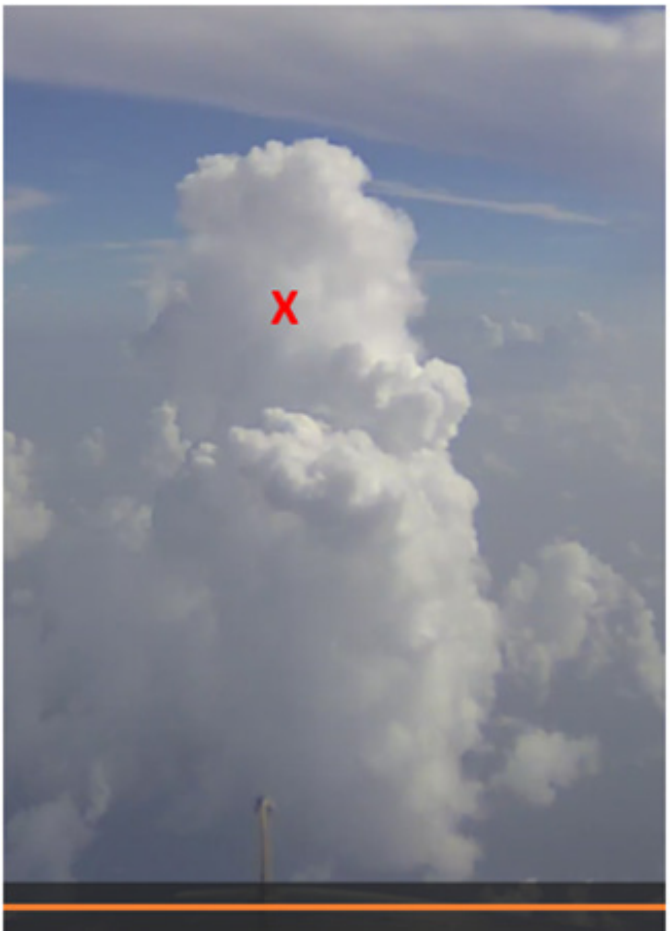

Figure 4.27.—Frame from DC–8 forward video before entry into cloud of 2022-07-26 at 3.8 °C. Red X is approximate location of entry. In-cloud time was 10 s.

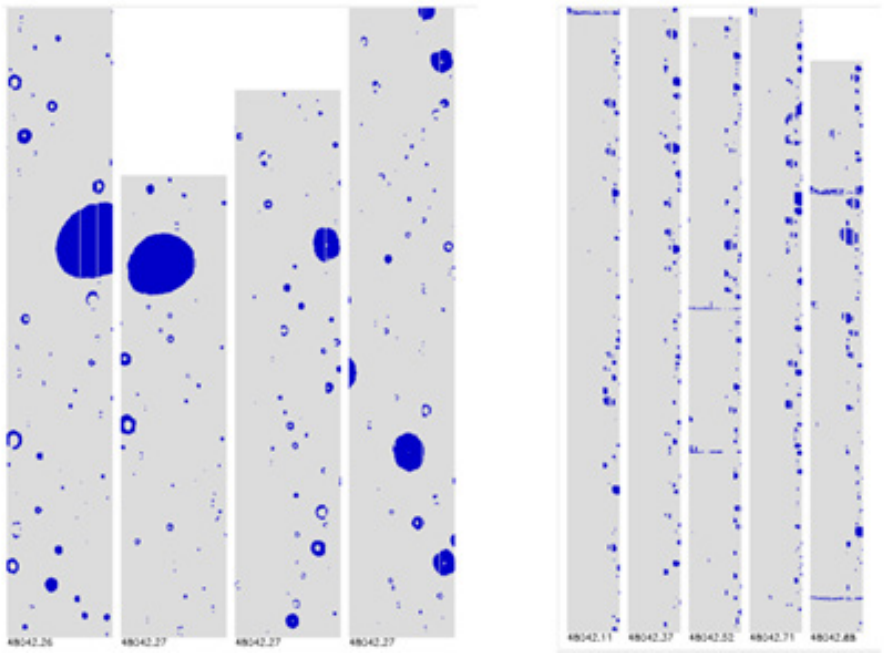

Figure 4.28.—Sample 2D–S (left) and PIP (right) imagery from cloud of 2022-07-26 at approximately 3.8 °C. Width of each 2D–S image strip is 1,408 µm. Width of each PIP image strip is 6,400 µm. PIP imagery shows evidence of fogging.

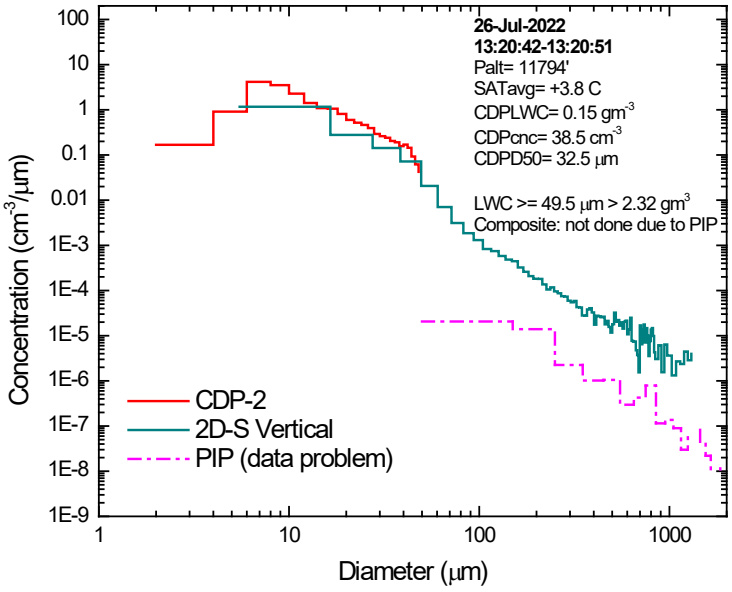

Figure 4.29.—PSD for 3.8 °C run on 2022-07-26. PIP was fogged.

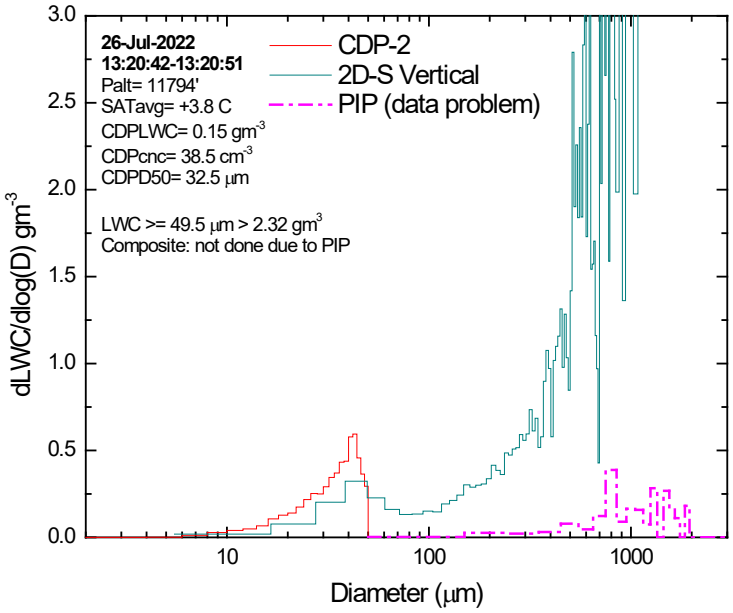

Figure 4.30.—Corresponding LWC distribution for 3.8 °C run of cloud on 2022-07-26. PIP was fogged.

The DC–8 also sampled the approximate –9 °C level, where one run at –9.8 °C exhibited what was concluded to be liquid-only conditions; this run is described here. Figure 4.31 shows a frame from the DC–8 before entry into the cloud. Note that the aircraft did not pass through the cloud in the background of the frame. Figure 4.32 shows sample 2D–S and PIP imagery from the run. The 2D–S imagery was good, but the PIP imagery again showed signs of fogging or misalignment; for example, note the gaps in particles and the lack of small particles on the left side of the image frame. The 2D–S imagery showed small droplets in the condensation mode, drizzle, and large drops to about 900 µm. Even though this run was at –9.8 °C, there was no evidence of significant ice presence in the 2D–S imagery. Figure 4.33 and Figure 4.34 show the average number concentration and normalized LWC spectrum for the run, respectively. The average and maximum 1-s CDP–2 concentrations were 37 and 105 cm^{-3}, respectively. Again, the combination of the CDP–2 and 2D–S did not close the LWC spectrum. The flawed PIP spectrum, included in the figures as a dotted line, provided a LWC spectrum lower than but parallel to the 2D–S. If it were to be believed, it would suggest that the LWC spectrum closed at a little over 2 mm. Nevertheless, it can be stated that the warm rain mode dominated the LWC spectrum. The average unclosed PSD LWC was at least 0.94 gm^{-3}, and the IKP2 average TWC estimate was 1.77 gm^{-3}. The rainfall rate was at least 10.6 mm/h.

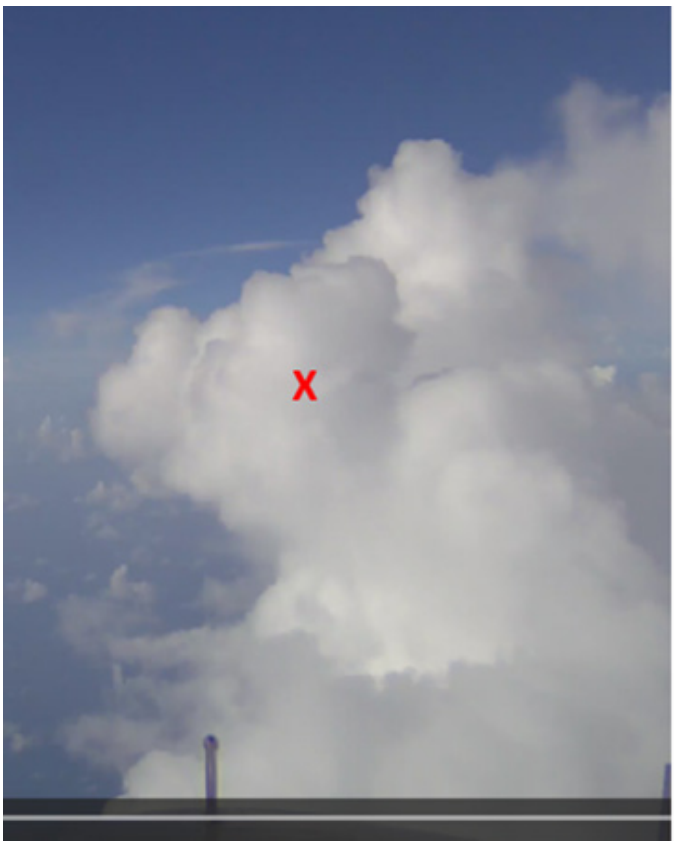

Figure 4.31.—Frame from DC–8 forward video before entry into cloud of 2022-07-26 at approximately –9.8 °C. Red X is approximate location of entry. In-cloud time was 16 s.

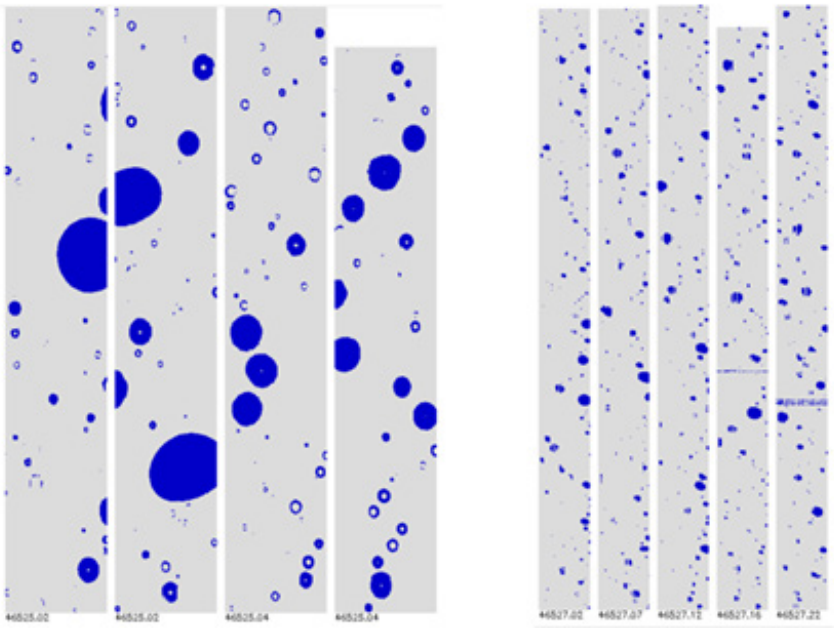

Figure 4.32.—Sample 2D–S (left) and PIP (right) imagery from cloud of 2022-07-26 at approximately –9.8 °C. Width of each 2D–S image strip is 1,408 µm. Width of each PIP image strip is 6,400 µm. PIP was fogged.

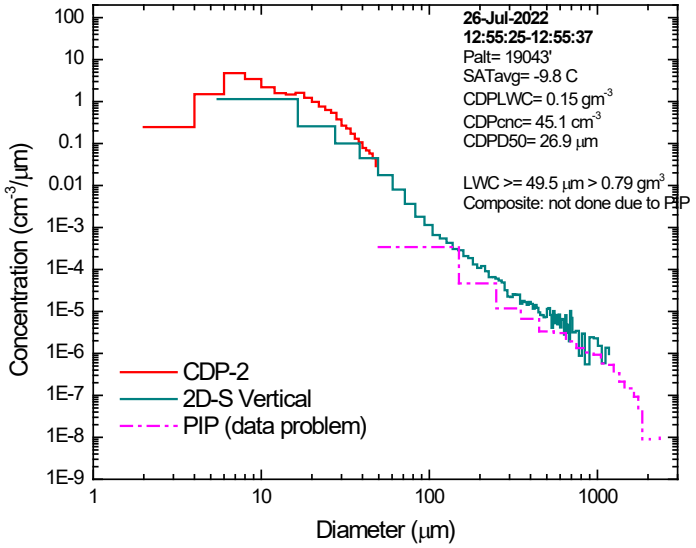

Figure 4.33.—PSD for –9.8 °C liquid-only run on 2022-07-26. PIP was fogged.

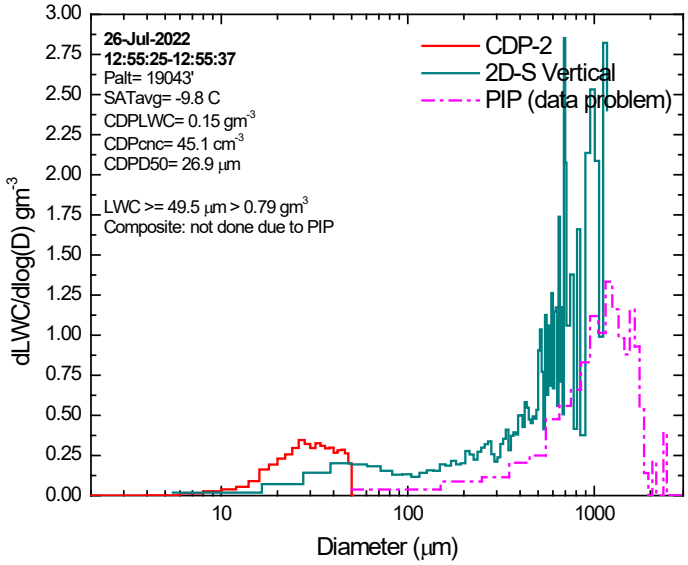

Figure 4.34.—Corresponding LWC distribution for –9.8 °C liquid-only run on 2022-07-26. PIP was fogged.

4.6 2022-07-30

The highest below-cloud-base aerosol measurements of the campaign were taken on this day, with PCASP and CCN averages of 840 and 1,239 cm^{-3}, respectively. Five cloud base runs, four runs at about 14 °C, and five runs at about –9.9 °C were performed. One of these runs at –9 °C was estimated to be liquid-only and has been chosen for the following analysis.

Figure 4.35 shows sample 2D–S probe imagery for a cloud base run on 2022-07-30. The imagery was highly dominated by small droplets, with the occasional larger drop to about 55 µm in these frames. This was likely a reflection of the higher number of aerosols activating high concentrations of small droplets. Figure 4.36 contains the average PSD number concentration for a cloud base run at 2,920-ft pressure altitude and 21.2 °C. The spectrum extended to about 66 µm. Average and maximum cloud droplet concentrations were 423 and 715 cm^{-3}, respectively, the highest of all cloud base runs in HIWC–2022.

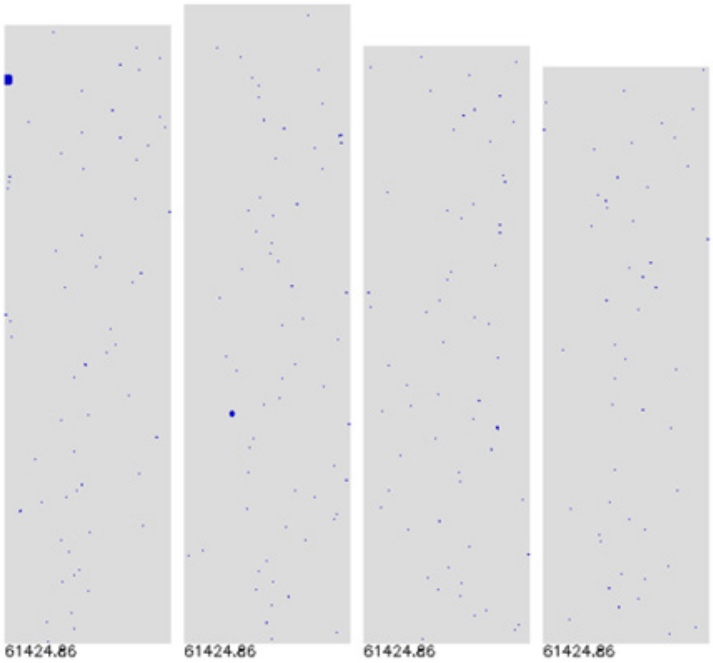

Figure 4.35.—Sample 2D–S OAP images of droplets from cloud base run of 2022-07-30 at 21.2 °C. Width of each image strip is 1,408 µm.

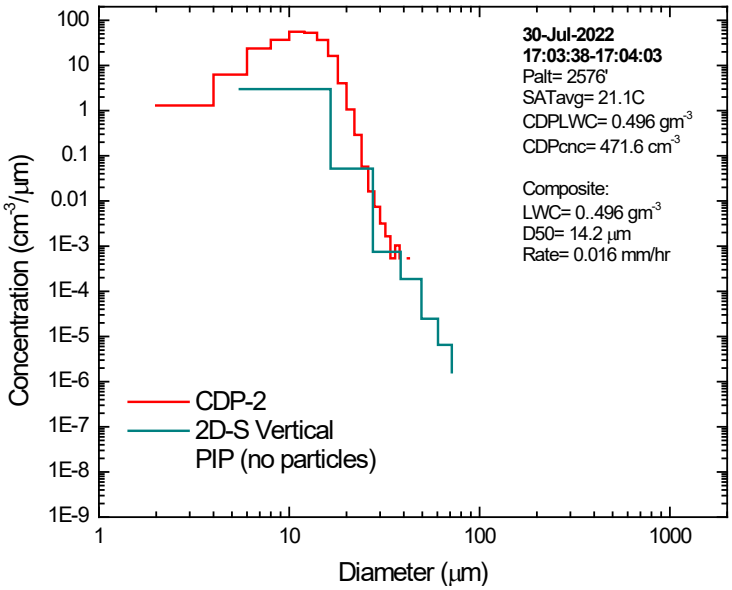

Figure 4.36.—Average PSD across cloud base run on 2022-07-30.

A DC–8 forward video frame before entry into a cloud at 14.6 °C and 7,012-ft pressure altitude is shown in Figure 4.37. Despite the general overcast that was evident before entry and after exit from the cloud, the probes did not detect any particles that might have been falling from aloft. Figure 4.38 shows sample 2D–S and PIP probe imagery. The 2D–S imagery was again dominated by small particles, and only occasional large drops were visible. The frames for the PIP probe, which was sensitive to only the larger drops, showed particles up to a few hundred microns.

Figure 4.37.—Frame from DC–8 forward video before entry into cloud of 2022-07-30 at 14.6 °C. Red X is approximate location of entry. In-cloud time was 24 s.

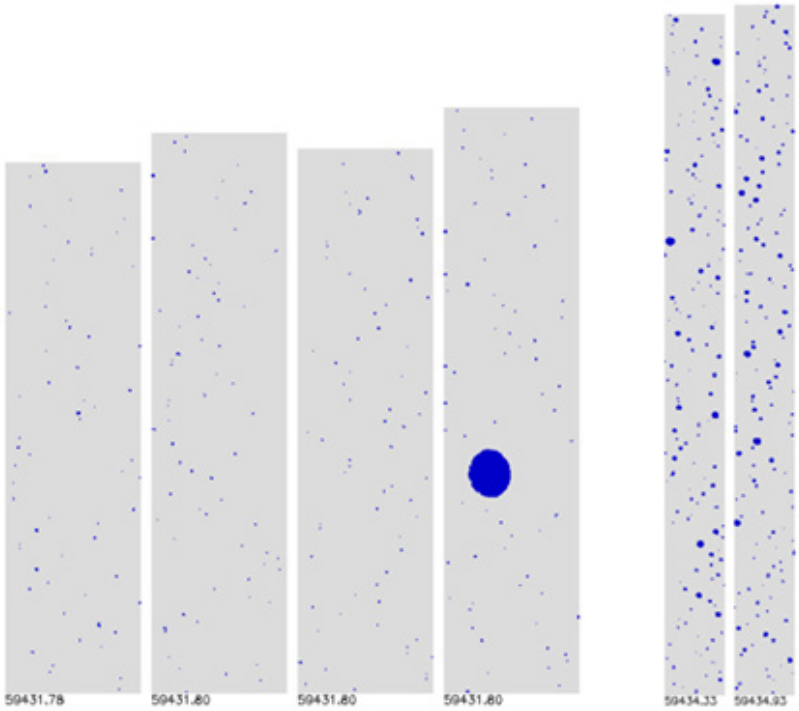

Figure 4.38.—Sample 2D–S (left) and PIP (right) imagery from cloud of 2022-07-30 at approximately 14.6 °C. Width of each 2D–S image strip is 1,408 µm. Width of each PIP image strip is 6,400 µm.

Figure 4.39 and Figure 4.40 show the average PSD number concentrations and LWC distribution for this case. The condensation mode completely dominated, with little evidence of a significant warm rain mode. Note the PIP data in 4.40 is nearly 0. The average and maximum CDP–2 number concentrations were 396 and 790 cm^{-3}, the latter even higher than at cloud base. The PSD LWC was 0.84 gm^{-3}, of which only about 0.04 gm^{-3} was at sizes above 49.5 µm. The IKP2 TWC was not accurate due to a BWV value of 13 gm^{-3}. The PSD rainfall rate was 0.38 mm/h.

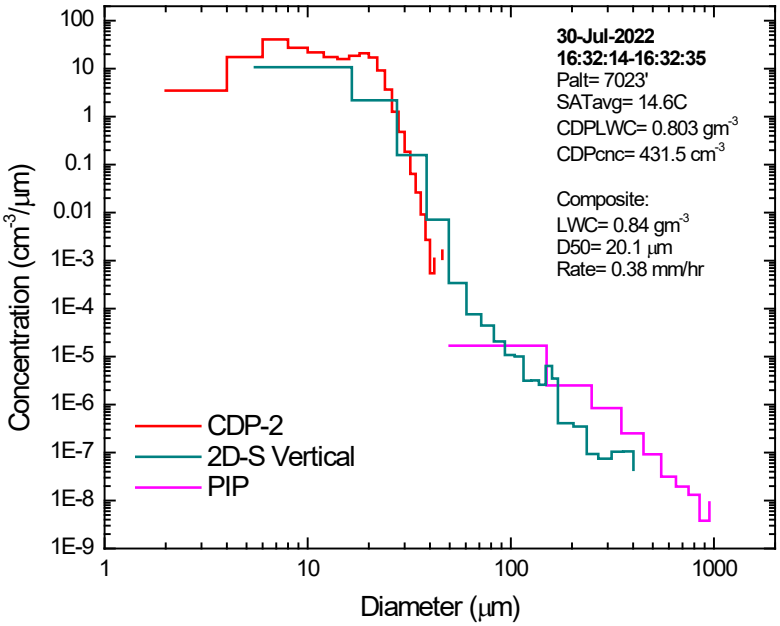

Figure 4.39.—PSD for 14.6 °C run on 2022-07-30.

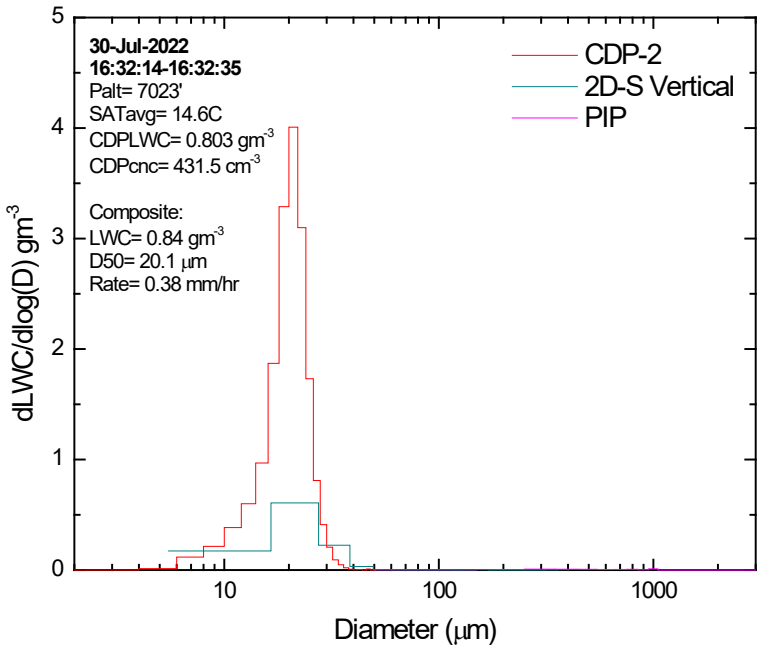

Figure 4.40.—Corresponding LWC distribution for 14.6 °C run on 2022-07-30.

A second example at 14.6 °C is given here as another example with an abrupt warm rain mode large-drop cutoff (see also 2022-07-26, 13.7 °C). The forward video camera frame is shown in Figure 4.41. The sample 2D–S and PIP probe particle imagery is shown in Figure 4.42. As in the previous 14.5 °C run, the 2D–S imagery was highly dominated by small droplets in the condensation mode with an occasional large drop. The PIP imagery showed larger drops reaching about 2 mm in the frame displayed. The average PSD number concentration and LWC distributions are shown in Figure 4.43 and Figure 4.44. The average and maximum CDP–2 concentrations were 124 and 385 cm^{-3}, respectively, about half of the previous 14.6 °C run. The warm rain mode was much more developed, with about 23 percent of the LWC at sizes larger than 49.5 μm. The PSD TWC was 0.34 gm^{-3}, less than half of the previous 14.5 °C run. The rainfall rate was 1.22 mm/h. Note the very abrupt cutoff of the PIP LWC spectrum in Figure 4.44. This is an interesting observation. It is speculated there that such a spectrum may be explained in the growth mode of the largest particles, as per the giant drops in the Hawaiian clouds of Rauber et al. (Ref. 67).

Figure 4.41.—Frame from DC–8 forward video before entry into cloud of 2022-07-30, second example at 14.6 °C. Red X is approximate location of entry. In-cloud time was 22 s.

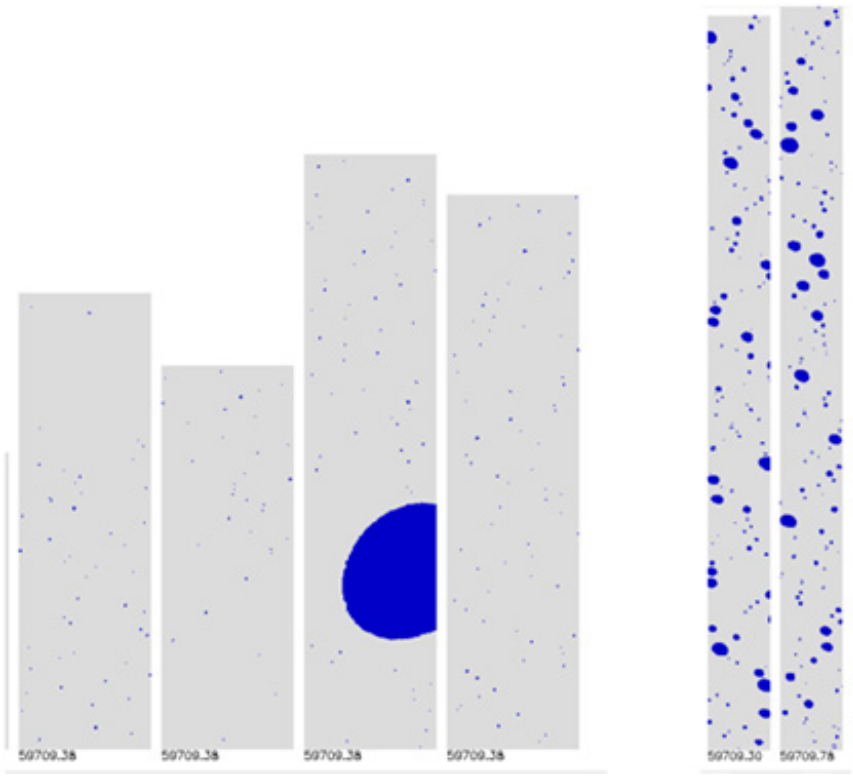

Figure 4.42.—Sample 2D–S (left) and PIP (right) imagery from cloud of 2022-07-30, second example at approximately 14.6 °C. Width of each 2D–S image strip is 1,408 µm. Width of each PIP image strip is 6,400 µm.

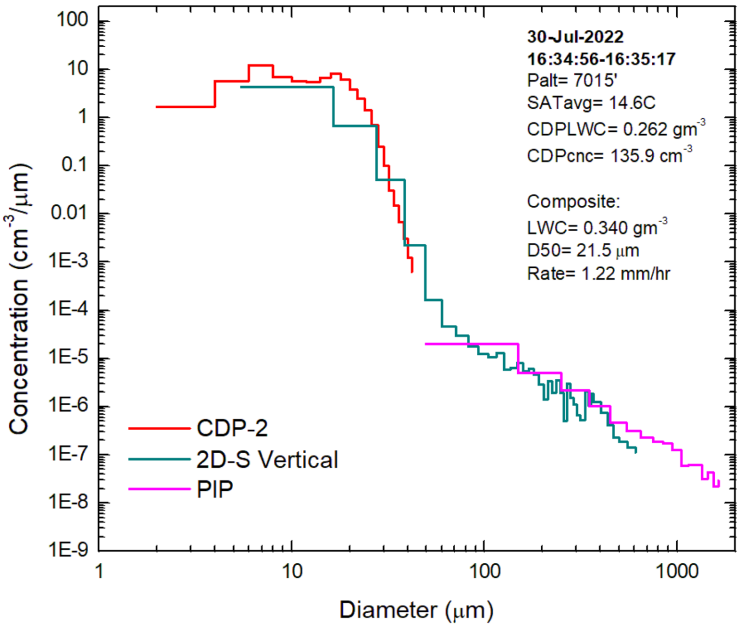

Figure 4.43.—PSD for second example of 14.6 °C run on 2022-07-30.

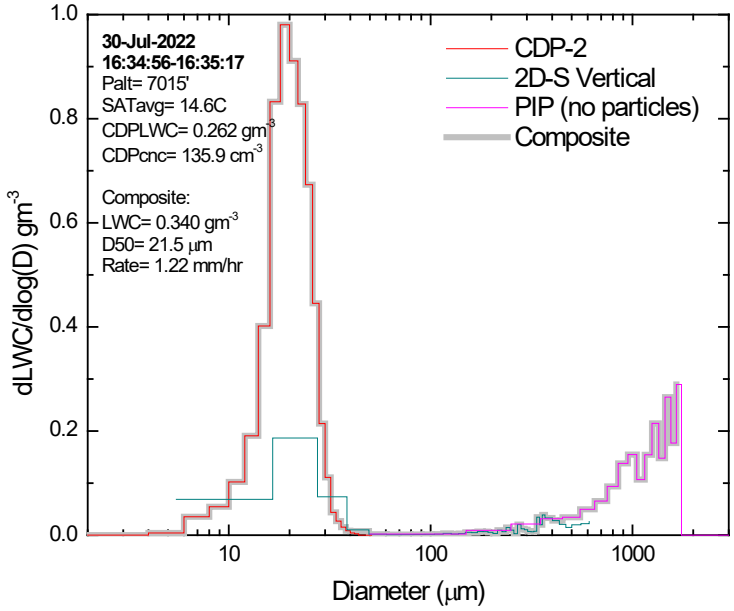

Figure 4.44.—Corresponding LWC distribution for second example of 14.6 °C run on 2022-07-30.

Figure 4.45 shows a DC–8 forward video frame before entry into a cloud at –9.0 °C. The aircraft was in a right turn lining up for the run. Figure 4.46 shows sample 2D–S and PIP imagery. The 2D–S imagery again showed an abundance of small droplets and a population of much larger drops. No significant ice particles were observed. The PIP imagery shows drops to a few hundred microns in the frame shown. It was concluded that there was an insignificant amount of ice in the cloud. Figure 4.47 and Figure 4.48 show the average PSD number concentration and LWC distributions. The LWC distributions exhibited significant condensation and warm rain modes. The CDP–2 average and maximum concentrations were 32 and 114 cm^{-3}, respectively. Seventy-two percent of the LWC was above 49.5 µm. As in most cases, the CDP–2 and 2D–S did not close the LWC spectrum, and the addition of the PIP was required to do so. The PSD and IKP2 average LWCs were 0.62 and 0.73 gm^{-3}, respectively. The rainfall rate was 6.3 mm/h.

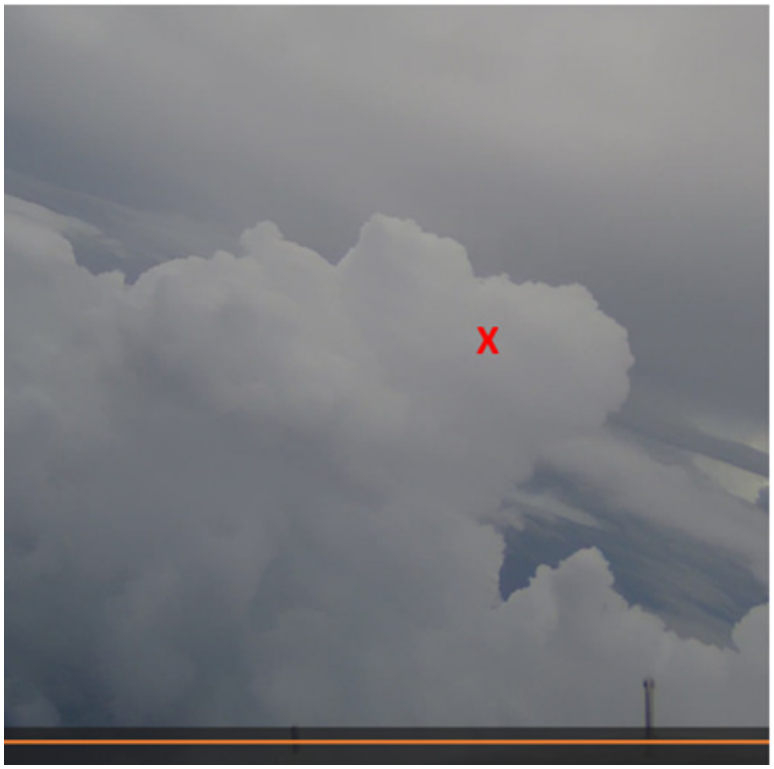

Figure 4.45.—Frame from DC–8 forward video before entry into cloud of 2022-07-30 at –9.0 °C. Red X is approximate location of entry. In-cloud time was 15 s.

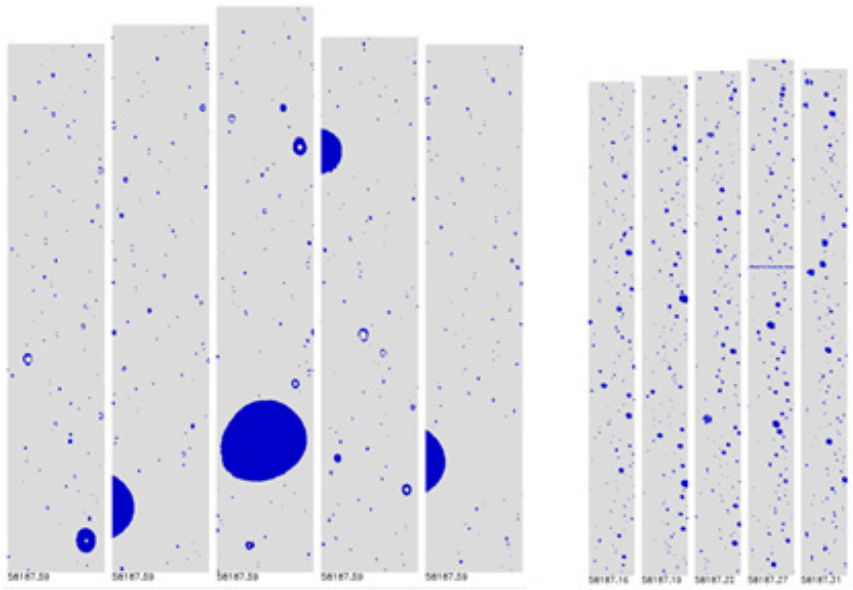

Figure 4.46.—Sample 2D–S (left) and PIP (right) imagery from cloud of 2022-07-30 at approximately –9.0 °C. Width of each 2D–S image strip is 1,408 µm. Width of each PIP image strip is 6,400 µm.

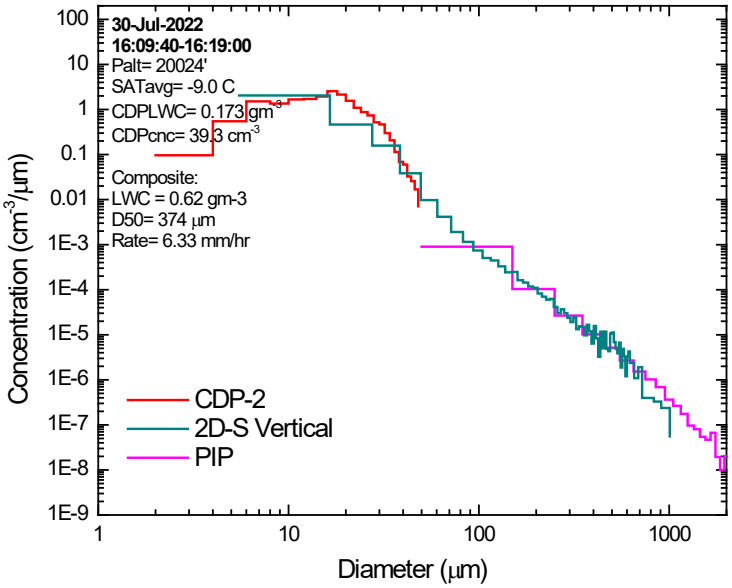

Figure 4.47.—PSD for –9.0 °C run on 2022-07-30.

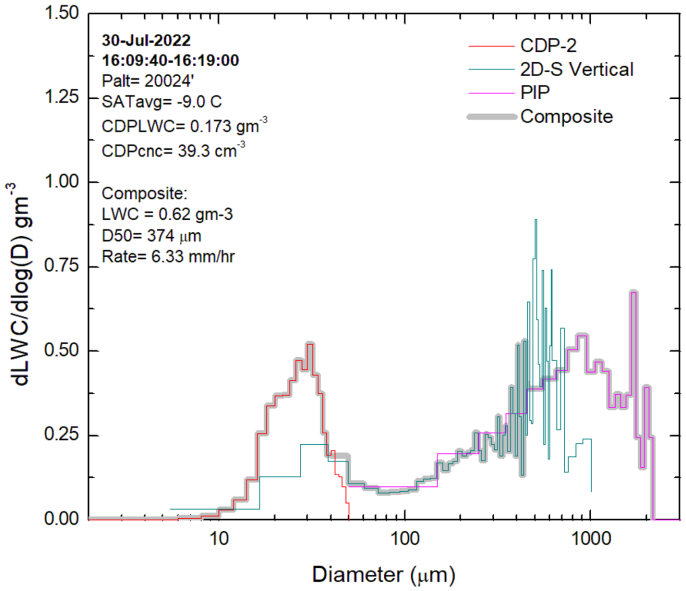

Figure 4.48.—Corresponding LWC distribution for –9.0 °C run on 2022-07-30.

In summary, this was the only day in which cloud base aerosol concentration were characterized as high, with average below-base PCASP and CCN concentrations of 840 and 1,239 cm^{-3}, respectively. Cloud droplet concentrations were also the highest measured during the campaign, reaching 1-s maxima of 715 and 790 cm^{-3} at 21.2 and 14.6 °C, respectively. The cloud base observations did reveal some coalescence embryos up to about 66 µm, and very limited warm rain development by the 14 °C level for one run and more pronounced development in the other run described. However, by –9 °C, a well-developed warm rain process was observed, with the majority of the LWC at sizes larger than 49.5 µm in the one liquid-only run at this temperature level. This case also exhibited a sharp cutoff in the warm rain LWC distribution for one of the two run analyses at 14 °C. It is notable that warm rain developed

significantly between 14 and –9 °C. It is unfortunate that the 4 °C level, where warm rain was always observed in other cases, was not sampled in this case. One can conclude that there was definitely an effect of the higher aerosol concentration in the lower level of the clouds, in terms of concentrating the LWC distribution to small sizes. Regardless, coalescence embryos were still present, and warm rain developed, perhaps at a higher level in clouds. By the –9 °C level, cloud droplet concentrations were relatively low, and warm rain was active and substantial.

References

1. Lawson, R.P.; Angus, L.J.; and Heymsfield, A.J.: Cloud Particle Measurements in Thunderstorm Anvils and Possible Weather Threat to Aviation. J. Aircr., vol. 35, no. 1, 1998, pp. 113–121. https://doi.org/10.2514/2.2268 Accessed Dec. 31, 2024.
2. Mason, J.G.; Strapp, J.W.; and Chow, P.: The Ice Particle Threat to Engines in Flight. AIAA 2006–206, 2006. https://arc.aiaa.org/doi/10.2514/6.2006-206 Accessed Dec. 31, 2024.
3. Grzych, M.L.; and Mason, J.G.: Weather Conditions Associated With Jet Engine Power Loss and Damage Due To Ingestion of Ice Particles: What We've Learned Through 2009. Presented at the American Meteorological Society Meeting, Atlanta, GA, 2010. https://ams.confex.com/ams/90annual/webprogram/Paper165923.html Accessed Sept. 17, 2024.
4. Mason, J.; and Grzych, M.: The Challenges Identifying Weather Associated With Jet Engine Ice Crystal Icing. SAE Technical Paper 2011–38–0094, 2011.
5. Bravin, M.; Strapp, J.; and Mason, J.: An Investigation Into Location and Convective Lifecycle Trends in an Ice Crystal Icing Engine Event Database. SAE Technical Paper 2015–01–2130, 2015.
6. Bravin, M.; and Strapp, J.: A Continuing Investigation of Diurnal and Location Trends in an Ice Crystal Icing Engine Event Database. SAE Int. J. Adv. Curr. Prac. Mobil. (SAE Technical Paper 2019–01–1964), vol. 2, no. 1, 2019, pp. 90–105.
7. Duviver, E.: High Altitude Icing Environment. Presented at the International Air Safety & Climate Change Conference (IASCC) 2010, pp. 8–9. https://www.easa.europa.eu/en/newsroom-and-events/events/international-air-safety-climate-change-conference-iascc-2010 Accessed Sept. 17, 2024.
8. National Transportation Safety Board: Northwest A330 Airspeed Anomaly in Cruise. NTSB DCA09IA064, 2011. https://data.ntsb.gov/Docket?ProjectID=74203 Accessed Sept. 17, 2024.
9. Bureau d'Enquetes et d'Analyses pour la securite de l'aviation civile: Final Report on the accident on 1st June 2009 to the Airbus A330-203 registered F-GZCP operated by Air France flight AF 447 Rio de Janeiro – Paris. 2012. https://www.bea.aero/docspa/2009/f-cp090601.en/pdf/f-cp090601.en.pdf Accessed Sept. 17, 2024.
10. Mazzawy, R.S.: Technical Compendium From Meetings of the Engine Harmonization Working Group, Revised. DOT/FAA/AR–09/13, R1, 2014.
11. Mazzawy, R.S.; and Strapp J.W.: Appendix D—An Interim Icing Envelope. SAE Transactions, vol. 116, 2007, pp. 634–642.
12. Strapp, J.W., et al.: The High Ice Water Content Study of Deep Convective Clouds: Report on Science and Technical Plan. DOT/FAA/TC–14/31, 2016. https://www.tc.faa.gov/its/worldpac/techrpt/tc14-31.pdf Accessed June 17, 2024.
13. Leroy, D., et al.: Ice Crystal Sizes in High Ice Water Content Clouds. Part I: On the Computation of Median Mass Diameter From In Situ Measurements. J. Atmos. Ocean. Technol., vol. 33, 2016, pp. 2461–2476. https://dx.doi.org/10.1175/JTECH-D-15-0151.1 Accessed Dec. 31, 2024.
14. Leroy, D., et al.: Ice Crystal Sizes in High Ice Water Content Clouds. Part II: Statistics of Mass Diameter Percentiles in Tropical Convection Observed During the HAIC/HIWC Project. J. Atmos. Ocean. Technol., vol. 34, 2017, pp. 117–136. https://doi.org/10.1175/JTECH-D-15-0246.1 Accessed Dec. 31, 2024.
15. Protat, A., et al.: The Measured Relationship Between Ice Water Content and Cloud Radar Reflectivity in Tropical Convective Clouds. J. Appl. Meteor. Climatol., vol. 55, 2016, pp. 1707–1729

16. Wolde, M., et al.: Characterization of the Pilot X-Band Radar Responses to the HIWC Environment During the Cayenne HAIC–HIWC 2015 Campaign. AIAA 2016–4201, 2016. https://doi.org/10.2514/6.2016-4201 Accessed Dec. 31, 2024.
17. Ratvasky, T.P., et al.: Summary of the High Ice Water Content (HIWC) RADAR Flight Campaigns. SAE Technical Paper 2019–01–2027 (NASA/TM—2020-220306), 2020. https://ntrs.nasa.gov
18. Strapp, J.W., et al.: An Assessment of Cloud Total Water Content and Particle Size From Flight Test Campaign Measurements in High Ice Water Content, Mixed Phase/Ice Crystal Icing Conditions: Primary In-Situ Measurements. DOT/FAA/TC–18/1, 2020. https://www.tc.faa.gov/its/worldpac/techrpt/tc18-1.pdf Accessed June 17, 2024
19. U.S. Code of Federal Regulations: Mixed Phase and Ice Crystal Icing Envelope (Deep Convective Clouds). Title 14, Part 33, Appendix D, 2015. https://www.ecfr.gov/on/2017-01-03/title-14/part-33/appendix-Appendix%20D%20to%20Part%2033 Accessed Dec. 31, 2024.
20. Strapp, J.W., et al.: Comparisons of Cloud In Situ Microphysical Properties of Deep Convective Clouds to Appendix D/P Using Data from the High-Altitude Ice Crystals-High Ice Water Content and High Ice Water Content-RADAR I Flight Campaigns. SAE Int. J. Aerosp., vol. 14, no. 2, 2021. https://doi.org/10.4271/01-14-02-0007 Accessed July 8, 2024.
21. Tritz, T., et al.: Correction: A Supplementary Analysis and Comparison of Flight Campaign Data to 14 CFR Part 33 Appendix D/CS 25 Appendix P. AIAA 2021–2644.c1, 2021. https://doi.org/10.2514/6.2021-2644.c1 Accessed July 8, 2024.
22. Rosenfeld, D.: TRMM Observed First Direct Evidence of Smoke From Forest Fires Inhibiting Rainfall. Geophys. Res. Lett., vol. 26, no. 20, 1999, pp. 3105–3108. https://doi.org/10.1029/1999GL006066 Accessed Dec. 31, 2024.
23. Rosenfeld, D., et al.: Flood or Drought: How Do Aerosols Affect Precipitation? Science, vol. 321, 2008, pp. 1309–1313. https://doi.org/10.1126/science.1160606 Accessed July 8, 2024.
24. Zhang, J., et al.: A System for Operational Aerosol Optical Depth Data Assimilation Over Global Oceans. J. Geophys. Res., vol. 113, no. D10208, 2008. https://doi.org/10.1029/2007JD009065 Accessed July 12, 2024.
25. Nowottnick, E., et al.: Overview of NASA's Convective Processes Experiment – Cabo Verde (CPEX-CV) in the East Atlantic in September 2022 and Collaboration With the Joint Aeolus Tropical Atlantic Campaign (JATAC). EGU23–8956, 2023. https://doi.org/10.5194/egusphere-egu23-8956 Accessed Dec. 31, 2024.
26. Nowottnick, E.P., et al.: Dust, Convection, Winds and Waves: The 2022 NASA CPEX-CV Campaign. Bull. Amer. Meteor. Soc., vol. 105, no. 11, 2024, pp. E2097–E2125. https://doi.org/10.1175/BAMS-D-23-0201.1 Accessed Dec. 31, 2024.
27. Strapp, J.W., et al.: Summary of Additional In-situ Cloud Data in High Ice Water Content Conditions From Three Recent Flight Campaigns. AIAA 2024–3931, 2024. https://doi.org/10.2514/6.2024-3931 Accessed Dec. 31, 2024.
28. Strapp, J.W., et al.: Isokinetic TWC Evaporator Probe: Development of the IKP2 and Performance Testing for the HAIC–HIWC Darwin 2014 and Cayenne Field Campaigns. AIAA 2016–4059, 2016. https://dx.doi.org/10.2514/6.2016-4059 Accessed Dec. 31, 2024.
29. Davison, C.R., et al.: Isokinetic TWC Evaporator Probe: Calculations and Systemic Uncertainty Analysis. AIAA 2016–4060, 2016. https://doi.org/10.2514/6.2016-4060 Accessed Dec. 31, 2024.
30. Lilie, Lyle E.; Sivo, C.P.; and Bouley, D.B.: Description and Results for a Simple Ice Crystal Detection System for Airborne Applications. AIAA 2016–4058, 2016. https://dx.doi.org/10.2514/6.2016-4058 Accessed Dec. 31, 2024.

31. Chen, R-C., et al.: Analysis of Hot-Wire Probe Ice Water Content Measurements in High Ice Water Content Conditions. AIAA 2024–3929. https://doi.org/10.2514/6.2024-3929 Accessed Dec. 31, 2024.
32. Diskin, G.S., et al.: Open-Path Airborne Tunable Diode Laser Hygrometer. Proc. SPIE, vol. 4817, 2002, pp. 196–204.
33. NASA Airborne Science Program: Diode Laser Hygrometer (DLH). 2019. https://airbornescience.nasa.gov/instrument/DLH Accessed July 24, 2024.
34. Korolev, A.; Emery, E.; and Creelman, K.: Modification and Tests of Particle Probe Tips to Mitigate Effects of Ice Shattering. J. Atmos. Oceanic Technol., vol. 30, 2013, pp. 690–708. https://doi.org/10.1175/JTECH-D-12-00142.1 Accessed Dec. 31, 2024.
35. Korolev, A.V., et al.: Small Ice Particles in Tropospheric Clouds: Fact or Artifact? Airborne Icing Instrumentation Evaluation Experiment. Bull. Amer. Met. Soc., vol. 92, 2011, pp. 967–973. https://doi.org/10.1175/2010BAMS3141.1 Accessed Dec. 31, 2024.
36. McNaughton, C.S., et al.: Results From the DC–8 Inlet Characterization Experiment (DICE): Airborne Versus Surface Sampling of Mineral Dust and Sea Salt Aerosols. Aerosol Sci. Tech, vol. 41, no. 2, pp. 136–159. https://doi.org/10.1080/02786820601118406 Accessed July 16, 2024.
37. Harrah, S., et al.: Radar Detection of High Concentrations of Ice Particles – Methodology and Preliminary Flight Test Results. SAE Technical Paper 2019–01–2028 (NASA/TP-2019-220433), 2019. https://doi.org/10.4271/2019-01-2028 Accessed Dec. 31, 2024.
38. Ratvasky, T.P., et al.: Air Data Probe Anomalies in Flight Through Measured High Ice Water Content Conditions. AIAA 2024–3930, 2024. https://doi.org/10.2514/6.2024-3930 Accessed Dec. 31, 2024.
39. National Aeronautics and Space Administration: Langley Satellite Support for High Ice Water Content (HIWC) Radar 2022 Campaign. https://satcorps.larc.nasa.gov/cgi-bin/site/showdoc?docid=4&cmd=flight-track-calendar&exp=HIWC–2022&ds=DC8&cc=2022 Accessed Dec. 31, 2024.
40. Konwar, M., et al.: Suppression of Warm Rain by Aerosols in Rain-Shadow Areas of India. Atmos. Chem. Phys. Discuss., vol. 10, 2010, pp. 17009–17027. https://doi.org/10.5194/acpd-10-17009-2010 Accessed Dec. 31, 2024.
41. Takemura, T., et al.: Global Three-Dimensional Simulation of Aerosol Optical Thickness Distribution of Various Origins. J. Geophys. Res., vol. 105, 2000, pp. 17853–17873. https://doi.org/10.1029/2000JD900265 Accessed Dec. 31, 2024.
42. Takemura, T., T. Nakajima, O. Dubovik, B. N. Holben, and S. Kinne, 2002: Single-scattering albedo and radiative forcing of various aerosol species with a global three-dimensional model. Journal of Climate, 15, 333-352.
43. Takemura, T., T. Nozawa, S. Emori, T. Y. Nakajima, and T. Nakajima, 2005: Simulation of climate response to aerosol direct and indirect effects with aerosol transport-radiation model. Journal of Geophysical Research, 110, D02202, doi:10.1029/2004JD005029
44. Svensmark, Henrik, et al.: Supersaturation and Critical Size of Cloud Condensation Nuclei in Marine Stratus Clouds. Geophys. Res. Lett., vol. 51, no. 9, 2024, p. e2024GL108140. https://doi.org/10.1029/2024GL108140 Accessed April 21, 2025.
45. Petters, M.D.; and Kreidenweis, S.M.: A Single Parameter Representation of Hygroscopic Growth and Cloud Condensation Nucleus Activity, Atmos. Chem. Phys., vol. 7, 2007, pp. 1961–1971. https://doi.org/10.5194/acp-7-1961-2007 Accessed Dec. 31, 2024.

46. Adachi, K., et al.: Mixing States of Amazon Basin Aerosol Particles Transported Over Long Distances Using Transmission Electron Microscopy. Atmos. Chem. Phys., vol. 20, 2020, pp. 11923–11939. https://doi.org/10.5194/acp-20-11923-2020 Accessed Dec. 31, 2024.
47. Iwata, A.; and Matsuki, A.: Characterization of Individual Ice Residual Particles by the Single Droplet Freezing Method: A Case Study in the Asian Dust Outflow Region. Atmos. Chem. Phys., vol. 18, 2018, pp. 1785–1804. https://doi.org/10.5194/acp-18-1785-2018 Accessed Dec. 31, 2024.
48. Price, H.C., et al.: Atmospheric Ice-Nucleating Particles in the Dusty Tropical Atlantic. JGR Atmos., vol. 123, 2018, pp. 2175–2193. https://doi.org/10.1002/2017JD027560 Accessed Jan. 15, 2025.
49. Orikasa, N., et al.: CCN and INP Abilities of Aerosol Particles Measured During HIWC–2022 and CPEX-CV Campaigns. 2023. https://www.eol.ucar.edu/sites/default/files/2024-10/3orikasaccninp20231129v1as.pdf Accessed Jan. 15, 2025.
50. Andreae, M.O.; and Rosenfeld, D.: Aerosol-Cloud-Precipitation Interactions, Part 1, The Nature and Sources of Cloud-Active Aerosols. Earth Sci. Rev., vol. 89, 2008, pp. 13–41. https://dx.doi.org/10.1016/j.earscirev.2008.03.001 Accessed Jan. 15, 2025.
51. Petters, M.D.; and Wright, T.P.: Revisiting Ice Nucleation From Precipitation Samples. Geophys. Res. Lett., vol. 42, 2015, pp. 8758–8766. https://doi.org/10.1002/2015GL065733 Accessed Jan. 15, 2025.
52. American Meteorological Society: Graupel. Glossary of Meteorology. 2012. https://glossarystaging.ametsoc.net/wiki/Graupel Accessed Oct. 17, 2024.
53. Bansemer, A.: abansemer/soda2: v2.24.0. Zenodo, 2024. https://doi.org/10.5281/zenodo.10914403 Accessed Jan. 15, 2025.
54. American Meteorological Society: Lightning. Glossary of Meteorology, 2012. https://glossary.ametsoc.org/wiki/Lightning Accessed Nov. 13, 2024.
55. Pruppacher, H.R.; and Klett, J.D.: Microphysics of Clouds and Precipitation. Kluwer Academic Publication, Second ed., 1997.
56. Rogers, R.R.; and Yau, M.K.: A Short Course in Cloud Physics. Pergamon Press, New York, 1989.
57. Lamb, D.; and Verlinde, J.: Physics and Chemistry of Clouds. Cambridge University Press, 2011.
58. Houghton, H.G.: Problems Connected With the Condensation and Precipitation Processes in the Atmosphere. Bull. Am. Meteorol. Soc., vol. 19, 1938, pp. 152–159. https://dx.doi.org/10.1175/1520-0477-19.4.152 Accessed Jan. 15, 2025.
59. Bowen, E.G.: The Formation of Rain by Coalescence. Aust. J. Sci. Res., vol. A3, 1950, pp. 192–213.
60. Ludlam, F.H.: The Production of Showers by the Coalescence of Cloud Droplets. Quart. J. Roy. Meteor. Soc., vol. 77, 1951, pp. 402–417. https://dx.doi.org/10.1002/qj.49707733306 Accessed Jan. 15, 2025.
61. Telford, J.W.: A New Aspect of Coalescence Theory. J. Meteor., vol. 12, 1955, pp. 436–444. https://dx.doi.org/10.1175/1520-0469(1955)012%3C0436:ANAOCT%3E2.0.CO;2 Accessed Jan. 15, 2025.
62. Twomey, S.: Influence of Pollution on Shortwave Albedo of Clouds. J. Atmos. Sci., vol. 34, 1977, pp. 1149–1152. https://dx.doi.org/10.1175/1520-0469(1977)034%3C1149:TIOPOT%3E2.0.CO;2 Accessed Jan. 15, 2025.
63. Myhre, G., et al.: Aerosols and Their Relation to Global Climate and Climate Sensitivity. Nature Education Knowledge, vol. 4, no. 5, 2013, p. 7.
64. Johnson, D.B.: The Role of Giant and Ultragiant Aerosol Particles in Warm Rain Initiation. J. Atmos. Sci., vol. 39, 1982, pp. 448–460. https://doi.org/10.1175/1520-0469(1982)039%3C0448:TROGAU%3E2.0.CO;2 Accessed Jan. 16, 2025.

65. Woodcock, A.H.: Salt Nuclei in Marine Air as a Function of Altitude and Wind Force. J. Meteor., vol. 10, 1953, pp. 362–371. https://doi.org/10.1175/15200469(1953)010%3C0366:SNIMAA%3E2.0.CO;2 Accessed Jan. 16, 2025.
66. Beard, K.V.; Johnson, D.B.; and Baumgardner, D.: Aircraft Observations of Large Raindrops in Warm, Shallow, Convective Clouds. Geophysical. Res. Lett., vol. 13, 1986, pp. 991–994. https://dx.doi.org/10.1029/GL013i010p00991 Accessed Jan. 16, 2025.
67. Rauber, R.M.; Beard, K.V.; and Andrews, B.M.: A Mechanism for Giant Raindrop Formation in Warm, Shallow, Convective Clouds. J. Atmos. Sci., vol. 48, 1991, pp. 1791–1797. https://dx.doi.org/10.1175/1520-0469(1991)048%3C1791:AMFGRF%3E2.0.CO;2 Accessed Jan. 16, 2025.
68. Rauber, R.M., et al.: Rain in Shallow Cumulus Over the Ocean: The RICO Campaign. Bull. Amer. Meteor. Soc., vol. 88, 2007, pp. 1912–1928. https://doi.org/10.1175/BAMS-88-12-1912 Accessed Jan. 16, 2025.
69. Khain, A., et al.: Mechanism of First Raindrops Formation in Deep Convective Clouds, J. Geophys. Res., vol. 118, 2013, pp. 9123–9140. https://doi.org/10.1002/jgrd.50641 Accessed Jan. 16, 2025.
70. Konwar, M., et al.: Aerosol Control on Depth of Warm Rain in Convective Clouds. J. Geophys. Res., vol. 117, no. D13204, 2012. https://doi.org/10.1029/2012JD017585 Accessed Jan. 16, 2025.
71. Wendisch, M., et al.: ACRIDICON–CHUVA Campaign: Studying Tropical Deep Convective Clouds and Precipitation Over Amazonia Using the New German Research Aircraft HALO. Bull. Amer. Meteor. Soc., vol. 97, no. 10, 2016, pp. 1885–1908. https://doi.org/10.1175/BAMS-D-14-00255.1 Accessed Jan. 16, 2025.
72. Braga, R.C., et al.: Further Evidence for CCN Aerosol Concentrations Determining the Height of Warm Rain and Ice Initiation in Convective Clouds Over the Amazon Basin. Atmos. Chem. Phys., vol. 17, no. 23, 2017a, pp. 14433–14456. https://doi.org/10.5194/acp-17-14433-2017 Accessed Jan. 16, 2025.
73. Braga, R.C., et al.: Comparing Parameterized Versus Measured Microphysical Properties of Tropical Convective Cloud Bases During the ACRIDICON–CHUVA Campaign. Atmos. Chem. Phys., vol. 17, no. 12, 2017b, pp. 7365–7386. https://doi.org/10.5194/acp-17-7365-2017 Accessed Jan. 16, 2025.
74. Feingold, G., et al.: The Impact of Giant Cloud Condensation Nuclei on Drizzle Formation in Stratocumulus: Implications for Cloud Radiative Properties. J. Atmos. Sci., vol. 56, no. 24, 1999, pp. 4100–4117. https://doi.org/10.1175/1520-0469(1999)056<4100:TIOGCC>2.0.CO;2 Accessed Jan. 16, 2025.
75. Yin, Y., et al.: The Effects of Giant Cloud Condensational Nuclei on the Development of Precipitation in Convective Clouds: A Numerical Study. Atmos. Res., vol. 53, nos. 1–3, 2000, pp. 91–116. https://dx.doi.org/10.1016/S0169-8095(99)00046-0 Accessed Jan. 16, 2025.
76. Rosenfeld, D., et al.: The Role of Sea Spray in Cleansing Air Pollution Over Ocean via Cloud Processes. Science, vol. 297, no. 5587, 2002, pp. 1667–1670. https://dx.doi.org/10.1126/science.1073869 Accessed Jan. 16, 2025.
77. Lu, M.-L.; and Seinfeld, J.H.: Study of the Aerosol Indirect Effect by Large-Eddy Simulation of Marine Stratocumulus. J.Atmos. Sci., vol. 62, no. 11, 2005, pp. 3909–3932. https://doi.org/10.1175/JAS3584.1 Accessed Jan. 16, 2025.
78. Teller, A.; and Levin, Z.: The Effects of Aerosols on Precipitation and Dimensions of Subtropical Clouds: A Sensitivity Study Using a Numerical Cloud Model, Atmos. Chem. Phys., vol. 6, no. 1, 2006, pp. 67–80. https://dx.doi.org/10.5194/acp-6-67-2006 Accessed Jan. 16, 2025.

79. Jensen, J.B.; and Lee, S.: Giant Sea-Salt Aerosols and Warm Rain Formation in Marine Stratocumulus. J. Atmos. Sci., vol. 65, no. 12, 2008, pp. 3678–3694. https://doi.org/10.1175/2008JAS2617.1 Accessed Jan. 16, 2025.
80. Cheng, W.Y.Y., et al.: Influence of Cloud Condensation and Giant Cloud Condensation Nuclei on the Development of Precipitating Trade Wind Cumuli in a Large Eddy Simulation. JGR Atmos., vol. 114, no. D08201, 2009. https://doi.org/10.1029/2008JD011011 Accessed Jan. 16, 2025.
81. Dagan, G.; Koren, I.; and Altaratz, O.: Competition Between Core and Periphery-Based Processes in Warm Convective Clouds—From Invigoration to Suppression. Atmos. Chem. Phys., vol. 15, no. 5, 2015, pp. 2749–2760. https://doi.org/10.5194/acp-15-2749-2015 Accessed Jan. 16, 2025.
82. Hudson, J.G.; and Yum, S.S.: Maritime-Continental Drizzle Contrasts in Small Cumuli. J. Atmos. Sci., vol. 58, no. 8, 2001, pp. 915–926. https://dx.doi.org/10.1175/1520-0469(2001)058%3C0915:MCDCIS%3E2.0.CO;2 Accessed Jan. 17, 2025.
83. Ochs III, H.T.; and Semonin, R.G.: Sensitivity of a Cloud Microphysical Model to an Urban Environment. J. Appl. Meteor. Climatol., vol. 18, no. 9, 1979, pp. 1118–1129. https://dx.doi.org/10.1175/1520-0450(1979)018%3C1118:SOACMM%3E2.0.CO;2 Accessed Jan. 17, 2025.
84. Beard, K.V.; and Ochs III, H.T.: Warm-Rain Initiation: An Overview of Microphysical Mechanisms. J. Appl. Meteorol. Climatol., vol. 32, no. 4, 1993, pp. 608–625. https://dx.doi.org/10.1175/1520-0450(1993)032%3C0608:WRIAOO%3E2.0.CO;2 Accessed Jan. 17, 2025.
85. Szumowski, M.J.; Rauber, R.M.; and Ochs III, H.T.: The Microphysical Structure and Evolution of Hawaiian Rainband Clouds. Part III: A Test of the Ultragiant Nuclei Hypothesis. J. Atmos. Sci., vol. 56, no. 12, 1999, pp. 1980–2003. https://doi.org/10.1175/1520-0469(1999)056<1980:TMSAEO>2.0.CO;2 Accessed Jan. 17, 2025.
86. Lasher-Trapp, S.G.; Knight, C.A.; and Straka, J.M.: Early Radar Echoes From Ultragiant Aerosol in a Cumulus Congestus: Modeling and Observations. J. Atmos. Sci., vol. 58, no. 23, 2001, pp. 3545–3562. https://dx.doi.org/10.1175/1520-0469(2001)058%3C3545:EREFUA%3E2.0.CO;2 Accessed Jan. 17, 2025.
87. Blyth, A.M., et al.: The Role of Giant and Ultragiant Nuclei in the Formation of Early Radar Echoes in Warm Cumulus Clouds. J. Atmos. Sci., vol. 60, no. 21, 2003, pp. 2557–2572. https://doi.org/10.1175/1520-0469(2003)060%3C2557:TROGAU%3E2.0.CO;2 Accessed Jan. 17, 2025.
88. Lowenstein, J.H.; Blyth, A.M.; and Lawson, R.P.: Early Evolution of the Largest-Sized Droplets in Maritime Cumulus Clouds. Quart. J. Roy. Meteor. Soc., vol. 136, no. 648, 2010, pp. 708–717. https://doi.org/10.1002/qj.597 Accessed Jan. 17, 2025.
89. Kogan, Y.L.; Mechem, D.B.; and Choi, K.: Effects of Sea-Salt Aerosols on Precipitation in Simulations of Shallow Cumulus. J. Atmos. Sci., vol. 69, no. 2, 2012, pp. 463–483. https://doi.org/10.1175/JAS-D-11-031.1 Accessed Jan. 17, 2025.
90. Cooper, W.A.; Lasher-Trapp, S.G.; and Blyth, A.M.: The Influence of Entrainment and Mixing on the Initial Formation of Rain in a Warm Cumulus Cloud. J. Atmos. Sci., vol. 70, no. 6, 2013, pp. 1727–1743. https://doi.org/10.1175/JAS-D-12-0128.1 Accessed Jan. 17, 2025.
91. Jensen, J.B.; and Nugent, A.D.: Condensational Growth of Drops Formed on Giant Sea-Salt Aerosol Particles. J. Atmos. Sci., vol. 74, no. 3, 2017, pp. 679–697. https://doi.org/10.1175/JAS-D-15-0370.1 Accessed Jan. 17, 2025.
92. Gerber, H.; and Frick, G.: Drizzle Rates and Large Sea-Salt Nuclei in Small Cumulus. J. Geophy. Res., vol. 117, no. D01205, 2012. https://doi:10.1029/2011JD016249 Accessed Jan. 17, 2025.

93. Khain, A., et al.: Notes on the State-of-the-Art Numerical Modeling of Cloud Microphysics. Atmos. Res., vol. 55, nos. 3–4, 2000, pp. 159–224. https://dx.doi.org/10.1016/S0169-8095(00)00064-8 Accessed Jan. 17, 2025.
94. Zhang, L.; Michelangeli, D.V.; and Taylor, P.A.: Influence of Aerosol Concentration on Precipitation Formation in Low Level, Warm Stratiform Clouds. J. Aerosol Sci., vol. 37, no. 2, 2006, pp. 203–217. https://doi.org/10.1016/j.jaerosci.2005.04.002 Accessed Jan. 17, 2025.
95. Goke, S.; Ochs III, H.T.; and Rauber, R.M.: Radar Analysis of Precipitation Initiation in Maritime Versus Continental Clouds Near the Florida Coast: Inferences Concerning the Role of CCN and Giant Nuclei. J. Atmos. Sci., vol. 64, no. 10, 2007, pp. 3695–3707. https://doi.org/10.1175/JAS3961.1 Accessed Jan. 17, 2025.
96. Reiche, C.H.; and Lasher-Trapp, S.: The Minor Importance of Giant Aerosol to Precipitation Development Within Small Trade Wind Cumuli Observed During RICO. Atmos. Res., vol. 95, no. 4, 2010, pp. 386–399. https://doi.org/10.1016/j.atmosres.2009.11.002 Accessed Jan. 17, 2025.
97. Blyth, A.M., et al.: The Production of Warm Rain in Shallow Maritime Cumulus Clouds. Quart. J. Roy. Meteor. Soc., vol. 139, no. 670, 2013, pp. 20–31. https://doi.org/10.1002/qj.1972 Accessed Jan. 17, 2025.
98. Dziekan, P., et al.: Impact of Giant Sea Salt Aerosol Particles on Precipitation in Marine Cumuli and Stratocumuli: Lagrangian Cloud Model Simulations. J. Atmos. Sci., vol. 78, no. 12, 2021, pp. 4127–4142. https://doi.org/10.1175/JAS-D-21-0041.1 Accessed Jan. 17, 2025.
99. Twomey, S.: Computations of Rain Formation by Coalescence. J. Atmos. Sci., vol. 23, no. 4, 1966, pp. 405–411. https://doi.org/10.1175/1520-0469(1966)023<0405:CORFBC>2.0.CO;2 Accessed Jan. 17, 2025.
100. List, R.; and Gillespie, J.R.: Evolution of Raindrop Spectra With Collision-Induced Breakup. J. Atmos. Sci., vol. 33, no. 10, 1976, pp. 2007–2013. https://doi.org/10.1175/1520-0469(1976)033%3C2007:EORSWC%3E2.0.CO;2 Accessed Jan. 21, 2025.
101. Gillespie, J.R.; and List, R.: Effects of Collision-Induced Breakup on Size Distributions in Steady-State Rainshafts. Pure Appl. Geophys., vol. 117, 1978, pp. 599–626. https://dx.doi.org/10.1007/BF00879971 Accessed Jan. 21, 2025.
102. Low, T.B.; and List, R.: Collision, Coalescence and Breakup of Raindrops. Part I: Experimentally Established Coalescence Efficiencies and Fragment Size Distributions in Breakup. J. Atmos. Sci., vol. 39, no. 7, 1982, pp. 1591–1606. https://doi.org/10.1175/1520-0469(1982)039%3C1591:CCABOR%3E2.0.CO;2 Accessed Jan. 21, 2025.
103. Strapp, J.W.: Inventory and Overview of Microphysical Observations From TCu Sampling. 2023. https://www.eol.ucar.edu/sites/default/files/2024-10/6strappinventory-and-overview-tcusampling.pdf Accessed Jan. 21, 2025.
104. Hallett, J.; and Mossop, S.C.: Production of Secondary Ice Particles During the Riming Process. Nature, vol. 249, 1974, pp. 26–28. https://doi.org/10.1038/249026a0 Accessed Jan. 21, 2025.
105. Takahashi, C.: Deformations of Frozen Water Drops and Their Frequencies. J. Meteorol. Soc. Jpn. vol. 53, no. 6, 1975, pp. 402–411. https://doi.org/10.2151/jmsj1965.53.6_402 Accessed Jan. 21, 2025.
106. Wildeman, S., et al.: Fast Dynamics of Water Droplets Freezing from the Outside In. Phys. Rev. Lett., vol. 118, no. 014101, 2017. https://doi.org/10.1103/PhysRevLett.118.084101 Accessed Jan. 21, 2025.
107. Field, P.R., et al.: Secondary Ice Production: Current State of the Science and Recommendations for the Future. Meteor. Monogr., vol. 58, no. 1, 2017, pp. 7.1–7.20. https://doi.org/10.1175/AMSMONOGRAPHS-D-16-0014.1 Accessed Jan. 21, 2025.

108. Korolev, A.; and Leisner, T.: Review of Experimental Studies of Secondary Ice Production. Atmos. Chem. Phys., vol. 20, no. 20, 2020, pp. 11767–11797. https://doi.org/10.5194/acp-20-11767-2020 Accessed Jan. 21, 2025.
109. Korolev, A., et al.: High Ice Water Content in Tropical Mesoscale Convective Systems (A Conceptual Model). Atmos. Chem. Phys., vol. 24, no. 20, 2024, pp. 11849–11881. https://doi.org/10.5194/acp-24-11849-2024. Accessed Jan. 21, 2025.
110. Beard, K.V.: Ice Initiation in Warm-Base Convective Clouds: An Assessment of Microphysical Mechanisms. Atmos. Res., vol. 28, no. 2, 1992, pp. 125–152. https://doi.org/10.1016/0169-8095(92)90024-5 Accessed Jan. 21, 2025.
111. Lauber, A., et al.: Secondary Ice Formation During Freezing of Levitated Droplets. J. Atmos. Sci., vol. 75, no. 8, 2018, pp. 2815–2826. https://doi.org/10.1175/JAS-D-18-0052.1 Accessed Jan. 21, 2025.
112. Lawson, P., et al.: Aircraft Observations of Cumulus Microphysics Ranging From the Tropics to Midlatitudes: Implications for a "New" Secondary Ice Process. J. Atmos. Sci., vol. 74, no. 9, 2017, pp. 2899–2920. https://doi.org/10.1175/JAS-D-17-0033.1 Accessed Jan. 21, 2025.
113. Lawson, R.P.; Woods, S.; and Morrison, H.: The Microphysics of Ice and Precipitation Development in Tropical Cumulus Clouds. J. Atmos. Sci., vol. 72, no. 9, 2015, pp. 2429–2445. https://doi.org/10.1175/JAS-D-14-0274.1 Accessed Jan. 21, 2025.
114. Yano, J-I.; Phillips, V.T.J.; and Kanawade, V.: Explosive Ice Multiplication by Mechanical Break-Up in Ice–Ice Collisions: A Dynamical System-Based Study. Quart. J. Roy. Meteor. Soc., vol. 142, no. 695, 2016, pp. 867–879. https://doi.org/10.1002/qj.2687 Accessed Jan. 21, 2025.
115. Phillips, V.T.J., et al.: Secondary Ice Production by Fragmentation of Freezing Drops: Formulation and Theory. J. Atmos. Sci., vol. 75, no. 9, 2018, pp. 3031–3070. https://doi.org/10.1175/JAS-D-17-0190.1 Accessed Jan. 21, 2025.
116. American Meteorological Society: Large eddy simulation. Glossary of Meteorology, 2012. https://glossary.ametsoc.org/wiki/Large_eddy_simulation Accessed Feb. 4, 2025.
117. Proctor, F.H.: The Terminal Area Simulation System, Volume I: Theoretical Formulation. NASA Contractor Report 4046 (DOT/FAA/PM-86/50-VOL-1), 1987. https://ntrs.nasa.gov
118. Proctor, F.H.; and Switzer, G.F.: High Ice Water Content Associated With a Darwin, Australia, Mesoscale Convective System. NASA/TM-20205010032, 2020. https://ntrs.nasa.gov
119. Proctor, F.H., et al.: High Ice Water Content in Tropical Cyclones During NASA/FAA Radar Flight Campaigns With Comparisons to Numerical Simulations. NASA/TM-20205010118, 2020. https://ntrs.nasa.gov
120. Proctor, F.H., et al.: High Ice Water Concentrations in the 19 August 2015 Coastal Mesoconvective System. AIAA 2017–4370, 2017. https://doi.org/10.2514/6.2017-4370 Accessed Jan. 21, 2025.
121. Houze, R.A., Jr.: Observed Structure of Mesoscale Convective Systems and Implications for Large-Scale Heating. Quart. J. Roy. Meteor. Soc., vol. 115, no. 487, 1989, pp. 425–461. https://doi.org/10.1002/qj.49711548702 Accessed Jan. 21, 2025.
122. Simpson, J.; and Wiggert, V.: Models of Precipitating Cumulus Towers. Mon. Wea. Rev., vol. 97, no. 7, 1969, pp. 471–489. https://doi.org/10.1175/1520-0493(1969)097%3C0471:MOPCT%3E2.3.CO;2 Accessed Jan. 21, 2025.
123. Knight, C.A.; and Squires, P., eds.: Hailstorms of the Central High Plains, Vol. 1. The National Hail Research Experiment. Colorado Associated University Press, Boulder, CO, 1982.
124. Tsuboki, K.; and Sakakibara, A.: CReSS: Cloud Resolving Storm Simulator User's Guide Ver 2, 2000. http://www.rain.hyarc.nagoya-u.ac.jp/~tsuboki/kyoto_dpri_17g-c1/cress_html/guide_eng/CReSS_users_guide_Eng_draft01.pdf Accessed Jan. 21, 2025.

125. Lee, S.S., et al.: The Dependence of Aerosol Effects on Clouds and Precipitation on Cloud-System Organization, Shear and Stability. JGR Atmos., vol. 113, no. D16, 2008. https://doi.org/10.1029/2007JD009224 Accessed Dec. 31, 2024.
126. Strapp, J.W.: Investigation of Warm Rain During HIWC–2022 TCu Runs. Presented at the HIWC–2022 Science Team Workshop, Boulder, CO, 2023. https://www.eol.ucar.edu/sites/default/files/2024-10/8strappinvestigationofwarmrainduringtcuruns.pdf Accessed Feb. 7, 2025.